Chemical Vapor Deposition of Diamond in Flames and Fluidized Beds

Thesis by

Ho Seon Shin

In Partial Fulfillment of the Requirements

for the Degree of

Doctor of Philosophy

California Institute of Technology

Pasadena, California

1996

(Submitted July 13, 1995)

Acknowledgments

First of all, I would like to express my deep gratitude and indebtedness to my advisor, Professor David Goodwin, for his guidance, support, and encouragement over the past five years. His insight, ideas, and enthusiasm for research have always been an inspiration for me. When I encountered difficulties with my research, he was always there to offer me direction and encouragement. I also would especially like to thank Nick Glumac, who has been a good friend and was available for expert advice at crucial points during my experiments. Much of what I have learned about experimental techniques was available only from him, and his tremendous work done for our laboratory made my research a lot easier and more fruitful.

I am grateful to Joong Soo Kim, Evaldo Corat, Stephen Harris, and Dale Capewell for insightful discussions and their helpful suggestions. I would like to thank Nancy Winfree, Joe Kang, Vassilis Christophilos, and Haseo Ki, for their friendship and encouragement. I especially thank Ashok Tripathi who willingly helped in proof reading. This thesis is much improved by his comments and suggestions.

Finally, my deepest thanks to my parents, Hyun Hee, and Seungyoon for the greatest love, unwavering support, and constant encouragement. Without them, I could not have been what I am.

This work was supported in part by the National Science Foundation and the Naval Research Laboratory. Partial scholarship support was provided by the Korean Government.

Abstract

An experimental and computational study of chemical vapor deposition (CVD) of diamond in low pressure flames, and an experimental study of microwave plasma-enhanced CVD of diamond on particles in fluidized beds are presented. Diamond film growth experiments were performed in low pressure (30–52 Torr) acetylene/oxygen flames and the effects of varying substrate temperature, equivalence ratio, and pressure on diamond growth were examined. Uniform diamond films fully covering 5 cm diameter substrates at growth rates of up to 2.3 μm/hr were grown at 30 Torr using a 4 cm diameter flat flame burner. A carbon-conversion efficiency of up to 3.5×10^{-5} was obtained which was comparable to that observed in the atmospheric pressure torch method. The Raman spectrum of the deposited film showed good diamond film quality.

To extend the combustion synthesis technique for diamond to fuels other than acetylene, and to reduce the cost of diamond produced by combustion synthesis, growth experiments using several alternative hydrocarbon fuels (MAPP, propylene, ethylene, and propane) were performed at 50–180 Torr. Well-faceted diamond films at growth rates of up to 1.0 μm/hr were grown in these alternative fuel flames. The Raman spectrum analysis showed that good quality diamond films were grown in MAPP/oxygen and propylene/oxygen flames. An economic comparison study showed that switching from acetylene to propylene may be able to lower the fuel cost per unit mass of diamond by roughly a factor of three.

A numerical modeling study was performed to analyze the growth environment. The model predicts peak flame temperatures above the adiabatic flame temperature, and a chemical environment near the substrate far from its equilibrium state. Surface concentrations of H and CH_3, and the ratio of H to CH_3 mole fractions in low pressure acetylene/oxygen flames are similar to those observed in hot filament reactors. The simulations of low pressure (25–30 Torr) acetylene/oxygen flames near diamond growth conditions suggest that increasing the mass flow rate while reducing the pressure is favorable for increasing the growth rate, and high quality diamond can be grown in leaner flames.

Although the values are slightly lower than for acetylene/oxygen flames, alternative fuel flames are predicted to have high enough H and CH_3 concentrations at the substrate to grow diamond at a reasonable growth rate. The results indicate that nonequilibrium flame chemistry is important in the low pressure combustion environment. This suggests that still other fuels may be worth considering for diamond growth at low pressures. Further studies employing alternative fuels other than acetylene could potentially further reduce the cost of diamond produced by combustion synthesis, and could potentially reduce the barriers to commercializing the combustion synthesis of diamond for many applications.

To grow continuous, conformal diamond coatings on small, irregular objects, experiments were performed using microwave plasma-enhanced fluidized beds. Studies were carried out to map the parameter space leading to diamond growth and to deter-

mine the relationship between gas composition and diamond growth rate. The effects of varying gas composition and pressure on deposited carbon morphology, growth rate, and nucleation density were examined in these experiments.

Oxygen addition had a strong influence on growth rate and morphology over the range of gas compositions studied. No diamond deposition was obtained without O_2. Well-faceted diamond at a growth rate of up to 6 μm/hr was observed to grow on 0.25–0.7 mm diameter silicon and SiO_2 seed particles using up to 15.0% CH_4 in H_2 with addition of O_2. Unlike diamond deposition on bulk substrates, no surface pretreatment was necessary for diamond nucleation. Well-faceted continuous diamond coatings were deposited on seed particles after 8 hours at a pressure of 9 Torr and 120 Watts of microwave power with flow rates of 160 sccm of 2.0% CH_4 in H_2 and 3 sccm of O_2. The micro-Raman spectrum of the deposited diamond crystal confirmed good diamond quality. These results show that plasma-enhanced fluidized beds can be effectively used to deposit diamond coatings on small objects of complex shape.

Contents

List of Figures

List of Tables

Chapter 1

Introduction

1.1 Background

Diamond is one of the most attractive industrial materials because of its unique combination of excellent mechanical, electrical and chemical characteristics. Still the hardest known material, diamond is resistant to wear, the best thermal conductor at room temperature, an excellent electric insulator, immune to attack from most chemicals, and transparent not only to visible light but also to infrared and ultraviolet. Other important properties of diamond include low friction coefficient, high bandgap, high Young's modulus, high free carrier saturation velocity, high resistance to radiation damage, semiconducting properties with doping, and high refractive index. These properties of diamond make it desirable for numerous applications, which include cutting tools, electronic substrates, semiconductor devices, infrared optical windows, ultraviolet detectors, and prosthetics. Figure 1-1 lists the key properties of diamond and potential applications of diamond coatings.

A carbon phase diagram is shown schematically in Figure 1-2. At room temperature and atmospheric pressure, the stable carbon phase is graphite (sp^2 bonded carbon), and diamond (sp^3 bonded carbon) is metastable.

Diamond synthesis has held a special attraction ever since it was established that diamond was a crystalline form of carbon. In 1955, General Electric first demonstrated synthetic diamond growth by high-pressure high-temperature (HPHT) process [1, 2], and these synthetic diamonds have been widely used in cutting tools, grinding wheels and polishing powders. Even though these HPHT process can make

Properties	Applications
Hardest known material Low coefficient of friction High thermal conductivity (highest known at room temperature) Low thermal expansion	Coatings for cutting tools Abrasive coatings Coatings for bearings
Heat resistive	Heat sinks for electronic devices
Acid resistive Radiation resistive (to X-ray, ultraviolet, γ-ray)	High-power microwave devices Radio-frequency electronic devices
Eletrical insulator High band gap semiconductor (either p- or n-doped)	High-speed electronic devices Sensors for severe environments
Low dielectric constant High hole mobility Visible and infrared transparent Large refractive index	Window and lens materials Electrooptic devices

Figure 1-1: Properties of diamond and potential applications of diamond coatings.

diamond particles inexpensively and in large quantities, there are some other potential applications of diamond which require thin films or coatings, and these can not be produced from either natural or HPHT synthetic diamonds.

Although diamond is the stable form of carbon at high pressure, synthetic diamond can be produced at low pressure. In fact, diamond is only slightly unstable with respect to graphite. At 298 K and 1 atm pressure, graphite is more stable than diamond only by a small free energy difference of 2.9 kJ/mole. However, there is a very large activation energy barrier ($\sim$ 730–1060 kJ/mole, depending on surface type

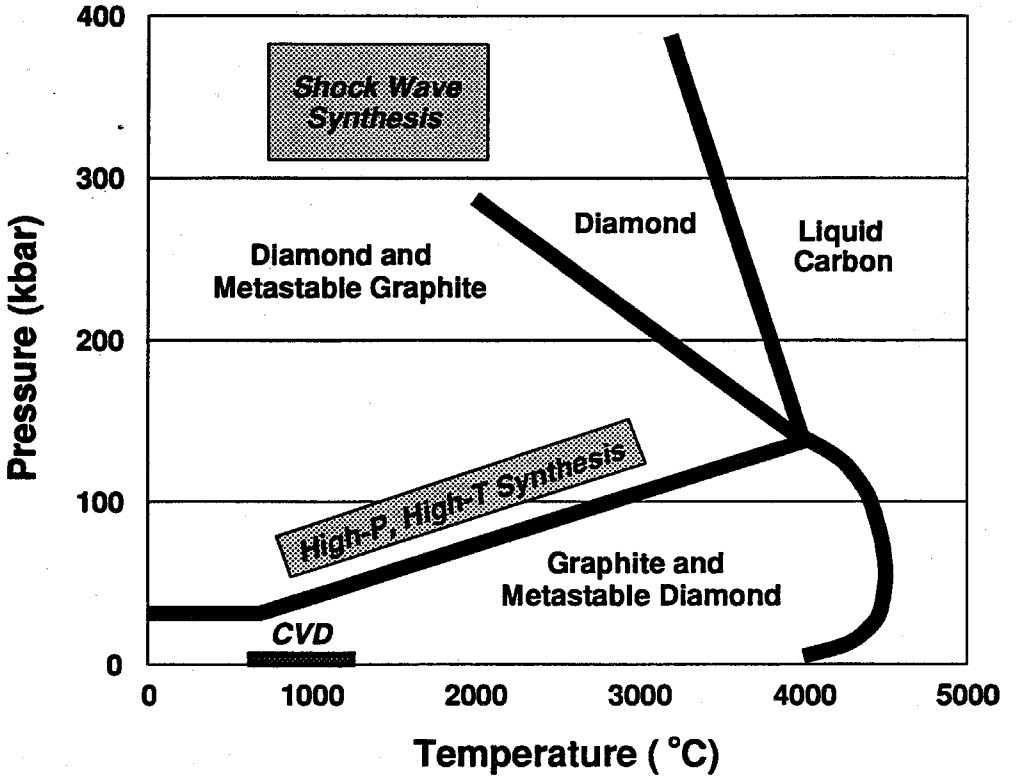

Figure 1-2: Carbon phase diagram.

[3]) inhibiting the spontaneous transformation of diamond to graphite. Because the activation energy between stable and metastable carbon states is so high, it serves as a barrier to interconversion, and metastable diamond can be formed under kinetically controlled conditions.

Diamond synthesis at pressures and temperatures where diamond is metastable with respect to graphite was first achieved by Eversole in 1962 [4]. Unpublished reports show that Eversole achieved growth of new diamond in 1953, two years earlier

than the first report of HPHT synthetic diamond by General Electric in 1955. Eversole grew new diamond on pre-existing diamond seeds, and Angus and co-workers [5] first confirmed Eversole's results in 1968. Angus *et al.* also first reported the use of atomic hydrogen, generated by a heated tungsten filament, for removing graphitic deposits and for conditioning the diamond surface for future diamond growth.

Chemical vapor deposition (CVD) is a process for depositing thin films from a chemical reaction of a vapor or gas. During a CVD process, gases that contain the atoms of the material to be deposited are introduced into the controlled environment of the process chamber. These gases react on the heated substrate surface, forming a thin film of desired solid material. It has been widely used to deposit thin films for microelectronic and micromechanical devices, as well as to deposit optical and wear coatings.

Since the breakthrough reports of diamond CVD onto non-diamond substrates with reasonable growth rates (~ 1 μm/hr) [6, 7] in early 1980's, there has been rapid progress in depositing diamond films from the gas phase onto suitable substrates [8], and a wide variety of low pressure synthesis methods have emerged. These methods involve producing diamond films at temperatures and pressures in which graphite is the thermodynamically stable phase of carbon and diamond is in the metastable state.

Typical CVD diamond films are polycrystalline with (111) or (100) faces (occasionally (110) faces). The crystallites usually contain many defects, for example,

twin planes, stacking faults, and point defects. However, advances in this technology have demonstrated that it is possible to fabricate free-standing, optically-transparent diamond wafers over 10 cm in diameter, up to 1 mm thick and with a finished surface roughness of less than 0.2 microns [9]. Extremely high quality material ("white diamond") can be produced with thermal, optical and electronic properties similar to natural IIa diamond. CVD diamond is now available in free-standing wafers for applications in electronic packaging and optics, and already being used in the production of laser diode and laser diode array heat sinks, and microwave substrates. However, for CVD diamond to be used in a wider range of applications would require a significant reduction in cost.

A variety of techniques, including hot filaments, RF and DC plasmas, microwave plasmas, arc jets, and combustion flames have been used to activate precursor gases to grow diamond films by CVD. Some typical CVD diamond growth techniques are shown schematically in Figure 1-3.

The two most common methods for achieving the required activation of the precursor gases are the use of a hot filament and a microwave plasma. In these methods, a mixture of $\sim$ 1% methane (CH_4) in hydrogen enters the reactor and flows past a heated filament ($\sim$ 2000 °C) or a plasma that decomposes the gases into atomic hydrogen and hydrocarbon radicals. The reactor is typically maintained at about 50 Torr, and the diamond film forms on a heated (700–1000 °C) substrate. Typical growth rates range from 0.1 to 10 μm/hr over a few cm^2 area.

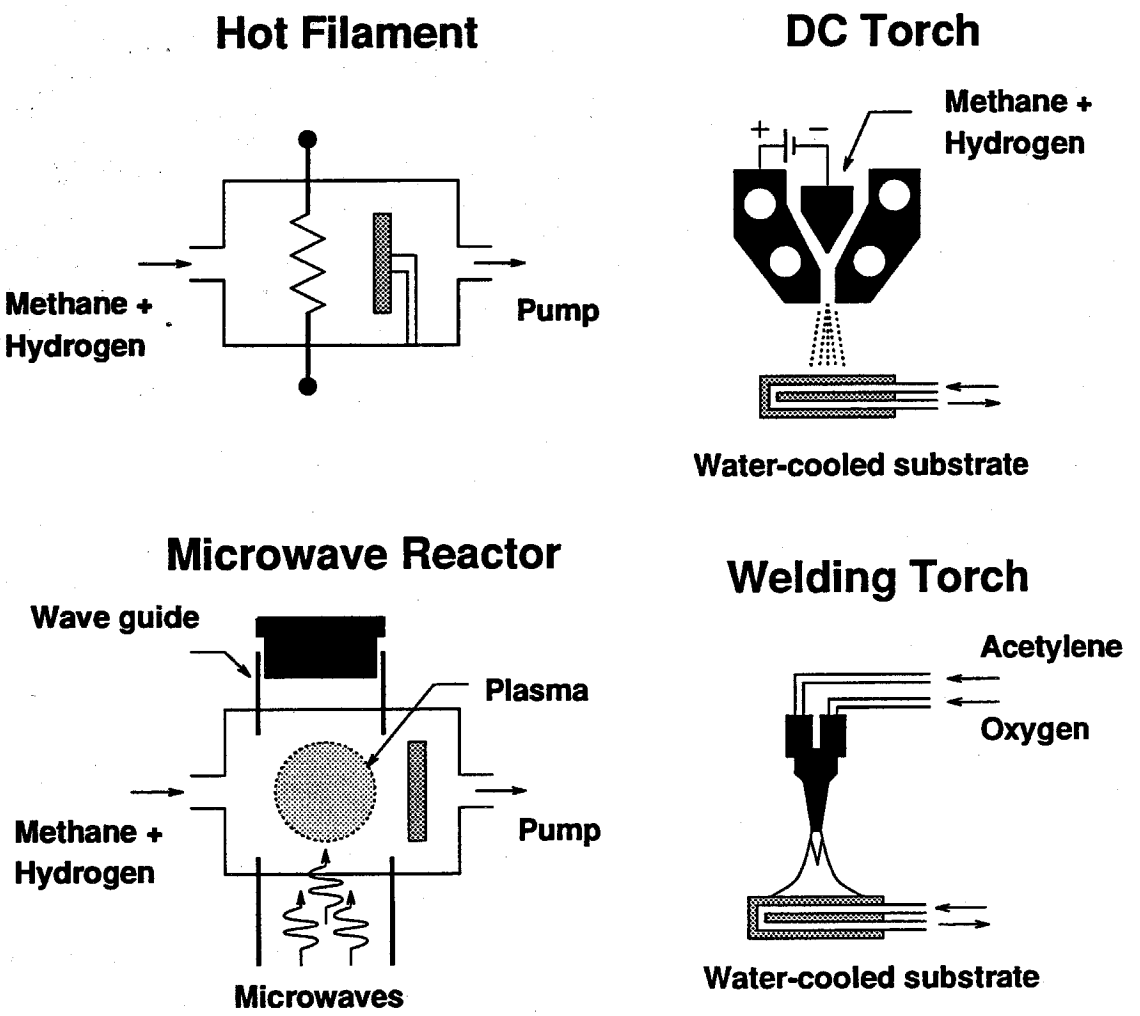

Figure 1-3: Typical CVD diamond growth techniques.

The DC torch (often called "DC arcjet") technique uses direct current to make a high temperature plasma in which nearly all molecules are completely dissociated. This method deposits a diamond film over a relatively small area (typically less than 1 cm^2), but a growth rate of more than several hundreds μm/hr is easily achieved. Since the flame-like plasma expands from the plasma torch nozzle and heats the deposition zone intensively, substantial substrate cooling is necessary. The highest

diamond growth rates for any method were achieved by this method, and the top value of 930 μm/hr has been reported by Ohtake *et al.* [10]. In low pressure synthesis of diamond, some common features are its substrate temperature (typically 600–1200 °C), gas pressure (10 Torr–1 atm), and dilution of carbon-containing reactant gas in 95%–99.9% hydrogen (sometimes with added oxygen).

In all techniques, atomic hydrogen is known to play an important role in the efficient growth of diamond on the substrate. The most widely recognized role played by atomic hydrogen is its selective etching of sp^2 bonded carbons (graphite) from the deposit [5, 11, 12, 13]. Graphite is gasified by atomic hydrogen much more quickly than diamond is. Another important role is to activate the growth surface by hydrogen abstraction reactions. Recently, Goodwin [14] proposed that both the quality and the growth rates of the diamond films are critically related to the H concentration near the surface.

There have been considerable efforts to identify the precursors from which diamond grows, and methyl radical (CH_3) and acetylene (C_2H_2) are considered to be the most likely two growth species [15]. Martin and Hill [16], and Harris and Martin [17] performed diamond growth experiments which allowed control of the gas phase environment above the substrate, and found that diamond films could be grown directly from CH_3 and from C_2H_2. To date, most studies have indicated that methyl radical is the dominant precursor for diamond films grown from CVD [18, 19, 15, 16, 17, 20, 21], although acetylene may grow diamond with lower growth rates [15, 16, 17, 22].

1.2 Combustion Synthesis of Diamond

Diamond film growth from products of combustion reactions in mixtures of acetylene and oxygen at atmospheric pressure was first demonstrated by Hirose and Mitsuizumi [23]. Using atmospheric pressure oxy-acetylene torches, diamond films grew at very high rates ($\sim$ 100 μm/hr) with excellent quality. However uniform growth occurred only over a small area ($\sim$ 10 mm^2).

Murayama *et al.* [24, 25] have developed an improved atmospheric pressure combustion synthesis process, in which high gas flow rates are used to lift the flame off the burner rim and a flat flame is obtained in front of the substrate. Using this approach, a 40 μm thick, 15 mm in diameter, free-standing high quality diamond disk was grown in one hour in acetylene/hydrogen/oxygen flame.

Even larger-area (5 cm $\times$ 10 cm), high quality, transparent diamond wafers have been grown by Ravi *et al.* [26] in atmospheric pressure acetylene/oxygen flames, but details are sketchy and no information on the burner design or experimental conditions was provided.

McCarty *et al.* [27] have introduced a trumpet-bell nozzle design which results in radially uniform fluxes to the substrate, and have produced uniform diamond films in atmospheric pressure, substrate-stabilized acetylene/hydrogen/oxygen flames.

Despite its simplicity and capability to produce high quality diamond films with high growth rates, the atmospheric pressure torch method still has problems which could limit the potential industrial use of this method. Scaling up to larger sub-

strates is still difficult to achieve, and the large gas flow rates require a sophisticated gas handling system for large area deposition. Also, the high flow rates of acetylene, oxygen, and hydrogen at atmospheric pressure require great care to eliminate explosion hazards.

An alternative to the atmospheric pressure method is to employ a low pressure flat flame burner for diamond growth. Since the low pressure flat flame method can produce radially uniform flames over arbitrarily large diameters, the diamond deposition area is easily scaled to large areas. This method is inherently safer than the atmospheric pressure combustion method and minimizes substrate cooling problems. On the other hand, the film growth rates will be less than those of atmospheric pressure methods, due to the reduced radical flux to the surface.

Cooper and Yarbrough [28] first demonstrated that diamond could be deposited in a low pressure (50 Torr) acetylene/oxygen flame. By using a conventional McKenna porous plug flat flame burner, isolated diamond crystals were grown in small areas on silicon wafers at flow rates of ~ 0.2 slm/cm^2.

Glumac and Goodwin [29] found similar results in 40 Torr acetylene/oxygen flames. This work employed a large area horizontal substrate in a stagnation-point flow geometry, and showed that isolated diamond particles could be deposited uniformly over a large area (12 cm^2) with flow rates of ~ 0.16 slm/cm^2. However, the film quality degraded severely as the particles grew together to form a continuous film.

The first continuous diamond film in low pressure flames was grown by Glumac and Goodwin [30], working at much higher flow rates ($\sim$ 1 slm/cm^2). At these high flow rates, the flame is able to deliver a much higher atomic hydrogen flux to the substrate, which is known to be critical in the suppression of graphitic carbon deposition [12, 13]. To handle higher flow rates and heat fluxes, they designed a low pressure burner consisting of an array of holes with enhanced water cooling. Well-faceted, continuous diamond films were grown at 52 Torr over a large area (13 cm^2), with the growth rate of 0.6 μm/hr. Kim and Cappelli [31] demonstrated continuous diamond deposition on a 16 mm diameter disk at growth rates as high as 4 μm/hr in 40 Torr acetylene/oxygen flames, using a higher flow rate of 1.35 slm/cm^2.

To understand and predict the flame chemistry occurring during diamond deposition and to optimize growth conditions, several numerical studies have been applied to atmospheric and low pressure acetylene/oxygen flames. Goodwin [32] assumed a postflame adiabatic equilibrium to model the diamond growth chemical environment, and resulted in good prediction of the major and minor species near the substrate.

Kim and Cappelli [33] employed a stagnation flow combustion model to predict the environment of low pressure acetylene/oxygen flames. Using two sets of gas phase reaction mechanisms (Miller–Bowman [34], and Miller–Melius [35]) and surface mechanism proposed by Harris [36], they predicted that increasing the flow velocity to stabilize the flame on the substrate surface, should result in significant increases in diamond growth rates.

Meeks *et al.* [37] modeled a stagnation flow reactor in atmospheric pressure acetylene/hydrogen/oxygen flames. Using the flow conditions reported by Murayama *et al.* [25], the model showed good qualitative agreement with observed growth parameters for the experimental conditions. However, they noted that the predicted flame temperature significantly exceeded the adiabatic temperature for the inlet condition. A similar superadiabatic flame temperature was also predicted in simulations of low pressure flat flames [38].

Recently, Bertagnolli and Lucht [39] employed a stagnation-flow diamond-forming flame similar to the Murayama and Uchida burner [25], and measured gas phase temperatures in this flame using Coherent anti-Stokes Raman Spectroscopy (CARS) of the hydrogen profile. Peak temperatures of above the adiabatic flame temperature were observed, and results were in excellent agreement with the numerical computations of Meeks *et al.* [37].

1.3 Alternative Fuels for Combustion Synthesis of Diamond

Since the original demonstration by Hirose and Mitsuizumi [23] using an oxy-acetylene welding torch, most studies of combustion synthesis of diamond have used acetylene/oxygen flames. The choice of acetylene as the fuel has been dictated by the uniquely high flame speed, temperature, and radical concentrations (such as H, CH_3,

or OH) found in acetylene flames compared to flames of other hydrocarbons. Since high values for radical concentrations and gas velocity generally lead to high growth rates, diamond films generated from acetylene are expected to grow at much higher rates than films generated from other fuels.

Unfortunately, acetylene is expensive and difficult to handle since it may detonate even in the absence of oxygen and is highly flammable in air (2.5%–100%). The cost of acetylene has been identified as the dominant cost of diamond produced by the combustion method. Ravi *et al.* [26] estimate that the acetylene cost accounts for 80% of the total cost for combustion-grown diamond. High costs of acetylene currently keep the combustion method from being competitive with plasma methods, despite its potential advantages for large area deposition.

There have been a few reports of diamond growth from combustion of hydrocarbon fuels other than acetylene to grow diamonds. Carrington *et al.* [40] deposited isolated diamond crystals using atmospheric pressure ethylene/oxygen torch flames, and Snail *et al.* [41] performed a detailed study of diamond deposition for ethylene/oxygen flames. The diamond growth rates were 5–10 μm/hr, and the general trends with substrate temperature and gas flow ratio that were observed with acetylene/oxygen flames also held for ethylene/oxygen flames.

Kim and Cappelli [42] grew continuous films in ethylene/oxygen flames at 50 Torr. High quality, continuous diamond films with the growth rate up to 1.3 μm/hr were observed over an area of 2 cm^2. In ethylene/oxygen flames, the carbon-conversion

efficiency was approximately one-half of that observed for acetylene/oxygen flames in the same combustion facilities.

1.4 Fluidized Bed Reactor for CVD of Diamond

When gas or liquid is forced to flow upwards through a porous bed of solid particles, a pressure drop is created across the bed. If this pressure drop is sufficient to support the weight of the particles, they become separated and free to move, and the bed is said to be fluidized [43].

When granular materials are brought to a fluidized state, they possess the property of a liquid, and the hydraulic resistance of the granular material and the capabilities of the bed as a heat transfer medium are exceptional. Its upper surface remains horizontal when the containing apparatus is tilted, and it hardly impedes the movement of objects floated on the surface. The same temperature can be quickly established throughout a fluidized system because the general agitation of the particles disperses local hot or cold regions. There is also a high rate of heat transfer to a solid object placed in the bed, so a gas fluidized bed can be used as a constant temperature bath in which to immerse a reactor that has to be at a high temperature. Since a fluidized bed system enables solid particles to be handled essentially as a liquid, it can be desirable for continuous processes. Fluidization is an excellent way of bringing a gas into contact with a solid, and therefore catalytic reactions are often well performed by this technique.

The use of fluidized beds has opened wide possibilities for improving various industrial technologies. Fluidization in CVD processes can be used for several operations such as the formation of fine particles by coagulation, growth of seed particles, and modification of powder surface [44].

So far, most work on diamond CVD has focused on diamond deposition on flat two-dimensional surfaces such as silicon wafers, but there are other potential applications where it is necessary to uniformly coat small, three-dimensional objects (for example, powders, abrasive particles, fibers, bearings, sensor components, or small machine parts). This is hard to do with standard diamond CVD methods, since it is difficult to expose the entire surface area uniformly to the activated gas or plasma.

One promising technique for uniformly coating small objects of complex shape or particulates is to fluidize them in a fluidized bed reactor. Due to the excellent mass transfer characteristics of a fluidized bed, transport of reactive radicals (such as H) to the particle surface is much more effective than it is for bulk substrates, for which H transport is usually diffusion-limited [45]. The particle-particle collisions may also be beneficial to diamond nucleation and growth. Additionally, growing diamond on particulate seed material (either diamond or non-diamond) in a fluidized bed may be an effective way to mass production of diamond by CVD because of the large specific surface area of the particulate material.

Fluidized bed reactors have been used for many years for deposition of other types of coatings on powders [44]. There have been a few studies of using plasma-enhanced

fluidized bed reactors. Okubo and co-workers have employed an RF plasma-enhanced fluidized bed for plasma nitriding of titanium particles [46] and for surface treatment of carbon fibers [47].

Also, two Japanese patent applications by Matsumoto and co-workers claimed to have grown diamond in a plasma-enhanced fluidized bed [48, 49]. They claimed that diamond particles of 30 μm grew to 50 μm after reaction for 3 hours in a 600 Watt microwave plasma at 0.06 atm [48, 49], but no evidence of diamond growth was presented. The only other reported work concerning diamond is the study of Takarada *et al.* [50] who showed that pretreating the surface of the particle substrate in a fluidized bed enhanced diamond nucleation density when they were later introduced into a conventional diamond CVD reactor.

1.5 The Present Study

The low pressure flat flame method for diamond thin film growth is a relatively new research area as compared to microwave and arcjet systems which have already been well developed beyond the stage of commercial use. Even though its advantages of excellent film uniformity and the ability to scale up to large areas, two major disadvantages currently prevent utilization of the low pressure flat flame technique for many applications. Growth rates of large area ($>$ 10 cm^2) diamond films are still relatively low (typically less than 1 μm/hr), and the cost of acetylene is high enough that this method still appears economically prohibitive when compared to

other diamond CVD methods (such as microwave plasma and arcjet).

In this report, both experimental and computational studies are performed to gain insight into the factors important for diamond growth in low pressure flames. For acetylene/oxygen flames, by carrying out detailed flame simulations to find optimal conditions, higher growth rate (> 1 μm/hr) diamond depositions over large areas (~ 20 cm^2) are achieved. In order to extend the combustion synthesis technique for diamond to fuels other than acetylene, and to reduce the cost of diamond produced by combustion synthesis, further studies are performed experimentally and numerically using several cheaper alternative hydrocarbon fuels.

In addition to the study of diamond CVD in low pressure flames, an experimental study of microwave plasma-enhanced CVD (MPECVD) of diamond on particles in fluidized beds is carried out, with the purpose of growing conformal diamond coatings on small, three-dimensional objects. By performing an extensive set of growth experiments, the effects of varying gas composition and pressure on deposited diamond quality, growth rate, and nucleation density are examined, and optimal conditions for conformal diamond coatings on small (0.25–0.7 mm diameter) silicon and SiO_2 particles are identified.

1.6 Outline of this Report

In Chapter 2, experiments on large area diamond growth in low pressure acetylene/oxygen flames are reported. General experimental details of the setup of the

low pressure combustion facility used in these experiments are described. The experimental setup described in this chapter is also employed for the low pressure diamond growth experiments using alternative fuels discussed in Chapter 4.

To analyze the experimental results of growth runs in acetylene/oxygen flames described in Chapter 2, numerical modeling studies are performed in Chapter 3. Mass spectrometry experiments are also carried out to verify that the numerical modeling correctly predicts the chemical environment in low pressure acetylene/oxygen flames. The details of modeling and experimental setup for mass spectrometry are described in Chapter 3, and these are also employed for modeling and diagnostics studies of alternative fuel flames discussed in Chapter 5.

Diamond film growth experiments with several hydrocabon fuels other than acetylene are reported in Chapter 4. Growth experiments using MAPP/oxygen, propylene/oxygen, ethylene/oxygen, and propane/oxygen flames are carried out. An economic comparison study is also carried out to examine the effectiveness of using these alternative fuels for diamond growth.

In Chapter 5, numerical modeling studies are performed to analyze the experimental results of diamond growth in low pressure alternative fuel flames described in Chapter 4. Mass spectrometry experiments are also carried out to determine if the numerical modeling correctly predicts the chemical environment in various hydrocarbon fuel flames.

Diamond growth experiments on non-diamond seed particles in a fluidized bed

reactor are discussed in Chapter 6. The effects of process parameters for diamond growth on silica and silicon particles in a microwave plasma-enhanced fluidized bed reactor are reported. Mass spectrometry studies are performed to analyze the chemical environment during diamond growth.

Two sets of gas phase mechanism and the surface chemistry mechanism are used in the numerical modeling studies of Chapters 3 and 5, and are listed in detail in Appendices A and B.

Chapter 2

Diamond Film Deposition in Low Pressure Acetylene/Oxygen Flames

2.1 Overview

In this chapter, experiments on large area diamond growth in low pressure acetylene/oxygen flames are described. In low pressure acetylene/oxygen flames, experiments in the low flow rate regime (0.1–0.2 slm/cm^2) have only resulted in isolated diamond crystal growth [28, 29]. This low flow rate results in a low flame temperature, which does not produce enough radical species near the substrate surface to grow continuous diamond films. This low flow rate also results in relatively thick substrate boundary layers, which hinder effective radical transport to the substrate surface.

Employing higher flow rates ($\sim$ 1 slm/cm^2), resulting in a hotter flame and thinner boundary layer at the substrate, continuous diamond films were grown at pressures of 40–52 Torr [30, 31]. In the work presented here, further high flow rate growth experiments have been performed at lower pressures (30–40 Torr). By employing lower pressure flames, a much hotter and faster flame could be obtained.

In this chapter, general experimental details of the setup of the low pressure combustion experiments and results of film growth experiments in high flow rate acetylene/oxygen flames at 30–52 Torr are reported. The experimental setup described here is also employed for the low pressure diamond growth experiments using alternative fuels discussed in Chapter 4.

The computational modeling studies and flame diagnostics used to analyze the experimental data of this chapter will be discussed in Chapter 3.

2.2 Experimental

The experimental setup is shown schematically in Figure 2-1. The experiments were carried out in the low pressure, flat flame combustion facility which developed for diamond growth experiments by Glumac [38].

The burner is housed in a water-cooled stainless steel bell jar vacuum chamber (45 cm diameter, 75 cm height), and vacuum is maintained by a Stokes mechanical sliding vane vacuum pump (50 cubic feet per minute). The burner face is a 13 mm thick copper plate, with an array of 1 mm diameter holes spaced 2.5 mm apart in a hexagonal array. The diameter of the array is 4 cm. Liberal water cooling is provided to keep the burner temperature low. Sometimes, an ice-point corrected thermocouple (type K) embedded in the side of the burner near the surface monitors the burner temperature, which for the runs discussed in this chapter was typically 200–250 °C. A flow straightener (not shown in Figure 2-1) with the same array of holes as the burner is placed inside the burner to increase the uniformity of the flow.

The burner is mounted in a downflow configuration above a horizontal molybdenum substrate (5 cm diameter, 6 mm thick). To enhance the nucleation densities and uniformities, a consistent pretreatment method is performed. The molybdenum substrate surface is cleaned with a sand blaster, and is sanded with a sequence of different grit sand papers (80, 180, 320, and 500 grit). The surface is then scratched with 0.25 μm diamond grit in paste. The grit and paste are removed by a final rinse with acetone.

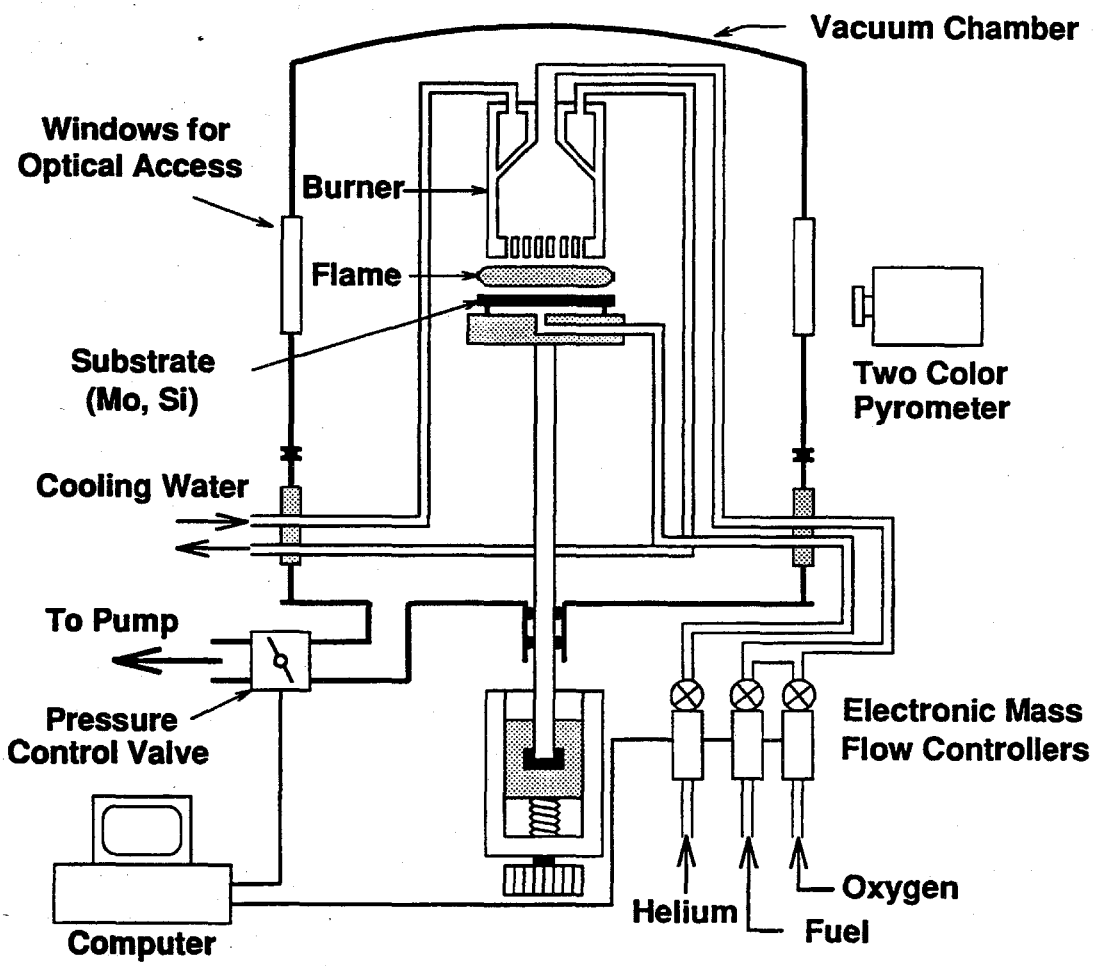

Figure 2-1: The low pressure, flat flame combustion facility.

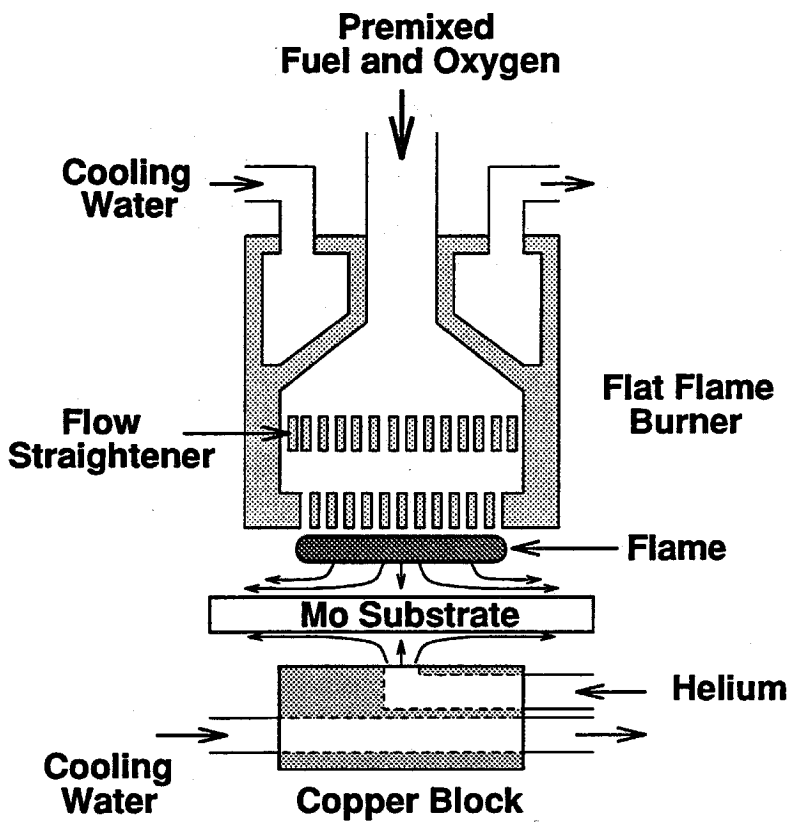

Figure 2-2: The schematic of burner, substrate, and cooling system.

By mounting the burner and substrate on external translation stages, independent controls of the burner to substrate, and the burner to water-cooled copper block distance are allowed. The burner to substrate distance is typically fixed at 10 mm, and the accuracy is about 0.1 mm. The substrate is thermally isolated from its support, such that the heat flux from the flame to the substrate is balanced largely by radiation to the chamber walls. Rapid radial conduction within the thick molybdenum substrate compared to slower radiative transfer maintains the substrate at a uniform temperature.

Additional substrate cooling is provided by a helium jet which impinges on the

underside of the molybdenum plate (see Figure 2-2). By adjusting the helium flow rate (1–5 slm) and the gap height (0.5–3 mm) between substrate and water-cooled copper block, the substrate temperature can be controlled effectively by the conduction heat flux through the helium to the cooling block. Under some flame conditions, this additional cooling is only used in the first 15–20 minutes of growth, since the emissivity of the substrate is low during that period, and increases as a film is deposited.

The gases used for the experiments discussed in this chapter are high-purity acetylene (99.6%, Matheson) and laboratory-grade oxygen. An activated charcoal filter (Matheson) in the acetylene line is used to remove the small amount of acetone present. Each gas flow is controlled by a separate electronic thermal mass flow controller (maximum 10 slm of N_2, MKS). The accuracy of the flow controllers as given by the manufacturer is $\pm$ 0.8% of full scale. A flashback arrestor is employed to prevent the flame flashback to the gas chambers.

The system pressure is maintained by a throttle valve controller, and the fluctuation of the pressure is less than 0.5 Torr. The gas flow rates for burner ignition and growth experiments are controlled by a personal computer. After pumping down and purging the chamber with inert gas (helium), the chamber is filled with inert gas to operating pressure. Then the flame is ignited by turning on a resistively heated nichrome wire ignitor (7–8 Amps, resulting in $\sim$ 1200 °C) which is placed 2–3 mm below the burner surface. Typical ignition conditions are gas flows of 0.6 slm of acetylene and 1 slm of oxygen, at the operating system pressure of 30–52 Torr. After

the flame is ignited, the ignitor power is turned off, and the ignitor is retracted from flame. During an ignition sequence, the flows are held at ignition values for 4 seconds, and then slowly ramped up to the values for growth run conditions in one minute by the computer. The computer control also monitors the run and shuts down if the pressure exceeds a pre-set maximum or if the flows deviate from the set point by a pre-set amount.

The substrate temperature is measured by a two-color infrared pyrometer. The pyrometer (Ircon) measures the relative intensities of two emission bands (0.7 to 1.08 μm, narrow band centered at 1.08 μm), and operates over a range of 700–1400 °C with resolution of 5 K. The substrate temperature as measured by the two-color pyrometer agrees with temperatures measured by thermocouples to within 50 °C.

For the experiments discussed here, the six experimental parameters which can be varied are the system pressure P (Torr), the equivalence ratio ϕ, the flow rate of premixed gases (fuel and oxygen) per unit area of substrate Q_T (slm/cm^2), the burner temperature T_B (°C), the substrate temperature T_S (°C), and the burner to substrate distance D_S (mm). The equivalence ratio ϕ is defined as the ratio of the volume flow rate of fuel to oxygen, divided by the ratio of the volume flow rate of fuel to oxygen for complete oxidation. For acetylene, the ratio of the volume flow rate of fuel to oxygen for complete oxidation is 1/2.5. The values of ϕ reported here are the ones based on the readout values from the mass flow controllers for acetylene and oxygen. However, it should be noted that considerable drifts (as high as 5%) are found in the

Parameter	Symbol	Unit	Range
System pressure	P	Torr	30–52
Equivalence ratio	ϕ		2.0–2.34
Total flow rate	Q_T	slm/cm^2	0.94–1.0
Burner temperature	T_B	°C	200–250
Substrate temperature	T_S	°C	770–1100
Burner to substrate distance	D_S	mm	5–10

Table 2.1: Experimental parameters and conditions.

flow rate calibration runs for acetylene and oxygen, leading to an uncertainty in ϕ of up to 5%.

Experimental parameters and conditions are listed in Table 2.1. The flow rates are limited by the mass flow controller capacity (10 slm of N_2). Since the gas correction factor (the ratio of a flow rate of specific gas compare to N_2 which produces the same output voltage from a flowmeter) of acetylene is 0.58 compared to 1 of N_2, the maximum acetylene flow rate in our mass flow controller is 5.8 slm. The low pressure limit is restricted by the pumping capacity, and the lowest pressure of $\sim$ 30 Torr is obtained with the total flow rate of 1 slm/cm^2 which corresponds to 5.8 slm of acetylene and 6.8 slm of oxygen. Also, since heat flux from the flame is higher at maximum flow rates, although additional cooling is provided from the high helium jet flow ($\sim$ 5 slm) in the small gap ($<$ 1 mm) between the substrate and the copper cooling block, the lowest substrate temperature obtained, 770 °C, is at the total flow rate (acetylene and oxygen) of 1 slm/cm^2.

Deposits obtained from the growth experiments are typically analyzed using scan-

Case	P (Torr)	ϕ	Q_T (slm/cm^2)	T_S (°C)	D_S (mm)	Growth Rate (μm/hr)	Area (cm^2)	C_{eff} ($\times 10^{-5}$)
1	52	2.15	0.94	800	10	0.6	12.7	0.8
2	50	2.15	1.0	800	10	0.7	13.5	0.9
3	30	2.11	1.0	800	10	1.5	19	2.7
4	30	2.12	1.0	870	10	2.3	16	3.5

Table 2.2: Experimental conditions, measured growth rates, deposit areas, and carbon-conversion efficiencies.

ning electron microscopy (SEM) for characterizing the surface morphology in high resolution (magnification of up to 15,000) images. Sometimes, micro- and macro-Raman spectroscopies are employed for further characterization of diamond quality.

2.3 Results

Four different experimental conditions which resulted in good quality diamond deposition are summarized in Table 2.2. The growth rates, deposition areas, and carbon-conversion efficiencies of these four runs are also listed in Table 2.2. The carbon-conversion efficiency (C_{eff}) is the efficiency in converting fuel carbon atoms into diamond, and is given by the ratio of the diamond mass deposition rate (g/sec) to the carbon mass flow rate (g/sec).

In all cases of growth experiments in the high flow rate regime (Q_T = 0.94–1.0 slm/cm^2), deposited carbons (either diamonds or non-diamond carbons) were in the form of continuous films.

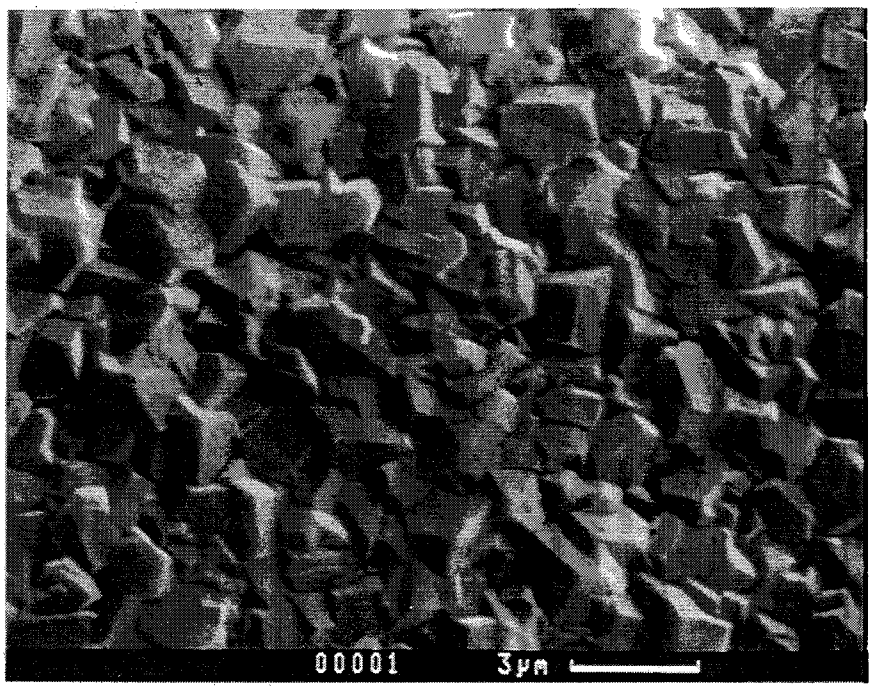

Figure 2-3: Continuous diamond film grown under the conditions of case 2.

The experimental conditions of case 1 were chosen from the growth experiments done in the same facility by Glumac [30]. The linear growth rates ranged from 0.6 to 2.3 μm/hr depending on the pressure and the substrate temperature; this range is comparable to that for plasma methods operating at the same pressure.

An SEM photograph of a uniform diamond coating grown under the conditions of case 2 is shown in Figure 2-3. The result was very similar to that of case 1. The surface typically shows rectangular (100) crystal faces. The film thickness was 2.8 μm after 4 hours, and the diamond film growth rate was estimated to be 0.7 μm/hr. The carbon-conversion efficiency was $C_{eff} = 0.9\times10^{-5}$ which is similar to typical values for atmospheric pressure combustion methods. The diamond coating covered an area roughly equal to the area of burner face (12.6 cm^2).

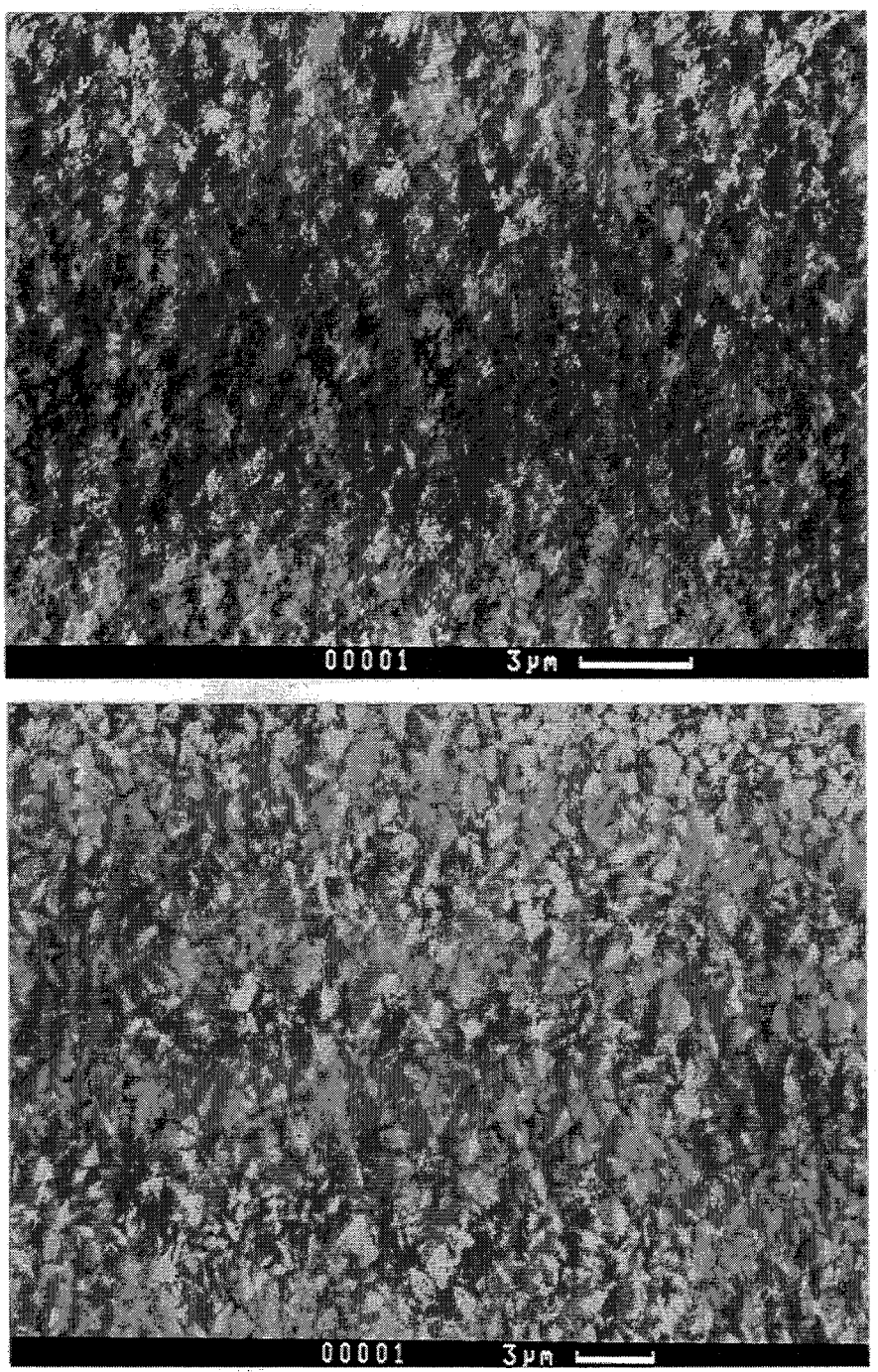

Figure 2-4: Film deposits at 30 Torr: (a) non-diamond film at $\phi = 2.15$; (b) poorly-faceted diamond film at $\phi = 2.13$.

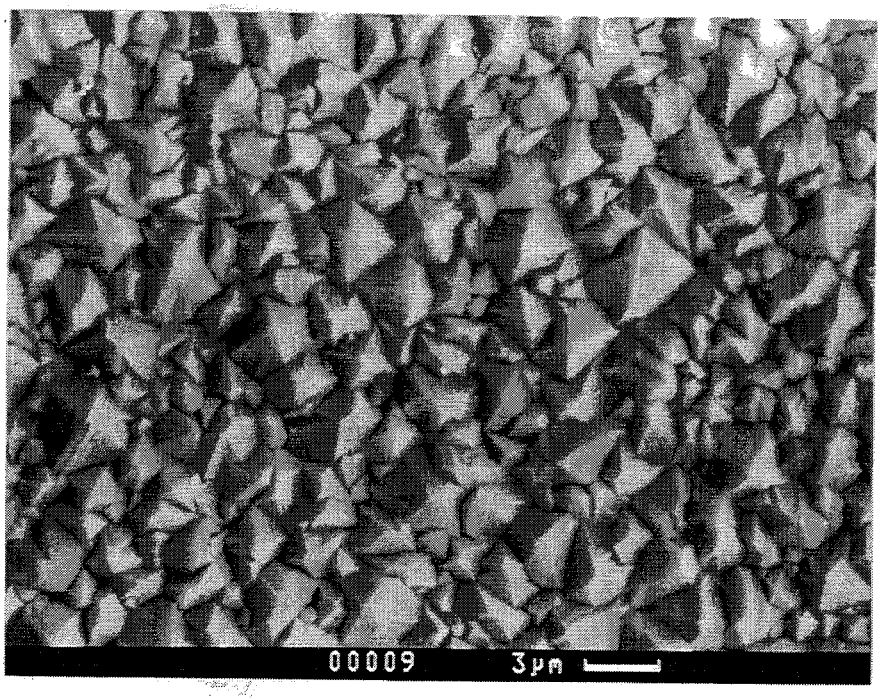

Figure 2-5: Near the center of diamond film grown under the conditions of case 3 for 12 hours.

Reducing the pressure from the conditions of case 2 only resulted in a non-diamond carbon film deposit as shown in Figure 2-4 (a). The pressure was 30 Torr and all other experimental conditions were same as case 2. These non-diamond carbon deposits were typically shown when the equivalence ratio ϕ was too high (flame was too rich) for diamond growth. Some diamond faces started to appear at $\phi = 2.13$, and the SEM micrograph is shown in Figure 2-4 (b).

Scanning electron micrographs of a thick (17–19 μm) film grown under the conditions of case 3 are shown in Figure 2-5 – 2-7. The run duration was 12 hours. Figure 2-5 shows well-faceted diamond growth near the center of the substrate, and the surface consists of triangular (111) crystal faces. At the edge of the substrate,

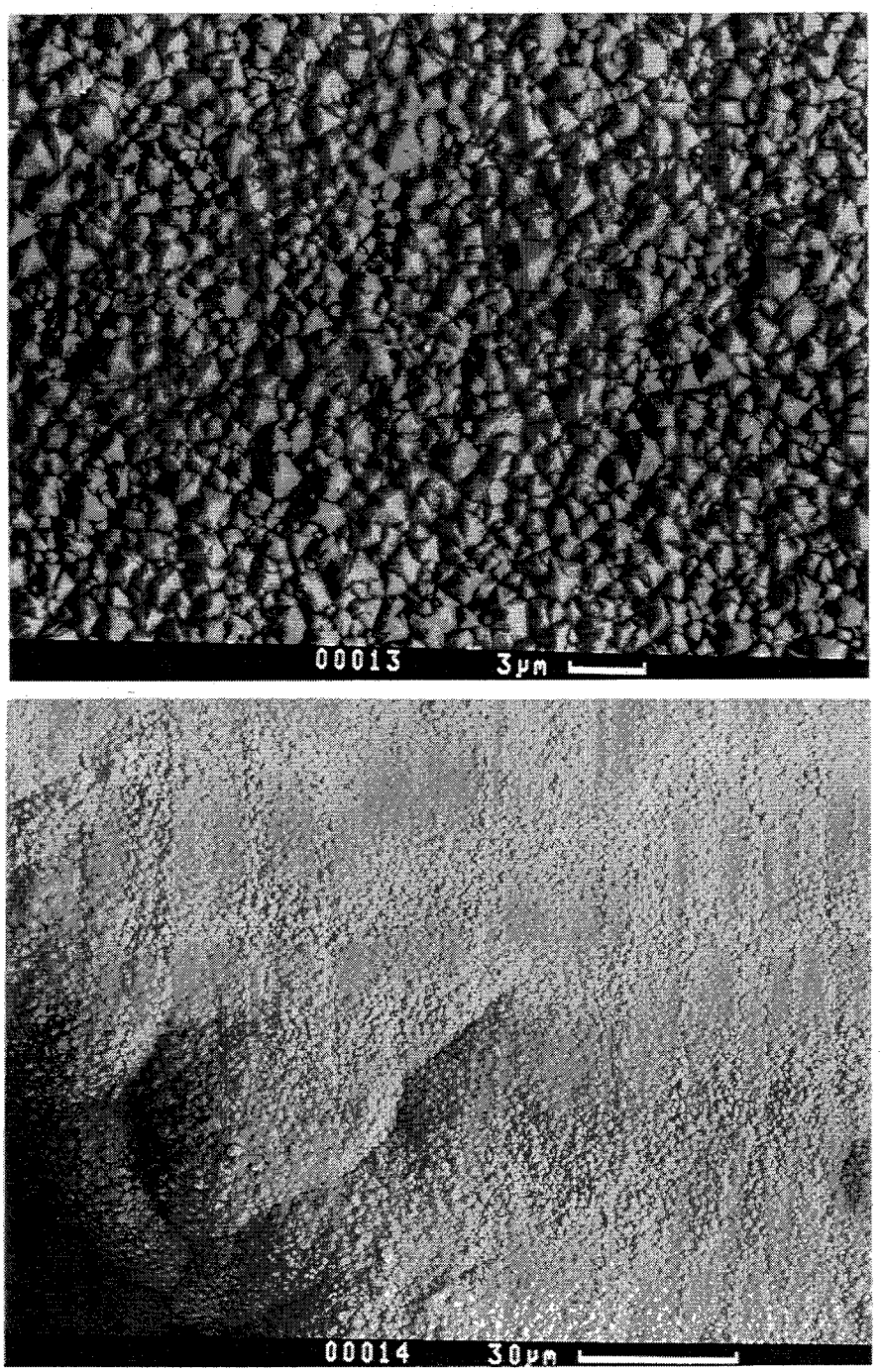

Figure 2-6: Edge of diamond film grown under the conditions of case 3 for 12 hours.

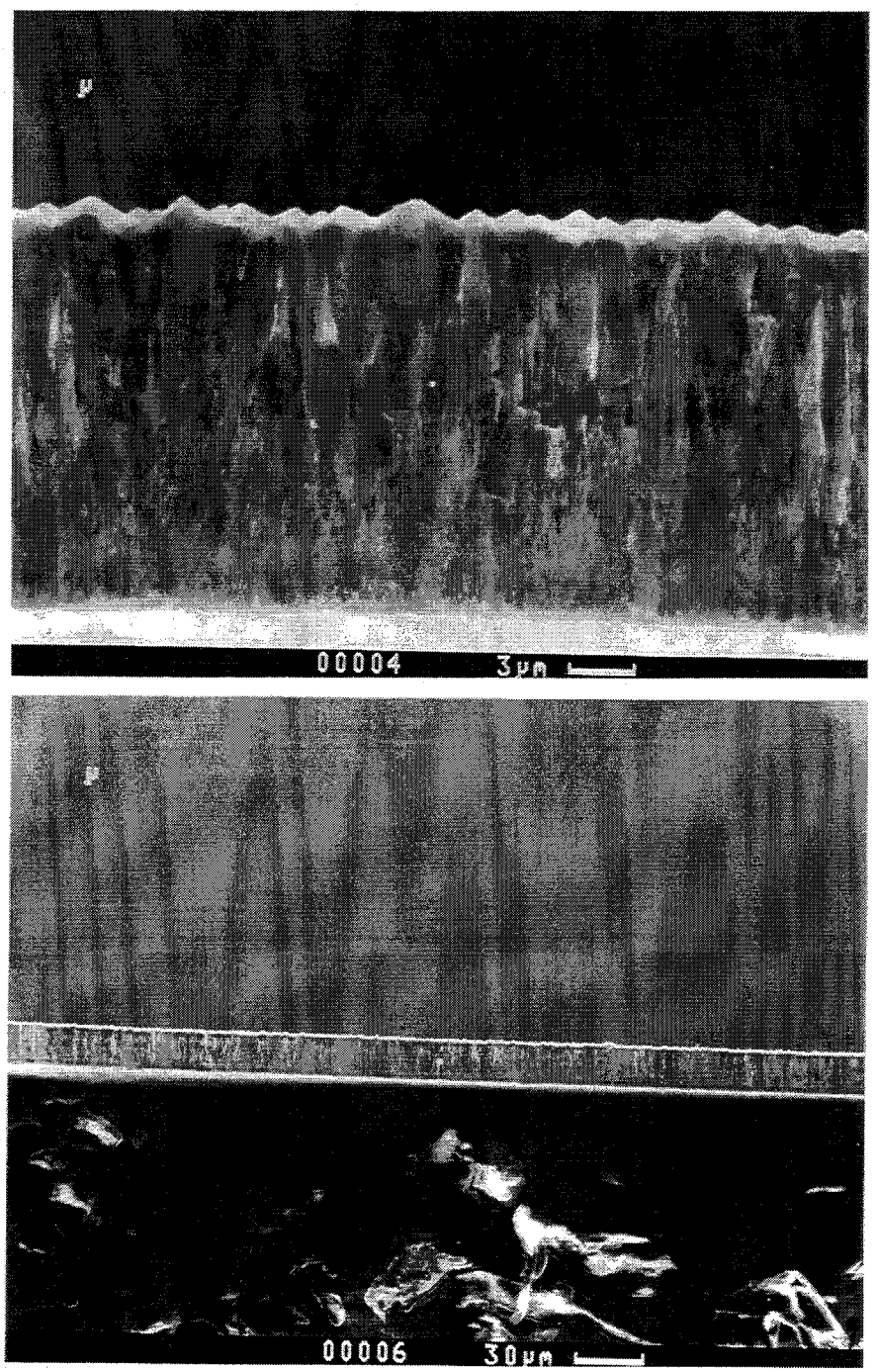

Figure 2-7: Side views of diamond film grown under the conditions of case 3 for 12 hours.

even though the quality is poorer than that at the center, clear diamond facets can still be seen, and the film fully covered the 5 cm diameter substrate as shown in Figure 2-6.

The observed equivalence ratios for diamond growth at 30–52 Torr were $\phi = 2.11$–2.15. These values are substantially lower than typical values at 1 atm ($\sim \phi = 2.5$). Also, the equivalence ratio for diamond growth shifted from $\phi = 2.15$ at 50 Torr to $\phi = 2.11$ at 30 Torr at the same other experimental conditions. This suggests that equivalence ratio necessary to deposit diamond growth decreases with decreasing the pressure, holding other parameters constant.

Side views of the diamond film grown under the conditions of case 3 are shown in Figure 2-7. The deposited films show the usual columnar morphology, and have a uniform thickness over the deposition area. Even though the film uniformity was not measured for this sample, diamond films grown under experimental conditions similar to case 1 in the same facility as the present experiments exhibited a thickness uniformity of approximately $\pm$ 3% [38]. This is a consequence of the uniform heat and species fluxes to the surface in a stagnation-point flow.

A photograph of a uniform diamond coating grown under the conditions of case 3 is shown in Figure 2-8. This coating, approximately 3 μm thick, covered the entire 19 cm^2 substrate and was deposited in 2 hours.

At 30 Torr, the diameter (5 cm) of the film in Figure 2-8 is larger than the burner diameter (4 cm). Since this film covered the entire substrate, it is not clear how large

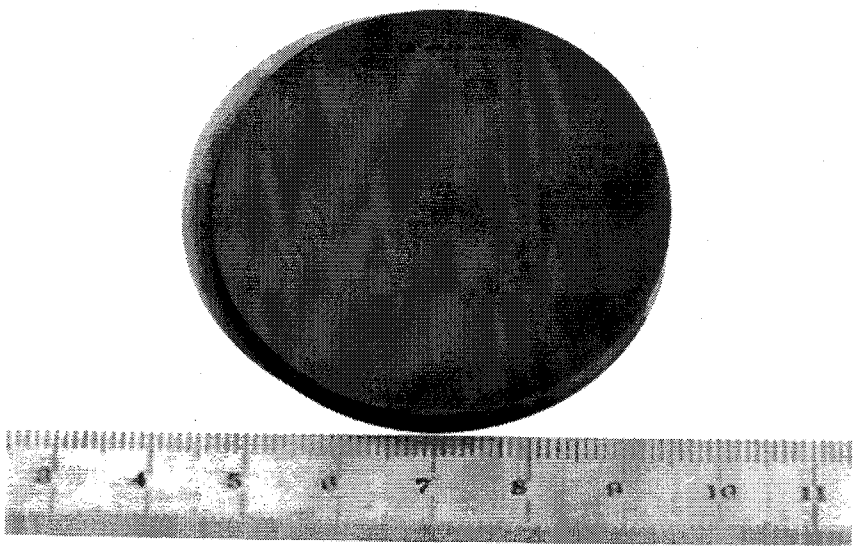

Figure 2-8: Uniform 3 μm thick diamond coating deposited on a 19 cm^2 molybdenum substrate after 2 hours using the flame conditions of case 3.

the deposit could have been if a larger substrate had been used. In contrast, the films grown at 50 Torr are close to the same diameter as the burner. This difference may result from the higher flow velocity at 30 Torr, or from more effective radial diffusion. Flames at 30 Torr looked much brighter and wider than flames at 50 Torr, and some more substrate cooling was necessary to maintain the same substrate temperature.

A Raman spectrum of the film shown in Figure 2-5 is shown in Figure 2-9. The spectrum of the growth side shows the characteristic diamond line at 1333 cm^{-1}, and a broad background around 1540 cm^{-1}, due to a small amount of non-diamond carbon. This Raman spectrum is comparable to that of diamond grown in other types of reactors. When equivalence ratio was 2.0, the flame became too oxidizing

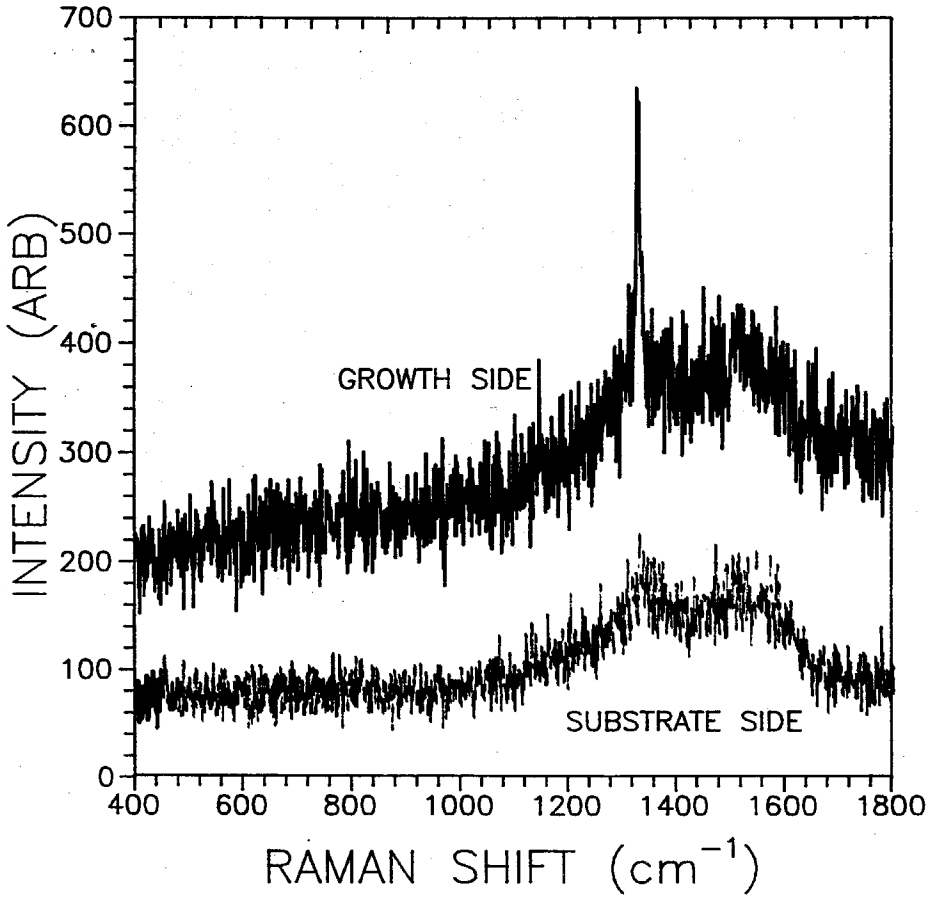

Figure 2-9: Raman spectrum of the film shown in Figure 2-5.

for growth, and no deposit was observed.

The diamond film grown under the conditions of case 4 is shown in Figure 2-10. At this higher substrate temperature (T_S = 870 °C), the linear growth rate increased to 2.3 μm/hr. The activation energy for diamond growth is known to be $\sim$ 23 kcal/mole [51]. This value was measured by an advanced hot filament CVD method, which accurately controls the substrate temperature independently against other CVD parameters. If the measured growth rates for case 3 (1.5 μm/hr at 1073 K) and case 4 (2.3 μm/hr at 1143 K) are employed to predict the activation energy for diamond

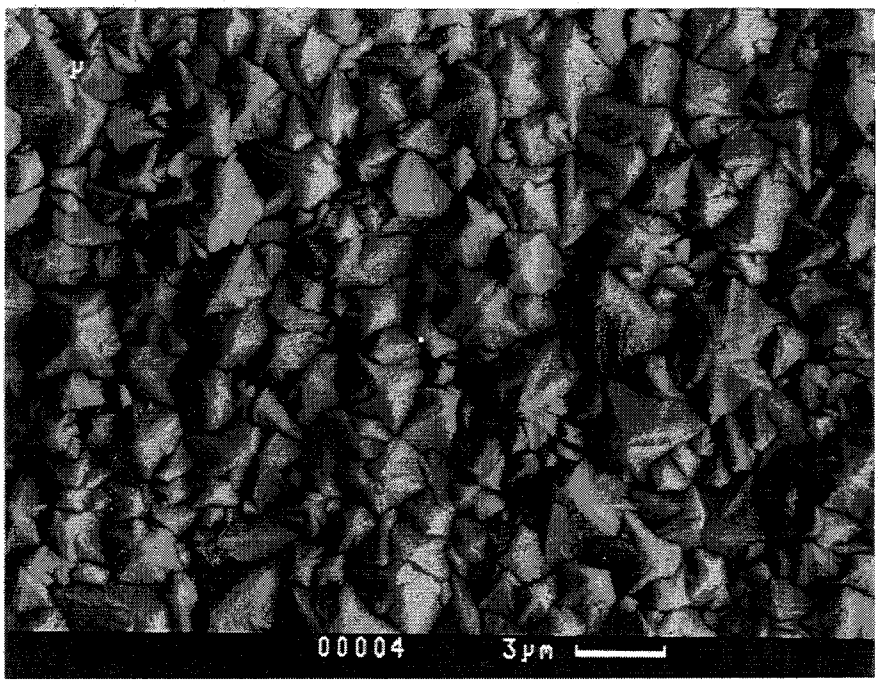

Figure 2-10: Continuous diamond film grown under the conditions of case 4.

growth in the flame environment, the growth rate ratio of 1.53 yields the activation energy of 14.9 kcal/mole.

The film surface consists of (111) faces which are the same as those of case 3, but becomes rougher than the diamond deposited surface at T_S = 800 °C. The carbon-conversion efficiency is found to be $C_{eff} = 3.5\times10^{-5}$ which is roughly a factor of four higher than that of case 2. In this case, the film did not cover the entire 19 cm^2 substrate, even though the pressure was 30 Torr. But this may have been a result of insufficient substrate polishing near the substrate edges, and not inadequate flame conditions.

2.4 Summary

Diamond film growth in low pressure, flat acetylene/oxygen flames has been performed. By employing lower pressure (30 Torr) flames, a much hotter and faster flame could be obtained than $\sim$ 50 Torr flames. At a pressure of 30 Torr, uniform, polycrystalline diamond films fully covering $\sim$ 5 cm diameter substrates (an area of 19 cm^2) at growth rates of up to 2.3 μm/hr, have been grown using a 4 cm diameter burner. The carbon-conversion efficiency of up to 3.5×10^{-5} was obtained which was comparable to that observed in the atmospheric pressure torch method. The Raman spectrum of the deposited film showed good diamond film quality.

The observed equivalence ratios for diamond growth at 30–52 Torr were ϕ = 2.11–2.15, which are substantially lower than typical values at 1 atm ($\sim \phi = 2.5$). The equivalence ratio for diamond growth decreased with reduced pressure. Only minor changes of surface morphology were observed with temperature change and the diamond growth rate was increased with increasing substrate temperature.

Chapter 3

Modeling and Diagnostics of Acetylene/Oxygen Flames

3.1 Overview

To analyze the experimental results of growth runs in acetylene/oxygen flames which are described in Chapter 2 and to seek improved flame conditions for high quality, high growth rate diamond growth deposition, numerical modeling studies have been performed. The simplified growth mechanism proposed by Goodwin [14] is employed to analyze the numerical results and to optimize the growth conditions. This model postulates that diamond growth rate and quality, for a given temperature, are functions only of the H and CH_3 concentrations at the substrate. When optimizing growth conditions for high growth rates, an H to CH_3 mole fraction ratio of 10 at the substrate is used as a standard to identify the minimum conditions for moderate quality diamond growth. The value of 10 is an accepted standard for moderate quality diamond growth [14, 32, 38, 52, 53].

Mass spectrometry experiments have also been carried out to verify that the numerical modeling correctly predicts the chemical environment in acetylene/oxygen flames. The details of modeling and experimental setup for mass spectrometry described in this chapter are also employed for modeling and diagnostics studies of alternative fuel flames which will be discussed in Chapter 5.

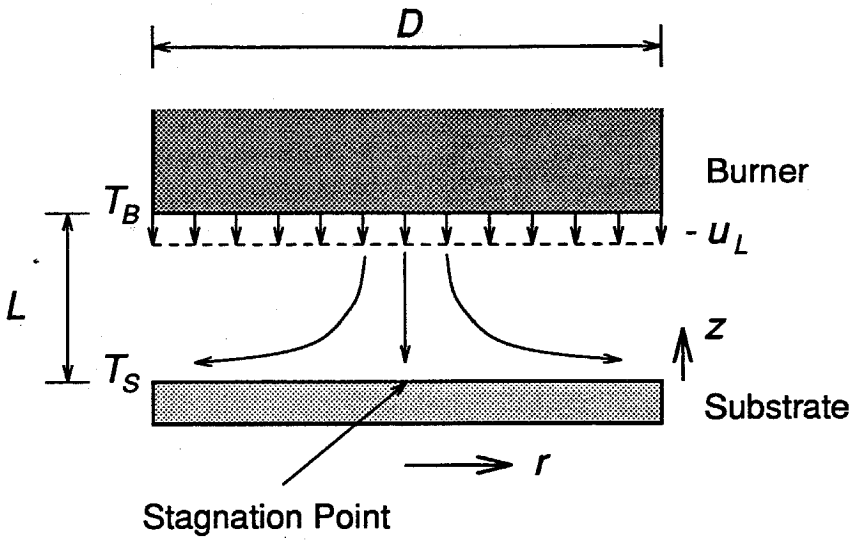

Figure 3-1: Schematic of flame deposition model.

3.2 Modeling

The numerical modeling studies are carried out using the STBL (STagnation Boundary Layer) code, which is a reacting flow code for axisymmetric stagnation point flows developed by Goodwin [54]. This code is based on the Chemkin-II subroutine package [55, 56], and utilizes the similarity solution for an infinite-radius burner and substrate to reduce the problem to a set of ordinary differential equations in the axial direction.

Figure 3-1 shows a schematic of the flame deposition model. The model assumptions and numerical solution scheme are similar to those of Meeks *et al.* [37] and Kim and Cappelli [57].

For the gas phase modeling, the governing equations are the conservation equations for mass, momentum, species, and energy, and the equation of state. The

solution assumes that the ratio of the burner diameter (D) to the burner/substrate separation (L) is large, and the Mach number at any point in the flowfield is small. In this limit, the axial velocity u, the temperature T, and species mass fractions Y_k are all functions of z and independent of r. The radial velocity v has the form $rV(z)$, and the pressure has the form $p(r,z) = P + \Lambda r^2/2$, where P and Λ are constants [58].

The conservation equations reduce to ordinary differential equations in z,

Continuity

$$\frac{du}{dz} + 2V + \frac{u}{\rho}\frac{d\rho}{dz} = 0 \tag{3.1}$$

Radial Momentum

$$\rho u\frac{dV}{dz} + \rho V^2 - \frac{d}{dz}\left(\mu\frac{dV}{dz}\right) + \Lambda = 0 \tag{3.2}$$

Energy

$$\rho c_p u\frac{dT}{dz} + \sum_k \left(\rho c_{p,k} U_k Y_k \frac{dT}{dz} + M_k \dot{\omega}_k h_k\right) - \frac{d}{dz}\left(\lambda\frac{dT}{dz}\right) = 0 \tag{3.3}$$

Species

$$\rho u\frac{dY_k}{dz} + \frac{d}{dz}(\rho U_k Y_k) - \dot{\omega}_k M_k = 0 \tag{3.4}$$

Equation of State

$$p = \rho RT \tag{3.5}$$

In these equations, u is the axial velocity, T is the temperature, V is the radial velocity divided by radius, ρ is the density, μ is the viscosity, λ is the thermal conductivity, and c_p is the specific heat. The quantity X_k is the mole fraction, Y_k is the mass fraction, M_k is the molecular weight, h_k is the specific enthalpy, and $\dot{\omega}_k$ is the molar chemical production rate, in reference to species k.

The diffusion velocities U_k are given by

$$U_k = \frac{1}{X_k \overline{M}} \sum_{j \neq k} M_j D_{kj} \frac{dX_j}{dz} - \frac{D_k^T}{\rho Y_k} \frac{1}{T} \frac{dT}{dz} \tag{3.6}$$

where D_{kj} is the multicomponent diffusion coefficient, D_k^T is the thermal diffusion coefficient, and $\overline{M}$ is the mean molecular weight of the gas mixture.

The transport properties μ, λ, D_{kj}, and D_k^T are calculated using the multicomponent transport software of Kee *et al.* [56]. The thermodynamic properties used are those of the CHEMKIN thermodynamic data base [59] and the chemical terms in the equations are evaluated with calls to the Chemkin-II [55] subroutine library.

The boundary conditions at the burner surface are that $\dot{m} = \rho u(L)$, $V = 0$, $T = T_B$, and $\dot{m} Y_{k,R} = -\rho(L) Y_k(L) [u(L) + U_k(L)]$, where $\dot{m}$ is the mass flux at the burner, and $Y_{k,R}$ is the mass fractions in the unreacted inlet premixed gases. At the substrate, the temperature is $T = T_S$ and the tangential velocity is $V = 0$ (no-slip condition). The mass flux of each species balances its mass deposition rate $\rho Y_k [u(0) + U_k(0)] = \dot{s}_k M_k$ where $\dot{s}_k$ is the net molar production (or consumption) rate for species k due to surface reactions.

The combustion mechanism employed for gas phase reactions is that of Miller and Melius [35] which is designed for simulating fuel-rich hydrocarbon flames. It consists of 49 species and 218 reactions, and is presented in detail in Appendix A.1. The Miller–Melius mechanism includes species and reactions that lead to formation of aromatic compounds, and has been previously used to simulate low pressure diamond synthesis in burner stabilized flames [38, 57]. It has also been used in simulations of the experimental conditions of Murayama *et al.* [25] with good qualitative agreement [37].

To describe the growth of diamond at the substrate surface, 21 surface reactions are considered. This surface mechanism is listed and described in detail in Appendix B. This mechanism includes deposition and etching of diamond and recombination of some radical species at the substrate surface.

Diamond growth is assumed to occur via a methyl growth mechanism, in agreement with most experimental data [17, 18, 20, 21]. A reduced version [14] of the mechanism proposed by Harris [36] is used to calculate diamond growth rates. This mechanism has been shown in many simulations to predict the growth rate at 1200 K reliably for a wide variety of reactors, typically within a factor of two [60]. The growth rate predicted by the Harris mechanism is reasonably well fit by the relation [14]

$$G = 1.8 \times 10^{11} \frac{[\mathrm{CH_3}][\mathrm{H}]}{5 \times 10^{-9} + [\mathrm{H}]} \tag{3.7}$$

where G is the growth rate for a substrate temperature of 1200 K in μm/hr, and the

concentrations are the values at the substrate in moles/cm^3.

In addition to the diamond growth mechanism, surface reactions that destroy hydrocarbon radicals [CH, CH_2, and $CH_2(S)$], C, OH, and O on the substrate are included as are reactions which implement the measured oxidation rate of diamond [61]. This same surface mechanism has been used by Glumac [38] to model diamond growth and radical recombination, and has effectively predicted the surface mole fractions of some important species as well as diamond growth rates with good experimental agreement.

3.3 Experimental

To measure stable species concentrations of interest, mass spectrometry was carried out with and without a substrate. A schematic of the setup for mass spectrometry with a substrate is shown in Figure 3-2. A quadrupole mass spectrometer (Inficon Quadrex 200) is used for gas analysis. The sensor of the gas analyzer analyzes the residual gases by ionizing some of the gas molecules, separating the resulting ions according to their respective masses, and measuring the quantity of ions at each mass. The masses of the various ion species (produced by the sensor) are used to identify the gas molecules from which they were created: masses are expressed in AMU's (atomic mass units).

Gas at the substrate surface is sampled through a 1 mm diameter orifice in the center of a molybdenum substrate (7.5 cm diameter, 0.8 cm thick) using a sampling

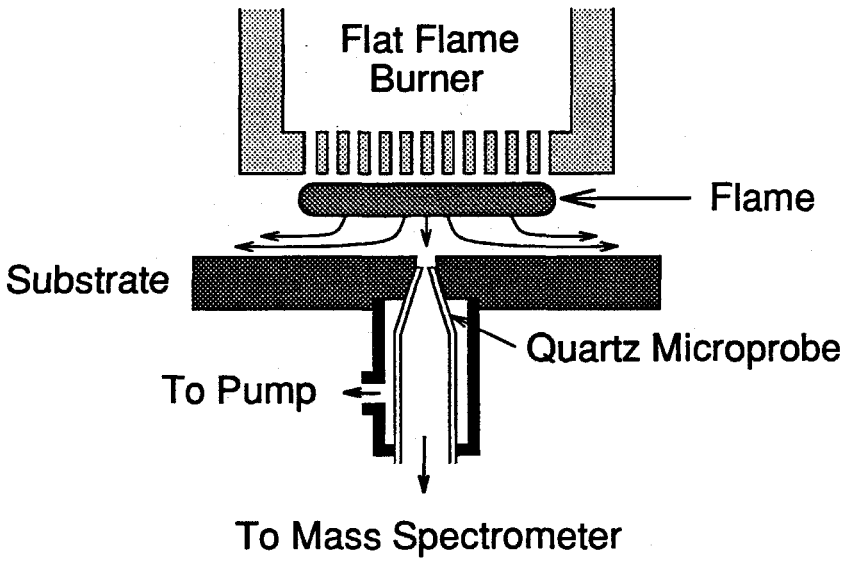

Figure 3-2: Schematic experimental setup for mass spectrometry.

microprobe. The sampling probe is a quartz tube (1 cm inner diameter, 50 cm long) with a 400 μm diameter orifice.

To insure sampled gas originates from the flame, gas in the region surrounding the sampling probe beneath the substrate is differentially pumped away. The pressure within the sampling probe is maintained at 0.3 Torr. A rapid pressure drop across the probe orifice is known to effectively keep sampled gas from further chemical reactions, except for radical recombinations [62]. Since the sampled gas travels through $\sim$ 1 m of tubing before entering the mass spectrometer, radical recombination occurs at the tube walls, and only stable species are detected.

The same quartz probe, tubing, and mass spectrometer are used for the case without a substrate. The sampling probe is mounted on a external translation stage to allow for control of the burner to probe tip distance. The accuracy of this distance

is $\pm$ 0.2 mm.

The magnitude of a signal representing a particular mass is characteristic of the number of ions produced, and therefore is also characteristic of the concentration of molecules for the particular substance indicated. To measure the absolute mole fractions of species, relative ionization cross section ratios with respect to argon are determined from a calibrated mixture of known composition. The calibrated mixture (Matheson) is composed of 59.98% CO, 20.01% H_2, 4.99% CO_2, 0.53% CH_4, 1% C_2H_2, and 10% Ar with the balance He (Matheson). This composition is similar to the calculated species concentrations except for water vapor for the diamond growth conditions at the substrate surface. The absolute mole fraction of argon at the substrate surface is calculated from the numerical model, and is measured from the magnitude of its signal in the mass spectrometer. The absolute mole fraction of a species of interest is then determined from the absolute argon mole fraction, the argon signal, the cross section ratio, and the species signal.

The mass peaks of 2, 15, 26, 28, 40, and 44 AMU are used to monitor relative number densities of H_2, CH_4, C_2H_2, CO, Ar, and CO_2, respectively. For H_2, CO, and CO_2, background levels are negligible, and signal fluctuations are typically less than $\pm$ 10%. For CH_4 and C_2H_2, signal fluctuations are much higher than for the major species, and experimental uncertainties are about $\pm$ 30%. For the leaner flames ($\phi <$ 1.8), the amounts of CH_4 and C_2H_2 present are typically below the detection limit of $\sim 10^{-4}$ mole fraction.

Case	P (Torr)	ϕ	Q_T (slm/cm^2)	$\dot{m}$ (g/cm^2/s)	T_S (K)	L (cm)
1	52	2.15	0.94	0.02	1073	1.0
2	50	2.15	1.0	0.022	1073	1.0
3	30	2.11	1.0	0.022	1073	1.0
4	30	2.12	1.0	0.022	1143	1.0

Table 3.1: Experimental conditions for diamond growth in acetylene/oxygen flames.

Absolute mole fractions for H_2, CO, CO_2, CH_4, and C_2H_2 were obtained at two different pressures (30 and 52 Torr), and the conditions were similar to the cases 1 and 3 of the growth experiments listed in Table 3.1.

3.4 Results

3.4.1 Modeling

Experimental conditions where well-faceted diamond films were grown with acetylene/oxygen flames are listed in Table 3.1. Here P is the pressure, ϕ is the equivalence ratio, Q_T is the flow rate of premixed gases (fuel and oxygen) per unit area of substrate, $\dot{m}$ is the mass flow rate of premixed gases per unit area of substrate, T_S is the substrate temperature, and L is the burner to substrate distance.

Calculated velocity and temperature profiles for the conditions of case 3 are shown in Figure 3-3. The peak temperature is predicted to be 3818 K for this case. The gas leaves the burner at about 8 m/s, and rapidly accelerates through the flame front

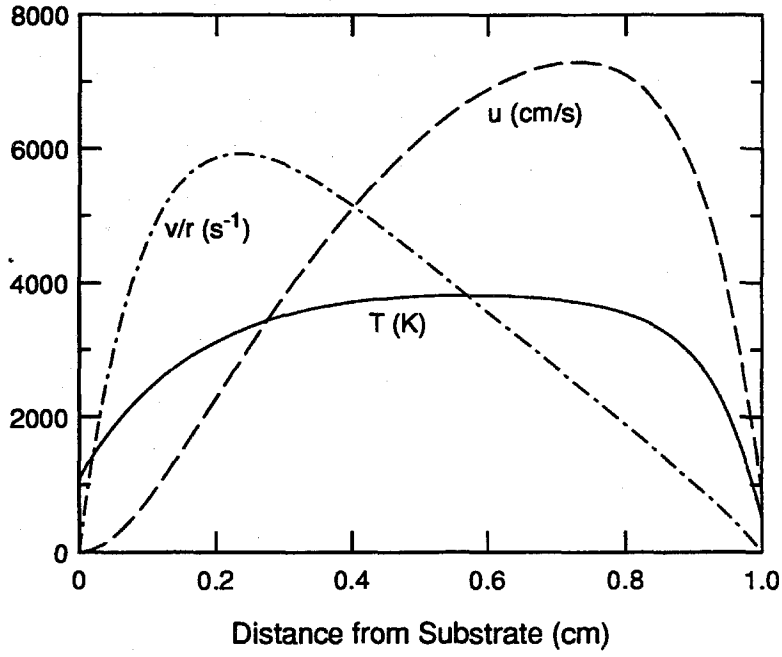

Figure 3-3: Calculated profiles of axial velocity (u), radial strain rate (v/r), and temperature (T) for the conditions of case 3.

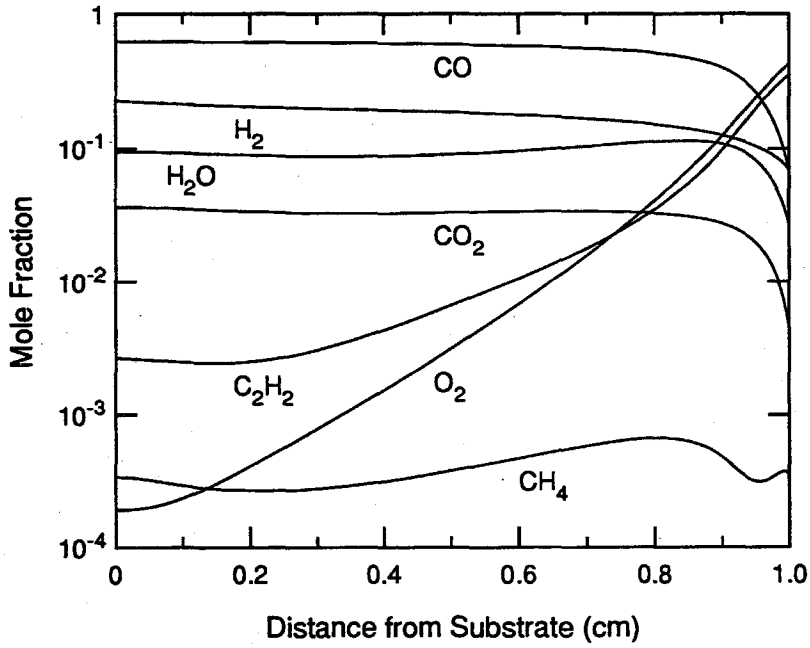

Figure 3-4: Major species profiles calculated for the conditions of case 3.

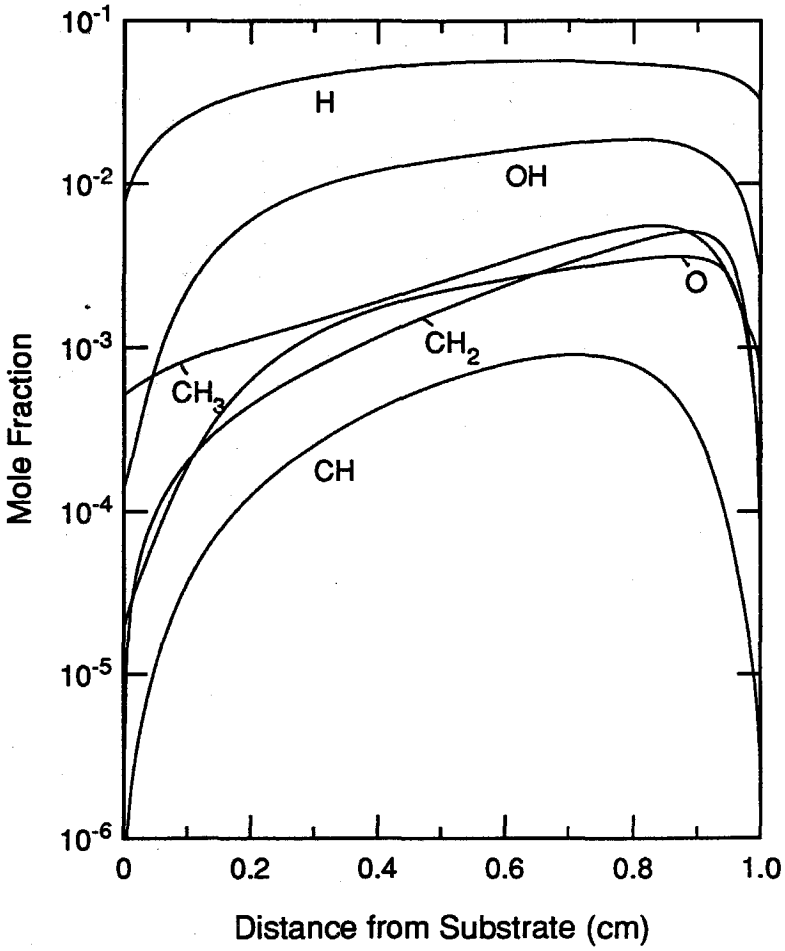

Figure 3-5: Key radical species profiles calculated for the conditions of case 3.

and then stagnates against the substrate. The peak radial strain rate in this flow is calculated to be about 5900 s^{-1}.

Figure 3-4 show calculated profiles of major species for the conditions of case 3. For many of the major stable species (CO, H_2, H_2O, CO_2, and CH_4), rapid changes in mole fraction occur only within 1 mm from the burner tip. On the other hand, C_2H_2 and O_2, which are the two feed gases to the burner, have mole fractions which change over the whole domain of burner to substrate separation. However, all the

	Case 2		Case 3	
Species	STBL	Equil.	STBL	Equil.
Major Stable Species				
[CO]	0.631	0.592	0.627	0.583
[H_2]	0.246	0.298	0.230	0.295
[H_2O]	0.084	0.035	0.095	0.039
[CO_2]	0.034	0.075	0.037	0.083
[C_2H_2]	0.021	5.0e-12	0.027	1.37e-12
[CH_4]	3.7e-4	1.2e-5	3.4e-4	3.7e-6
[C_2H_4]	2.4-5	9.4e-12	9.4e-5	1.5e-12
[O_2]	1.4e-5	9.0e-23	1.9e-4	1.9e-19
Key Radical Species				
[H]	3.1e-3	3.0e-8	7.8e-3	3.8e-8
[CH_3]	2.5e-4	2.6e-11	5.2e-4	1.0e-11
[OH]	1.9e-5	1.3e-11	1.4e-4	1.9e-11
[O]	1.3e-5	1.4e-18	2.0e-5	2.7e-18
[CH_2]	3.2e-7	1.6e-18	2.5e-6	8.2e-19
[C]	2.7e-7	1.2e-27	2.8e-6	1.1e-27
[CH]	2.1e-8	8.4e-25	2.6e-7	5.7e-25
[C_2H]	8.4e-9	8.6e-24	1.0e-7	3.1e-24
[C_2]	8.33e-12	6.4e-33	6.7e-10	3.0e-33

Table 3.2: Predicted mole fractions of some of the major and radical species.

major stable species shown here have almost flat profiles at the substrate. Plots of some of the key radical species profiles are shown in Figure 3-5. These profiles are seen to be markedly affected by the boundary layer chemistry at the substrate. Also all the profiles except for CH_3 show that they are typically diffusion limited at the substrate.

In Table 3.2, predicted mole fractions of some of the major and radical species at the substrate are listed. Equilibrium compositions are the values at the given ϕ, P,

	Case 2	Case 3
T_{flame} (K)	3433	3818
T_{equil} (K)	3006	2942
[H]/[CH_3]	12.3	15.0
[OH]/[H]	6.0e-3	1.8e-2
[O]/[H]	4.1e-4	2.5e-3
[O2]/[H]	4.4e-3	2.5e-2
G_{exp} (μm/hr)	0.7	1.5
G_{max} (μm/hr)	10.7	17.1
G_{model} (μm/hr)	2.1	*

Table 3.3: A comparison of cases 2 and 3. (*: etch rate exceeds deposit rate resulting in no growth.)

and T_S for each case. CO is found to be the most abundant species, and approaches its equilibrium value. Other than CO, low pressure simulations clearly show that mole fractions for species at the substrate are far from their equilibrium values. For low pressure flat flames, the major species except CO_2 and H_2 have typically much higher mole fractions than they would at equilibrium. In low pressure simulations, H is predicted to be the most abundant radical at the substrate. Methyl (CH_3) is estimated to have the highest mole fraction for a hydrocarbon radical at the substrate surface. The STBL model predicts surface concentrations of H ($\sim 10^{-9}$ moles/cm^3) and CH_3 ($\sim 10^{-10}$ moles/cm^3), and the ratio of H to CH_3 mole fractions (~ 10) that are similar to those observed in hot filament reactors [52, 63]. Because the flame method employs O_2 for combustion unlike other diamond CVD methods (such as hot filament and microwave), O_2, OH, and O exist in an appreciable amount (higher than

10 ppm) at the surface. For case 3, the mole fractions for O_2, OH, and O at the surface are predicted to be 190 ppm, 140 ppm, and 20 ppm, respectively.

Cases 2 and 3 are compared in Table 3.3. Some of the results from the equilibrium and STBL calculations are listed along with the measured and calculated growth rates (G). In STBL calculations, T_{flame} is the peak value in the flame, and [H], [CH_3], [O], [OH], and [O_2] are the mole fractions at the substrate. An upper bound estimate of the growth rate, G_{max}, is calculated from equation 3.7, while G_{model} is from the STBL code with the surface mechanism which includes reaction steps for diamond etching by O_2, O, and OH.

For case 2 (50 Torr), the peak flame temperature is predicted to be 3433 K at a distance of 3.8 mm from the burner, compared to the adiabatic flame temperature of 3006 K. For case 3 (30 Torr), the predicted temperature overshoot is even larger (3818 K at a distance of 4.3 mm from the burner, compared to 2942 K).

Similar temperature overshoots have been predicted by Kim and Cappelli [57] in simulations of low pressure acetylene/oxygen/argon flames, and Meeks *et al.* [37] in simulations of atmospheric pressure substrate-stabilized acetylene/hydrogen/oxygen flames. Recently, Bertagnolli and Lucht [39] measured the flame temperature at the computational conditions of Meeks *et al.* [37] using CARS spectroscopy of hydrogen, and observed a peak temperature above the adiabatic flame temperature.

A useful measure to predict diamond film quality is the ratio of H concentration to CH_3 concentration at the substrate [14]. For most environments which grow diamond,

the ratio of [H]/[CH_3] at the surface is measured to be on the order of 10:1 [14, 52, 53, 32]. Higher values of this concentration ratio more effectively suppress the growth of sp^2 non-diamond carbon, and result in higher quality diamond. For cases 2 and 3, predicted ratios of [H]/[CH_3] are 12.3 and 15, respectively. These values are similar to those observed from other environments which grow moderate quality "tool grade" diamond.

The predicted growth rates (G_{max}) are significantly higher (at least a factor of 10) than the measured growth rates (G_{exp}). Since the growth experiments (cases 2 and 3) are performed at a substrate temperature of 1073 K, if the activation energy for diamond growth is assumed to be $\sim$ 23 kcal/mole [51], the simulations which predict the growth rates for a substrate temperature of 1200 K will overpredict the absolute growth rates at 1073 K by a factor of 3. Instead, if the measured growth rates for case 3 ($G_{exp,3} = 1.5$ μm/hr at 1073 K) and case 4 ($G_{exp,4} = 2.3$ μm/hr at 1143 K) are employed to predict the activation energy for diamond growth in the flame environment, $G_{exp,4}/G_{exp,3} = 1.53$ yields the activation energy of 14.9 kcal/mole. The simulations then will overpredict the absolute growth rates at 1073 K by a factor of 2. Also, the Harris diamond growth mechanism only predicts measured diamond growth rates to within a factor of 2 for other diamond growth environments [60]. The remaining discrepancy may be due to overprediction of H and/or CH_3 at the substrate surface. Nevertheless, the relative variation in growth rate is reproduced reasonably well by equation 3.7. The simulations predict that $G_{max,3}/G_{max,2} = 1.6$,

compare to the measured ratio of $G_{exp,3}/G_{exp,2} = 2.1$.

In these calculations, G_{model} is much lower than G_{max}. The difference $G_{max} - G_{model}$ mainly represents the etching of diamond at the substrate due to oxidation. The surface chemistry mechanism used in STBL simulations includes diamond etching steps at the substrate by O_2, O, and OH. Diamond etching by O_2 (reactions 9 and 10 in Appendix B) is based on a measured oxidation rate of diamond [61]. Etching of diamond by O and OH (reactions 11 and 12 in Appendix B) is assumed to be maximum possible etching rate. (Sticking probabilities are set to 1.0.) At typical low pressure (52 Torr) diamond growth flame conditions, this surface reaction mechanism with the maximum etch rate by O and OH has resulted in good predictions of the measured diamond growth rates [38]. For case 2 ($P = 50$ Torr, $\phi = 2.15$), $G_{model,2}$ of 2.1 μm/hr is three times higher than the measured growth rate of $G_{exp,2} = 0.7$ μm/hr.

For case 3 ($P = 30$ Torr, $\phi = 2.11$), this surface mechanism overpredicts the total etch rate of diamond. $G_{model,3}$ is calculated to be -14.9 μm/hr, compared to the observed growth rate of $G_{exp,3} = 1.5$ μm/hr. For case 3, the flame is leaner ($\phi = 2.11$) than for case 2 ($\phi = 2.15$), and predicted mole fractions of O_2, O, and OH at the substrate are higher than those values of case 2 ($[O_2]$ is higher by a factor of 13.6, [OH] by a factor of 7.4, and [O] by a factor of 1.5).

STBL calculations for case 3 with different sets of surface chemistry mechanisms (with and without etching steps by O_2, OH, and O) show that the etch rate by O_2 is

relatively small (0.05 μm/hr), and the dominant etching of diamond is by OH (23.4 μm/hr) and O (3.1 μm/hr). For the cases including the etching reactions, sticking probabilities for OH and O are set to 1.0, thus the calculated etch rates are the maximum possible by OH and O. The true etch rates would be less than these values. These results show that etching reactions by OH and O in the surface mechanism should be carefully readjusted to predict the correct growth rate in leaner flames (ϕ < 2.15) at higher flow rates ($\dot{m}$ > 0.02 g/cm^2/s).

However, it should be noted that [H], [CH_3] and the [H]/[CH_3] ratio at the substrate are insensitive to the variations in the surface mechanism (with and without etching reactions), and the predicted ratios of [H]/[CH_3] for case 3 were found to be $\sim$ 15.

To examine general trends in parameter variations, and to seek improved flame conditions for high quality, high growth rate diamond deposition in acetylene/oxygen flames, numerical parametric studies were carried out. The six parameters for these simulations are: the pressure P (Torr), the equivalence ratio ϕ, the mass flow rate of premixed gases (fuel and oxygen) $\dot{m}$ (g/cm^2/s), the burner to substrate distance L (cm), the burner temperature T_B (K), and the substrate temperature T_S (K). For the simulations presented here, three of the parameters are fixed: L = 1 cm, T_B = 500 K, and T_S = 1200 K. The other three parameters are varied within the range of P = 30–60 Torr, ϕ = 2.0–2.30, and $\dot{m}$ = 0–0.04 g/cm^2/s. The surface chemistry mechanism with the maximum etch rates of diamond by OH and O was used in these

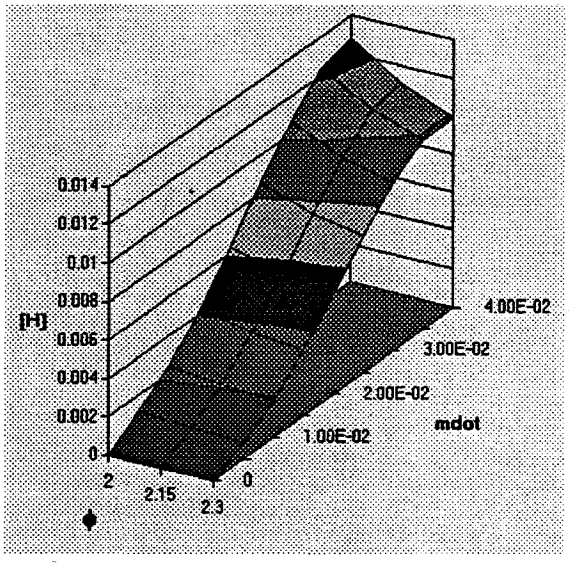

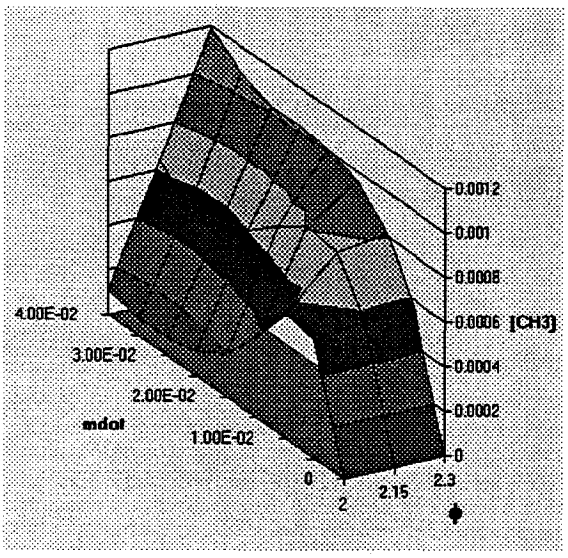

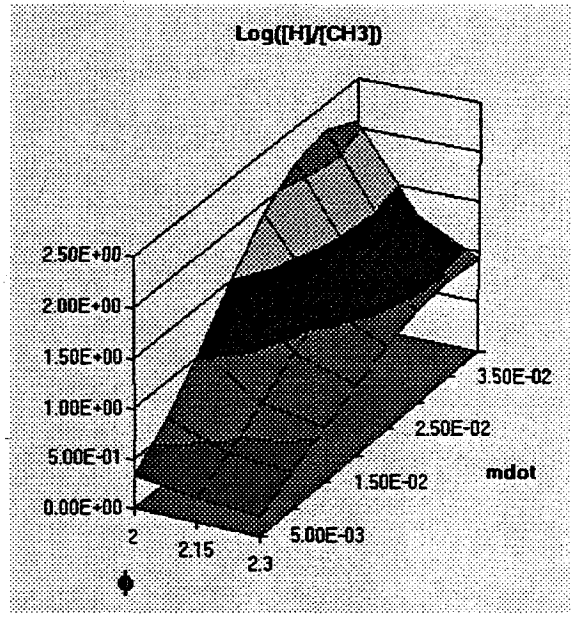

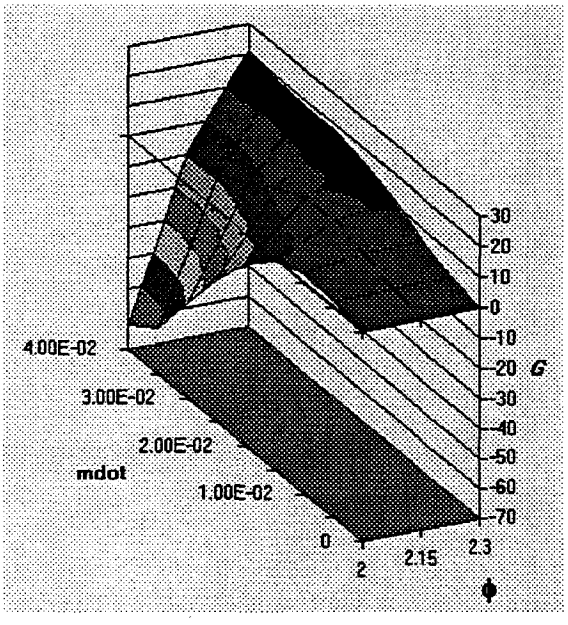

Figure 3-6: Predicted [H], [CH_3], [H]/[CH_3] ratio and G at 30 Torr. The unit of mdot ($\dot{m}$) is g/cm^2/s and G is given in μm/hr.

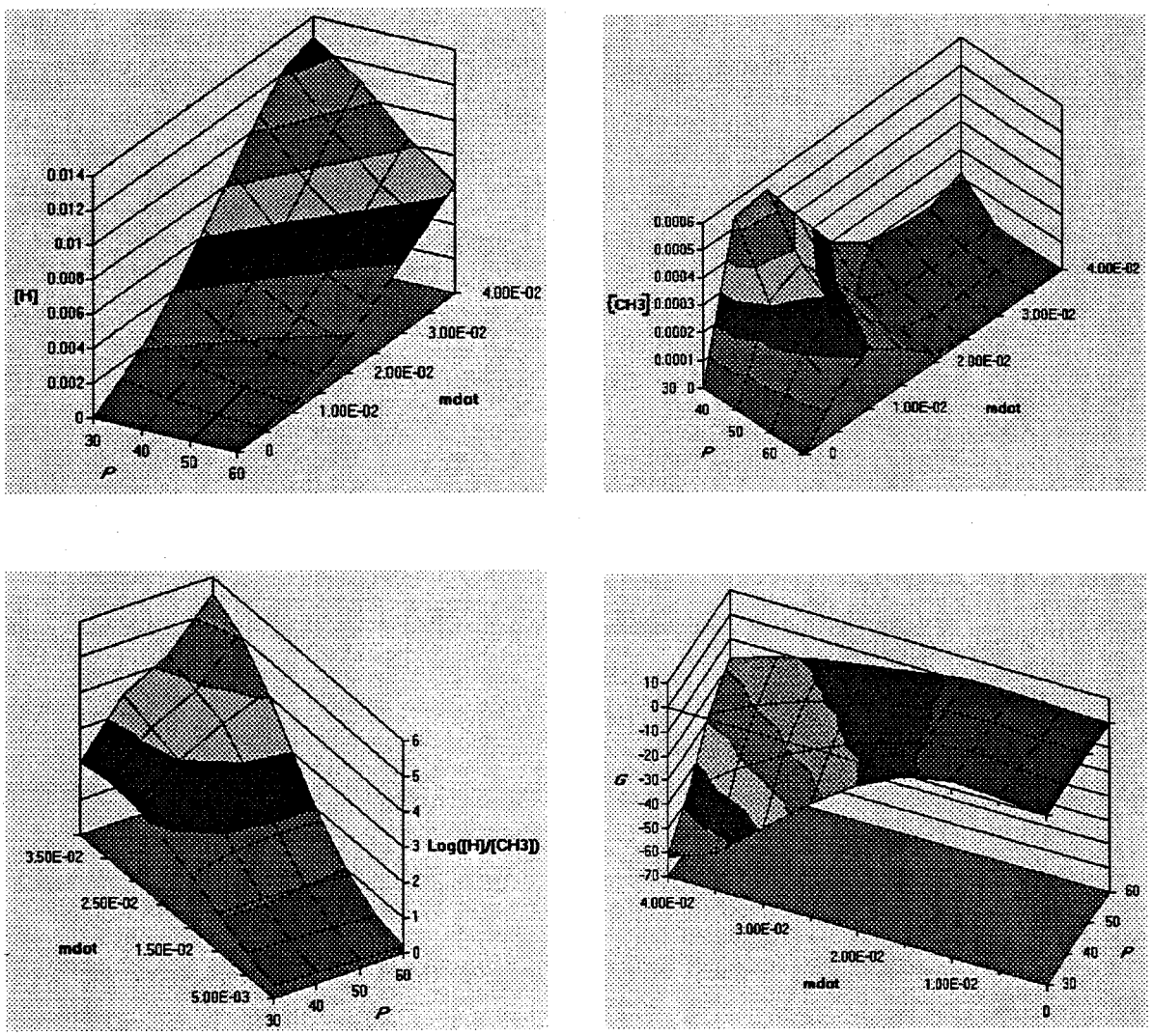

Figure 3-7: Predicted [H], [CH_3], [H]/[CH_3] ratio and G at $\phi = 2.0$. The unit of mdot ($\dot{m}$) is g/cm^2/s, P is given in Torr, and G is given in μm/hr.

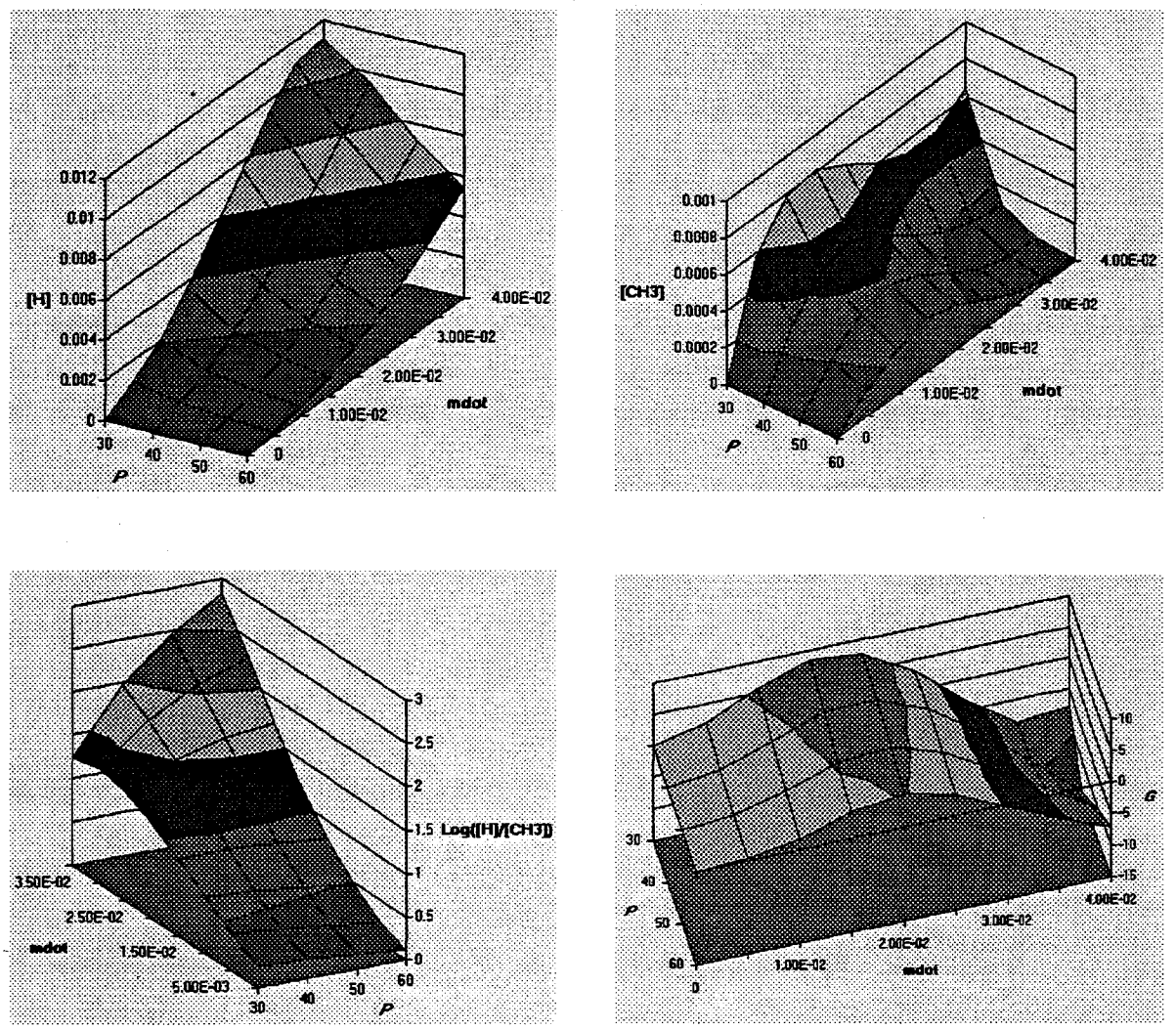

Figure 3-8: Predicted [H], [CH_3], [H]/[CH_3] ratio and G at $\phi = 2.15$. The unit of mdot ($\dot{m}$) is g/cm^2/s, P is given in Torr, and G is given in μm/hr.

simulations.

Figure 3-6 shows the variations in predicted [H], [CH_3], and the [H]/[CH_3] ratio at the substrate and the calculated growth rate G (μm/hr) with respect to ϕ and $\dot{m}$. At constant ϕ, increasing $\dot{m}$ leads to an increase in the mole fraction of H. At constant $\dot{m}$, the mole fraction of H increases as the ϕ decreases. Higher mole fraction of H is predicted at higher $\dot{m}$ and lower ϕ. For the methyl radical (CH_3), it has a higher mole fraction at higher ϕ and higher $\dot{m}$.

A higher ratio of [H]/[CH_3] is predicted at lower ϕ and higher $\dot{m}$. This suggests that high quality diamond can be obtained in leaner flames with higher flow rates. Ratios of [H]/[CH_3] > 10:1 at the substrate are predicted for $\dot{m} > 0.015$ g/cm^2/s with $\phi = 2.0$, or for $\dot{m} > 0.023$ g/cm^2/s with $\phi = 2.15$.

G is predicted to increase as ϕ and $\dot{m}$ increase. However, at $\phi = 2.3$, the [H]/[CH_3] ratio is always predicted to be less than 10:1, so even moderate grade diamond growth is not expected. At $\phi = 2.0$, even though the ratio of [H]/[CH_3] is predicted to rapidly increase for $\dot{m} > 0.015$ g/cm^2/s, flames become too oxidizing for diamond growth and no diamond growth is predicted for those values of $\dot{m}$. At 30 Torr, moderate grade diamond is predicted to grow near $\phi = 2.15$, and $\dot{m} = 0.025$ g/cm^2/s.

As pointed out earlier, since the predicted value of G is very sensitive to the choice of surface mechanism (with or without etch reactions), the etch rate of diamond by OH and O could be overpredicted in higher flow rate, leaner flames. However, since [H] and [CH_3] are relatively insensitive to the variations of surface mechanism, the

calculated ratio of [H]/[CH_3] can be effectively used to seek high quality diamond growth conditions and to narrow the possible set of experimental conditions by excluding poor diamond and non-diamond growth regions ([H]/[CH_3] < 10:1).

Figure 3-7 shows the variations in predicted [H], [CH_3], [H]/[CH_3], and the calculated growth rate G with respect to P and $\dot{m}$ for $\phi = 2.0$. At this equivalence ratio, the mole fraction of H at the substrate increases as P decreases and $\dot{m}$ increases. The mole fraction of CH_3 increases as P increases, and has its maximum value at $\sim \dot{m} = 0.01$ g/cm^2/s and $P = 30$ Torr. The [H]/[CH_3] ratio rapidly increases as P and $\dot{m}$ increase, and the acceptable ratio of [H]/[CH_3] > 10:1 for diamond growth is predicted at about $\dot{m} > 0.015$ g/cm^2/s for a pressure range of $P = 30$–60 Torr. However, no diamond growth is expected at higher $\dot{m}$, and only moderate quality diamond is predicted to grow at $P = 40$–50 Torr, and $\dot{m} = 0.015$ g/cm^2/s. Since the [H]/[CH_3] ratio at the surface is very sensitive to any change in $\dot{m}$ at this pressure of 40–50 Torr, high quality diamond may be grown by small increases in $\dot{m}$.

The variations in [H], [CH_3], [H]/[CH_3] ratio, and G with P and $\dot{m}$ at $\phi = 2.15$ are shown in Figure 3-8. H, CH_3 and the ratio of H to CH_3 mole fractions at the surface have the same trends as the case of $\phi = 2.0$. At $\phi = 2.15$, the acceptable ratio of [H]/[CH_3] > 10:1 for diamond growth is predicted at about $\dot{m} > 0.022$ g/cm^2/s for a pressure range of 30–60 Torr. At this $\dot{m}$ range, reducing P is favorable for increasing G, but at the cost of lowering the quality. This trend was observed experimentally as well. When moving conditions from case 2 ($P = 50$ Torr, $\phi = 2.15$) to case 3 ($P = 30$

	Case 2	Case 3	Case A	Case B	Case C	Case D
P (Torr)	50	30	50	30	25	25
ϕ	2.15	2.11	2.15	2.15	2.15	2.08
$\dot{m}$ (g/cm^2/s)	0.022	0.022	0.025	0.025	0.025	0.035
[H]/[CH_3]	12.3	15.0	22.2	15.7	12.7	17.0
G_{max} (μm/hr)	10.7	17.1	8.9	20.9	28.0	27.5

Table 3.4: Improved conditions for diamond growth: $T_B = 500$ K, $T_S = 1073$ K, and $L = 1.0$ cm.

Torr, $\phi = 2.11$), a slightly leaner flame was necessary in case 3 to keep the diamond quality, which resulted in an increase in the [H]/[CH_3] ratio at the substrate.

Within the parametric space investigated, the ratio of [H]/[CH_3] (thus the diamond film quality) is predicted to increase as ϕ decreases (flame becomes leaner), and as $\dot{m}$ and P increase. However, as ϕ decreases, the growth rate G also decreases. These general trends which are predicted from the modeling study match well with the observed trends from experiment.

Growth rate G is predicted to be very sensitive to variation of $\dot{m}$, and this has been observed experimentally. At constant P and ϕ near the diamond growth conditions ($\sim \phi = 2.1$–2.15), G is predicted to have its maximum value G_{max} as $\dot{m}$ reaches its value of $\dot{m}_{max}$. At $\dot{m} > \dot{m}_{max}$, G continuously decreases as $\dot{m}$ increases, and finally reaches a point of no deposition. This is mainly due to the etching of diamond by O and OH.

Combined with the observed experimental results, STBL simulations can be effectively used to seek improved conditions for higher quality and higher growth rate.

Well-faceted, continuous diamond films have been grown in high flow rate ($\sim \dot{m} = 0.02$ g/cm^2/s) acetylene/oxygen flames at $P = 30$–52 Torr and $\phi = 2.11$–2.15. Typical conditions are cases 2 and 3 as listed in Table 3.4. The observed diamond grow rates are 0.7 μm/hr for case 2 and 1.5 μm/hr for case 3.

Since there is no available information on etch rates of diamond by OH and O, and since the relative variation in measured growth rate is reproduced reasonably well by G_{max} calculated from equation 3.7 at these conditions, simulations near these conditions (cases 2 and 3) are more reliable for predicting the correct growth rate by comparison with the predicted growth rate G_{max}. Some of the improved conditions (cases A–D) for diamond growth, which are predicted near to the conditions of cases 2 and 3, are tabulated in Table 3.4.

For case A, higher quality diamond film with a lower growth rate than case 2 is expected to grow due to a small increase in $\dot{m}$ over the conditions of case 2. For case B, a small increase in $\dot{m}$ and ϕ over the conditions of case 3, leads to a higher predicted growth rate without lowering diamond quality.

For case C, the simulations indicate that higher growth rate diamond is predicted to grow by reducing P from the conditions of case B. Moderate quality diamond which is similar to the quality of case 2 is predicted to grow with higher growth rate for this case. For case D, by increasing $\dot{m}$ and decreasing ϕ from the conditions of case C, higher quality diamond can grow with a growth rate similar to case C.

3.4.2 Mass Spectrometry

Absolute mole fractions for CO, H_2, CO_2, CH_4, and C_2H_2 were obtained at two different pressures (30 and 52 Torr), with and without a substrate. The total flow rate Q_T was $\sim$ 0.5 slm/cm^2 (half the value of case 1 or 3), and other experimental conditions were similar to case 3 (30 Torr) and case 1 (52 Torr). Figure 3-9 shows the mass spectrometry results at various distances from the burner for P = 30 Torr without a substrate, and with a substrate at a distance of 1 cm from the burner. The symbols represent measured experimental data, and the curves are the predictions from the STBL simulations. Experimental conditions were: P = 30 Torr, Q_T = 0.5 slm/cm^2, ϕ = 2.13, T_B = 450 K, and Ar dilution of $\sim$ 8%. With a substrate, L was 1.0 cm and T_S was 973 K.

With and without a substrate, measured H_2, CO, and CO_2 mole fractions generally match well with the predictions. The model predicts that these major species rapidly change their amounts near the burner surface ($\sim$ < 2 mm from the burner) and have roughly flat profiles after $\sim$ 5 mm from the burner. Measured mole fractions also have same trends, but their profiles are shifted $\sim$ 1–2 mm from the predicted profiles.

With a substrate at L = 1.0 cm, predicted CO and H_2 profiles and measured data at the substrate are very similar to those without a substrate. For CO_2, the effect of the substrate is clearly seen, and both values from the model and experiment are higher than for without a substrate.

The signal to noise ratio is typically lower for CH_4 and C_2H_2, so measured mole

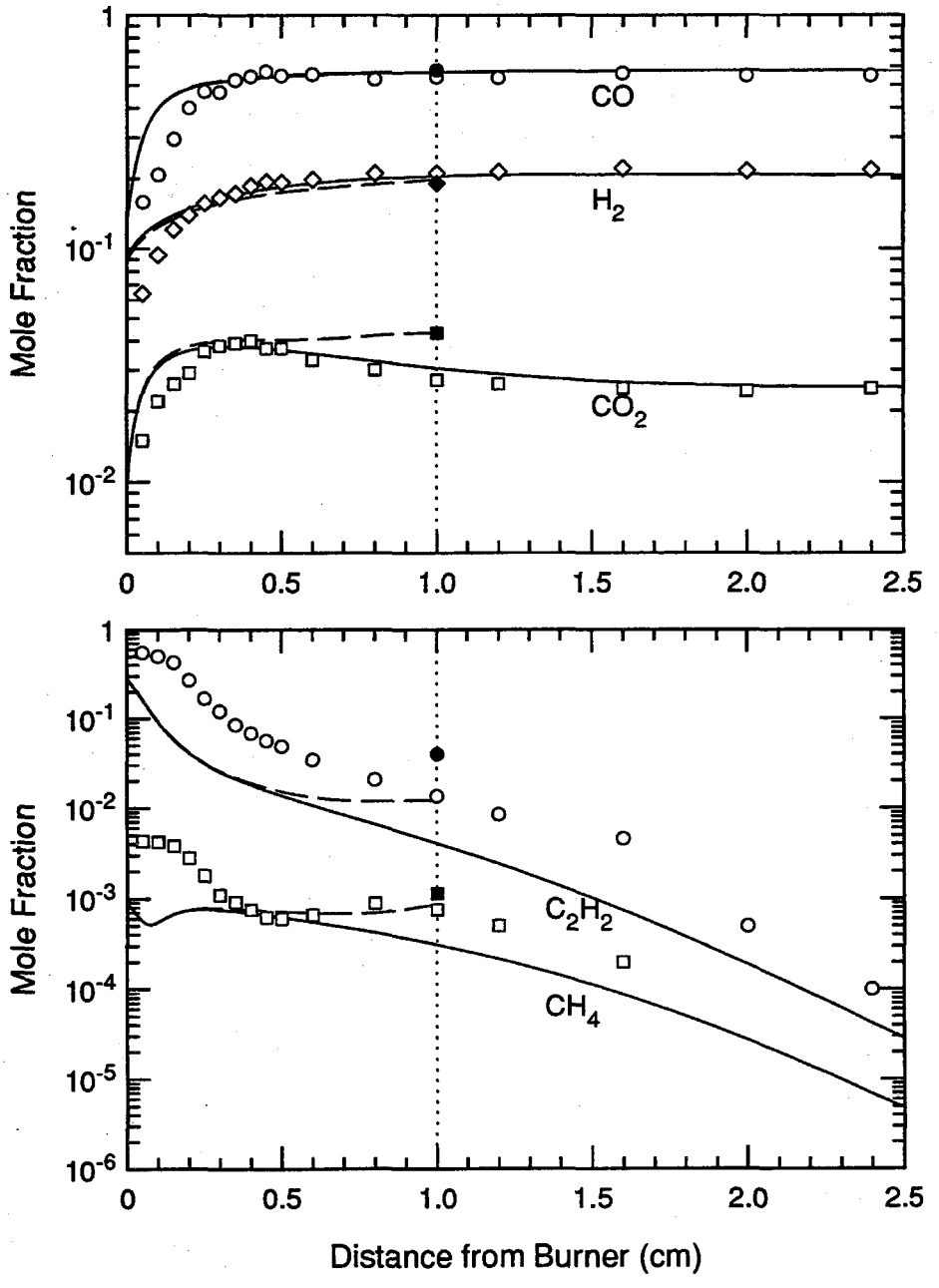

Figure 3-9: Stable species mole fractions at $P = 30$ Torr and $\phi = 2.13$: predictions of the STBL model without a substrate (solid lines) and with a substrate at $L = 1.0$ cm (dashed lines); experimental data without a substrate (open symbols) and with a substrate at $L = 1.0$ cm (solid symbols).

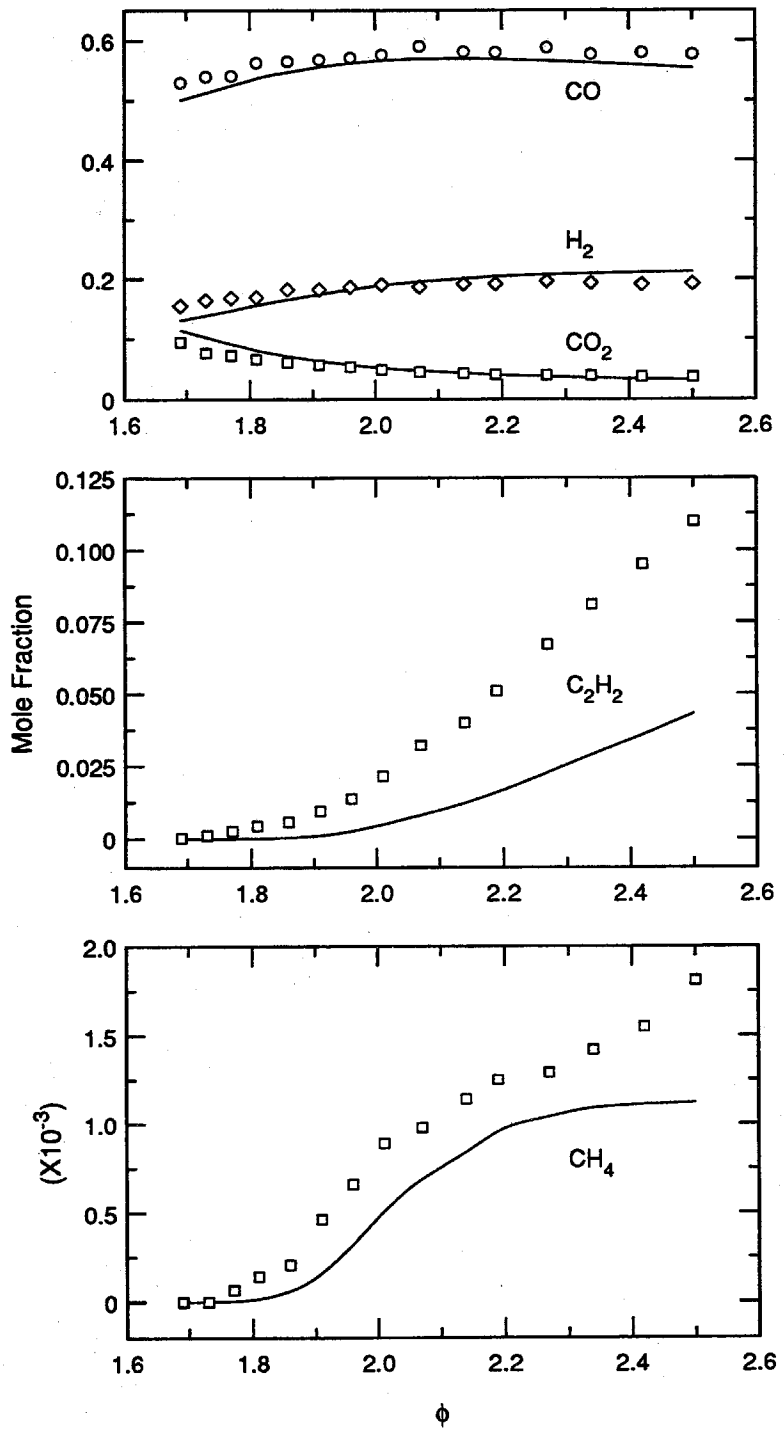

Figure 3-10: Stable species mole fractions at the substrate at $P = 30$ Torr.

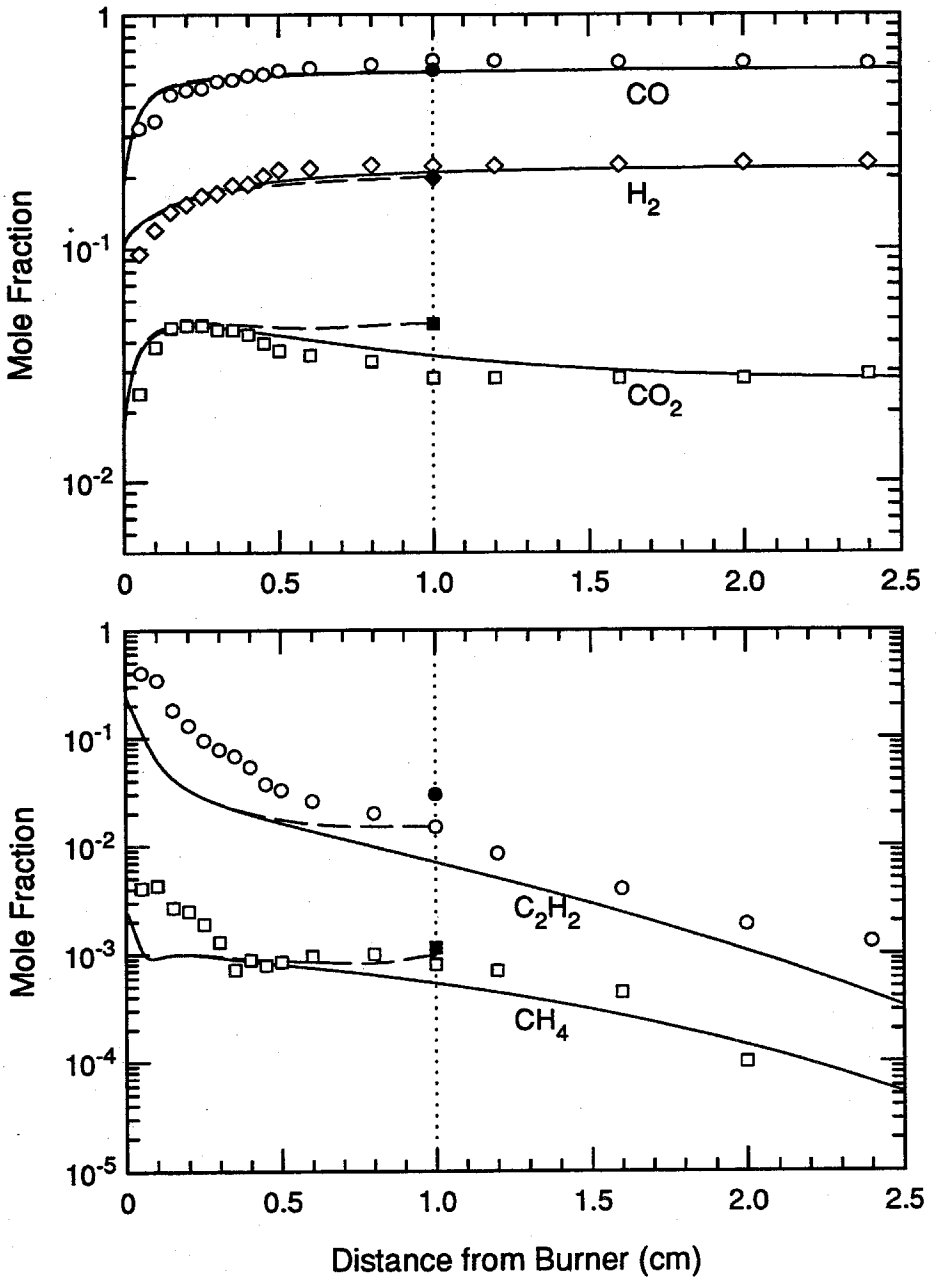

Figure 3-11: Stable species mole fractions at $P = 52$ Torr and $\phi = 2.13$: predictions of the STBL model without a substrate (solid lines) and with a substrate at $L = 1.0$ cm (dashed lines); experimental data without a substrate (open symbols) and with a substrate at $L = 1.0$ cm (solid symbols).

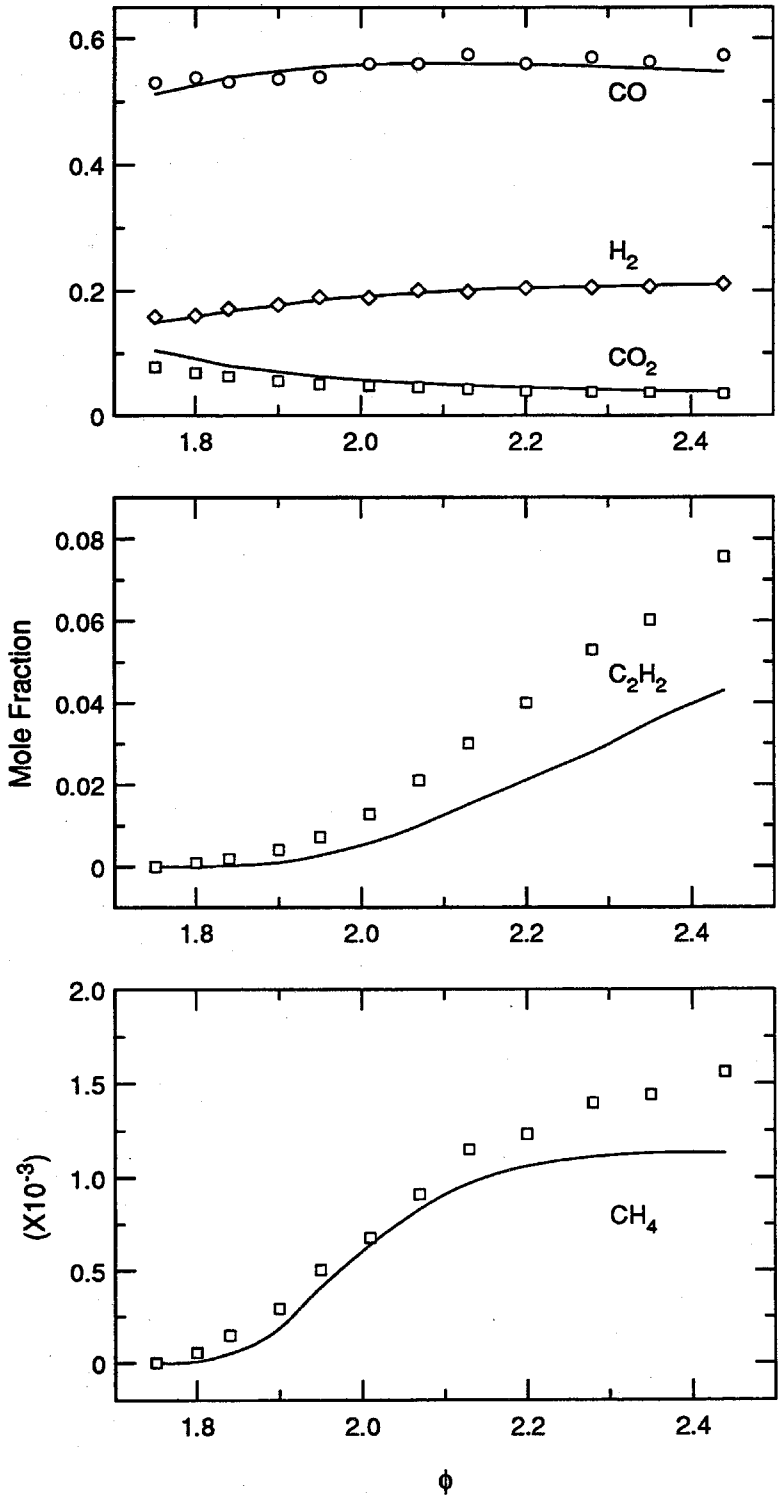

Figure 3-12: Stable species mole fractions at the substrate at $P = 52$ Torr.

fractions of these species have larger uncertainties (± 30%). Since the detection limit of the mass spectrometer is a mole fraction of about 10^{-4}, CH_4 can not be detected at distances greater than 16 mm from the burner without a substrate. Mole fractions of CH_4 and C_2H_2 are typically measured to be higher than the predicted mole fractions for both with and without a substrate. With a substrate, mole fractions of CH_4 and C_2H_2 at 1.0 cm from the burner are much higher than without a substrate.

For C_2H_2, measured mole fractions are consistently much higher than the predicted values. Since C_2H_2 is a provided fuel to the system and the flame is rich ($\phi = 2.13$) and fast, it may be possible that some excess of C_2H_2 survives through the flame because of such short residence time. However, the mole fraction of C_2H_2 at 0.5 mm from the burner surface is measured to be 0.55 and this is even higher than the mole fraction of C_2H_2 (0.42) provided to the burner. Since the measured mole fractions of all other major stable species (CO, H_2, and CO_2) match well with the predicted values for $\phi = 2.13$, it is likely that the measured cross section ratio of C_2H_2 to Ar from the calibrated mixture had a significant error (at least 30%). If a correction of 30% is applied to the calibrated cross section ratio of C_2H_2 to Ar, measured C_2H_2 mole fractions better match the predictions.

Additional discrepancy near the burner surface can be caused by the burner design. The burner face consists of an array of 1 mm diameter holes, so the gas exit velocity at the burner holes is much higher ($\sim$ 28 m/s) than the average velocity ($\sim$ 4 m/s). Since the prediction from the model only accounts for the average velocity at the

burner surface, this causes a discrepancy in the calculation near the burner surface.

Experimental data from mass spectrometry typically show $\sim$ 2 mm shifts from the predicted profiles. This discrepancy may be due to the resolution limit of a microprobe. It has been found that measured species profiles can be shifted from the true profiles, typically by an amount which is of the order of several probe orifice diameters [62]. In these experiments the tip diameter of the microprobe was $\sim$ 400 μm, so a spatial shift of 1–2 mm is expected. If all measured mole fractions are shifted $\sim$ 2 mm toward the burner surface, the mass spectrometry results match the predictions much better.

Mass spectrometry experiments were also performed with a substrate at the same conditions. Figure 3-10 shows the results of mass spectrometry at the substrate with varying stoichiometric ratios ranging from $\phi = 1.75$ to $\phi = 2.45$. The substrate temperature was 973 K and L was 1 cm. As shown in Figure 3-10, measured mole fractions of CO, H_2, and CO_2 at the substrate match well with the predictions of the model within the experimental uncertainty. For CH_4 and C_2H_2, the mole fractions are measured to be consistently higher than the predicted mole fractions, but the qualitative trends seen experimentally are well-reproduced by the simulations.

Figures 3-11 and 3-12 show the mass spectrometry results for the 52 Torr case. Experimental conditions were: $P = 52$ Torr, $Q_T = 0.47$ slm/cm^2, $\phi = 2.13$, $T_B = 420$ K, and Ar dilution of $\sim$ 9%. In the case of employing a substrate, T_S was 953 K, L was 1 cm, and ϕ was 1.75–2.45. Mole fractions from experiments and calculations

generally match better than the 30 Torr case.

The modeling predicts the mole fractions of major species (H_2, CO, and CO_2) within the experimental uncertainty. For CH_4, up to $\phi = 2.2$, the modeling predicts the mole fractions within the experimental uncertainty. The modeling typically shows higher discrepancy than the experimental uncertainty in predicting the mole fractions of C_2H_2. However, for C_2H_2, the discrepancy is lower than for the 30 Torr case.

3.5 Summary

Flame simulations were carried out to analyze the growth environment in low pressure acetylene/oxygen flames which were described in Chapter 2. The model predicts peak flame temperatures above the adiabatic flame temperature, and surface concentrations of H and CH_3, and the ratio of H to CH_3 mole fractions similar to those observed in hot filament reactors. In contrast to other CVD environments, the etch rate of diamond by OH and O may be important in determining the grow rate of diamond in a low pressure flame environment.

The simulations of low pressure (25–30 Torr) acetylene/oxygen flames near diamond growth conditions suggest that increasing the mass flow rate while reducing the pressure is favorable for increasing the growth rate, and higher quality diamond can be grown in leaner flames. Mass spectrometry results show that the numerical modeling generally predicts the mole fractions of CO_2, CO, and H_2 within the experimental uncertainty. For CH_4 and C_2H_2, even with the larger uncertainty, the

qualitative trends observed experimentally are well reproduced by the simulations.

Chapter 4

Diamond Film Growth in Alternative Fuel Flames

4.1 Overview

In this chapter, diamond film growth experiments with several hydrocarbon fuels other than acetylene are described. The experiments are carried out in the same low pressure combustion facility described in Chapter 2. MAPP/oxygen, propylene/oxygen, ethylene/oxygen, and propane/oxygen flames at low pressures (50–180 Torr) are employed for growth experiments.

The numerical analysis of acetylene/oxygen flames discussed in Chapter 3 indicates that high surface concentrations of [H], [CH_3], and the ratio of [H]/[CH_3] are important in growing high quality diamond films, as well as in achieving a high growth rate. High radical concentrations at the substrate are readily achieved with high temperature, high speed flames such as acetylene/oxygen flames.

In a low pressure flame environment, the model predicts that H and CH_3 have much higher surface concentrations than they would at equilibrium. This suggests that the nonequilibrium chemistry at low pressures may allow other hydrocarbon fuels (such as propylene and propane) to deposit diamond with reasonable growth rates, although diamond is less likely to grow in these flames since their flame temperature and flame speed are significantly less than acetylene/oxygen flames. The computational modeling studies and flame diagnostics used to analyze the experimental data from these flames will be described in Chapter 5.

4.2 Experimental

The experiments were carried out in the same low pressure combustion facility described in detail in Chapter 2. Premixed flames were stabilized on a water-cooled burner housed in a water-cooled bell jar vacuum chamber. Some experiments were carried out with the 4 cm diameter burner which was used in the acetylene/oxygen flame experiments.

To explore higher total flow rates (> 1 slm/cm^2) while employing the same cooling system, mass flow controllers, and vacuum pump described in Chapter 2, a new small diameter burner face was designed. The modified burner for higher flow rates is shown schematically in Figure 4-1. A 2 cm diameter copper burner face, with 1 mm diameter holes spaced 2 mm in a hexagonal array was fabricated and attached to the face of the 4 cm diameter burner.

Experiments were conducted using silicon wafers [0.5 mm thick, (100) orientation], molybdenum disks (5 cm diameter, 0.6 cm thick), and molybdenum foils (0.25 mm thick) as substrates. Silicon and molybdenum foil were pretreated with 0.25 μm diamond grit in paste (some cases, with 500 grit sand paper), and were rinsed with acetone. The molybdenum disks were pretreated by the series of steps described in Chapter 2. The substrate is radiatively cooled, and typically reaches a steady-state temperature of 700–940 °C during growth. No additional substrate cooling or heating was used in the present work. The substrate temperature was measured using a two-color infrared pyrometer.

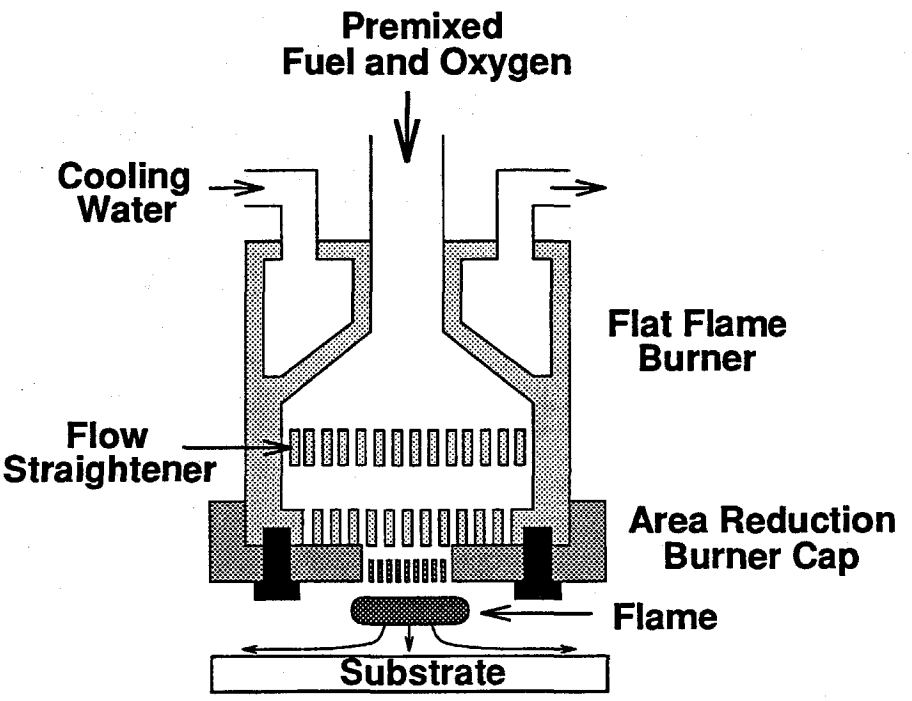

Figure 4-1: Small burner (2 cm diameter) for high flow rate experiments.

Some of the fuels used in these experiments and their characteristics are listed in Table 4.1. Listed values of flame temperature T_f, flame speed V_f, and explosive limit are for combustion with oxygen. MAPP (a trademark of the BOC Group, Inc.) gas used is a commercially-available stabilized mixture of about half liquefied petroleum gas (mainly propylene and a small amount of propane) and half C_3H_4. There are two isomers of C_3H_4 contained in MAPP gas, methyl acetylene (also called propyne), and propadiene (also called allene). (The concentration of a third isomer, cyclopropene is very low.) Two different sources of propylene gas were used. The first was a commercially-available mixture of propylene and propane ("HPG" gas, Airco, greater than 80% propylene) and the second was 99.0% propylene (Matheson).

Fuel	T_f (°C)	V_f (m/s)	Total heat value (kJ/kg)	Expl. limit (%)	Shock Sens.	Handling
C_2H_2	3160	6.9	50185	3–93	unstable	comp. gas
MAPP	2927	4.7	48791	2.5–60	stable	liquefied
C_3H_6	2893	4.6	46468	5–60	stable	liquefied
C_3H_8	2526	3.7	47796	2.4–57	stable	liquefied

Table 4.1: Characteristics of selected hydrocarbon fuels [64].

Diamond was grown using both gases, under very similar conditions. The other two hydrocarbon fuels used were 98% ethylene (Matheson) and 96% propane (Matheson). The oxygen used was from a laboratory-grade gas cylinder.

In these experiments, flames were ignited using acetylene under the ignition conditions of the acetylene/oxygen flames described in Chapter 2, and then slowly ramped up to growth run conditions. For the experiments reported here, diamond was deposited for pressures ranging from 50 to 180 Torr. The burner to substrate distance was D_S = 3.75–10.5 mm, and the total flow rate was Q_T = 0.5–1.9 slm/cm^2.

4.3 Results

4.3.1 MAPP/Oxygen Flames

Four different experimental conditions which resulted in diamond deposits on silicon in MAPP/oxygen flames are summarized in Table 4.2. Since MAPP is a commercial mixture of C_3H_4, propylene, and propane, the C:O ratio is listed instead of the equiv-

Case	Burner Size (cm)	P (Torr)	Q_T (slm/cm^2)	C:O	T_S (°C)	D_S (mm)	Growth rate (μm/hr)
1	4	70	0.5	0.77	750	12	0.5
2	4	90	0.65	0.73	780	10	2
3	4	120	0.94	0.71	820	7.6	4
4	2	180	1.9	0.69	830	3.75	8

Table 4.2: Experimental conditions for diamond growth on silicon substrate in MAPP/oxygen flames.

alence ratio ϕ. On silicon substrate, only isolated diamond crystals were grown, so the averaged diameter was chosen as the growth rate.

With MAPP/O_2 flames, diamond was deposited for pressures ranging from 70 to 180 Torr. Lower pressures were attempted, but the flame was unstable and no diamond could be grown. The required fuel to oxygen ratio for diamond growth was found to depend on pressure, and varied from 0.46 (C:O = 0.69) at 180 Torr to 0.51 (C:O = 0.77) at 70 Torr. The total flow rate (MAPP and oxygen) was typically 0.5 to 1.9 standard liters per minute (slm) per cm^2 of burner area.

SEM micrographs of carbon deposits on silicon under the conditions of case 1 are shown in Figures 4-2 and 4-3. At this pressure (70 Torr) and C:O ratio, the flame was slightly distorted and not flat. This resulted in nonuniform carbon deposits over the deposition areas and the deposited carbon morphology varied with position. Figure 4-2 shows well-faceted diamond crystals grown in a 5 hour run. The diamond crystal growth rate was approximately 0.5 μm/hr. Longer duration runs of up to 10 hours were performed under these conditions, but only resulted in isolated diamond

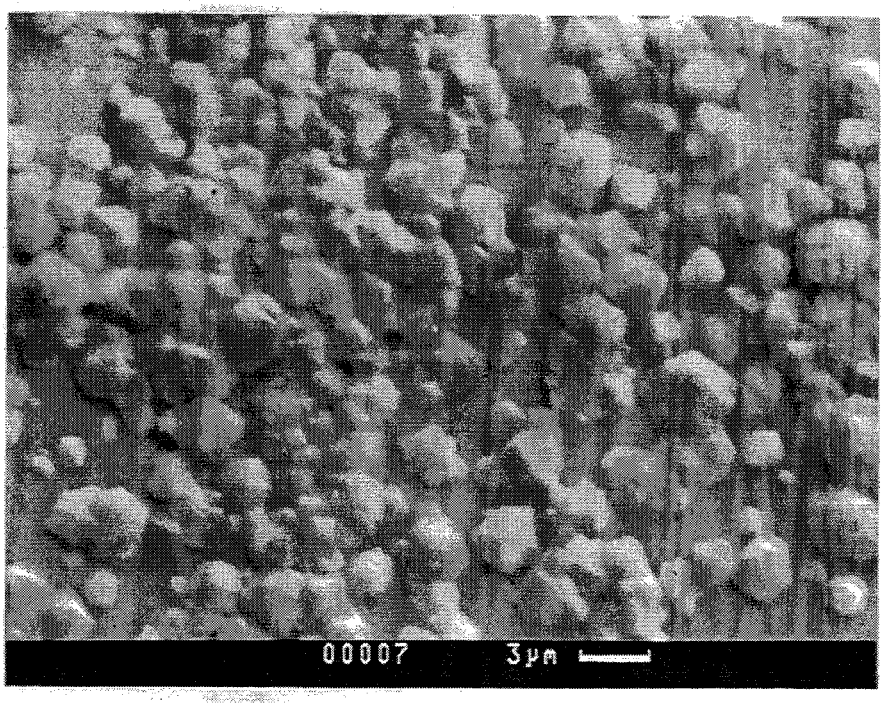

Figure 4-2: SEM micrograph of isolated diamond crystals grown on silicon in a 70 Torr MAPP/oxygen flame.

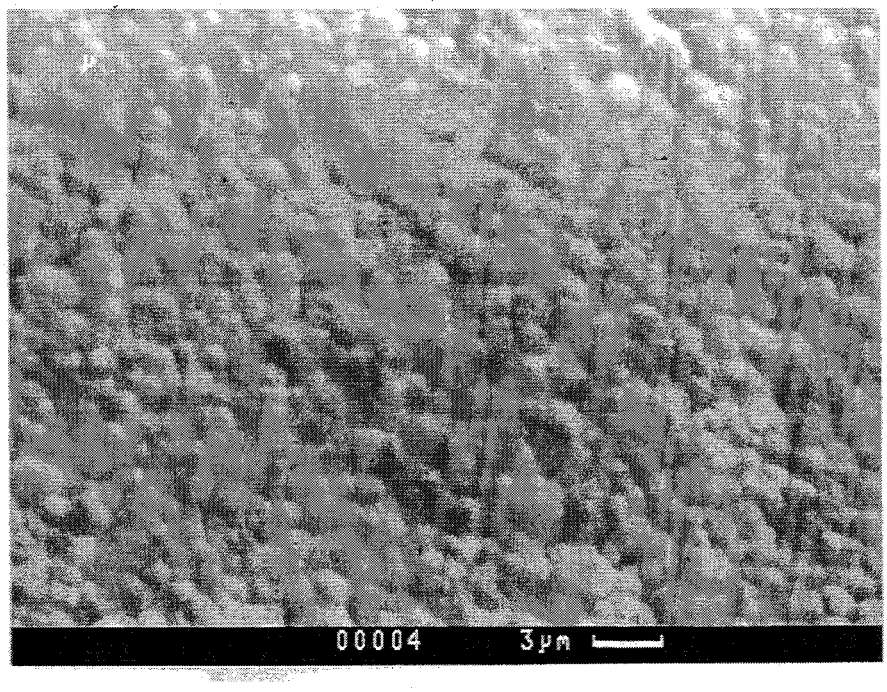

Figure 4-3: SEM micrograph of non-diamond carbon film grown on silicon in a 70 Torr MAPP/oxygen flame.

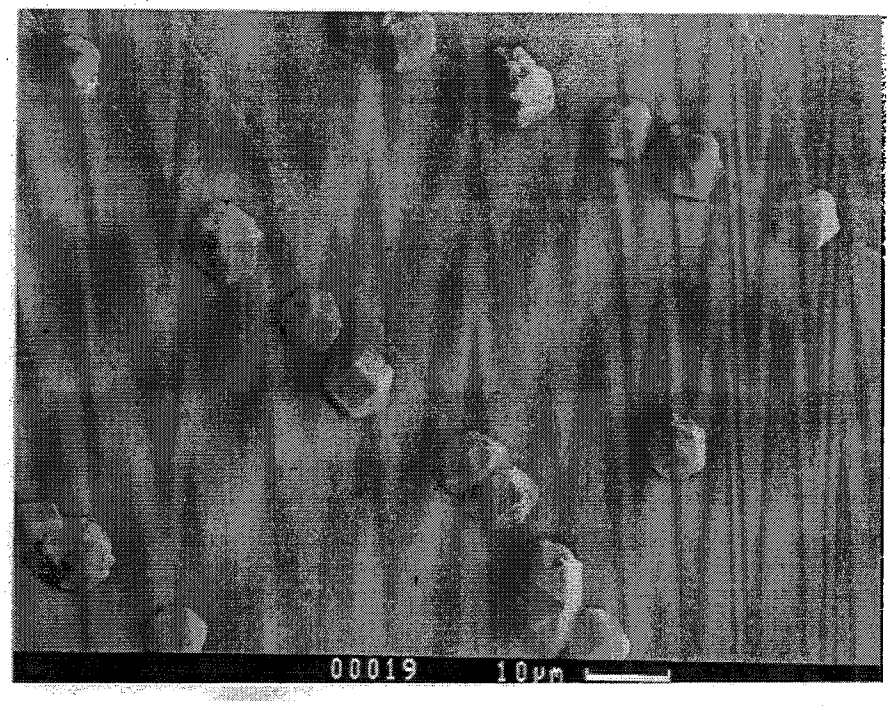

Figure 4-4: SEM micrograph of high quality diamond crystals grown on silicon in a 180 Torr MAPP/oxygen flame.

deposits. On other portions of the same substrate, continuous non-diamond carbon films were deposited as shown in Figure 4-3. With higher flow rates (> 0.5 slm/cm^2) at this pressure, the flame was either too unstable to perform growth experiments or was blown out.

By increasing the pressure, flames could be sustained at higher flow rates. Well-faceted isolated diamond crystals were grown at 90 Torr with $Q_T = 0.65$ slm/cm^2, and the crystal growth rate was ~ 2 μm/hr. At 120 Torr, the flame was sustained up to $Q_T = 0.94$ slm/cm^2, and isolated diamond crystals were grown at C:O $= 0.71$, $D_S = 7.6$ mm. The growth rate was approximately 4 μm/hr.

SEM micrographs of carbon deposits on silicon under the conditions of case 4 are

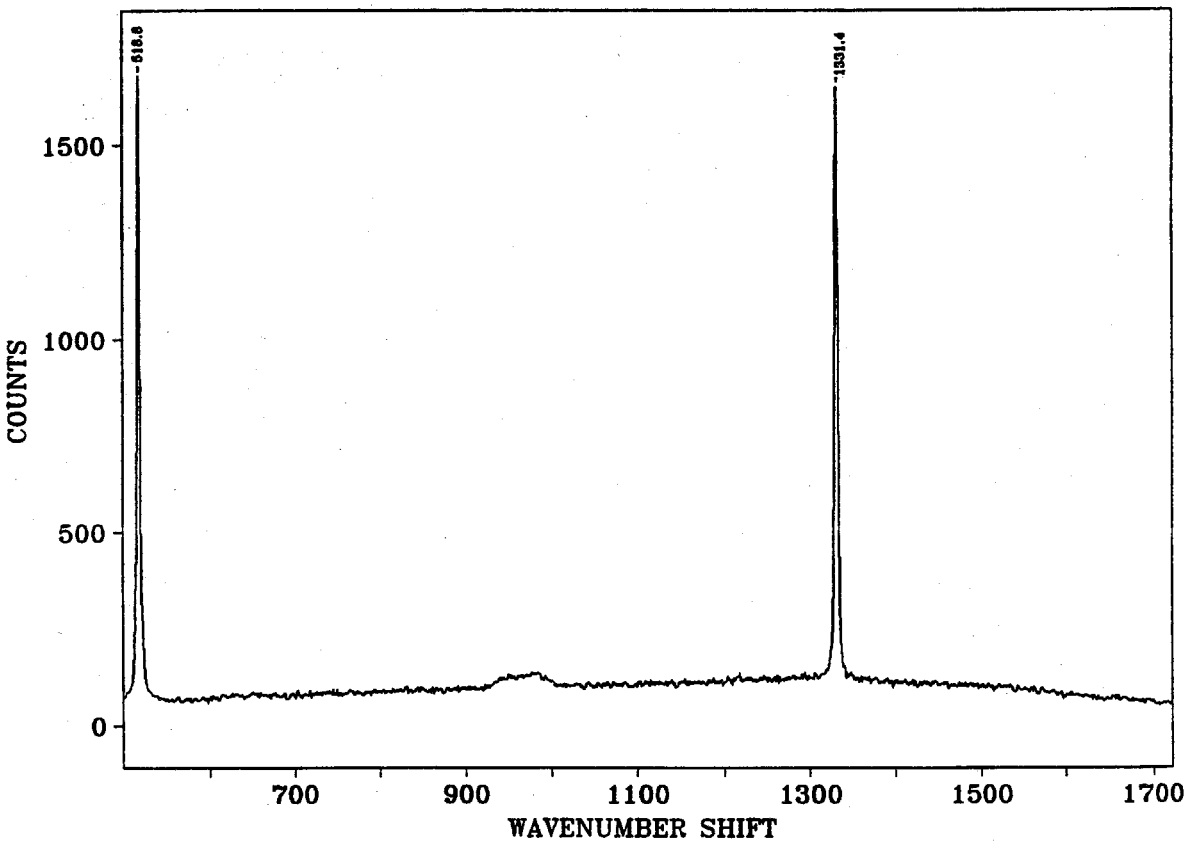

Figure 4-5: Micro-Raman spectrum taken from the diamond crystals shown in Figure 4-4.

shown in Figures 4-4, 4-6, and 4-7. In Figure 4-4, well-faceted diamond crystals were found at 180 Torr with the total flow rate of 1.9 slm/cm^2. The substrate temperature was 830 °C, and the burner to substrate distance was 3.75 mm. The nucleation density was typically higher along the scratched line, and the crystal growth rate was approximately 8 μm/hr.

Figure 4-5 shows a micro-Raman spectrum of the diamond crystals which are shown in Figure 4-4. The sharp peak at 1331.4 cm^{-1} Raman shift corresponds to

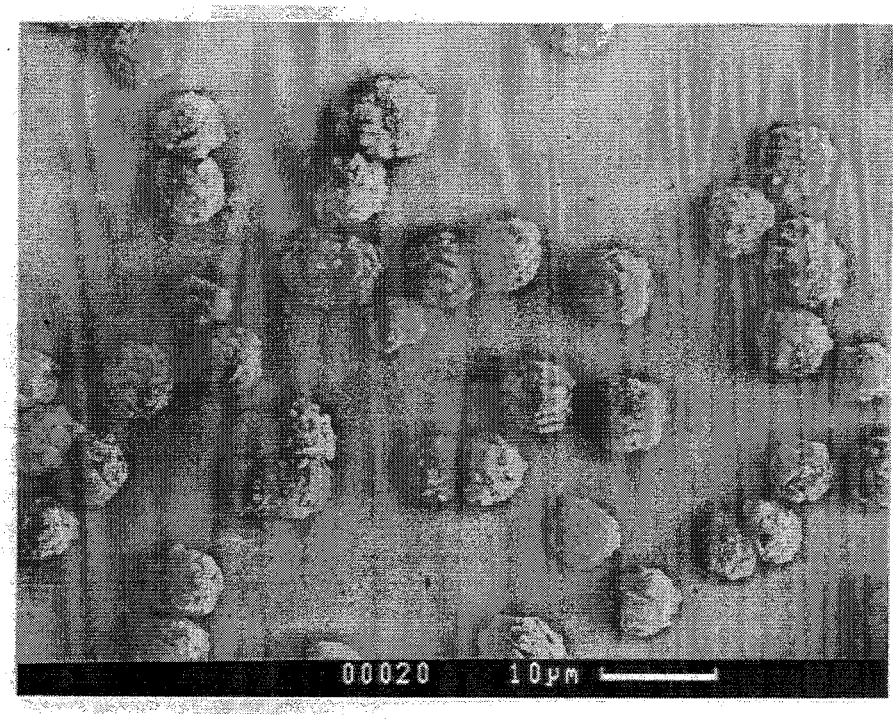

Figure 4-6: SEM micrograph of low quality diamond crystals grown on silicon in a 180 Torr MAPP/oxygen flame.

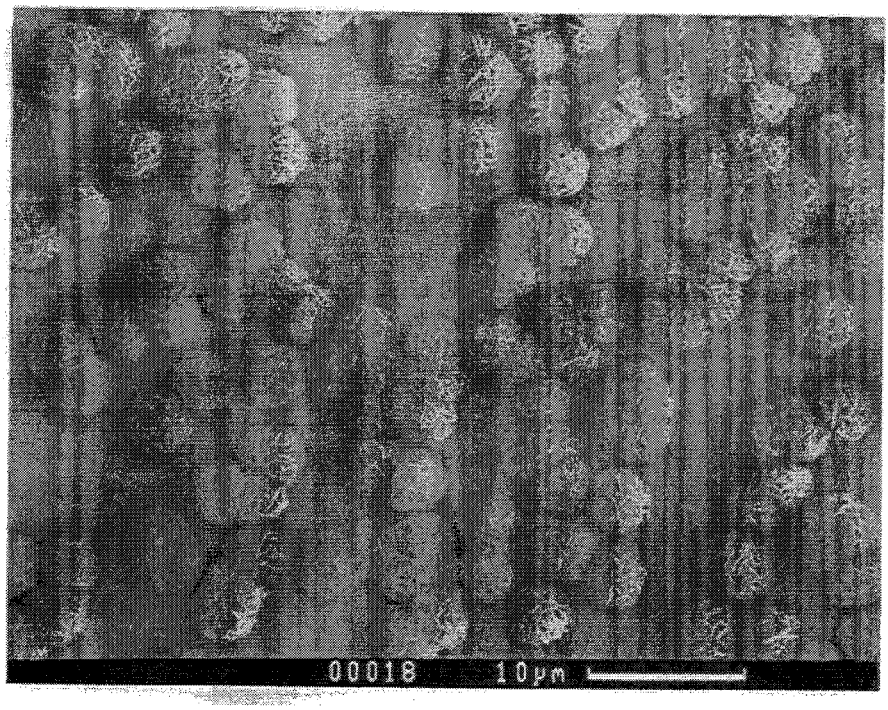

Figure 4-7: SEM micrograph of micro crystalline graphite grown on silicon in a 180 Torr MAPP/oxygen flame.

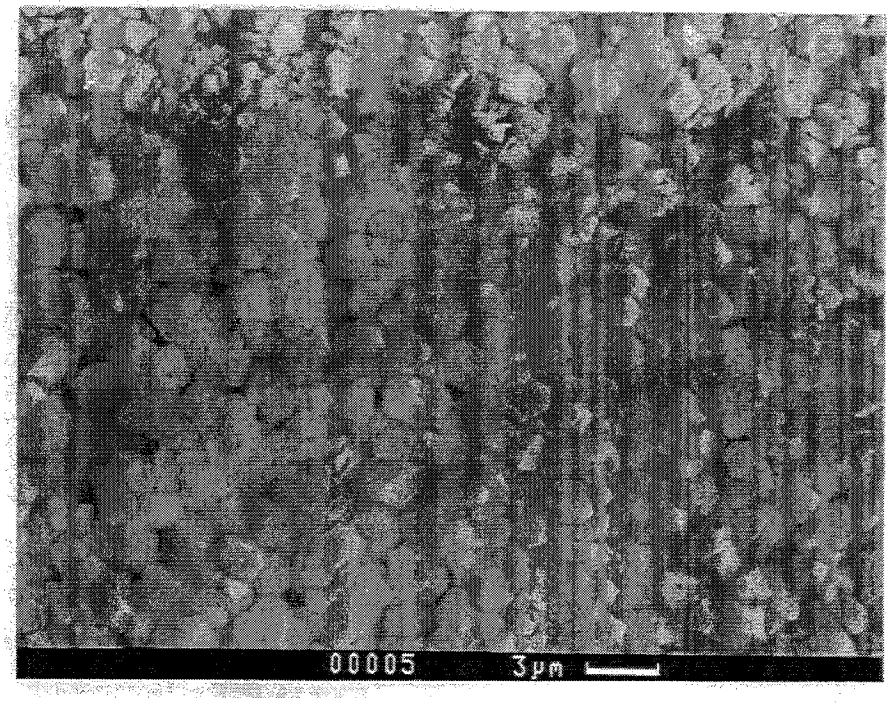

Figure 4-8: SEM micrograph of semi-continuous diamond film grown with a nucleation enhancement step in a 180 Torr MAPP/oxygen flame.

diamond, and the second peak at 518.8 cm^{-1} comes from the silicon substrate.

The burner used here was designed for lower pressure work (typically 30–60 Torr), where the substrate can be placed farther from the burner. In this experiment, the films were nonuniform, since the burner hole spacing (2 mm) was comparable to the burner to substrate distance (3.75 mm). This resulted in nonuniform carbon deposits. A portion of the substrate was found to contain high quality diamond crystals such as shown in Figure 4-4. The remainder of the substrate had either low quality diamond crystals or micro crystalline graphite deposits as shown in Figures 4-6 and 4-7.

In general, for the same pretreatment, a richer flame results in higher nucleation density than a leaner flame. To enhance the nucleation density, employing richer

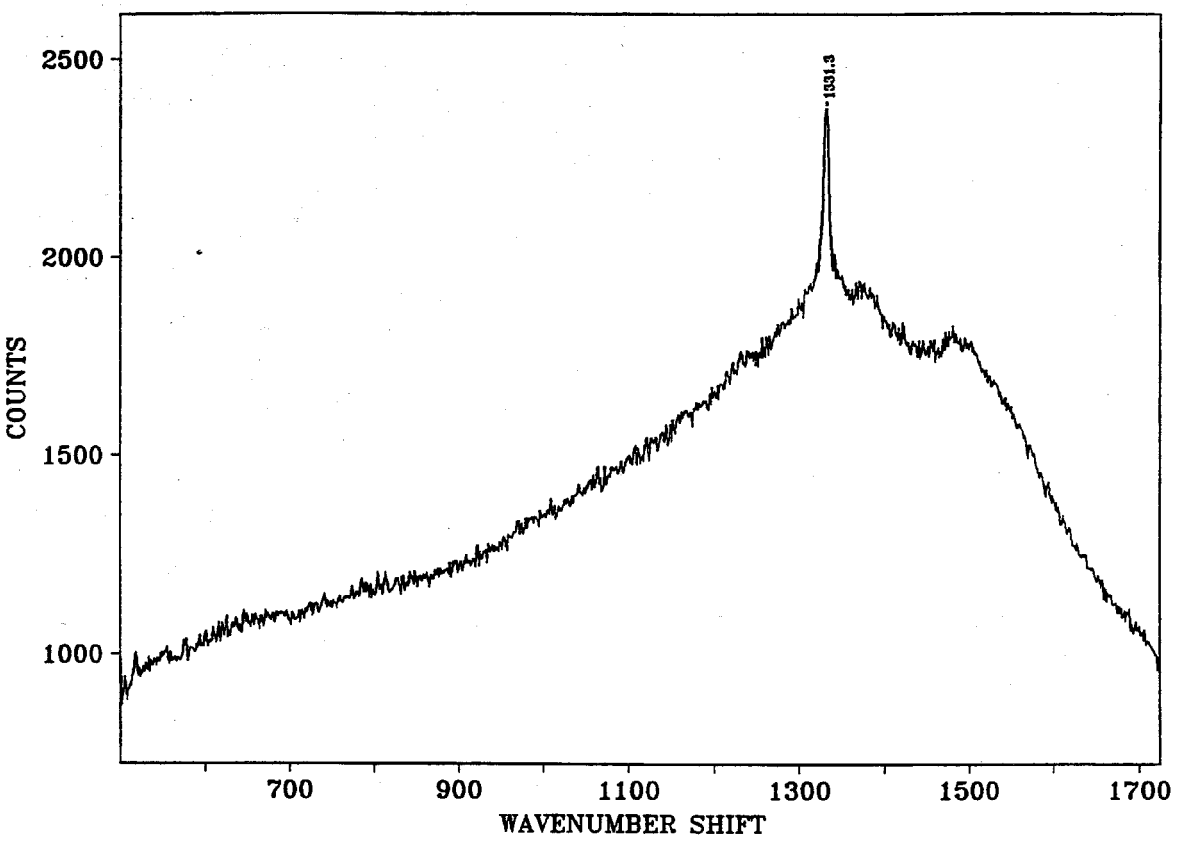

Figure 4-9: Micro-Raman spectrum of semi-continuous diamond film shown in Figure 4-8.

flame conditions for a short period during the early stage of the experiment and then switching to the desired flame condition was attempted. Figure 4-8 shows typical diamond growth results with a nucleation enhancement step. The flame was maintained at C:O = 0.75 for first 10 minutes, and then switched to the diamond growth condition (C:O = 0.69) of case 4. The diamond nucleation density was enhanced considerably, but the quality was poorer than diamond grown without the nucleation enhancement step. Semi-continuous film was found after 1 hour run. The micro-

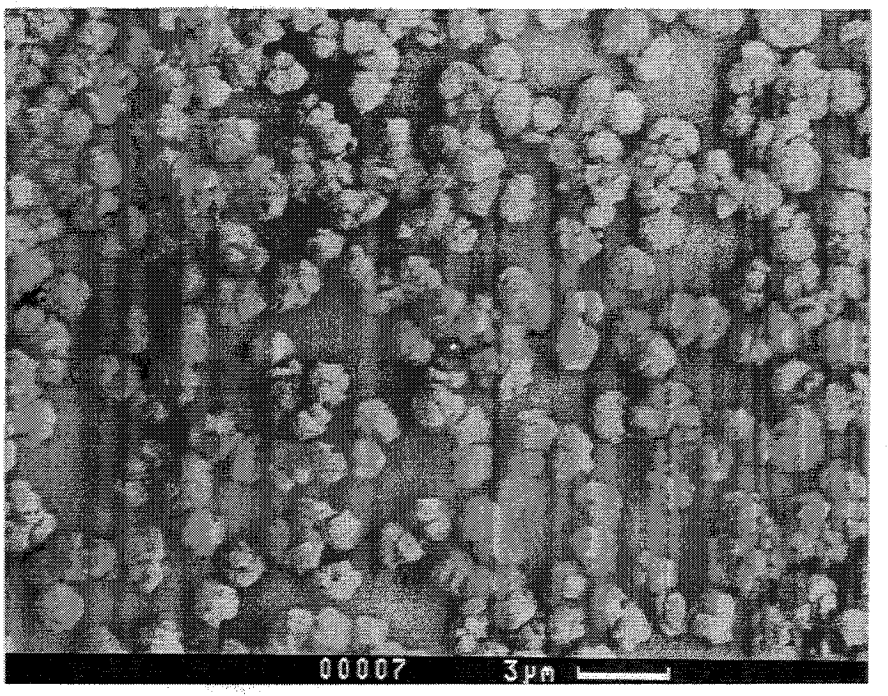

Figure 4-10: SEM micrograph of etched diamond crystals grown with nucleation enhancement step in a 180 Torr MAPP/oxygen flame.

Raman spectrum of this sample at the center of a diamond cluster is shown in Figure 4-9. A sharp diamond peak was found at 1331.3 cm^{-1} with a broad peak near 1500 cm^{-1} from non-diamond carbon. In Figure 4-10, a run with slightly leaner growth condition (C:O = 0.66) after the same nucleation step is shown. This run resulted in high quality etched diamond crystals with good nucleation density.

Some experiments were performed with molybdenum foil (0.25 mm thick) substrates. For similar experimental conditions, the molybdenum foil substrate was typically hotter (> 900 °C) than the silicon wafer or molybdenum disk. Figures 4-11 and 4-12 show carbon particles deposited at 180 Torr with the total flow rate of 1.9 slm/cm^2. The substrate temperature was nonuniform (940–1000 °C), and the burner

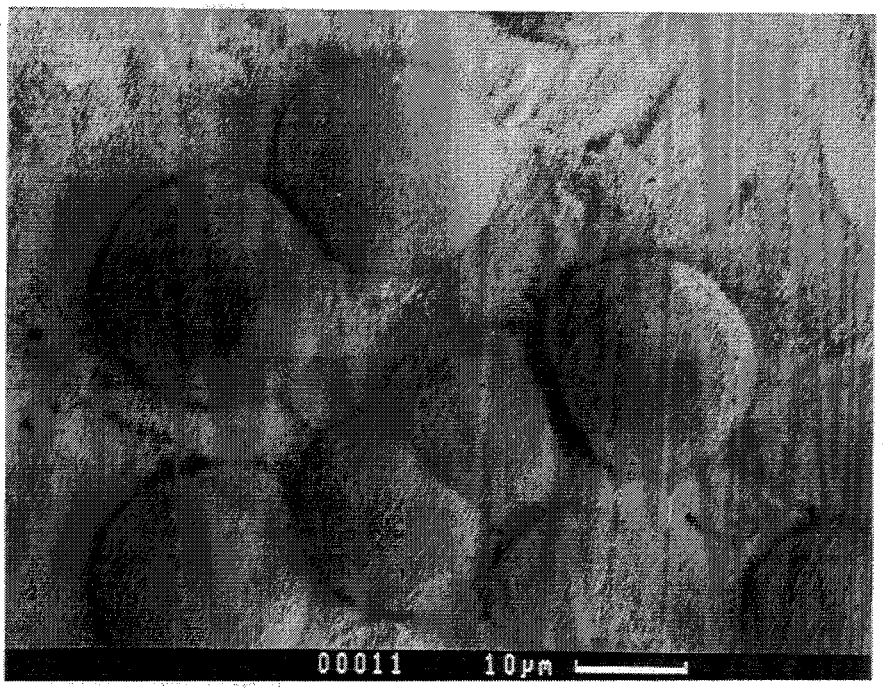

Figure 4-11: SEM micrograph of non-diamond carbon particles grown on molybdenum foil in a 180 Torr MAPP/oxygen flame.

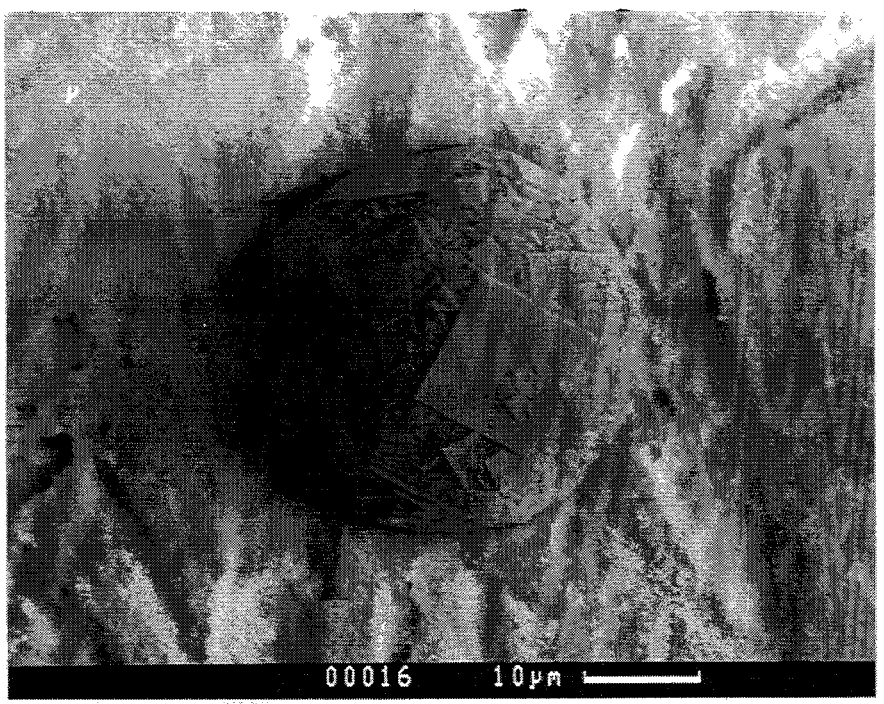

Figure 4-12: SEM micrograph of a carbon particle with some diamond facets grown on molybdenum foil in a 180 Torr MAPP/oxygen flame.

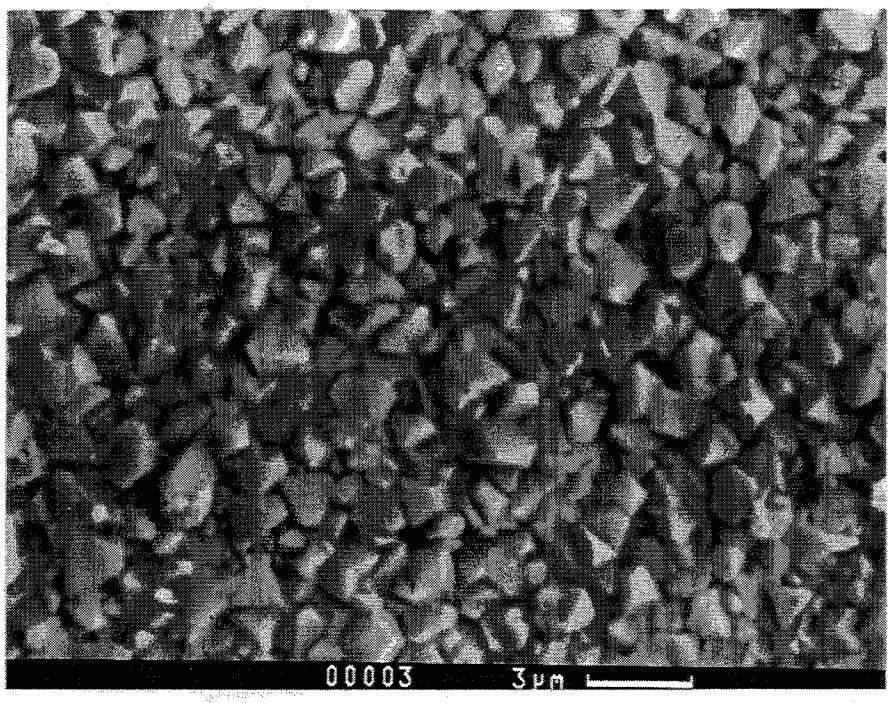

Figure 4-13: SEM micrograph of continuous diamond film grown on molybdenum in a 180 Torr MAPP/oxygen flame.

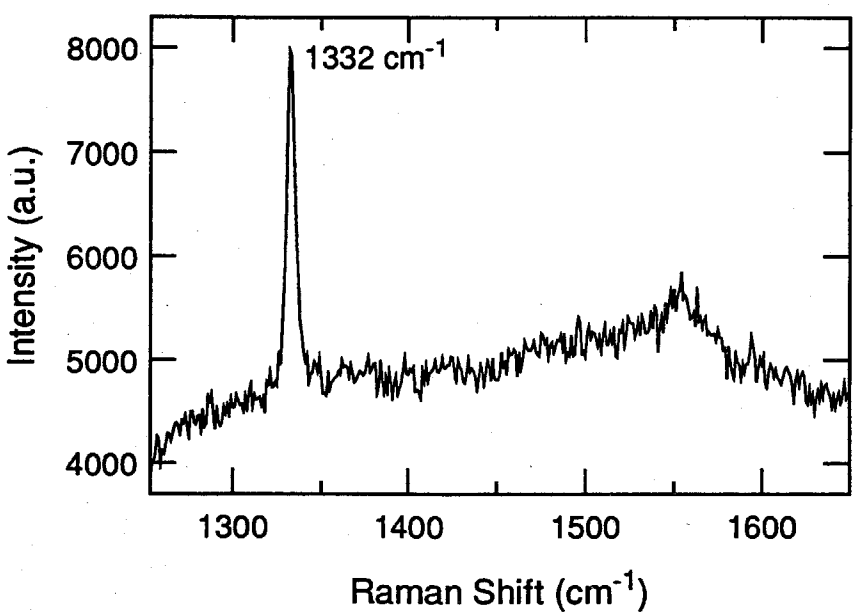

Figure 4-14: Raman spectrum of the continuous diamond film shown in Figure 4-13.

to substrate distance was 4.25 mm. Some deposited particles were much bigger than other particles as shown in Figure 4-12. This carbon particle was 33 μm in diameter after 1 hour. Typical (100) diamond faces were well developed along the ball-shape carbon surface.

By employing silicon as the substrate, no continuous diamond film was observed. This was mainly due to the lower nucleation density on silicon. On the molybdenum disk, by applying the series of pretreatment steps described in Chapter 2, nucleation was enhanced, and continuous diamond films were obtained.

An SEM micrograph of a diamond film grown on a molybdenum disk under the conditions of case 4 is shown in Figure 4-13. This film was grown for 2.5 hours at 180 Torr. The substrate temperature was 830 °C, and the burner to substrate distance was 3.75 mm. The MAPP flow rate was 0.6 slm/cm^2 and the oxygen flow rate was 1.3 slm/cm^2. The film growth rate was approximately 1 μm/hr. The macro-Raman spectrum for a film grown under these conditions is shown in Figure 4-14. There is a sharp diamond peak at 1332 cm^{-1} and the broad peak near 1550 cm^{-1} corresponds to non-diamond carbon.

As pointed out earlier, the diamond films were nonuniform, and only a small portion of the substrate was found to contain diamond such as shown in Figure 4-13. The remainder of the substrate had either no deposit or non-diamond carbon. However, an optimized burner design could greatly improve the film uniformity and area coverage at this pressure.

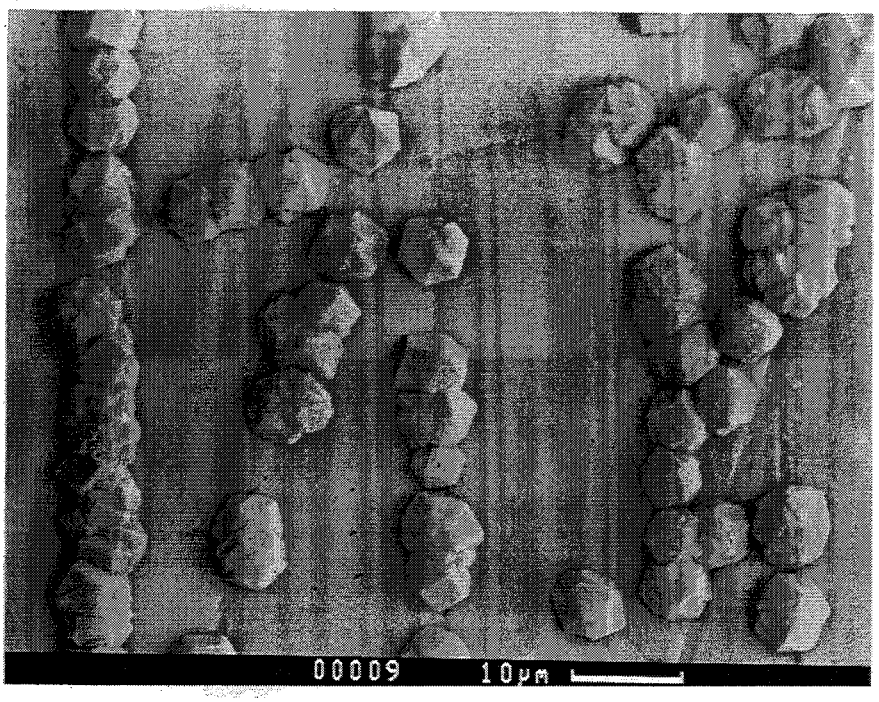

Figure 4-15: SEM micrograph of isolated diamond crystals grown on silicon in a 180 Torr propylene/oxygen flame.

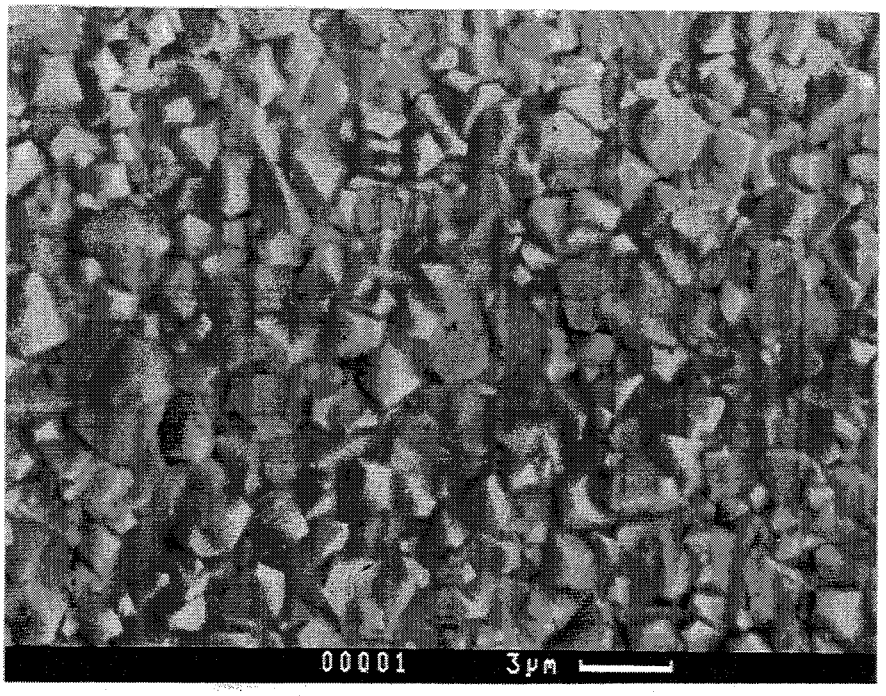

Figure 4-16: SEM micrograph of the diamond film grown on molybdenum in a 180 Torr propylene/oxygen flame.

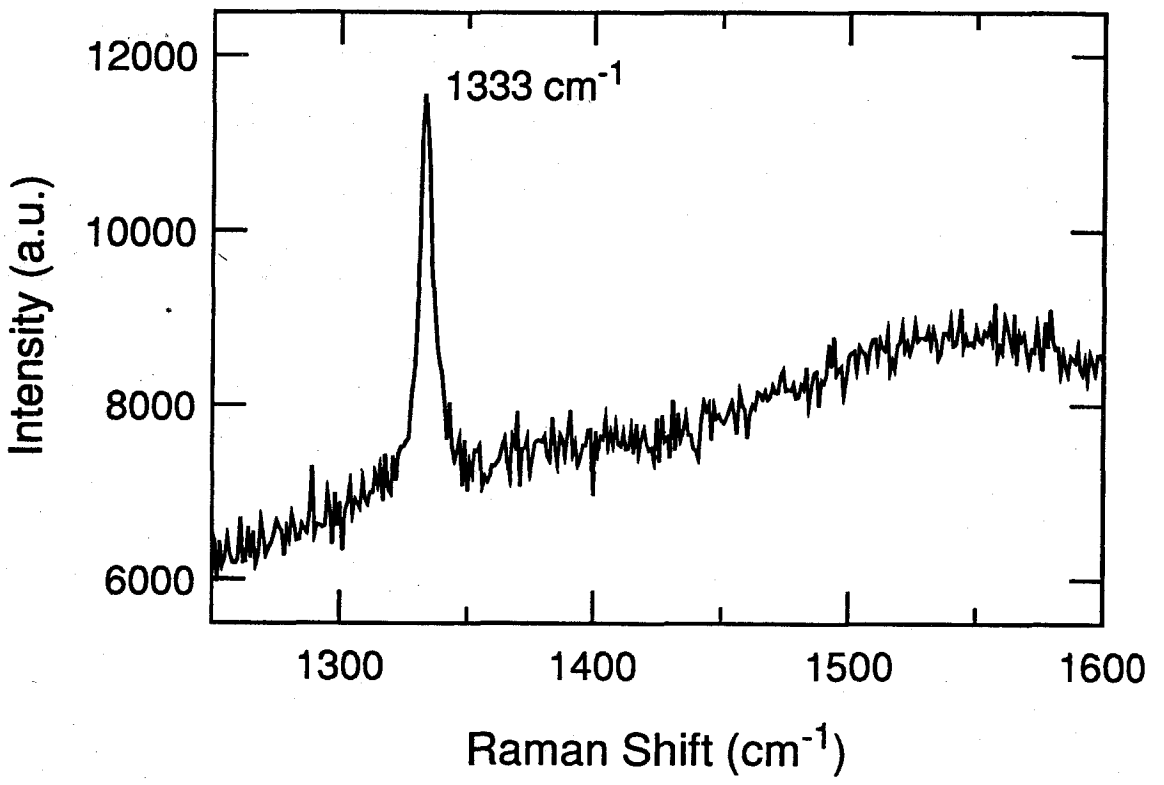

Figure 4-17: Raman spectrum of the film shown in Figure 4-16.

4.3.2 Propylene/Oxygen Flames

The pressure used for propylene/oxygen flames was 180 Torr, which is also the pressure at which the best diamond was grown in MAPP/oxygen flames. A 2 cm diameter burner was used in these experiments.

SEM micrographs of typical diamond grown in propylene/oxygen flames are shown in Figure 4-15 and 4-16. The substrate was either a silicon wafer or a molybdenum disk, and the both experimental conditions were the same. The total flow rate (fuel and oxygen) was 1.88 standard liters per minute (slm) per cm^2 of burner area. The fuel/oxygen ratio was 0.47 (C:O = 0.70). The substrate temperature was 800 °C, and

the burner to substrate distance was 4.25 mm.

Well-faceted diamond crystals were grown on silicon as shown in Figure 4-15. The typical crystal size was 13 μm after 1 hour. As illustrated in Figure 4-16, diamond film was grown on molybdenum. The film thickness was 2.7 μm after 3 hours, from which the diamond film growth rate was estimated to be 0.9 μm/hr. A Raman spectrum of this film is shown in Figure 4-17. This Raman spectrum is similar to that of MAPP/oxygen flames, and is comparable to that found in acetylene/oxygen flames. As with the MAPP/oxygen flame experiments, the diamond films were nonuniform, and only a small portion of the substrate was found to contain diamond such as shown in Figure 4-16.

4.3.3 Ethylene/Oxygen Flames

A diamond film was grown on molybdenum at a pressure of 50 Torr, with a total flow rate of 0.71 slm/cm^2. The burner to substrate distance was 10 mm, and the substrate temperature was 800 °C. Figure 4-18 shows a continuous diamond film grown after 5 hours. Diamond faceting was somewhat poor, and no Raman analysis was performed for this sample. The diamond coating covered an area roughly equal to the area of burner face (12.6 cm^2). The diamond growth rate was approximately 0.6 μm/hr.

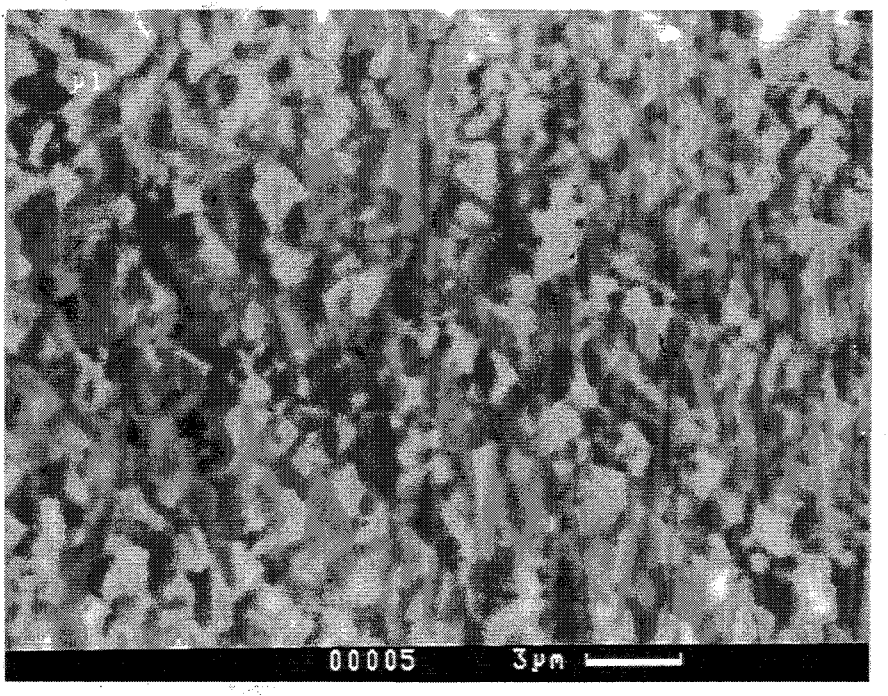

Figure 4-18: SEM micrograph of the diamond film grown in a 50 Torr ethylene/oxygen flame.

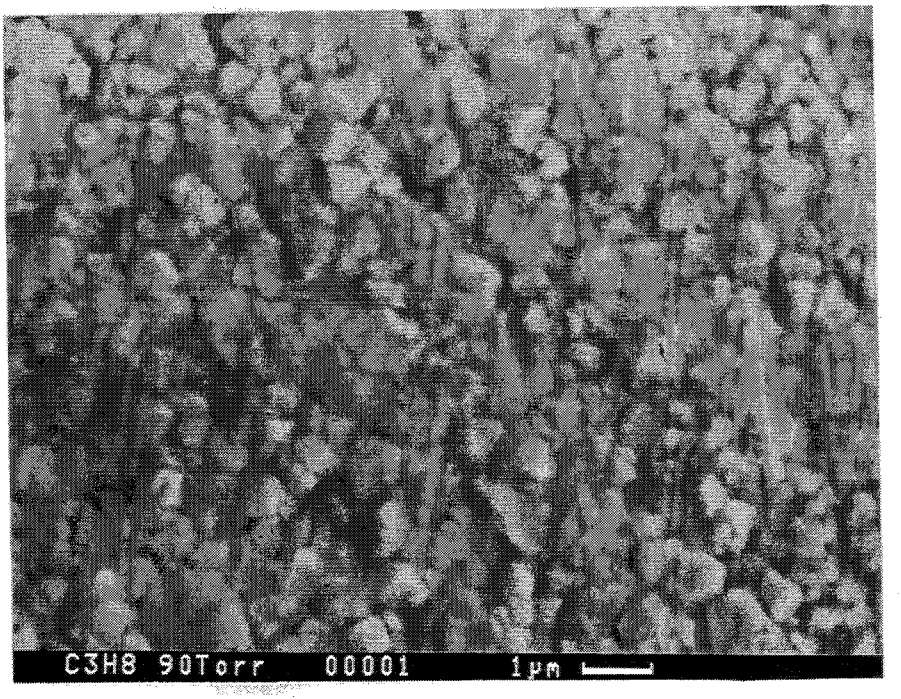

Figure 4-19: SEM micrograph of the diamond film grown in a 90 Torr propane/oxygen flame.

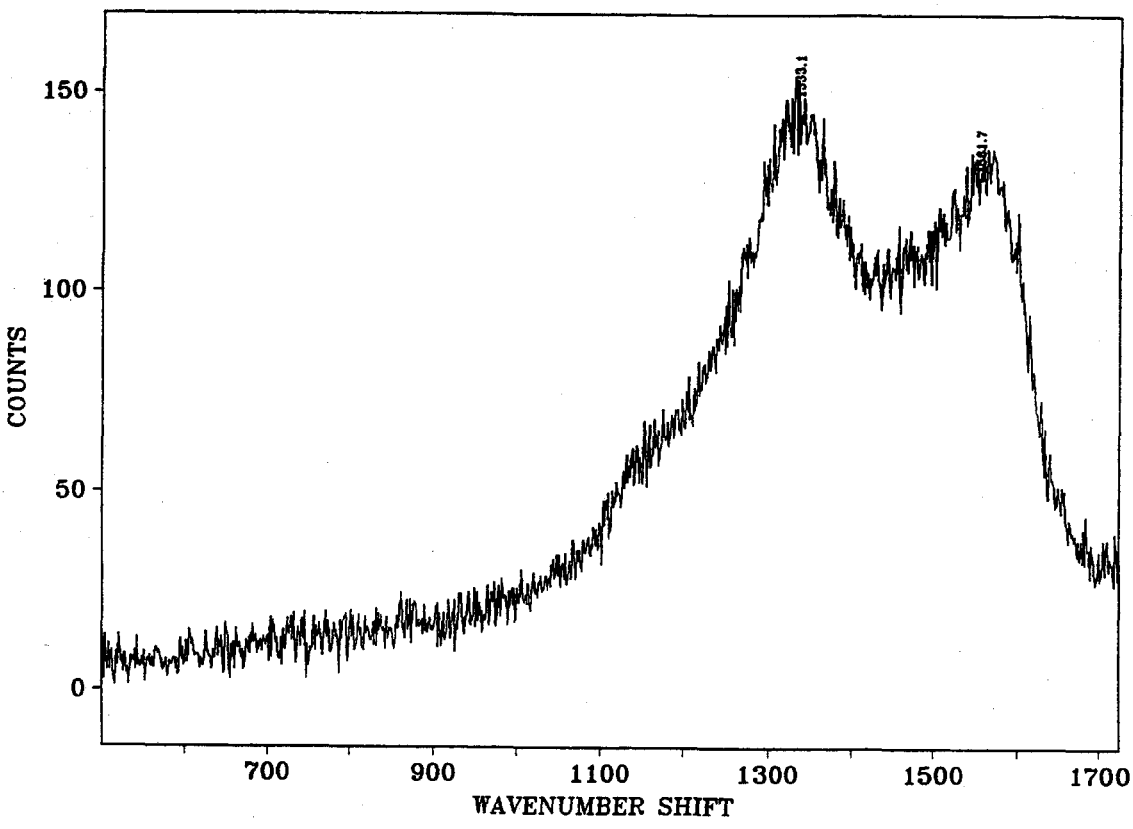

Figure 4-20: Micro-Raman spectrum of the film shown in Figure 4-19.

4.3.4 Propane/Oxygen Flames

With propane/oxygen flames, experiments were performed with a 4 cm diameter burner at 90 Torr. A typical diamond film grown with propane is shown in Figure 4-19. This film was grown for 5 hours, with a total flow rate (propane and oxygen) of 0.52 slm/cm^2 of burner area. The equivalence ratio ϕ was 2.1 (C:O = 0.63). The substrate temperature was 700 °C, and the burner to substrate distance was 10.5 mm. The diamond film growth rate was estimated to be 0.15 μm/hr.

Although the quality is poor, a uniform, continuous diamond film was grown over

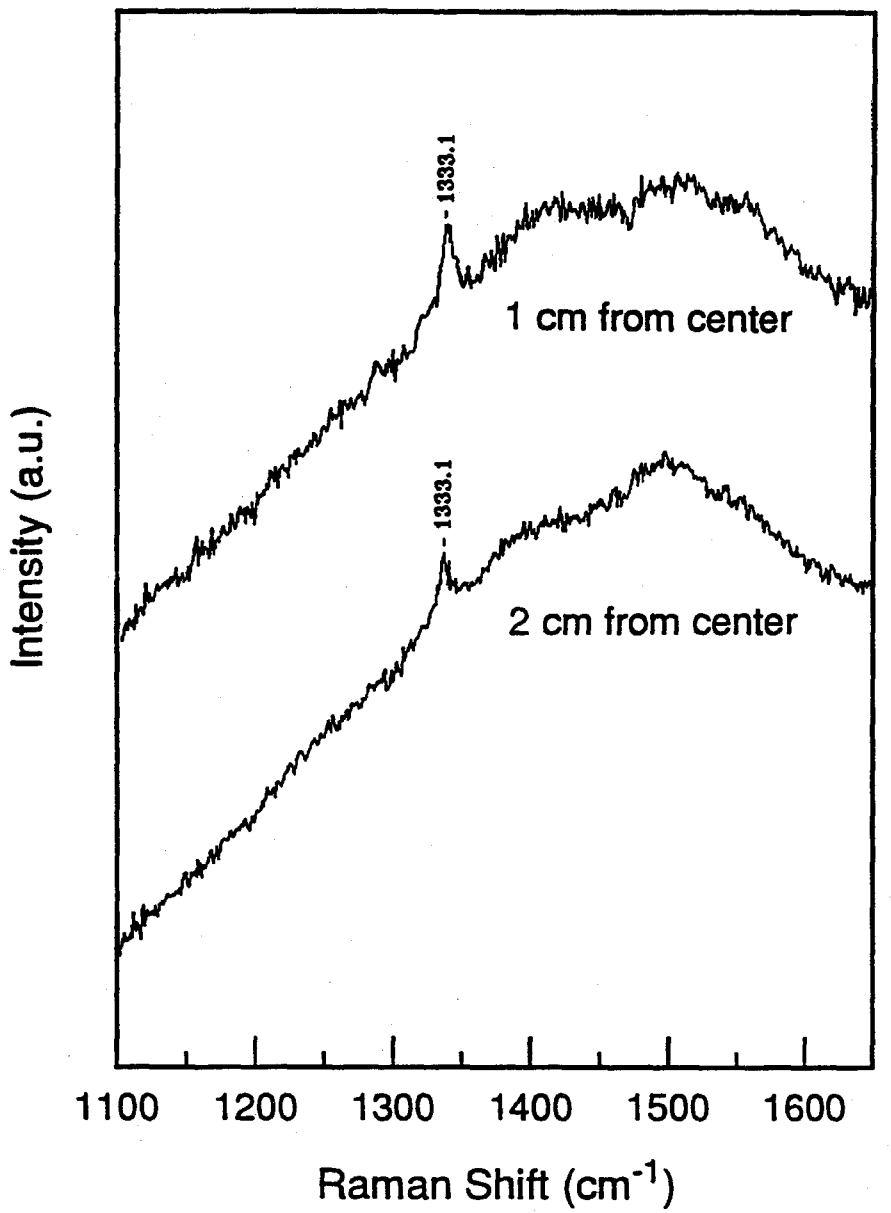

Figure 4-21: Micro-Raman spectra at two locations shown in Figure 4-19.

Fuel	P (Torr)	Q_T (slm/cm^2)	ϕ	C:O	T_S (°C)	D_S (mm)	Growth Rate (μm/hr)	C_{eff} ($\times 10^{-6}$)
C_2H_2	30	1.0	2.11	0.84	800	10	1.5	17.6
MAPP	180	1.9	–	0.69	830	3.75	1.0	6.1
C_3H_6	180	1.88	2.12	0.70	800	4.25	0.9	5.5
C_2H_4	50	0.71	2.15	0.72	800	10	0.6	(11)
C_3H_8	90	0.52	2.1	0.63	700	10.5	0.15	(3.5)

Table 4.3: Experimental conditions, measured growth rates, and carbon-conversion efficiencies.

an area of 15 cm^2 which is larger than the area of burner face (12.6 cm^2).

Micro-Raman spectra of this film are shown in Figures 4-20 and 4-21. Figure 4-20 was taken from the center of the deposit, and shows a weak diamond peak at 1333.1 cm^{-1} and a broad peak near 1540 cm^{-1}. Figure 4-21 shows micro-Raman spectra at two different radial locations on the film: 1 cm from the center, and 2 cm from the center. There is small variation in film quality as we move out from the center of the deposit, and a small but recognizable diamond Raman peak at 1333.1 cm^{-1} was observed throughout the deposition area.

4.4 Discussion

Experimental conditions and results of five different hydrocarbon fuels which have been used to deposit diamond are summarized in Table 4.3. The acetylene values come from growth at low pressure (30 Torr) in the same facility as described in

Chapter 2. The efficiency in converting fuel carbon atoms into diamond is given by the ratio of the diamond mass deposition rate ($g/cm^2/s$) to the carbon mass flow rate ($g/cm^2/s$).

At chemical equilibrium, diamond deposition flames must be run close to a 1:1 C:O ratio to achieve the gas composition needed for diamond growth (a reducing flame with high H and moderately low residual hydrocarbon concentrations). The observed C:O ratio for diamond growth (0.63–0.84) would produce an oxidizing flame at equilibrium, which would be unable to deposit diamond. The need for a lower C:O ratio than that needed at equilibrium indicates that nonequilibrium flame chemistry is important at these pressures. This is consistent with other low pressure flame growth experiments [30, 42, 28] and with simulation results [30, 37, 57]. This nonequilibrium flame chemistry allow fuels such as propylene and propane to deposit diamond, even though they are poor candidates for diamond growth because their heats of formation, adiabatic flame temperatures, and equilibrium H mole fractions are all significantly less than in acetylene/oxygen flames. This suggests that other fuels also may be worth considering for diamond growth at low pressures.

High quality diamond films were found to be grown at low pressures with acetylene/oxygen, MAPP/oxygen, and propylene/oxygen flames. On the other hand, low pressure ethylene/oxygen and propane/oxygen flames in the same facility resulted in low quality diamond film with less faceting. However it should be noted that ethylene/oxygen flames can grow high quality diamond [42]. Even though propane only

grew a low quality diamond film, propane could be used as the fuel for combustion synthesis of diamond coatings for some applications where the diamond quality is not important, such as hard coatings on cutting tools.

The ability to grow diamond in these alternative hydrocarbon fuels may significantly improve the viability of the combustion synthesis method, and may finally make it competitive with plasma methods. For example, propylene is produced industrially in great quantities, it is inexpensive and readily available. Also propylene is safer than acetylene, ethylene, or MAPP gas. Its flammability limits in air are 2%–11.1%, compared to 2.7%–36% for ethylene, and 2.5%–100% for acetylene. It may also be easily stored as a liquid, unlike acetylene or ethylene.

A tentative economic comparison of these fuels for diamond growth is possible by considering their costs and carbon-conversion efficiencies (C_{eff}). As expected, acetylene has the highest value of $C_{eff} = 17.6\times10^{-6}$ at the substrate temperature of 800 °C. This value is about three times higher than the value for MAPP or propylene at similar substrate temperatures (800–830 °C). Ethylene has a value of $C_{eff} = 11\times10^{-6}$ at $T_S = 800$ °C which is about 60% of the value of acetylene at the same temperature. But this was a film of low quality diamond with less faceting. However, Kim and Cappelli [42] have reported high quality diamond film in ethylene/oxygen flames is grown with the carbon-conversion efficiency of approximately one-half of that observed for acetylene/oxygen flames.

The cost of propylene in large quantities is approximately \$0.18/lb, which is less

than that of ethylene ($0.22–0.24/lb) [65] or MAPP ($0.37/lb). In contrast, acetylene costs $1.45–$2.00/lb, depending on purity. Therefore, since the carbon-conversion efficiency for propylene is roughly one-third of that for acetylene, while its cost is an order of magnitude lower, switching from acetylene to propylene may be able to lower the fuel cost per unit mass of diamond by roughly a factor of three. This may well make the combustion method competitive with arcjet, microwave, and hot filament methods for many applications.

4.5 Summary

Diamond film growth experiments were performed at low pressures (50–180 Torr) using MAPP/oxygen, propylene/oxygen, ethylene/oxygen, and propane/oxygen flames. Well-faceted diamond films were grown in these flames, and these results indicated that nonequilibrium flame chemistry is important in the low pressure combustion environment. The Raman spectrum analysis showed that good quality diamond films were grown in MAPP/oxygen and propylene/oxygen flames. The equivalence ratio for diamond growth (2.1–2.15) and observed trends of growth experiments in these alternative flames were same as those found in acetylene/oxygen flames.

MAPP and propylene are considerably cheaper, safer, and easier to handle than acetylene, and can produce high quality diamond films with roughly one-third the carbon-conversion efficiency of acetylene. Most notably, an economic comparison study shows that the use of propylene/oxygen flames could potentially reduce the

barriers to commercializing the combustion synthesis of diamond, since it is considerably cheaper than acetylene.

Since very little attempt has been made to find the optimal conditions for high quality diamond growth with ethylene/oxygen and propane/oxygen flames, further studies employing these fuels could potentially further reduce the cost of diamond produced by combustion synthesis.

Chapter 5

Modeling and Diagnostics of Alternative Fuel Flames

5.1 Overview

In Chapter 3, mass spectrometry results in acetylene/oxygen flames verify that the low pressure flame simulations using STBL code predict the mole fractions of some major stable species (CO, CO_2, and H_2) at the substrate within the experimental uncertainty and correctly reproduce the qualitative trends seen experimentally. In addition, the model predicts general trends which are observed in experiments and could be effectively used to seek improved flame conditions for diamond growth.

In this chapter, numerical modeling studies have been performed to analyze the experimental results of diamond growth in low pressure alternative fuel flames which are described in Chapter 4. The Dagaut–Cathonnet–Boettner mechanism [66] has been employed as the gas phase mechanism. Mass spectrometry experiments have been carried out to determine if the numerical modeling employing this gas phase mechanism correctly predicts the chemical environment in various hydrocarbon fuel (propylene, ethylene, and propane) flames. The details of the modeling and experimental setup for mass spectrometry described in Chapter 3 have been also used for modeling and diagnostics studies of alternative fuel flames in this chapter.

5.2 Gas Phase and Surface Chemistry

The combustion mechanism employed for gas phase reactions of alternative fuel flames (MAPP, propylene, ethylene, and propane) is that of Dagaut, Cathonnet, and Boet-

Case	Fuel	P (Torr)	Q_T (slm/cm^2)	$\dot{m}$ (g/cm^2/s)	ϕ	C:O	T_S (K)	L (cm)
1	C_2H_2	30	1.0	0.022	2.11	0.84	1073	1.0
2	MAPP	180	1.9	0.04	–	0.69	1103	0.375
3	C_3H_6	180	1.88	0.041	2.12	0.70	1073	0.425
4	C_2H_4	50	0.71	0.016	2.15	0.72	1073	1.0
5	C_3H_8	90	0.52	0.0137	2.1	0.63	973	1.05

Table 5.1: Experimental conditions for diamond growth in various hydrocarbon fuels.

tner [66]. The Dagaut–Cathonnet–Boettner mechanism was designed for modeling the oxidation of various hydrocarbon fuels, and has been used to model the kinetics of the combustion of methane (CH_4), ethane (C_2H_6), ethylene (C_2H_4), propylene (C_3H_6), and propane (C_3H_8) flames over a wide range of conditions (T = 800–1300 K, P = 1–10 atm, ϕ = 0.1–4.0) in good agreement with experimental data [66, 67]. This mechanism has never been used to model the combustion kinetics at low pressures ($P < 1$ atm). It consists of 391 reactions among 57 species, and is presented in detail in Appendix A.2.

To describe the diamond growth chemistry at the substrate, reactions 1–16 of Appendix B are used. Since the gas phase mechanism of Dagaut–Cathonnet–Boettner does not include C and CH_2(S) in its species, reactions 17–21 of Appendix B are neglected.

5.3 Results

5.3.1 Modeling

Five different hydrocarbon fuels and the experimental conditions which resulted in good quality diamond deposition are summarized in Table 5.1. Here P is the pressure, Q_T is the volumetric flow rate of premixed gases (fuel and oxygen) per unit area of substrate, $\dot{m}$ is the mass flow rate of premixed gases per unit area of substrate, ϕ is the equivalence ratio, C:O is the carbon to oxygen ratio, T_S is the substrate temperature, and L is the burner to substrate distance. MAPP gas is a mixture of about half C_3H_4 and half LPG (mainly propylene and a small amount of propane); the exact composition is not available thus the equivalence ratio ϕ is not given for the MAPP case. However, these hydrocarbon fuels contain three carbon atoms in one molecule, and an exact C:O ratio can be calculated.

The spatial variations of the major stable species and key radical species for the conditions of cases 2–5 are shown in Figures 5-1 – 5-4. For case 2 (MAPP/oxygen flame), MAPP is assumed to be a mixture of 35% methyl acetylene (also called propyne, PC_3H_4), 15% propadiene (also called allene, AC_3H_4), and 50% propylene, which is similar to the real composition.

For all cases, the profiles of each species in the various fuel flames show similar trends, even though their absolute mole fractions are predicted to be different. All species show rapid changes in their mole fractions near the burner tip. The feed fuels to the burner (C_2H_4, C_3H_4, C_3H_6, and C_3H_8) are consumed, thus their mole fractions decrease through the flames, and rebound near the substrate. Many of the major

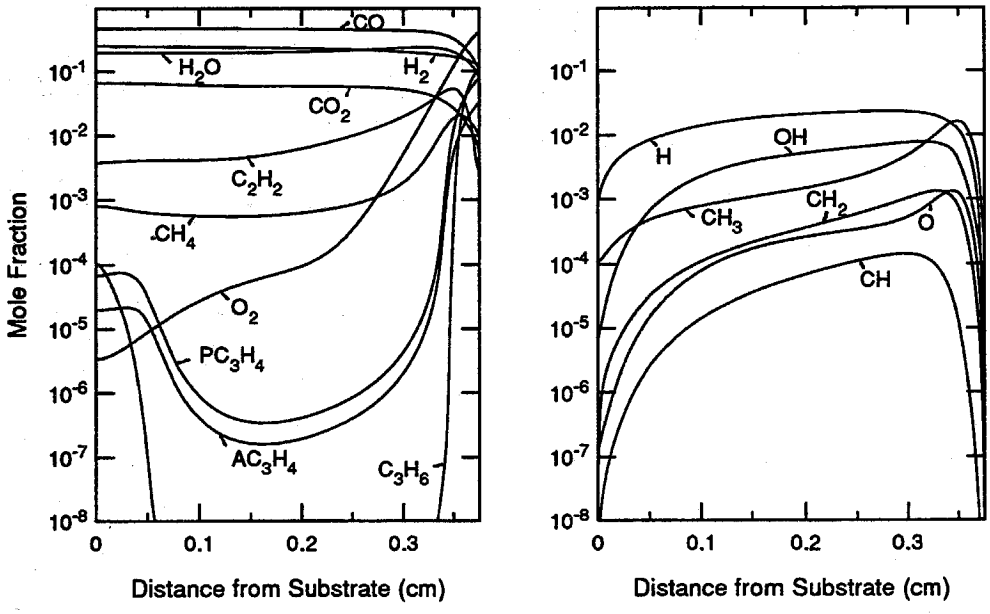

Figure 5-1: Major and key radical species profiles in a MAPP/oxygen flame for the conditions of case 2.

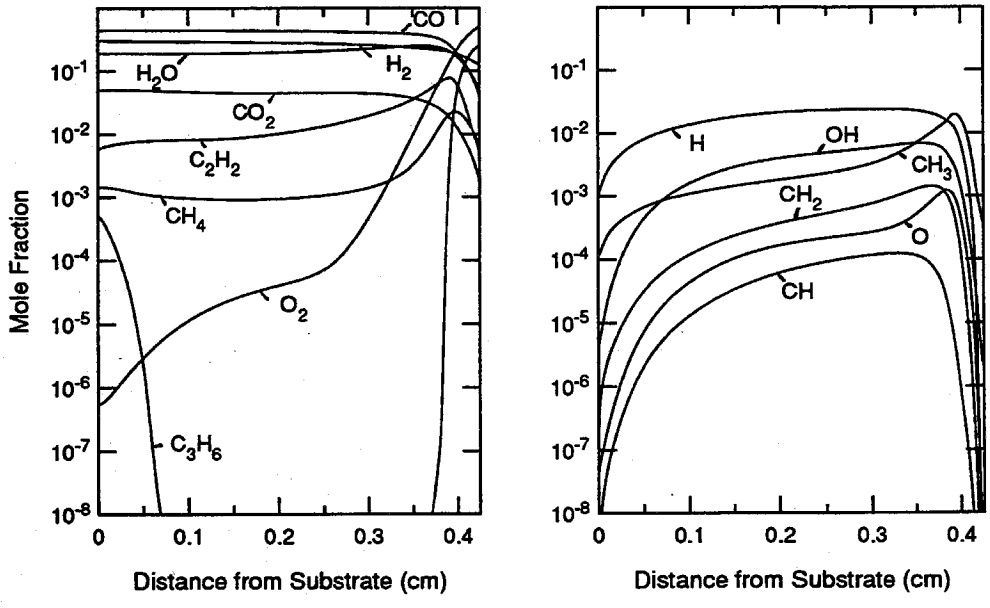

Figure 5-2: Major and key radical species profiles in a propylene/oxygen flame for the conditions of case 3.

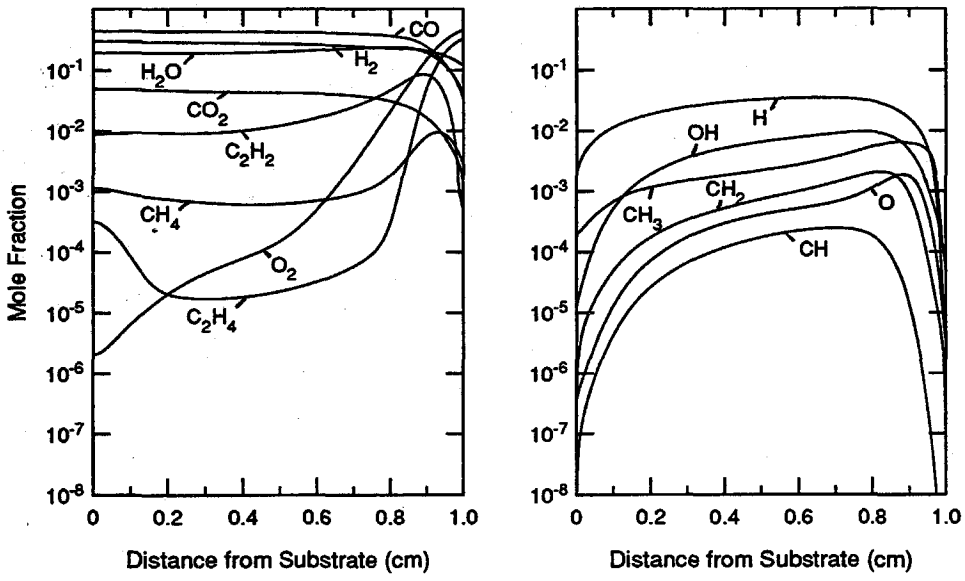

Figure 5-3: Major and key radical species profiles in an ethylene/oxygen flame for the conditions of case 4.

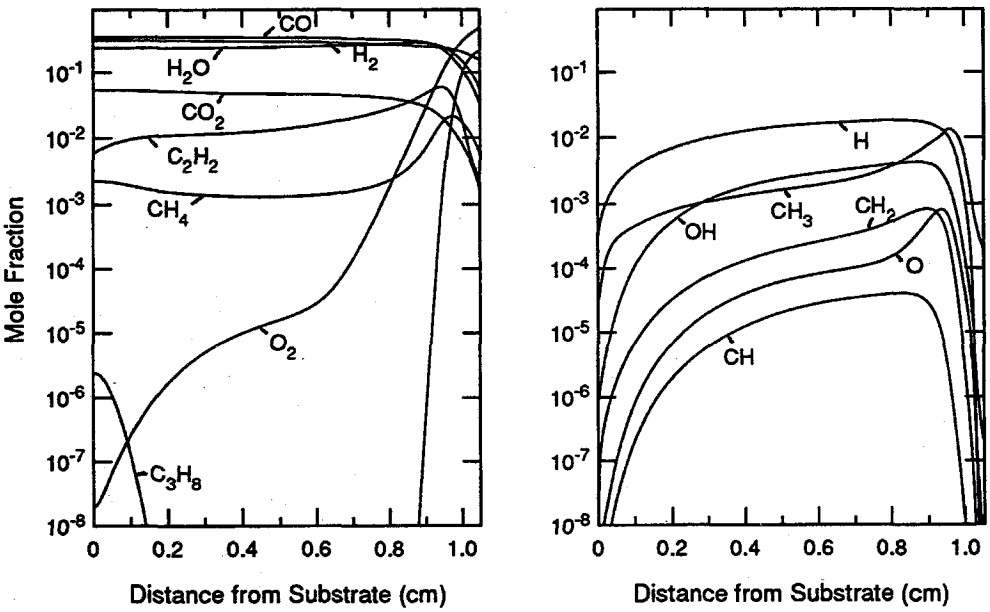

Figure 5-4: Major and key radical species profiles in a propane/oxygen flame for the conditions of case 5.

stable species typically have flat profiles at the substrate. On the other hand, radical species rapidly change their mole fractions near the substrate. For all cases, atomic H is the most abundant radical species at the substrate, and CH_3 is the highest mole fraction hydrocarbon radical at the substrate.

In Table 5.2, predicted mole fractions of some of the major stable species and radical species at the substrate are listed. Equilibrium compositions are the values at the given ϕ, P, and T_S for each case. For all cases, CO is predicted to approach its equilibrium value. All major species except CO_2 and H_2 have higher mole fractions than they would at equilibrium. Low pressure simulations show that the mole fractions for species at the substrate are far from their equilibrium values.

In low pressure simulations, the radical species typically have several orders of magnitude higher values than those for equilibrium. The mole fraction for H is predicted to be the most abundant radical at the substrate and CH_3 is predicted to be the most abundant hydrocarbon radical at the substrate.

The predicted flame temperature, the ratio of H to CH_3 mole fractions at the substrate, and the growth rates from experiment and prediction are listed in Table 5.3. T_{flame} is the peak temperature in the flame, while T_{equil} is the adiabatic flame temperature at the equilibrium state. G_{max} is the predicted growth rate which is calculated from equation 3.7. The low pressure simulation for case 1 (acetylene/oxygen flame) is performed using the Miller–Melius mechanism, while the Dagaut–Cathonnet–Boettner mechanism is used for cases 2–5 in low pressure simulations.

	Case 2 (MAPP)		Case 3 (C_3H_6)		Case 4 (C_2H_4)		Case 5 (C_3H_8)	
Species	STBL	Equil.	STBL	Equil.	STBL	Equil.	STBL	Equil.
Major Stable Species								
[CO]	0.48	0.41	0.44	0.39	0.44	0.40	0.36	0.30
[H_2]	0.25	0.34	0.30	0.40	0.30	0.40	0.32	0.45
[H_2O]	0.20	0.11	0.19	0.10	0.19	0.09	0.25	0.12
[CO_2]	0.07	0.13	0.05	0.11	0.05	0.10	0.05	0.13
[O_2]	3.2e-6	3.2e-18	5.5e-7	1.1e-19	2.0e-6	3.6e-19	2.0e-8	8.8e-22
[CH_4]	8.2e-4	2.0e-6	1.5e-3	8.7e-5	1.1e-3	7.5e-6	2.2e-3	2.6e-4
[C_2H_2]	3.7e-3	3.1e-13	5.8e-3	8.4e-12	8.7e-3	7.8e-13	6.1e-3	2.0e-12
[C_2H_4]	2.0e-4	3.8e-13	8.2e-4	7.6e-11	3.2e-4	2.0e-12	2.0e-3	8.8e-11
[C_3H_4A]	2.0e-5	3.6e-21	5.3e-5	3.1e-18	4.8e-5	2.5e-20	7.8e-5	1.1e-18
[C_3H_4P]	6.8e-5	1.4e-20	1.4e-4	1.2e-17	1.7e-4	9.5e-20	1.5e-3	4.5e-18
[C_3H_6]	1.0e-4	7.2e-21	5.0e-4	4.5e-17	2.0e-4	1.0e-19	9.7e-4	7.6e-17
[C_3H_8]	7.6e-8	3.7e-23	6.6e-7	1.5e-18	1.0e-7	9.3e-22	2.4e-5	6.2e-18
Key Radical Species								
[H]	9.3e-4	6.3e-8	8.2e-4	1.8e-8	2.1e-3	3.5e-8	3.1e-4	2.1e-9
[CH_3]	1.1e-4	7.9e-12	1.1e-4	8.4e-11	2.0e-4	1.4e-11	3.2e-5	2.5e-11
[OH]	6.8e-6	9.6e-11	3.6e-6	1.8e-11	1.4e-5	3.1e-11	8.1e-7	1.1e-12
[O]	1.2e-7	1.9e-17	4.3e-8	8.6e-19	3.7e-7	2.9e-18	3.6e-9	5.8e-21
[CH]	1.4e-9	9.1e-25	7.5e-10	5.7e-25	8.0e-9	3.3e-25	4.6e-11	5.5e-20
[CH_2]	5.5e-8	9.6e-19	4.5e-8	2.4e-18	2.1e-7	7.3e-19	7.1e-9	2.2e-22
[C_2H]	2.5e-10	1.4e-24	5.1e-11	6.6e-24	6.6e-10	1.2e-24	6.5e-12	4.3e-26

Table 5.2: Predicted mole fractions of some of the major stable species and radical species at the substrate.

	Case 1 (C_2H_2)	Case 2 (MAPP)	Case 3 (C_3H_6)	Case 4 (C_2H_4)	Case 5 (C_3H_8)
T_{flame} (K)	3818	2840	2799	2814	2516
T_{equil} (K)	2942	2778	2738	2671	2530
[H]	7.8e-3	9.3e-4	8.2e-4	2.1e-3	3.1e-4
[H]/[CH_3]	15.0	8.8	7.7	10.4	9.7
G_{exp} (μm/hr)	1.5	1.0	0.9	0.6	0.15
G_{max} (μm/hr)	17.1	16.3	15.8	6.3	0.72

Table 5.3: A comparison of various hydrocarbon fuels.

In MAPP/oxygen, propylene/oxygen, and ethylene/oxygen flames (cases 2–4), the peak flame temperature is predicted to be higher than the adiabatic flame temperature, but the discrepancy is much smaller than that of case 1, a 30 Torr acetylene/oxygen flame. For case 5 (propane/oxygen flame), the predicted peak temperature is slightly lower than the adiabatic flame temperature. For cases 2–5, the ratios of [H]/[CH_3] at the substrate in MAPP, propylene, ethylene, and propane fueled flames are predicted to be 8.8, 7.7, 10.4, and 9.7, respectively. The values in MAPP and propylene flames are lower than the acceptable ratio of 10 for moderate quality diamond growth. In these two cases, the deposited diamond films were nonuniform, since the burner hole spacing (2 mm) was comparable to the burner/substrate separation (3.75–4.25 mm). Only a small portion of the substrate was found to contain diamond, and the remainder of the substrate had either no deposit or non-diamond carbon. It is believed that since the flame was nonuniform the equivalence ratio ϕ varied locally from too low (lean flame) to too high (rich flame) values for diamond

growth. This also resulted in variations of [H]/[CH_3] ratio at the substrate surface, and only the portions of the substrate with the adequate ϕ and [H]/[CH_3] ratio had diamond deposits. For cases 4 and 5, the predicted [H]/[CH_3] ratios are about 10 which is the marginal ratio for moderate quality diamond growth. In experiments, poor quality diamonds were grown under the condition of cases 4 and 5, and the model predicted the experimental results relatively well.

In alternative fuel flames (cases 2–5), the H concentrations near the substrate are predicted to be slightly lower than that of the acetylene/oxygen flame, but high enough to grow diamond at a reasonable growth rate. The predicted growth rates (G_{max}) for cases 2 and 3 are considerably higher than the measured growth rates (G_{exp}). However, since the predictions are based on non-diamond growing [H]/[CH_3] ratios, these growth rates are not relevant data for examining the validity of the model. For case 4 in an ethylene/oxygen flame, $G_{max,4}$ is predicted to be higher than $G_{exp,4}$ by a factor of 10.5, which is in good agreement with the $G_{max,1}/G_{exp,1}$ of 11.7 found for an acetylene/oxygen flame at the same substrate temperature of 1073 K. For case 5, if the activation energy for diamond growth is assumed to be $\sim$ 23 kcal/mole [51], the simulations which correctly predict the growth rates for a substrate temperature of 1200 K will overpredict the absolute growth rates at 973 K by a factor of 9.5. So $G_{max,5}/G_{exp,5}$ of 4.8 is much smaller than expected.

With this limited data set, it is hard to determine the validity of the Dagaut–Cathonnet–Boettner mechanism for the modeling of low pressure alternative fuel

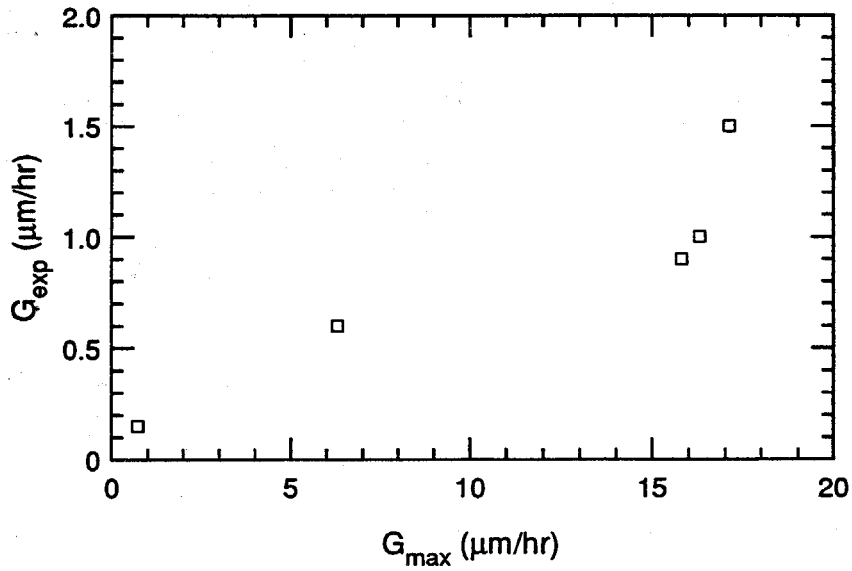

Figure 5-5: A correlation between G_{max} and G_{exp}.

flames. However, at least some of the features found in acetylene/oxygen flame simulations are well reproduced by the simulations using the Dagaut–Cathonnet–Boettner mechanism. The peak flame temperature is predicted to be higher than the adiabatic flame temperature and the chemical environment near the substrate surface is far from its equilibrium state. The peak flame temperature and the concentrations of H and CH_3 at the substrate are predicted to be slightly lower than those predicted in acetylene/oxygen flames, but high enough to grow diamond with reasonable growth rates ($\sim$ 1 μm/hr). Also, the predicted growth rates rank in an order similar to that the measured growth rates observed in experiments (from the highest for case 1, to the lowest for case 5) as shown in Figure 5-5.

Even though the Dagaut–Cathonnet–Boettner (D–C–B) mechanism was not developed for a kinetic modeling study of acetylene oxidation, since this mechanism has

been effectively used to model various hydrocarbon fuels (such as methane, ethane, ethylene, propylene, and propane), it is worthwhile to verify that this mechanism can also be used to model acetylene/oxygen flames. In Chapter 3, simulations using the Miller–Melius (M–M) mechanism effectively modeled low pressure acetylene/oxygen flames. Predicted results of both simulations are summarized in Table 5.4. Cases 2 and 3 are the cases of diamond-growing acetylene/oxygen flames which were described in Chapter 2. Equilibrium compositions are the values at the given ϕ, P, and T_S for each case.

Both mechanisms predict the peak flame temperature to be higher than the adiabatic flame temperature. However, the predicted temperature overshoot from the D–C–B mechanism is much smaller than the temperature overshoot from the M–M mechanism. The mole fraction for CO at the substrate predicted from the D–C–B mechanism approaches its equilibrium value more closely than the value from the M–M mechanism. For stable species, the D–C–B mechanism predicts lower mole fractions for H_2, C_2H_2, and CH_4 at the substrate than the values from the M–M mechanism. The mole fractions for H predicted by both mechanisms are similar, but the predicted mole fraction for CH_3 from the D–C–B mechanism is much lower than that from the M–M mechanism. Even though the absolute mole fractions for each species predicted by the D–C–B mechanism are quite different from the values predicted by the M–M mechanism, the simulations using the D–C–B mechanism reproduce the trend in the mole fraction for each species (whether it will have a higher

	Case 2			Case 3		
.	M–M	D–C–B	Equil.	M–M	D–C–B	Equil.
T_{flame} (K)	3433	3143	3006	3818	3355	2942
Major Stable Species						
[CO]	0.631	0.606	0.592	0.627	0.594	0.583
[H_2]	0.246	0.231	0.298	0.230	0.216	0.295
[H_2O]	0.084	0.102	0.035	0.095	0.116	0.039
[CO_2]	0.034	0.047	0.075	0.037	0.052	0.083
[C_2H_2]	0.021	5.6e-3	5.0e-12	0.027	3.5e-3	1.4e-12
[CH_4]	3.7e-4	3.2e-4	1.2e-5	3.4e-4	1.7e-4	3.7e-6
[C_2H_4]	2.4e-5	1.1e-4	9.4e-12	9.4e-5	9.1e-5	1.5e-12
[O_2]	1.4e-5	1.4e-5	9.0e-23	1.9e-4	1.4e-4	1.9e-19
Key Radical Species						
[H]	3.1e-3	3.4e-3	3.0e-8	7.8e-3	8.8e-3	3.8e-8
[CH_3]	2.5e-4	9.1e-5	2.6e-11	5.2e-4	9.8e-5	1.0e-11
[OH]	1.9e-5	2.2e-5	1.3e-11	1.4e-4	1.6e-4	1.9e-11
[O]	1.3e-5	1.8e-6	1.4e-18	2.0e-5	3.3e-5	2.7e-18
[CH_2]	3.2e-7	3.8e-7	1.6e-18	2.5e-6	2.0e-6	8.2e-19
[CH]	2.1e-8	3.4e-8	8.4e-25	2.6e-7	5.0e-7	5.7e-25
[C_2H]	8.4e-9	7.4e-9	8.6e-24	1.0e-7	2.6e-8	3.1e-24
	Case 2			Case 3		
	M–M	D–C–B	Exp.	M–M	D–C–B	Exp.
[H]/[CH_3]	12.3	37.5	–	15.0	89.8	–
G (μm/hr)	10.7	4.1	0.7	17.1	3.5	1.5

Table 5.4: A comparison of simulation results of acetylene/oxygen flames from Miller–Melius (M–M) and Dagaut–Cathonnet–Boettner (D–C–B) mechanisms. Cases 2 and 3 are those from Chapter 2. Predicted G is calculated from equation 3.7.

or a lower value than for the equilibrium). predicted from the simulations using the M–M mechanism.

For cases 2 and 3, the ratios of $[H]/[CH_3]$ predicted from D–C–B mechanism are 37.5 and 89.8, respectively. These are much higher than the predicted values (12.3 and 15.0) from the M–M mechanism. The predicted growth rates G from the D–C–B mechanism are significantly lower than the values from the M–M mechanism and much closer to the measured growth rates.

However, the simulations employing the D–C–B mechanism do not correctly reproduce the relative variation in growth rate for cases 2 and 3, while the simulations employing the M–M mechanism reasonably reproduce the relative variation in growth rate for cases 2 and 3. The simulations predict that $G_{DCB,3}/G_{DCB,2} = 0.85$ and $G_{MM,3}/G_{MM,2} = 1.6$, compared to the measured ratio of $G_{exp,3}/G_{exp,2} = 2.1$.

Even though the modeling using the Dagaut–Cathonnet–Boettner mechanism also predicts some of the general trends predicted by the simulation using the Miller–Melius mechanism in low pressure acetylene/oxygen flames, since it fails to predict the experimentally observed results, the Dagaut–Cathonnet–Boettner mechanism may not be used as a gas phase mechanism to model acetylene/oxygen flames, though some more investigations are necessary.

5.3.2 Mass Spectrometry

Absolute mole fractions of CO, H_2, CO_2, CH_4, and C_2H_2 were obtained in propylene/oxygen, ethylene/oxygen, and propane/oxygen flames. For the measurements, the same experimental setup for mass spectrometry described in Chapter 3 was employed.

In Figures 5-6 and 5-7, mass spectrometry results and model predictions for propylene/oxygen flames are presented. Experimental conditions were: P = 70 Torr, Q_T = 0.3 slm/cm^2, ϕ = 2.15, and Ar dilution of $\sim$ 9%. With a substrate, L was 1.2 cm and T_S was 873 K.

Figure 5-6 shows the mole fractions of CO, H_2, CO_2, C_2H_2, and CH_4 at various distances from the burner without a substrate. The symbols represent the measured experimental data, and the curves are the predictions from modeling. After about 5 mm from the burner, the measured mole fractions of CO, H_2, and CO_2 match the predictions well. The measured mole fractions of C_2H_2 and CH_4 generally match well with the predictions at distances greater than 7–8 mm from the burner.

The model predicts that the flame front is at a distance of $\sim$ 1 mm from the burner surface. and all the major species mole fractions rapidly change near the burner surface (0–3 mm from the burner). The measured mole fractions show the same trends, but their profiles are shifted $\sim$ 3 mm from the predicted profiles, and the flame front is located about 4 mm from the burner surface. This discrepancy may be due to the resolution limit of the microprobe and the burner design. Similar

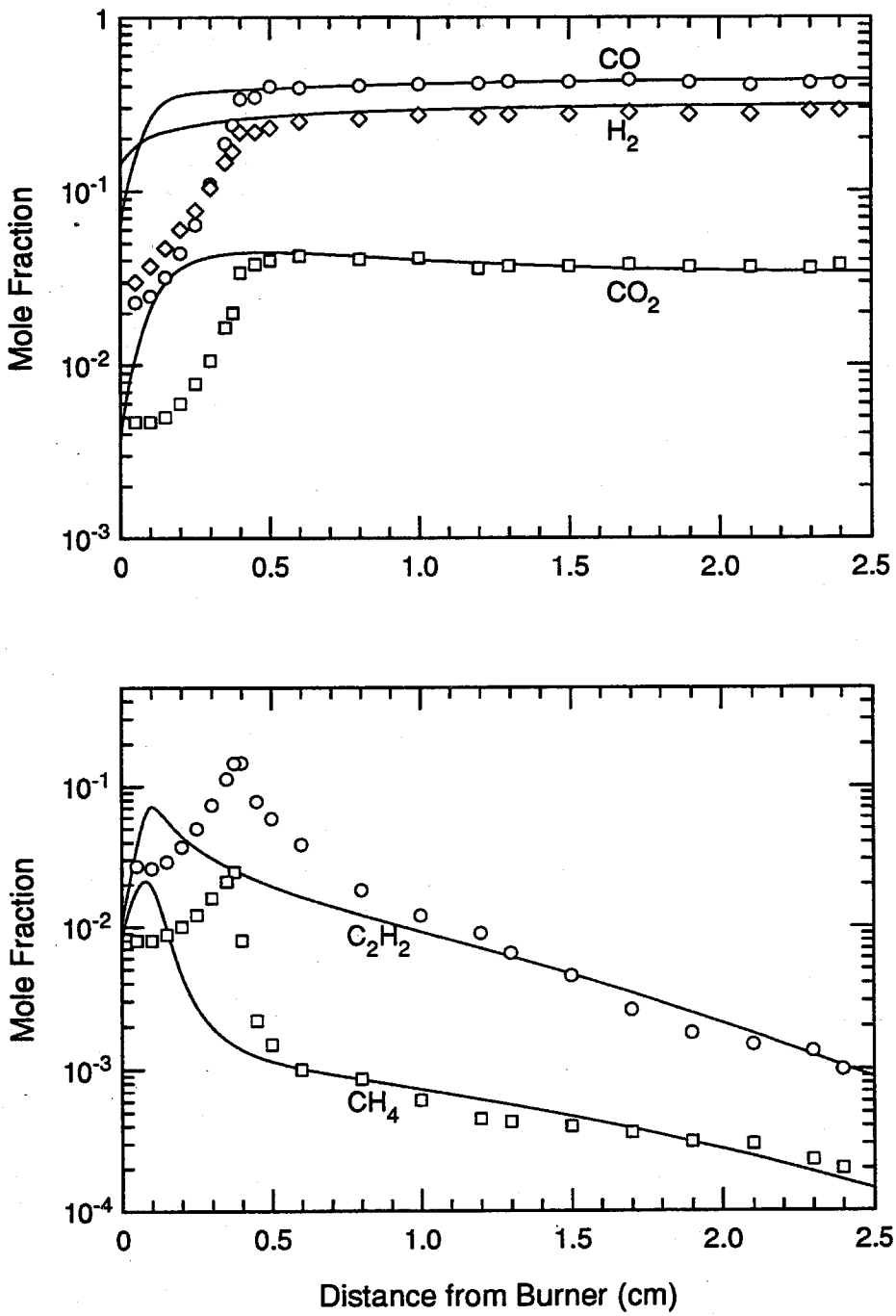

Figure 5-6: Stable species mole fractions without a substrate in a propylene/oxygen flame: $P = 70$ Torr, $\phi = 2.15$.

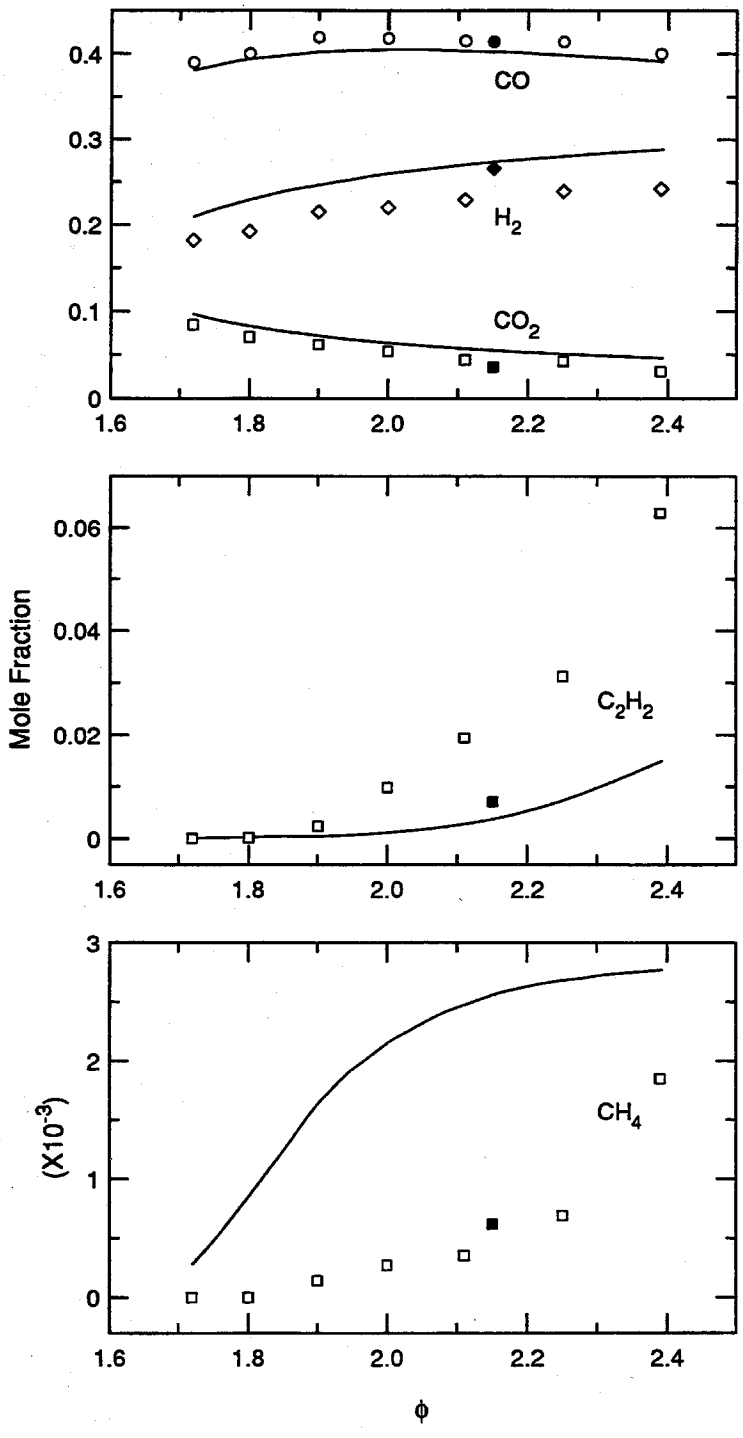

Figure 5-7: Stable species mole fractions at the substrate in propylene/oxygen flames: $P = 70$ Torr and $L = 1.2$ cm; experimental data with a substrate (open symbols) and without a substrate (solid symbols).

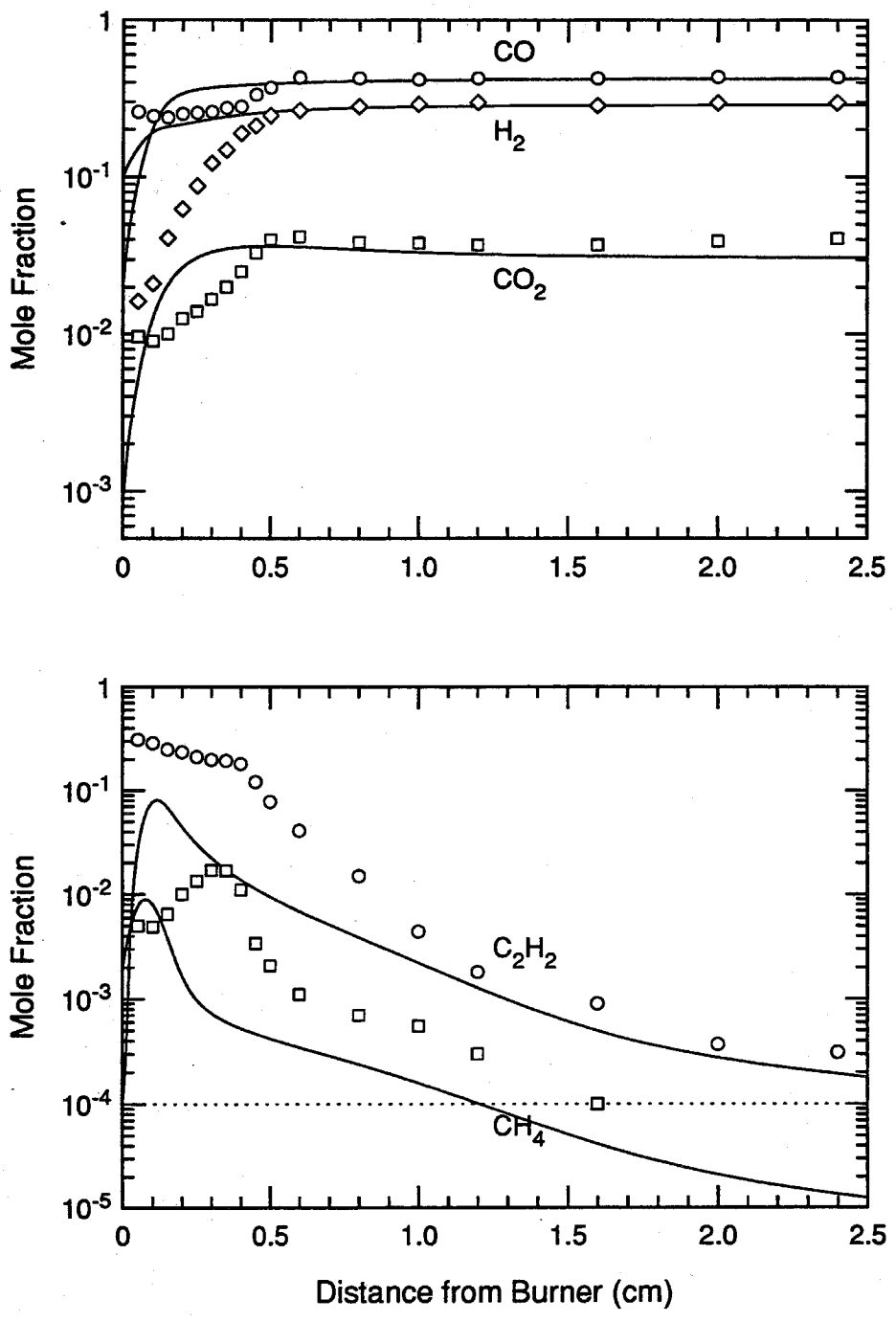

Figure 5-8: Stable species mole fractions without a substrate in an ethylene/oxygen flame: $P = 50$ Torr, $\phi = 2.16$.

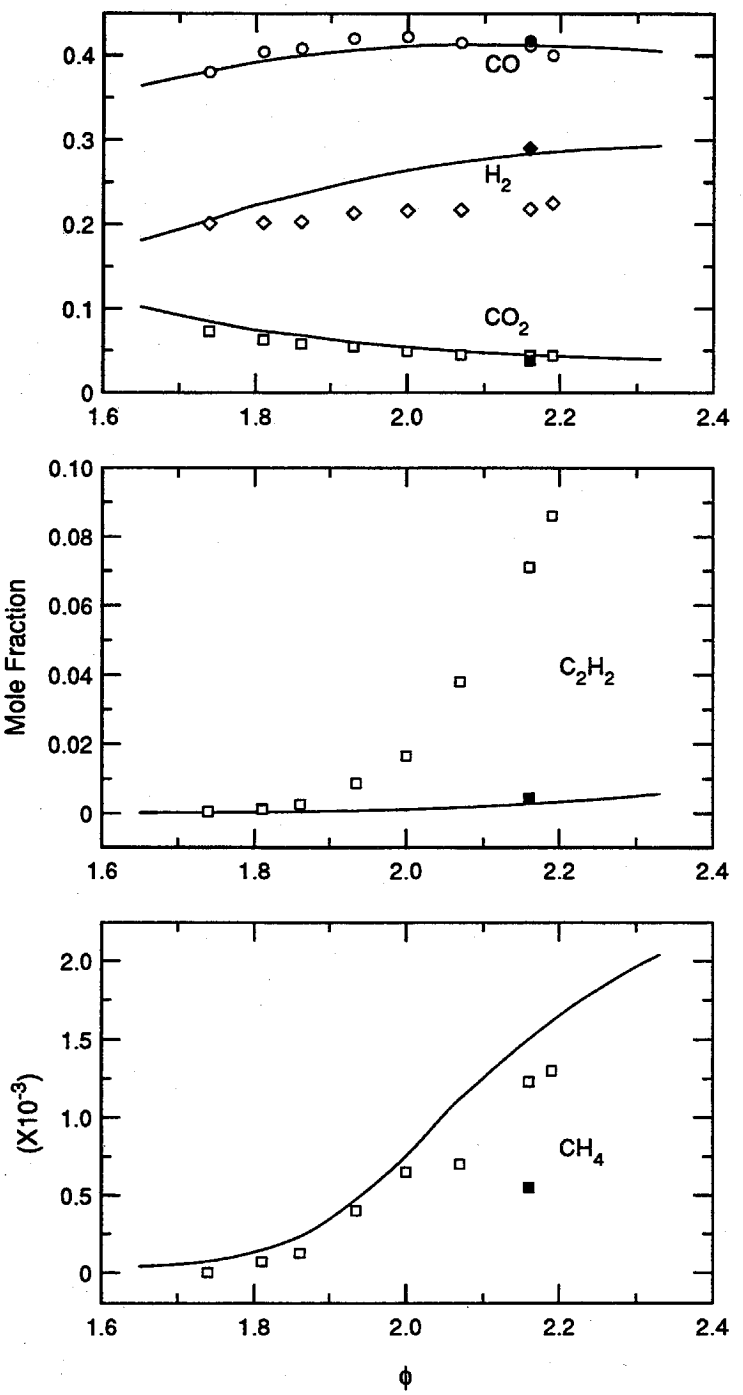

Figure 5-9: Stable species mole fractions at the substrate ethylene/oxygen flames: $P = 50$ Torr, $L = 1.0$ cm; experimental data with a substrate (open symbols) and without a substrate (solid symbols).

profile shifts are also observed for acetylene/oxygen flames, and discussed in detail in Chapter 3.

For C_2H_2 and CH_4, the model predicts their peak mole fractions at a distance of $\sim$ 1 mm from the burner, but the measured mole fractions for these species show the peak values at a distance of $\sim$ 4 mm from the burner, and the measured peaks for absolute mole fractions of C_2H_2 and CH_4 are much higher than in the predictions.

In Figure 5-7, the results of mass spectrometry at the substrate with varying stoichiometric ratios ranging from $\phi = 1.7$ to $\phi = 2.4$ are presented. Here L was 1.2 cm and T_S was 873 K. The curves are from model predictions. The experimental data measured at $L = 1.2$ cm without a substrate are also presented. The effect of the substrate is clearly seen for H_2 and C_2H_2. With a substrate, the predictions generally match with the measured values of CO and CO_2, but the model slightly overpredicts the mole fractions for H_2 at the substrate. For C_2H_2, the mole fractions are measured to be higher than the predictions. On the other hand, the measured mole fractions of CH_4 are consistently lower than the predicted mole fractions.

Figures 5-8 and 5-9 present mass spectrometry results and model predictions found in ethylene/oxygen flames. Experimental conditions were: $P = 50$ Torr, $Q_T = 0.71$ slm/cm^2, $\phi = 2.11$, and Ar dilution of $\sim$ 10%. When employing a substrate, L was 1.0 cm and T_S was 1023 K.

Since ethylene (C_2H_4) and CO have the same molecular weight of 28, the measured mole fractions for CO at the mass peak of 28 are overpredicted near the burner surface

by the provided ethylene. Similarly, since C_2H_4 produces a fragment signal at the mass peak of 26, the measured mole fractions of C_2H_2 are also overpredicted near the burner, as shown in Figure 5-8. After $\sim$ 5 mm from the burner surface, the model generally predicts the mole fractions of CO, H_2, and CO_2 well. For C_2H_2 and CH_4, the measured mole fractions are higher than the predicted mole fractions.

With a substrate, the predictions generally match with the measured values of CO and CO_2, and the model typically overpredicts the mole fractions of H_2 at the substrate. For C_2H_2, the mole fractions at the substrate are measured to be much higher than the predicted mole fractions. For CH_4, the measured mole fractions at the substrate match with the predicted values, which is inconsistent with the results without a substrate. The measured mole fractions of H_2, C_2H_2, and CH_4 at a distance of 10 mm are clearly changed by removing the substrate.

Figures 5-10 and 5-11 show the mass spectrometry and the modeling results in propane/oxygen flames. Experimental conditions were: P = 90 Torr, Q_T = 0.52 slm/cm^2, ϕ = 2.1, and Ar dilution of $\sim$ 10%. With a substrate, L was 1.05 cm and T_S was 953 K.

Propane (C_3H_8) and CO_2 have the same molecular weight of 44, so the measured mole fractions for CO_2 at the mass peak of 44 are overpredicted by the provided propane near the burner surface. Because of the detection limit of the mass spectrometer ($\sim 10^{-4}$), C_2H_2 and CH_4 can not be detected at distances greater than 12 mm from the burner surface without a substrate. Again, the measured profiles show

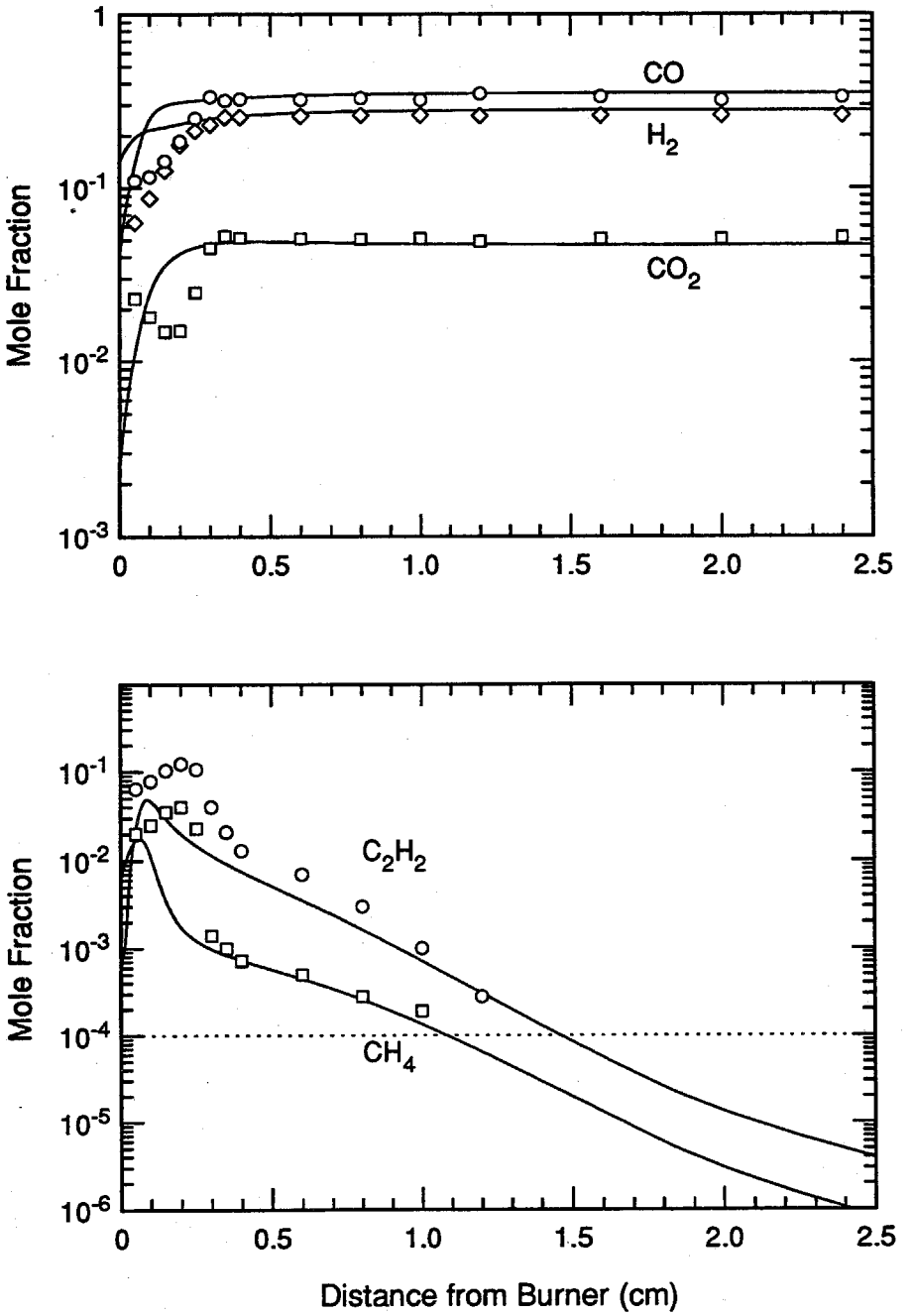

Figure 5-10: Stable species mole fractions without a substrate in a propane/oxygen flame: $P = 90$ Torr, $\phi = 1.92$.

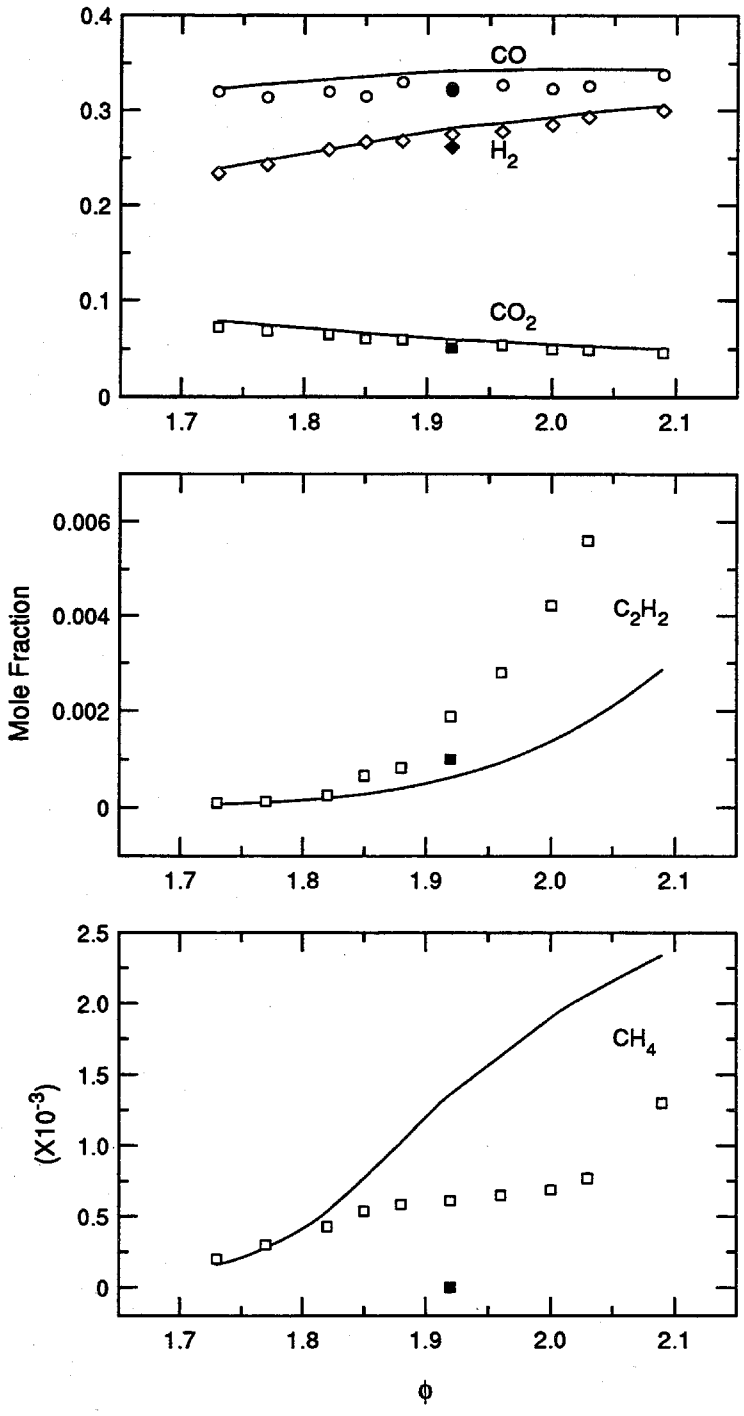

Figure 5-11: Stable species mole fractions at the substrate in propane/oxygen flames: $P = 90$ Torr, $L = 1.05$ cm; experimental data with a substrate (open symbols) and without a substrate (solid symbols).

a shift of $\sim$ 2 mm near the burner surface. The predictions for CO, H_2, and CO_2 generally match with the measured mole fractions. For C_2H_2 and CH_4, the measured peak mole fractions are much higher than those predicted by the model.

With a substrate, the mass spectrometry results for CO, H_2, and CO_2 match the predictions of the model within the experimental uncertainty. No significant change in mole fractions of CO, H_2, and CO_2 is found for conditions with and without a substrate. For C_2H_2 and CH_4, the measured mole fractions are not well reproduced by the predictions. However, significant changes in their mole fractions are found with and without a substrate.

5.4 Summary

Flame simulations were carried out to analyze the growth environment in low pressure alternative fuel flames (MAPP/oxygen, propylene/oxygen, ethylene/oxygen, and propane/oxygen) which were described in Chapter 4. The model employing the Dagaut–Cathonnet–Boettner mechanism predicts that the peak flame temperatures could be higher than the adiabatic flame temperature in these flames and the chemical environment at the substrate is far from its equilibrium state. Although slightly lower than acetylene/oxygen flames, these alternative fuel flames are also predicted to have high enough H and CH_3 concentrations at the substrate to grow diamond at a reasonable growth rate.

Mass spectrometry experiments indicate that the model correctly predicts the

mole fractions of CO and CO_2 at the substrate and slightly overpredicts the mole fraction of H_2 in these alternative fuel flames. The model typically underpredicts the mole fraction of C_2H_2 at the substrate, but correctly predicts the rise in mole fractions as the equivalence ratio increases. For CH_4, the measured results are rather inconsistent with and without a substrate in these flames. Without a substrate, although some discrepancies in absolute values are observed near the burner surface, the model generally predicts the trends in the mole fractions of stable species.

Chapter 6

Diamond Growth on Particles in a Fluidized Bed Reactor

6.1 Overview

To grow continuous diamond coatings on small, three-dimensional objects, experiments are performed using microwave plasma-enhanced fluidized beds. Studies are carried out to map the parameter space leading to diamond growth and to determine the relationship between gas composition and diamond growth rate. A small amount of oxygen is found to be necessary for well-faceted diamond growth on seed particles in a fluidized bed.

In this chapter, the effects of process parameters for diamond growth on small (< 1 mm diameter) silica and silicon particles in a microwave plasma-enhanced fluidized bed reactor are reported, and mass spectrometry results obtained by measuring stable species produced from a methane/hydrogen/oxygen mixture in the microwave plasma are presented.

6.2 Experimental

The experimental setup is shown schematically in Figure 6-1. A 12 mm OD, 10 mm ID quartz flow tube with tapered bottom is inserted through a 13 mm ID McCarroll microwave cavity (Optos Instruments). The McCarroll cavity is connected to a 2.45 GHz, 120 Watt microwave power source by a coaxial cable.

The quartz tube wall is passivated by soaking for 15 hours in 10 M NaOH and then for 15 hours in 10 M HNO_3. This treatment is known to effectively make quartz

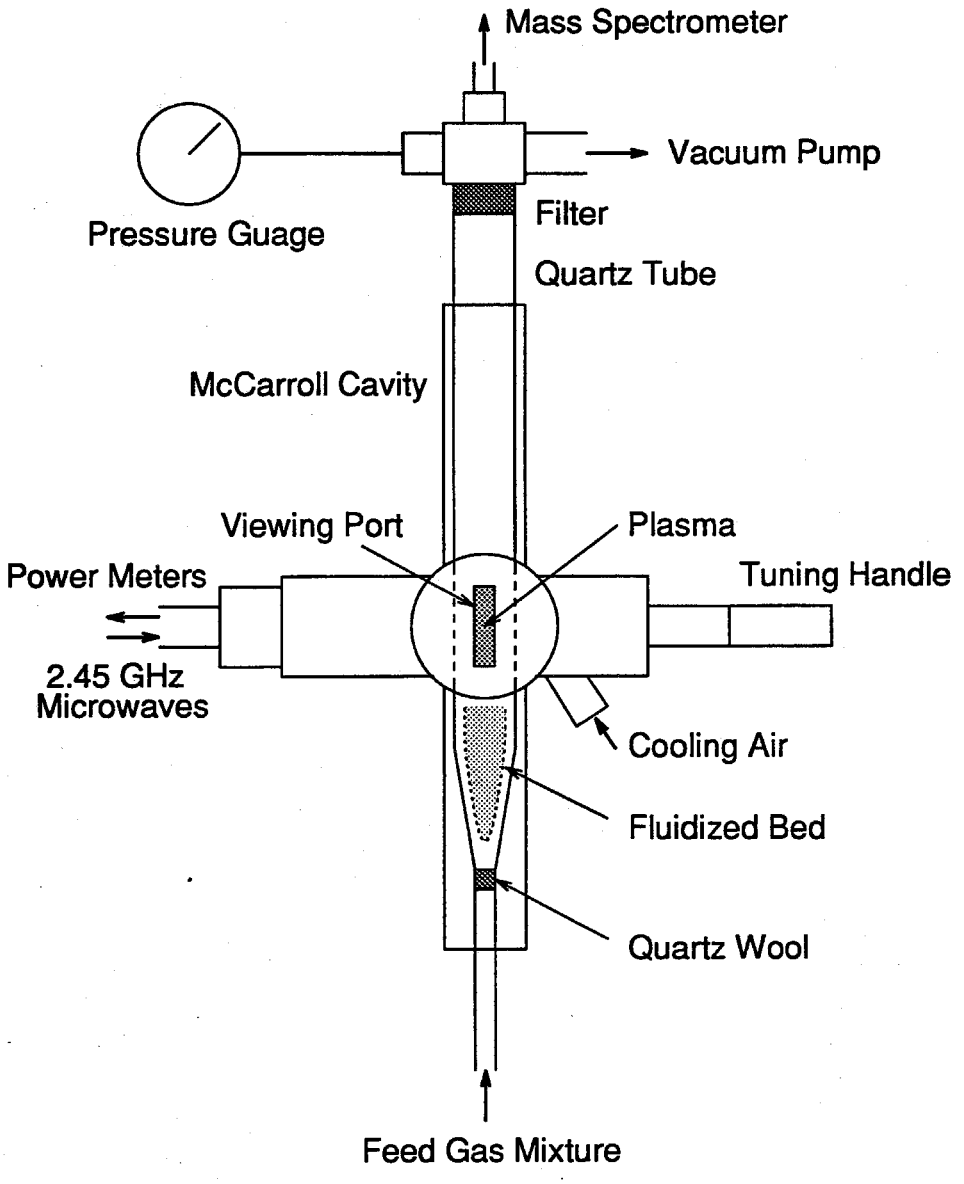

Figure 6-1: Experimental setup.

surfaces stable and inactive at high temperatures of up to $\sim$ 800 K [68].

The gases used are calibrated diluted mixtures of methane in a hydrogen carrier gas (Matheson) and laboratory-grade oxygen. The methane percentage ranges from 0.5 to 15.0%, while the oxygen to carbon ([O]/[C]) ratio varies from 0 to 4. The total gas flow rates are 160–200 sccm. The gas is introduced from the bottom of the tube to fluidize the seed particles as well as to provide a carbon source. The system pressures are 9–40 Torr. In most cases, a system pressure of 9 Torr, which is lower than that used under typical diamond CVD conditions, is selected to broaden the plasma region, and maximum microwave power of 120 Watts is maintained to maximize the plasma intensity.

Quartz wool is packed into the lower part of the tube to act as a gas diffuser and into the top of the tube to prevent fluidized particles from flowing to the vacuum pump. An external air jet is introduced into the side of the microwave cavity to cool the quartz tube.

Si and SiO_2 seed particles are used without pretreatment. The Si particles are produced by crushing and sieving a silicon wafer, resulting in particle sizes of 0.25–0.7 mm diameter. The SiO_2 particles are a silica gel (purity 99%, surface area 300 m^2/g, pore volume 1.15 cm^3/g, 0.25–0.6 mm diameter). Figure 6-2 and 6-3 show the SiO_2 and Si particles used in the experiments. Approximately 0.5 g of seed particles is introduced into the reactor for each run.

The center of the cavity is located above the fluidized bed. After microwave power

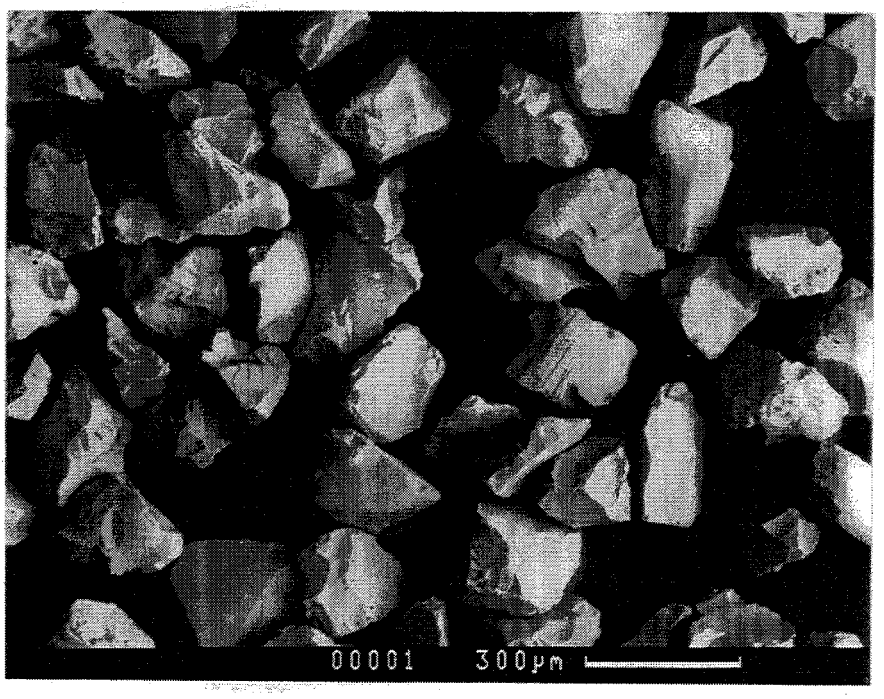

Figure 6-2: SiO_2 particles.

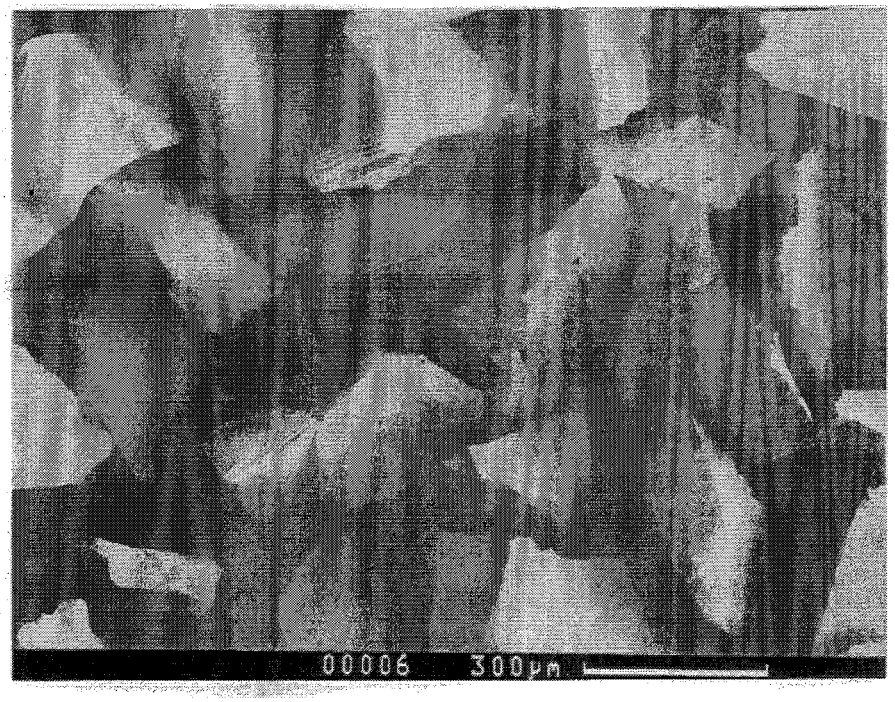

Figure 6-3: Silicon particles.

of approximately 20 Watts is applied, the plasma is initiated by a brief spark from a high frequency coil and the cavity tuned. When the microwave power is increased to about 80 Watts, some seed particles in the plasma attach to the reactor walls, presumably due to electrostatic charging. In some cases, mechanical vibration or occasional reduction of the microwave power are used to detach particles from the reactor walls.

The difficulty of measuring the temperature of small fluidized particles through the viewing slit prevents this measurement from being made. In some cases, a 0.5 mm diameter graphite rod is put in the plasma and the brightness temperature is measured with a one-color disappearing-filament pyrometer (Leeds and Northrup), giving readings of 800–900 °C. Since there is severe background emission from the discharge and the temperature of the graphite was measured in the plasma, the temperature of fluidized seed particles are estimated to be lower than that measured. No external control of particle temperature is provided.

For measurements of stable species concentrations, the exhaust gas is sampled from the top of the tube and analyzed with a differentially-pumped quadrupole mass spectrometer (Inficon Quadrex 200). The pressure within the sampling probe is maintained at 0.3 Torr. Since the sampled gas travels through several meters of copper tubing before entering the spectrometer, only stable species are detected. Mass spectrometry is performed at a system pressure of 9 Torr, a mass flow rate of 160 sccm of 2% CH_4 in H_2 , and for variable amounts of O_2 . At this pressure, the plasma extends

Figure 6-4: Silicon particles after the growth run.

to the reactor tube walls, assuring that the sampled exhaust gas has passed through the plasma.

6.3 Results

Figure 6-4 shows a typical result after the growth run. Si powders were used as seed particles, and carbon particles were deposited on surfaces of Si powders.

Typical deposits on seed particles with variable [O]/[C] ratios are shown in Figures 6-5 and 6-6. These deposits were obtained on SiO_2 particles at a pressure of 9 Torr and 120 Watts of microwave power, with flow rates of 160 sccm of 2.0% CH_4 in H_2 and various specified [O]/[C] ratios. In Figure 6-5 (a), only "ball-like" non-diamond car-

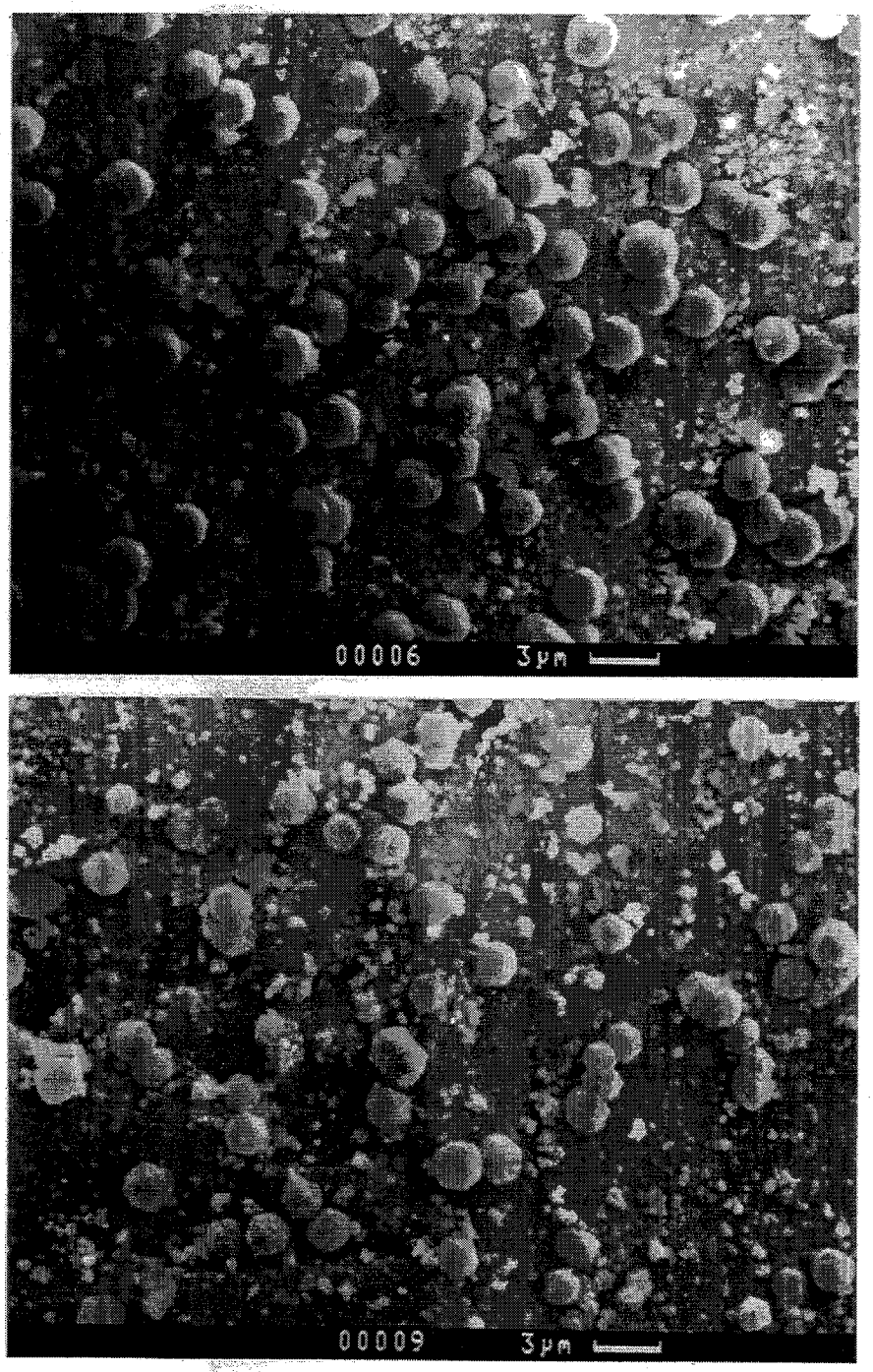

Figure 6-5: SEM micrographs of typical deposits on SiO_2 particles at 9 Torr, 120 Watts microwave power, with flow rates of 160 sccm of 2.0% CH_4 in H_2 and variable [O]/[C] ratios: (a) 2 hours, [O]/[C] = 0; (b) 1 hour, [O]/[C] = 1.6.

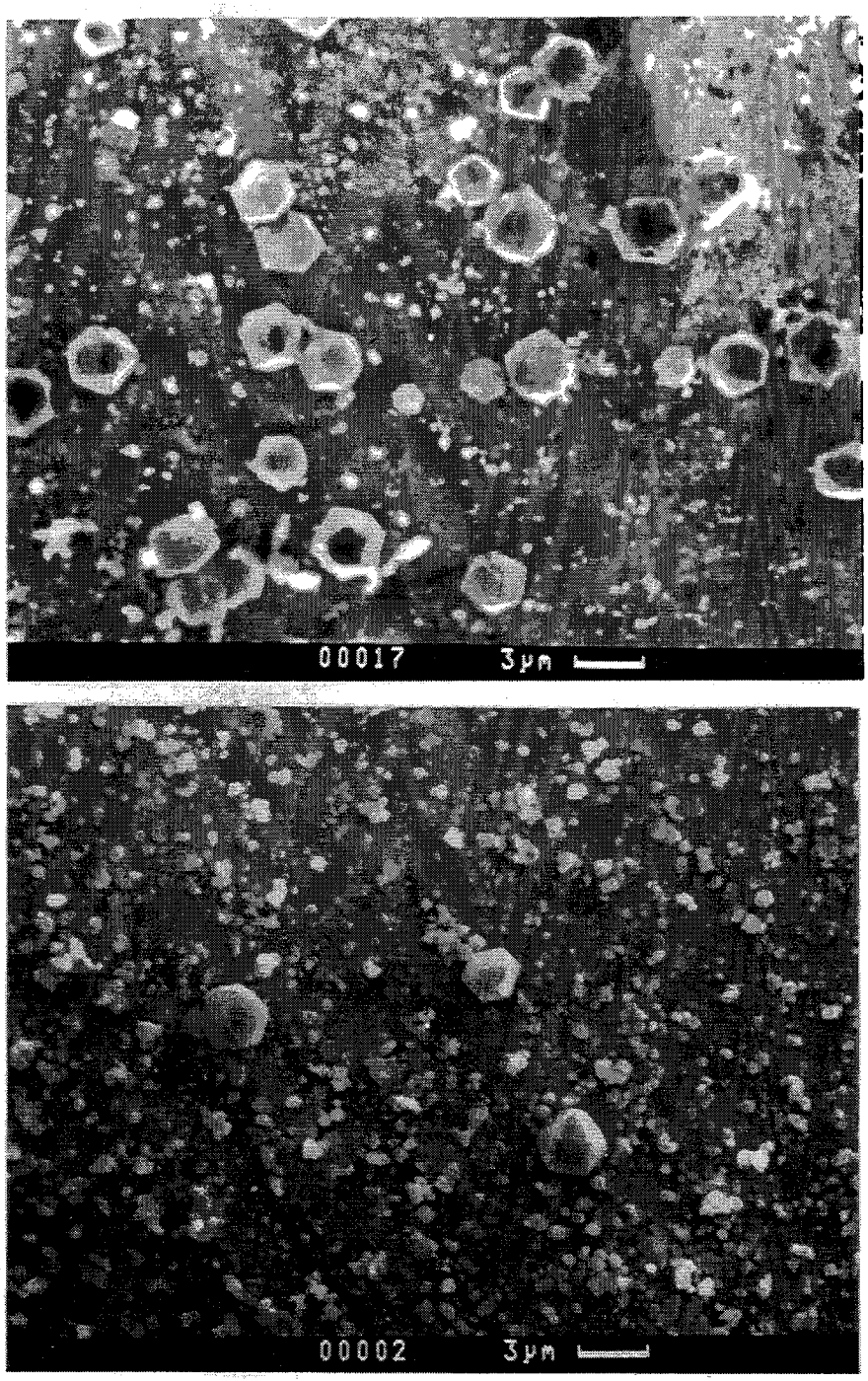

Figure 6-6: SEM micrographs of typical deposits on SiO_2 particles at 9 Torr, 120 Watts microwave power, with flow rates of 160 sccm of 2.0% CH_4 in H_2 and variable [O]/[C] ratios: (a) 1 hour, [O]/[C] = 1.9; (b) 1.5 hours, [O]/[C] = 2.8.

bon deposits of approximately 2 μm diameter were deposited after 2 hours without O_2 addition; the carbon growth rate was approximately 1 μm/hr.

The introduction of a small amount of O_2 is known to significantly relax the required substrate temperature for diamond growth on bulk substrates [69]. It is probable that it has a similar effect for growth on particles. Introducing oxygen significantly affects the deposited carbon morphology and growth rate, initially enhancing faceting and growth. Figure 6-5 (b) shows some faceted carbon deposits obtained with a growth rate of 2 μm/hr by adding O_2 at [O]/[C] = 1.6. In Figure 6-6 (a), well-faceted diamonds were deposited at [O]/[C] = 1.9. Increasing O_2 reduces the growth rate and nucleation density, due to oxidation of CH_4 to CO. Figure 6-6 (b) shows well-faceted diamond growth after 1.5 hours at [O]/[C] = 2.8. The nucleation density was decreased versus that of Figure 6-6 (a), and the growth rate was reduced to 2 μm/hr. No deposition was found at [O]/[C] = 3.3.

The smaller particles ($\sim$ 300 μm) typically showed higher nucleation density than the larger ones ($\sim$ 600 μm). Since no surface pretreatment was done, this is most likely a temperature effect. The smaller particles are expected to have a higher temperature, since the primary particle heating mechanism is recombination of atomic hydrogen on the surface, and diffusion-limited transport of H to the particle is more effective for smaller diameters.

The dependence of deposited diamond size on run time is shown in Figures 6-7 and 6-8. The run conditions were the same as those in Figure 6-6 (a). Cubooctahedral and

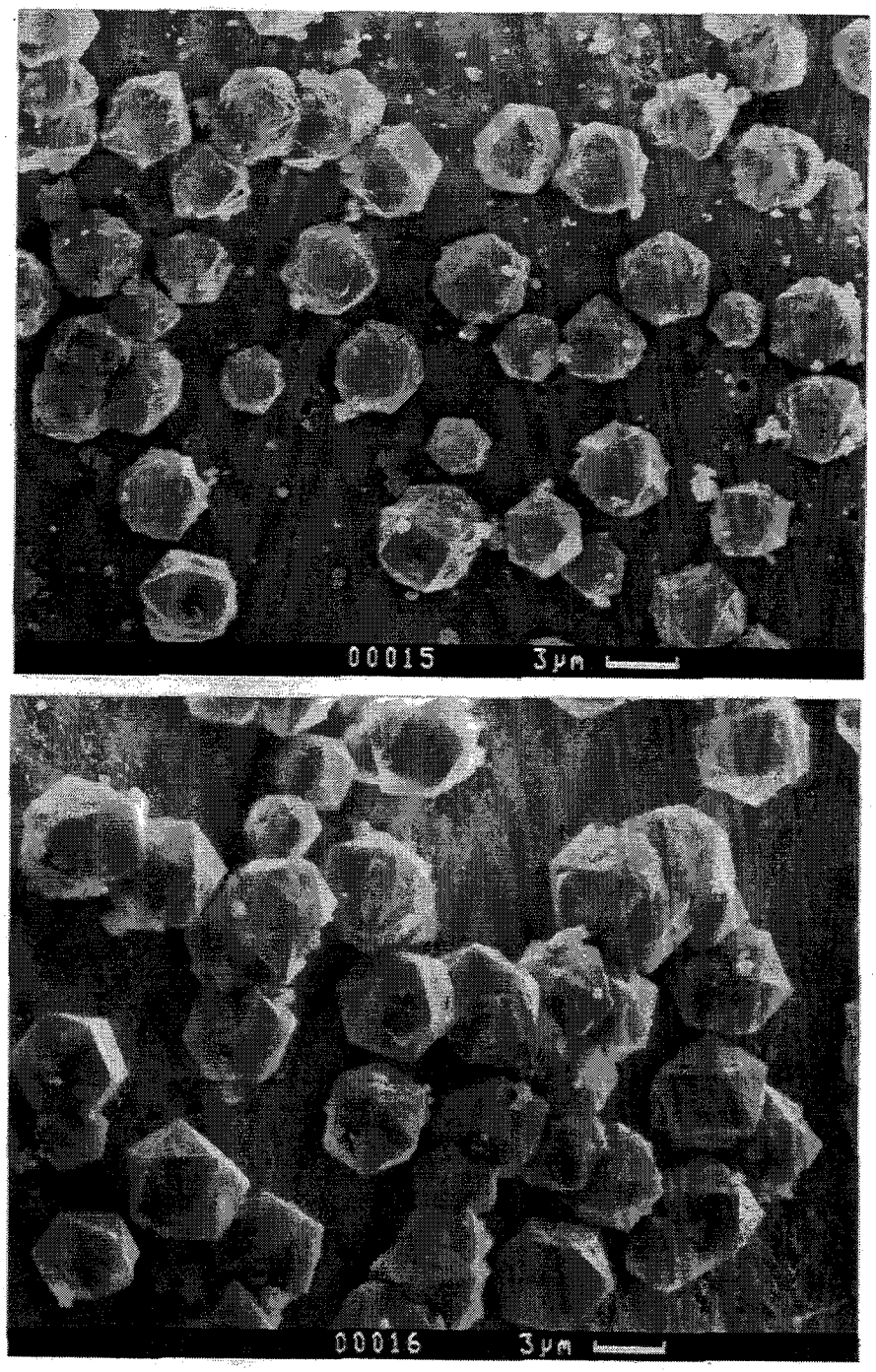

Figure 6-7: SEM micrographs of diamond coating on SiO_2 particles at 9 Torr, 120 Watts microwave power, with flow rates of 160 sccm of 2.0% CH_4 in H_2 and [O]/[C] = 1.9: (a) 1.5 hours; (b) 2 hours.

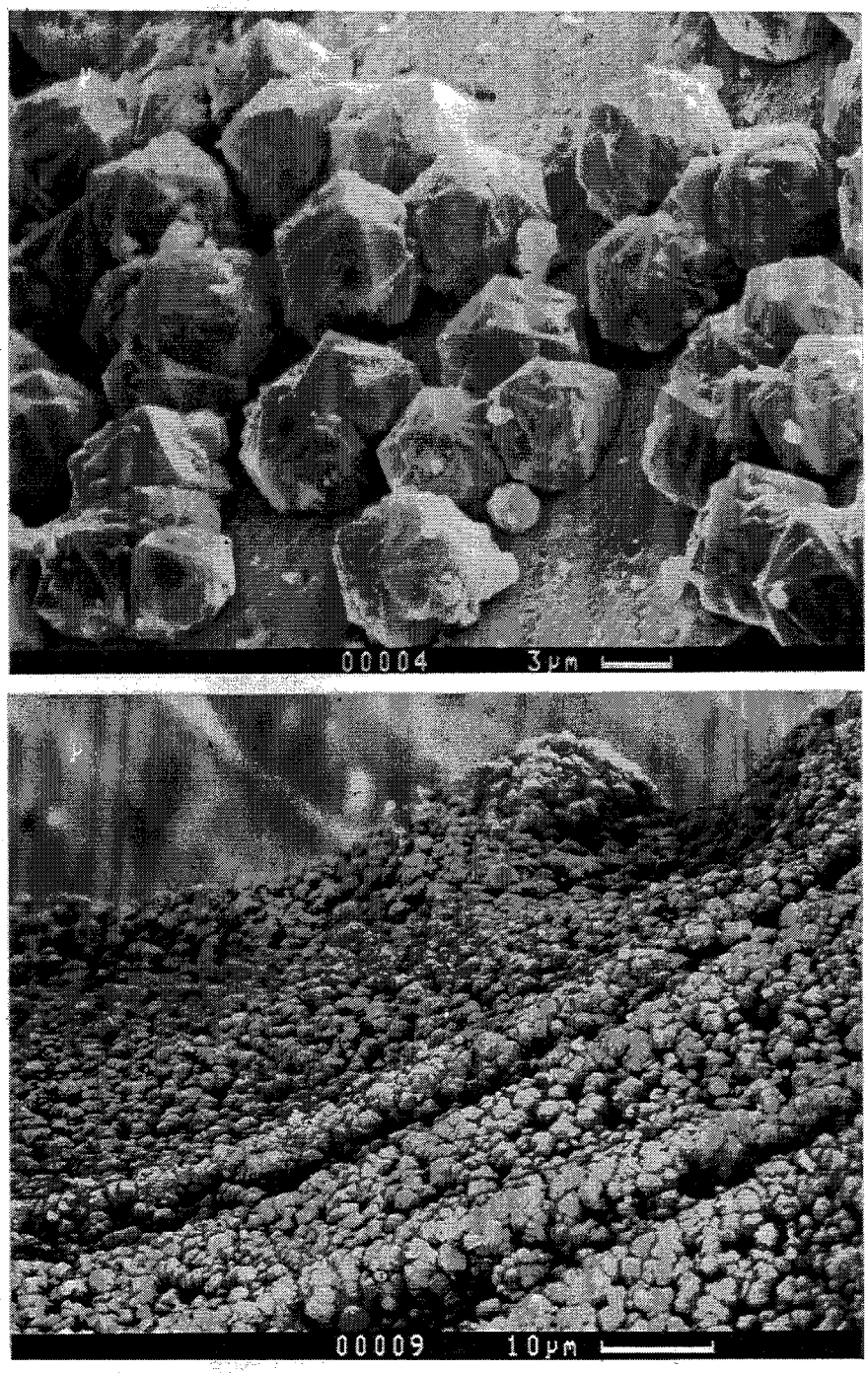

Figure 6-8: SEM micrographs of diamond coating on SiO_2 particles at 9 Torr, 120 Watts microwave power, with flow rates of 160 sccm of 2.0% CH_4 in H_2 and [O]/[C] = 1.9: (a) 3 hours; (b) 8 hours.

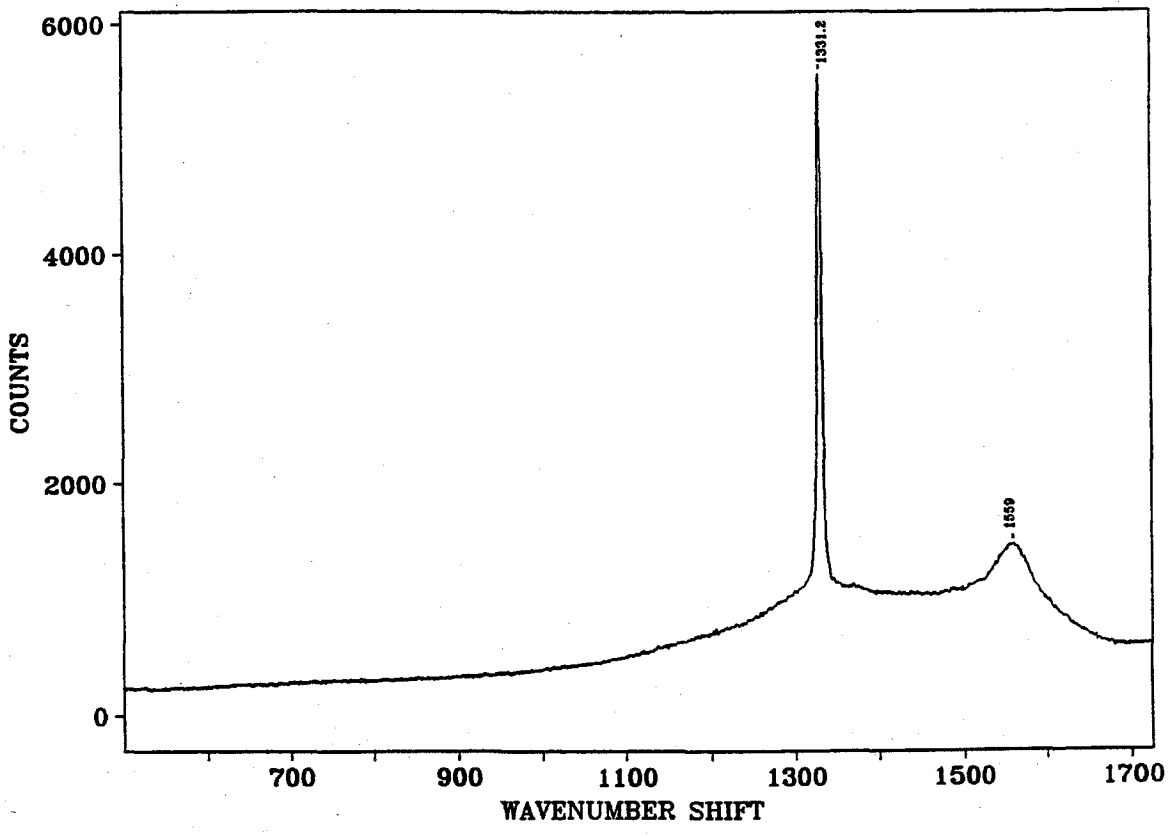

Figure 6-9: Micro-Raman spectrum of the diamond particles shown in Figure 6-7 (b).

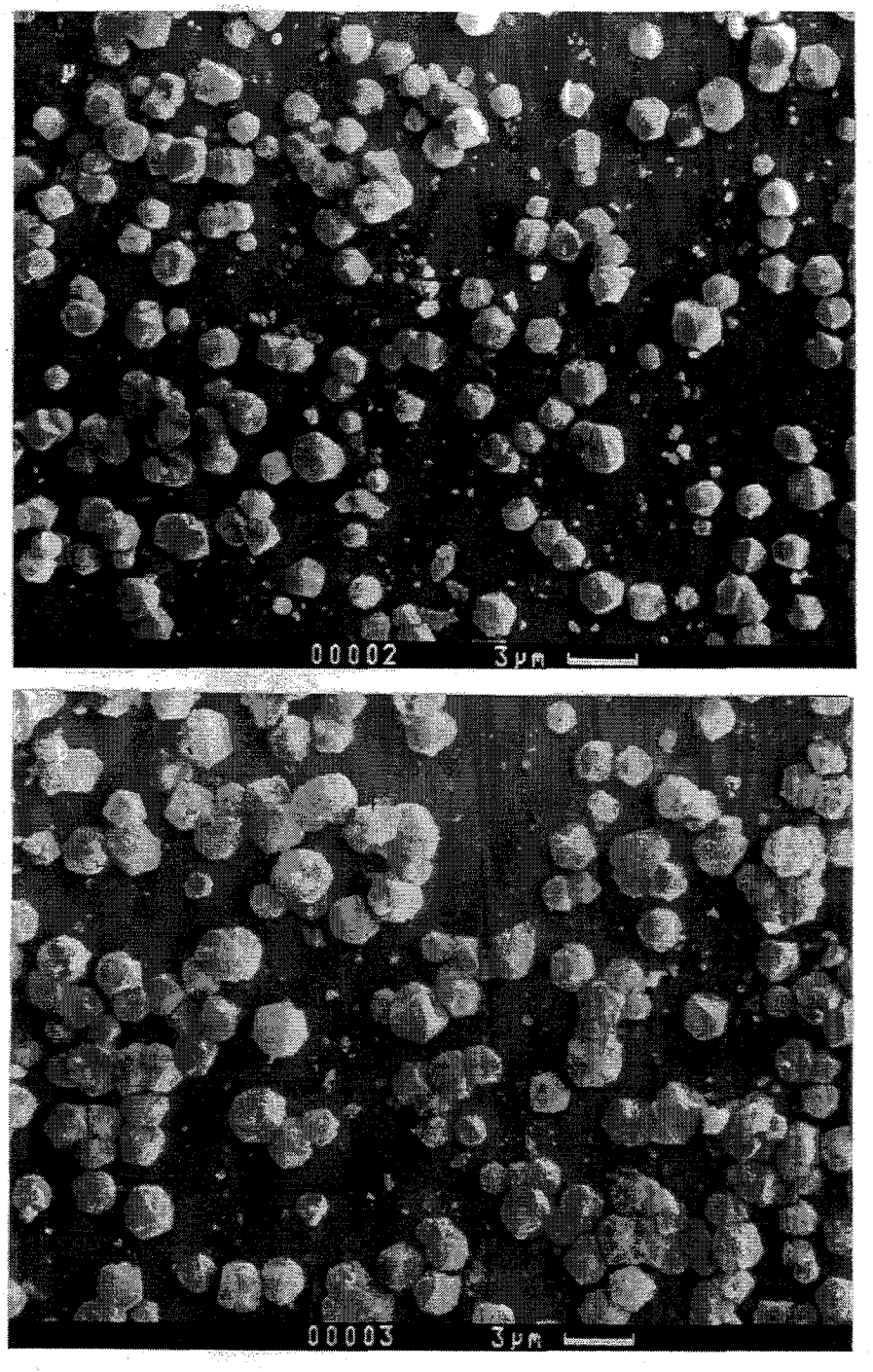

Figure 6-10: SEM micrographs of diamond coating on Si particles at 9 Torr, 120 Watts microwave power, with flow rates of 160 sccm of 2.0% CH_4 in H_2 and [O]/[C] = 1.9: (a) 1 hour; (b) 1.5 hours.

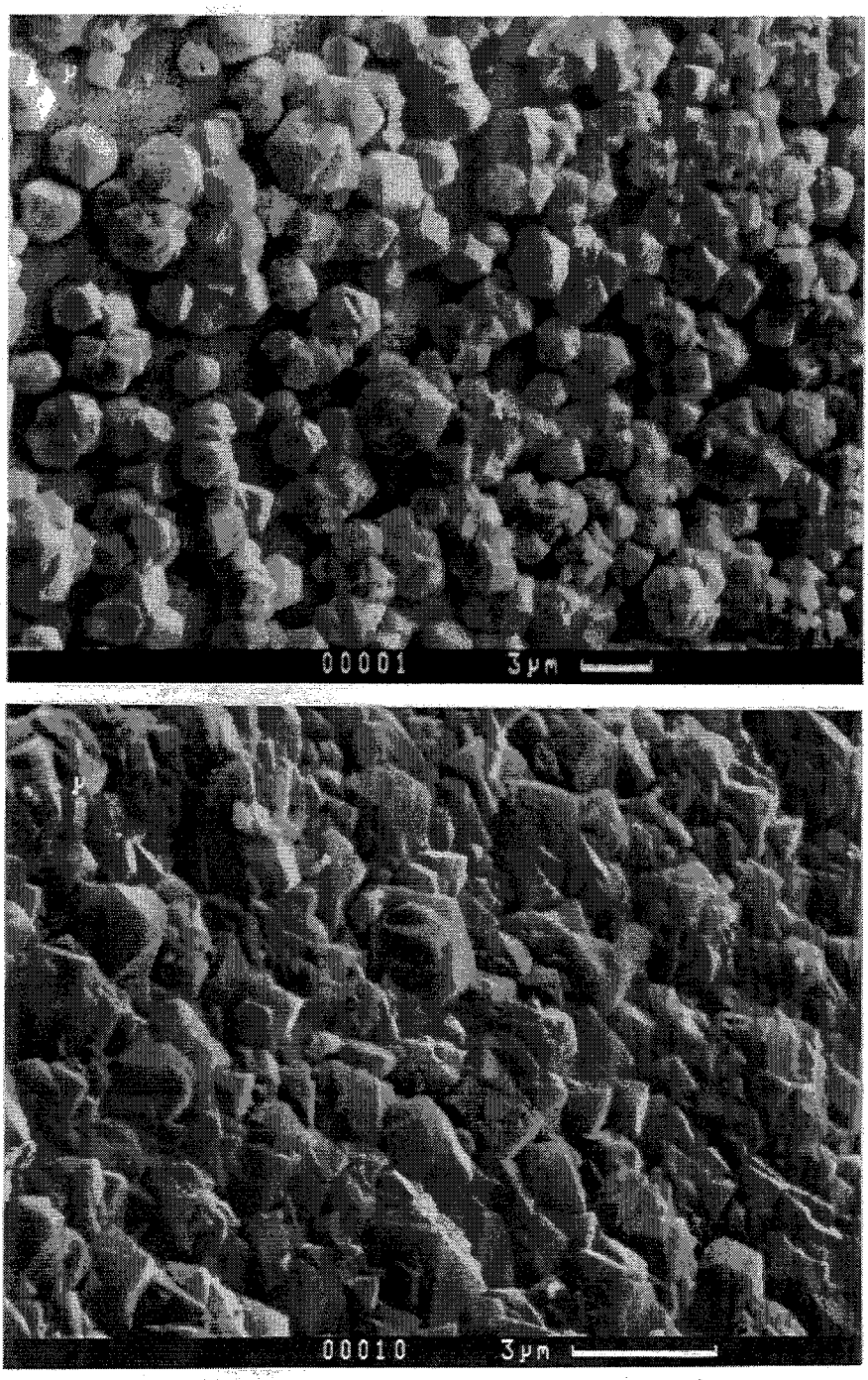

Figure 6-11: SEM micrographs of diamond coating on Si particles at 9 Torr, 120 Watts microwave power, with flow rates of 160 sccm of 2.0% CH_4 in H_2 and [O]/[C] = 1.9: (a) 3 hours; (b) 8 hours.

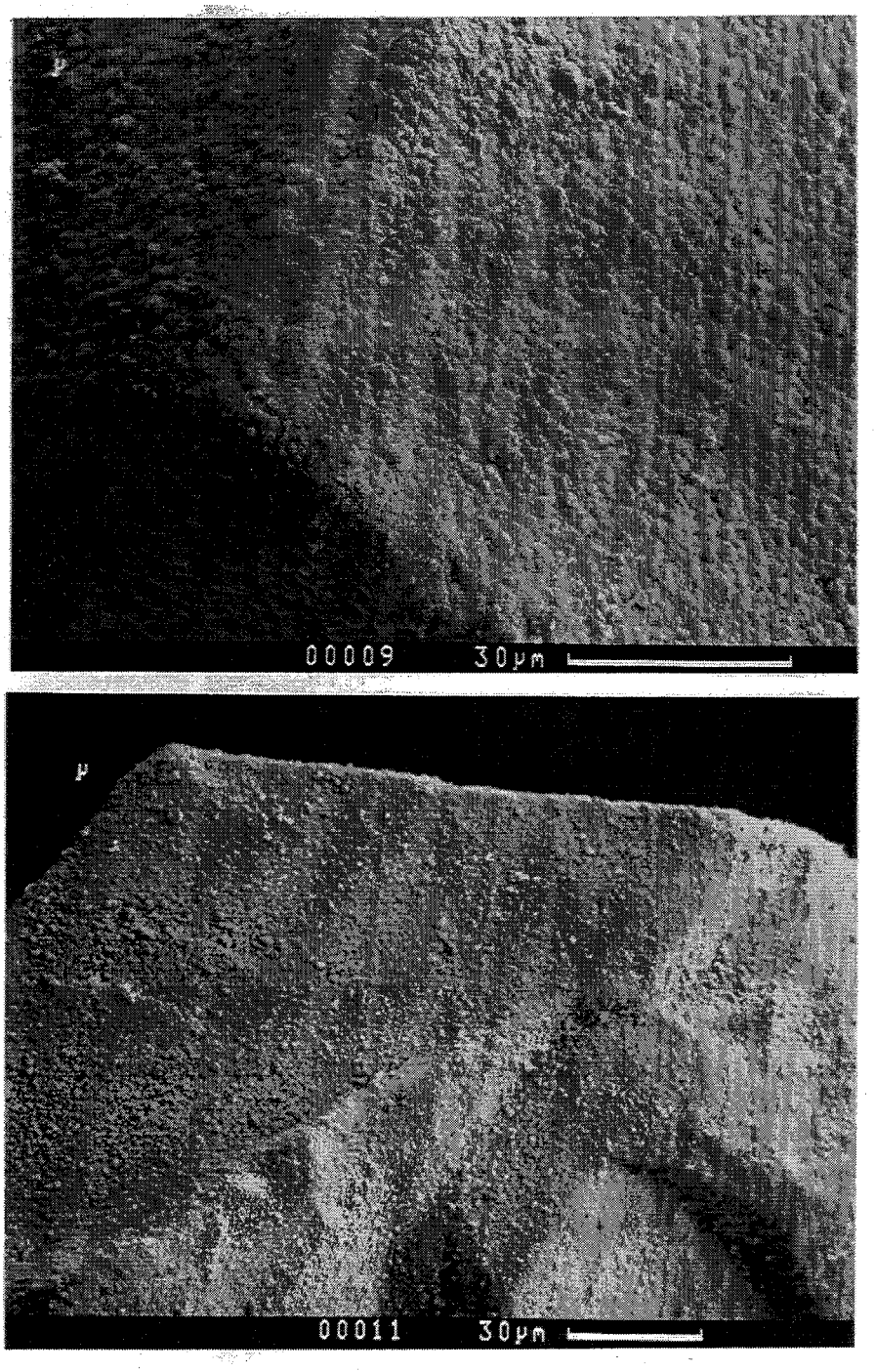

Figure 6-12: SEM micrographs of continuous diamond coating on Si particles at 9 Torr, 120 Watts microwave power, with flow rates of 160 sccm of 2.0% CH_4 in H_2 and [O]/[C] = 1.9 after 8 hours.

decahedral Wulff-polyhedral facets were commonly seen with secondary nucleations after 1.5 hours. The typical diamond crystal size increased nearly linearly with time until the deposited particles collided with each other, indicating that the growth rate is uniform until the particles interfere with each other. This uniform growth rate was approximately 2.7 μm/hr. Continuous diamond coatings covered the entire surface of the some seed particles after 8 hours, as shown in Figure 6-8 (b).

A micro-Raman spectrum of the diamond film shown in Figure 6-7 (b) is shown in Figure 6-9. A clear sharp peak at 1332 cm^{-1} indicates the presence of high quality diamond.

Even though all the fluidized particles examined showed some diamond growth on their surfaces, on some the nucleation density was lower, and on these the film was not continuous after 8 hours. Continuous films appeared to be mainly deposited on particles which had attached to the reactor walls adjacent to plasma, presumably due to particle charging. This may be due to these particles being maintained at an adequate temperature and chemical environment for diamond growth. Briefly reducing the microwave power from 120 Watts to about 50 Watts at one-hour intervals to detach the particles from the reactor walls resulted in more uniform diamond growth among the particles. This method was employed in all of the experiments lasting longer than one hour. Use of a continuous mechanical vibrator which greatly reduced attachment to the reactor walls resulted in very low density diamond growth.

Figures 6-10 and 6-11 show well-faceted diamond deposits grown on Si particles.

Run conditions were the same as those in Figure 6-6 (a). The diamond growth rate was approximately 1.3 μm/hr, lower than on SiO_2 particles at the same conditions. On the other hand, the diamond nucleation density on Si particles was much higher than that on SiO_2 particles. Well-faceted, continuous diamond coatings covered the entire surface of the some Si seed particles after 8 hours as shown in Figures 6-11 (b) and 6-12. Again, on some the nucleation density was lower, and on these the film was not continuous after 8 hours.

Well crystallized diamond is known to grow on two-dimensional flat substrates in a microwave plasma using mixtures of less than 2% CH_4 in H_2 without O_2, and up to 5% CH_4 in H_2 with O_2 addition [70]. Ravi has grown good quality diamond on flat silicon substrates using up to 15% of CH_4 in H_2 by alternating diamond synthesis with an oxidation step [71]. In our experiments, well-faceted diamond was deposited on SiO_2 particles using up to 15.0% CH_4 in H_2 with O_2 addition. Figures 6-13 and 6-14 show SEM micrographs of runs at 120 Watts of microwave power with flow rates 160 sccm of 15.0% CH_4 in H_2 and a variable amount of O_2 addition. Amorphous carbon obtained without O_2 addition is shown in Figure 6-13 (a), and Figure 6-13 (b) shows faceted diamonds grown at [O]/[C] = 1.8. In Figure 6-14 (a), well-faceted cubooctahedral diamonds were obtained at [O]/[C] = 2.2 after 1 hour. The growth rate was about 6 μm/hr. Since the nucleation density was low, no continuous coating was deposited, even after 8 hours at this condition, as shown in Figure 6-14 (b).

The variations in deposited carbon morphology, growth rate and relative nucle-

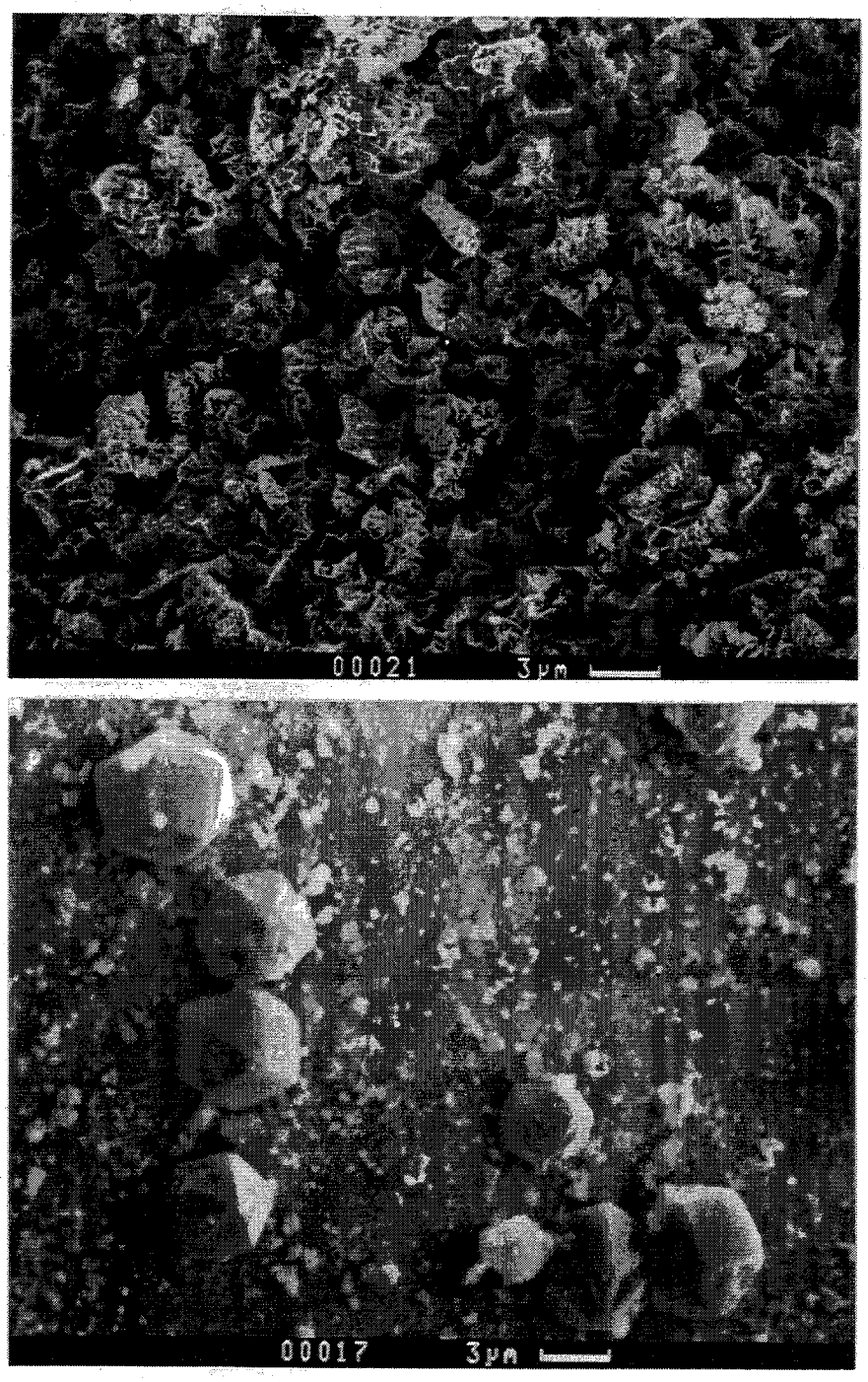

Figure 6-13: SEM micrographs of carbon deposits on SiO_2 particles at 9 Torr, 120 Watts microwave power, with flow rates of 160 sccm of 15.0% CH_4 in H_2 and variable [O]/[C] ratios: (a) 1 hour, [O]/[C] = 0; (b) 1 hour, [O]/[C] = 1.8.

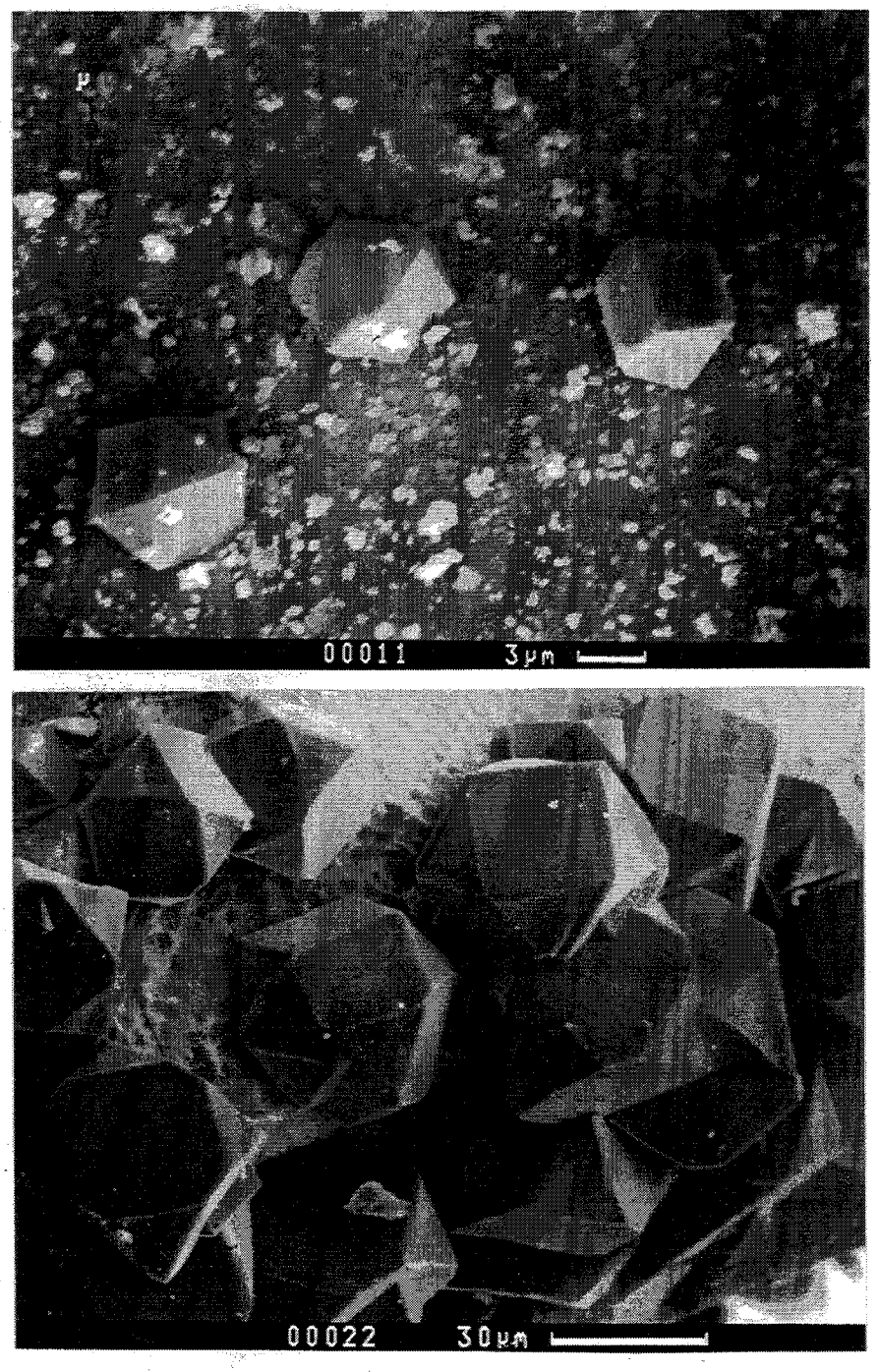

Figure 6-14: SEM micrographs of carbon deposits on SiO_2 particles at 9 Torr, 120 Watts microwave power, with flow rates of 160 sccm of 15.0% CH_4 in H_2 and variable [O]/[C] ratios: (a) 1 hour, [O]/[C] = 2.2; (b) 8 hours, [O]/[C] = 2.2.

ation density with gas composition are shown in Figure 6-15. SiO_2 particles were used, and run conditions were 9 Torr of pressure and 120 Watts of microwave power. Since individual particles within one batch show different nucleation densities, the nucleation density over all particles is averaged and assigned a relative value from very high (vh) to low (l). Without O_2 addition, only ball-like carbon or amorphous carbon was deposited on the seed particles over all ranges of CH_4 in H_2. With a fixed percentage of CH_4 in H_2, increasing the [O]/[C] ratio enhanced the carbon faceting and growth rate until a certain level of [O]/[C] ratio was reached, above which additional O_2 reduced the growth rate and nucleation density. Runs at [O]/[C] of 3 or higher resulted in no deposition. Nucleation densities were highest without O_2 addition, and typically decreased with increasing [O]/[C] ratio. Increasing the percentage of CH_4 at a fixed [O]/[C] ratio generally enhanced the carbon growth rate. No well-faceted diamond was grown at 0.5% CH_4 in H_2 for any [O]/[C] ratio tested. For continuous diamond coatings, high growth rates with relatively high nucleation densities are favorable. In our experiments of up to 10 hours optimal conditions for well-faceted continuous diamond coatings, on both Si and SiO_2 seed particles, were obtained at a pressure of 9 Torr, a microwave power of 120 Watts, and flow rates of 160 sccm of 2.0% CH_4 in H_2 and [O]/[C] = 1.9. Under these conditions, well-faceted continuous diamond coatings covered the entire surface of some of the Si and SiO_2 particles after 8 hours.

Figures 6-16 and 6-17 show the effects of system pressure on the deposited carbon.

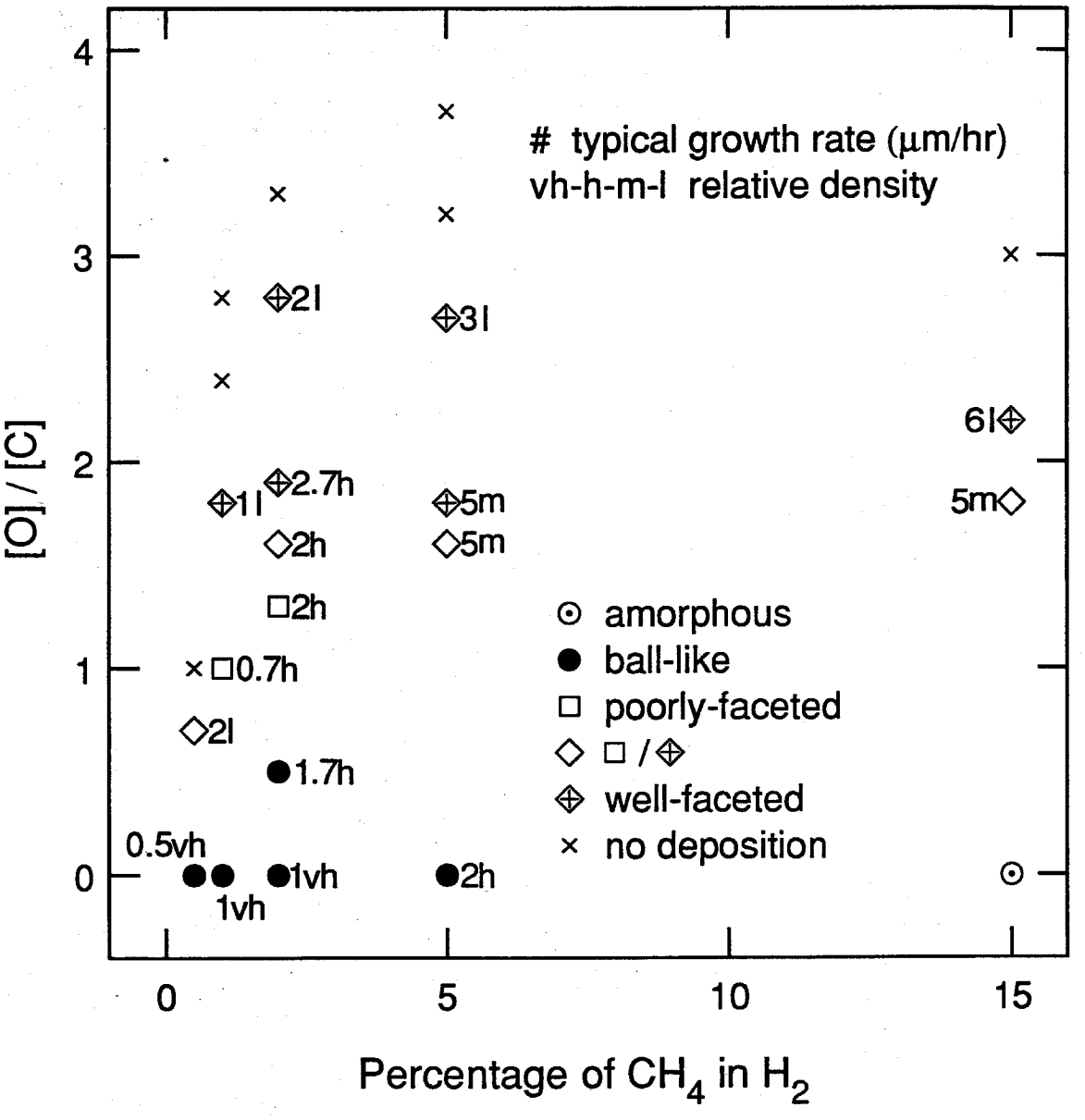

Figure 6-15: The variations in morphology, growth rate and nucleation density with gas composition at 9 Torr, 120 Watts microwave power on SiO_2 particles.

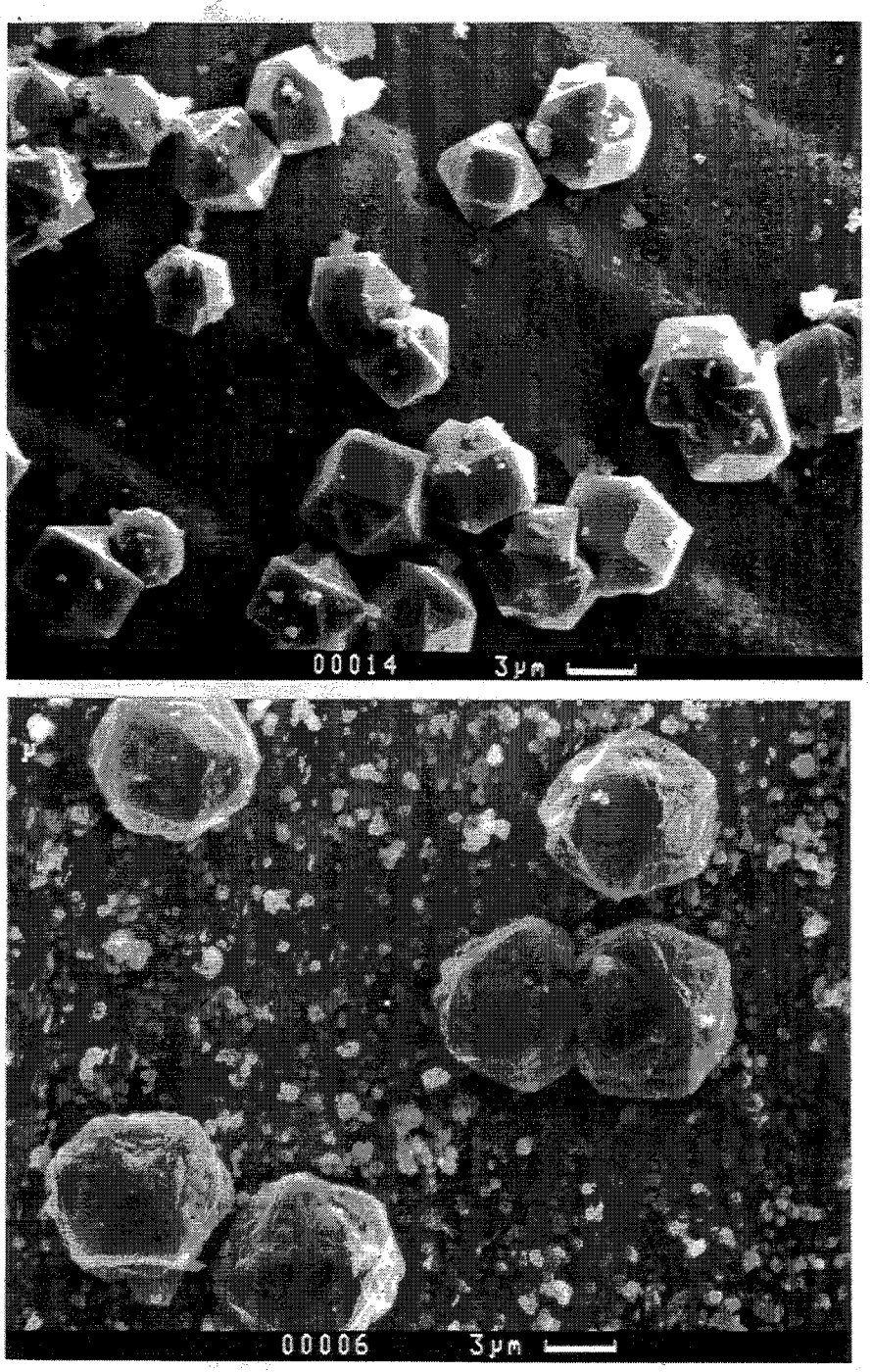

Figure 6-16: SEM micrographs of carbon deposits on SiO_2 particles after 1 hour at 120 Watts microwave power, with flow rates of 160 sccm of 5.0% CH_4 in H_2 and variable [O]/[C] ratios: (a) 9 Torr, [O]/[C] = 1.8; (b) 20 Torr, [O]/[C] = 1.8.

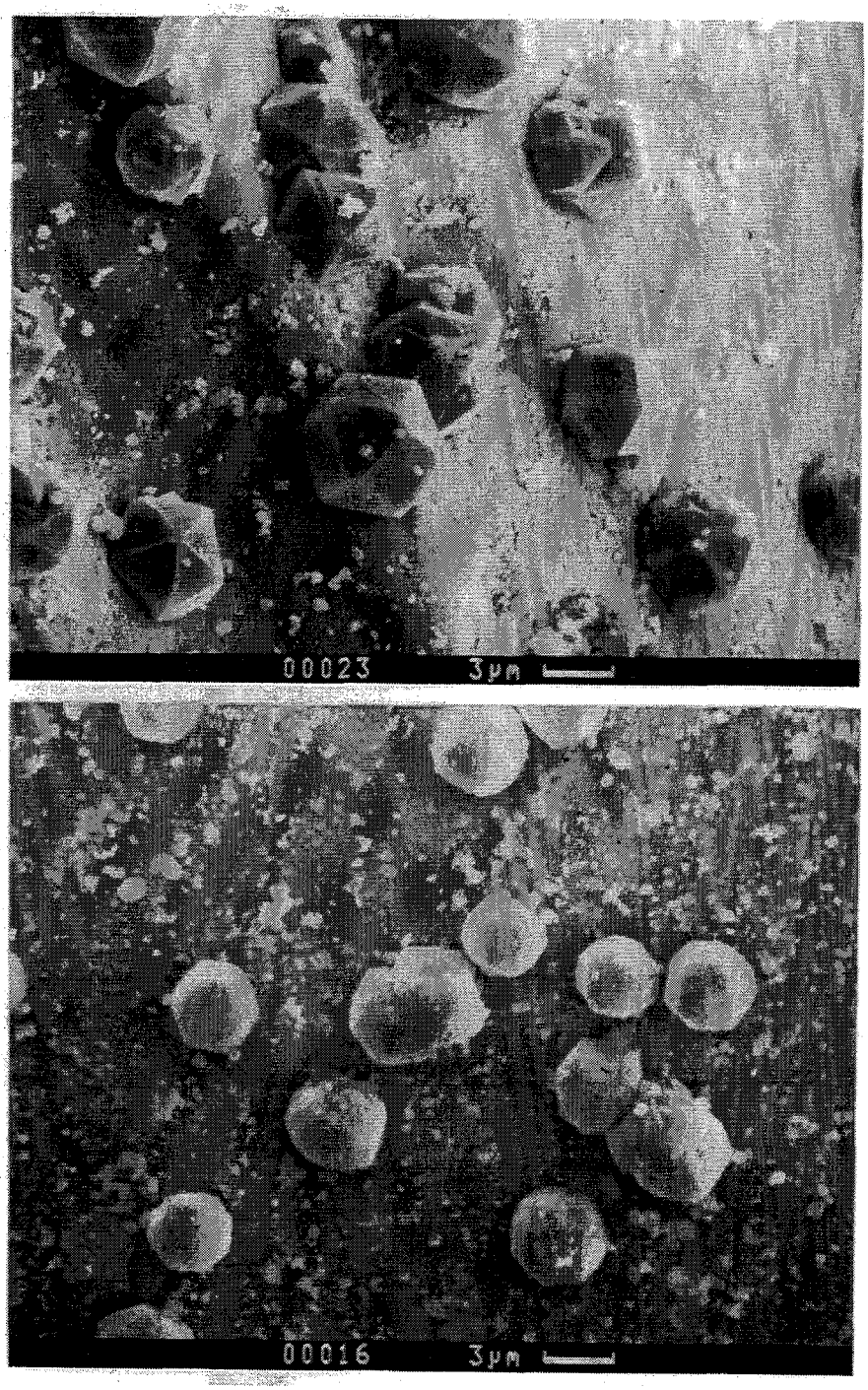

Figure 6-17: SEM micrographs of carbon deposits on SiO_2 particles after 1 hour at 120 Watts microwave power, with flow rates of 160 sccm of 5.0% CH_4 in H_2 and variable [O]/[C] ratios: (a) 20 Torr, [O]/[C] = 2.3; (b) 40 Torr, [O]/[C] = 2.3.

These deposits were obtained on SiO_2 particles after 1 hour at 120 Watts of microwave power with flow rates of 160 sccm of 5.0% CH_4 in H_2 and variable O_2 addition. In Figure 6-16 (a), well-faceted diamond crystals were obtained at a pressure of 9 Torr and [O]/[C] = 1.9. Increasing the pressure to 20 Torr at a fixed [O]/[C] ratio resulted in an increased carbon growth rate but reduced faceting, as shown in Figure 6-16 (b). Figure 6-17 (a) shows enhanced diamond faceting at this pressure by increasing [O]/[C] ratio to 2.3. Figure 6-17 (b) shows ball-like carbon deposits at a pressure of 40 Torr and [O]/[C] = 2.3. At system pressures this high, the plasma became very narrow and unstable. It was extinguished several times in this run by disturbances from the fluidized particles, resulting in a lower growth rate than that in Figure 6-17 (a).

The variations in deposited carbon morphology, growth rate and nucleation density with the [O]/[C] ratio and pressure are shown in Figure 6-18. Experimental conditions were the same as those in Figure 6-16. Because of plasma instability at high pressures, no growth rate is given at 30 Torr and 40 Torr. The growth rate was typically enhanced at higher pressures, but faceting was reduced. The relative nucleation density decreased with increasing [O]/[C] ratio. At most [O]/[C] ratios, changing the pressure had no significant effect on nucleation density, although at [O]/[C] = 3.2, no deposition occurred at 9 Torr while well-faceted diamonds were deposited at 20 Torr. Deposited diamonds were typically cubooctahedral shapes with some decahedral Wulff-polyhedra in most of the well-faceted diamond particles.

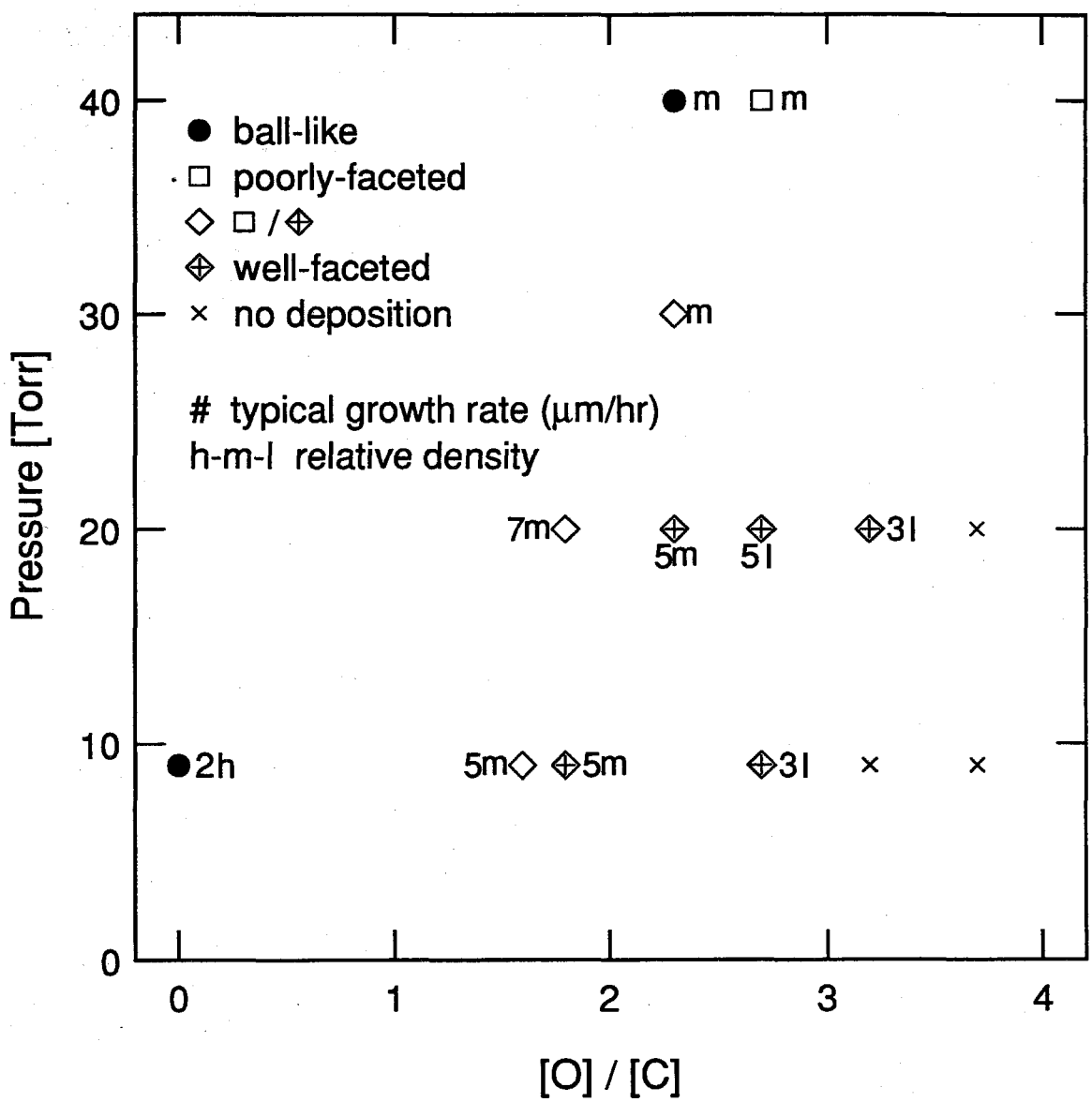

Figure 6-18: The variations in morphology, growth rate and nucleation density with pressure and [O]/[C] ratio at 120 Watts microwave power, with flow rates of 160 sccm of 5.0% CH_4 in H_2 on SiO_2 particles.

Mass spectrometry for stable species was performed without fluidized particles at a pressure of 9 Torr and a microwave power of 120 Watts with flow rates of 160 sccm of 2% CH_4 in H_2. When no O_2 was added to the feed gas mixture, the major stable species in the reactor were H_2, CH_4 and C_2H_2. About 50% of the CH_4 was consumed in the plasma, and C_2H_2 was the major carbon-containing stable product in the plasma.

Addition of O_2 significantly affects the relative amounts of reaction products. H_2, CH_4, C_2H_2, CO and O_2 were the major stable species in the reactor with O_2 addition. (H_2O could not be measured.) Under typical diamond growth conditions with [O]/[C] =1.9, about 80% of CH_4 and more than 95% of O_2 were consumed in the plasma. Although H_2O was not measured, presumably much of the oxygen reacts with hydrogen to form water vapor in the plasma. C_2H_2 production was slightly enhanced as compared to the case of no O_2 addition; CO of about $X_{CO}/X_{H_2} = 0.02$ was found to be a stable product. No CO_2 was observed, indicating that oxidation of CH_4 to CO is more favorable. Weimer and Johnson have reported similar results, in which the CH_4 dissociation created only C_2H_2 and CO [72]. Mass spectrometry with the fluidized particles was also performed, and no significant change was observed.

6.4 Summary

Parametric studies of diamond growth on non-diamond seed particles in a microwave plasma-enhanced fluidized bed reactor have been carried out. Oxygen addition had a

strong influence on growth rate and morphology over the range of gas compositions studied. No diamond deposition was obtained without O_2. Well-faceted diamond with a growth rate of 1–6 μm/hr was observed to grow on Si and SiO_2 seed particles using up to 15.0% CH_4 in H_2 with addition of O_2. Unlike diamond deposition on bulk substrates, no surface pretreatment was necessary for diamond nucleation.

Well-faceted continuous diamond coatings were deposited on seed particles after 8 hours at a pressure of 9 Torr and 120 Watts of microwave power with flow rates of 160 sccm of 2.0% CH_4 in H_2 and 3 sccm of O_2. The micro-Raman spectrum of the deposited diamond crystal confirmed good diamond quality.

Stable species produced in the microwave plasma were measured using mass spectroscopy. Addition of O_2 significantly affected the relative amount of reaction products. Mass spectrometry indicated that C_2H_2 and CO were the major carbon-containing stable products in the plasma under typical diamond growth conditions.

Chapter 7

Summary and Conclusions

In this report, studies of chemical vapor deposition of diamond in low pressure flames and in fluidized beds have been presented. Both experimental and computational studies were performed to gain insight into the factors important for diamond growth in low pressure flames, and an experimental study was performed to investigate the environment necessary to grow diamond on small objects of complex shape in microwave plasma-enhanced fluidized beds.

Diamond films were deposited in low pressure (30–52 Torr) acetylene/oxygen flames using the low pressure flat flame combustion facility developed for growth experiments by Glumac. Initial growth experiments were performed at $\sim$ 50 Torr with high flow rates ($\sim$ 1.0 slm/cm^2) which was previously developed by Glumac to grow continuous diamond films. Good quality diamond films at growth rates of up to 0.7 μm/hr were deposited over areas roughly equal to the area of the burner face (12.6 cm^2).

Further growth experiments were performed at lower pressures (30–40 Torr). By employing lower pressure flames, a much hotter and faster flame could be obtained than $\sim$ 50 Torr flames. At a pressure of 30 Torr, uniform diamond films fully covering $\sim$ 5 cm diameter substrates (an area of 19 cm^2) at growth rates of up to 2.3 μm/hr, were grown using a 4 cm diameter burner. The carbon-conversion efficiency of up to 3.5×10^{-5} was obtained which was comparable to that observed in the atmospheric pressure torch method. The Raman spectrum of the deposited film showed good diamond film quality. The effects of varying substrate temperature, equivalence ratio,

and pressure on diamond growth were examined. In these experiments, the low pressure combustion synthesis method was found to be very effective for growing continuous, uniform diamond films over large areas and could be used to deposit thin diamond coatings for many applications.

To analyze the growth environment in low pressure acetylene/oxygen flames and to seek improved flame conditions for high quality, high growth rate diamond depositions, a numerical modeling study was performed. The STBL code, which is a reacting flow code for axisymmetric stagnation point flows developed by Goodwin, was used in this study. The combustion mechanism employed for gas phase reactions was that of Miller and Melius. The surface mechanism included the Harris diamond growth mechanism, recombination of some radical species, and etching of diamond by OH, O, and O_2.

The model predicts peak flame temperatures above the adiabatic flame temperature, and predicts the chemical environment near the substrate to be far from its equilibrium state. Surface concentrations of H and CH_3, and the ratio of H to CH_3 mole fractions are similar to those observed in hot filament reactors. Unlike in other diamond CVD environments, OH, O, and O_2 exist in an appreciable amount at the surface, and the etch rate of diamond by OH and O may be important in predicting the growth rate of diamond in a low pressure, high flow rate flame environment.

The simplified growth mechanism proposed by Goodwin was employed to analyze the numerical results and to optimize the growth conditions, and an H to CH_3 mole

fraction ratio of 10 at the substrate was used as a standard to identify the conditions for moderate quality diamond growth. The simulations of low pressure (25–30 Torr) acetylene/oxygen flames near diamond growth conditions suggest that increasing the mass flow rate while reducing the pressure is favorable for increasing the growth rate, and high quality diamond can be grown in leaner flames.

The mass spectrometry results showed that the numerical modeling predicted the mole fractions of CO_2, CO, and H_2 at the surface within experimental uncertainty. The observed qualitative trends of the CH_4 and C_2H_2 mole fractions at the substrate were reproduced by the simulations.

In the study of low pressure acetylene/oxygen flames, the numerical analysis indicates that high surface concentrations of H and CH_3, and the ratio of H to CH_3 are important in growing high quality diamond films, as well as in achieving a high growth rate. High radical concentrations at the substrate are readily achieved with high temperature, high speed flames such as acetylene/oxygen flames. In a low pressure flame environment, the model predicts that H and CH_3 have much higher surface concentrations than they would at equilibrium. This suggests that the nonequilibrium chemistry at low pressures may allow other hydrocarbon fuels (such as propylene and propane) to deposit diamond with reasonable growth rates, although diamond is less likely to grow in these flames since their flame temperature and flame speed are significantly less than acetylene/oxygen flames.

To extend the combustion synthesis technique for diamond to fuels other than

acetylene, and to reduce the cost of diamond produced by combustion synthesis, several cheaper alternative hydrocarbon fuels were employed. Growth experiments using MAPP/oxygen, propylene/oxygen, ethylene/oxygen, and propane/oxygen flames at low pressures (50–180 Torr) were carried out in the same low pressure combustion facility used to grow diamonds in acetylene/oxygen flames. Well-faceted diamond films at growth rates of up to 1.0 μm/hr were grown in these alternative fuel flames. The Raman spectrum analysis showed that good quality diamond films were grown in MAPP/oxygen and propylene/oxygen flames. The carbon-conversion efficiencies of about 6×10^{-6} were obtained for MAPP and propylene which were about one-third of the value for acetylene. An economic comparison study showed that switching from acetylene to propylene may be able to lower the fuel cost per unit mass of diamond by roughly a factor of three.

In propane/oxygen flames only a low quality diamond film was grown in these preliminary experiments. However, since propane is much cheaper and safer than acetylene, is available in large quantities, and is easily stored in liquid form, propane could be used as the fuel for combustion synthesis of diamond coatings for applications where the diamond quality is not as important, such as hard coatings on cutting tools.

The results indicate that nonequilibrium flame chemistry is important in the low pressure combustion environment. This suggests that still other fuels may be worth considering for diamond growth at low pressures. Further studies employing alternative fuels other than acetylene could potentially further reduce the cost of diamond

produced by combustion synthesis, and may well make the combustion method competitive with arcjet, microwave, and hot filament methods for many applications.

To analyze the experimental results of diamond growth in low pressure alternative fuel (MAPP, propylene, ethylene, and propane) flames, a numerical modeling study was performed. For this study, the Dagaut–Cathonnet–Boettner mechanism was employed as the gas phase mechanism. The model predicts the chemical environment at the substrate to be far from its equilibrium state. Although the values are slightly lower than for acetylene/oxygen flames, the model predicts these alternative fuel flames having high enough H and CH_3 concentrations at the substrate to grow diamond at a reasonable growth rate. Mass spectrometry experiments showed that the model employing the Dagaut–Cathonnet–Boettner mechanism correctly predicted the mole fractions of CO and CO_2 at the substrate and slightly overpredicted the mole fraction of H_2.

Experiments were performed using microwave plasma-enhanced fluidized beds, to grow continuous, conformal diamond coatings on small, three-dimensional objects. A $CH_4/H_2/O_2$ mixture was used as the fluidizing gas as well as the carbon source. Studies were carried out to map the parameter space leading to diamond growth and to determine the relationship between gas composition and diamond growth rate. The effects of varying gas composition and pressure on deposited carbon morphology, growth rate, and nucleation density were examined in these experiments.

Oxygen addition had a strong influence on growth rate and morphology over the

range of gas compositions studied. No diamond deposition was obtained without O_2. Well-faceted diamond at a growth rate of up to 6 μm/hr was observed to grow on 0.25–0.7 mm diameter silicon and SiO_2 seed particles using up to 15.0% CH_4 in H_2 with addition of O_2. Unlike diamond deposition on bulk substrates, no surface pretreatment was necessary for diamond nucleation. Well-faceted continuous diamond coatings were deposited on seed particles after 8 hours at a pressure of 9 Torr and 120 Watts of microwave power with flow rates of 160 sccm of 2.0% CH_4 in H_2 and 3 sccm of O_2. The micro-Raman spectrum of the deposited diamond crystal confirmed good diamond quality.

Stable species produced in the microwave plasma were measured using mass spectrometry. Addition of O_2 significantly affected the relative amount of reaction products. Mass spectrometry indicates that C_2H_2 and CO are the major carbon-containing stable products in the plasma under typical diamond growth conditions. These results show that a plasma-enhanced fluidized bed reactor may be an effective means for mass production of diamond and the deposition of diamond coatings on small objects of complex shape.

Appendix A

Gas Phase Mechanism

A.1 Miller–Melius Mechanism

The gas phase chemistry mechanism for acetylene/oxygen flames is that of Miller and Melius [35]. It consists of 218 reactions among 49 species. The reaction rates are given in the Arrhenius form:

$$k = A\,T^n\,exp(-E_a/RT) \tag{A.1}$$

The unit for A is $cm^3/mol/sec$, and E_a is given in cal/mol. The following 49 species are considered in the model:

Monatomic species: H, O, C

Homonuclear diatomics: H_2, O_2, C_2

H-O compounds: OH, HO_2, H_2O, H_2O_2

C-O compounds: CO, CO_2, C_2O

C_1 hydrocarbons: CH, CH_2, CH_2^1, CH_3, CH_4

C_2 hydrocarbons: C_2H, C_2H_2, C_2H_3, C_2H_4, C_2H_5, C_2H_6

C_3 hydrocarbons: C_3H_2, H_2CCCH, C_3H_4, C_3H_4P

C_4 hydrocarbons: C_4H_2, H_2CCCCH, $HCCHCCH$, CH_2CHCCH, $CH_2CHCHCH_2$, $CH_2CHCHCH$, CH_2CHCCH_2

C_5 hydrocarbons: C_5H_2, C_5H_3

C_6 hydrocarbons: C_6H_2, C_6H_5, C_6H_6

H-C-O compounds: HCO, HCCO, HCCOH, CH_2O, CH_3O, CH_2OH, C_6H_5O,

H_2C_4O

No.	Reaction	A	n	E_a
1.	$H_2 + O_2 \rightleftharpoons 2OH$	0.170E+14	0.000	47780.000
2.	$OH + H_2 \rightleftharpoons H_2O + H$	0.117E+10	1.300	3626.000
3.	$O + OH \rightleftharpoons O_2 + H$	0.400E+15	-0.500	0.000
4.	$O + H_2 \rightleftharpoons OH + H$	0.506E+05	2.670	6290.000
5.	$H + O_2 + M \rightleftharpoons HO_2 + M$	0.361E+18	-0.720	0.000
	3rd body efficiencies: H_2O: 18.6, CO_2: 4.2, H_2: 2.86, CO: 2.11			
6.	$OH + HO_2 \rightleftharpoons H_2O + O_2$	0.750E+13	0.000	0.000
7.	$H + HO_2 \rightleftharpoons 2OH$	0.140E+15	0.000	1073.000
8.	$O + HO_2 \rightleftharpoons O_2 + OH$	0.140E+14	0.000	1073.000
9.	$2OH \rightleftharpoons O + H_2O$	0.600E+09	1.300	0.000
10.	$H + H + M \rightleftharpoons H_2 + M$	0.100E+19	-1.000	0.000
	3rd body efficiencies: H_2O: 0.0, H_2: 0.0, CO_2: 0.0			
11.	$H + H + H_2 \rightleftharpoons H_2 + H_2$	0.920E+17	-0.600	0.000
12.	$H + H + H_2O \rightleftharpoons H_2 + H_2O$	0.600E+20	-1.250	0.000
13.	$H + H + CO_2 \rightleftharpoons H_2 + CO_2$	0.549E+21	-2.000	0.000
14.	$H + OH + M \rightleftharpoons H_2O + M$	0.160E+23	-2.000	0.000
	3rd body efficiency: H_2O: 5			
15.	$H + O + M \rightleftharpoons OH + M$	0.620E+17	-0.600	0.000
	3rd body efficiency: H_2O: 5			
16.	$O + O + M \rightleftharpoons O_2 + M$	0.189E+14	0.000	-1788.000
17.	$H + HO_2 \rightleftharpoons H_2 + O_2$	0.125E+14	0.000	0.000
18.	$HO_2 + HO_2 \rightleftharpoons H_2O_2 + O_2$	0.200E+13	0.000	0.000
19.	$H_2O_2 + M \rightleftharpoons OH + OH + M$	0.130E+18	0.000	45500.000
20.	$H_2O_2 + H \rightleftharpoons HO_2 + H_2$	0.160E+13	0.000	3800.000
21.	$H_2O_2 + OH \rightleftharpoons H_2O + HO_2$	0.100E+14	0.000	1800.000
22.	$CH_3 + CH_3(+M) \rightleftharpoons C_2H_6(+M)$	9.030E+16	-1.200	654.000
	Low Pressure limit: 3.180E41 -7.000 2762.0			
	Troe: 0.604 6927. 132.			
	3rd body efficiencies: H_2: 2, CO: 2, CO_2: 3, H_2O: 5			
23.	$CH_3 + H(+M) \rightleftharpoons CH_4(+M)$	6.00E16	-1.000	0.000
	Low Pressure limit: 8.0E26 -3.0 0.0			
	SRI: 0.45 797. 979.			
	3rd body efficiencies: H_2: 2, CO: 2, CO_2: 3, H_2O: 5			
24.	$CH_4 + O_2 \rightleftharpoons CH_3 + HO_2$	0.790E+14	0.000	56000.000

Table A.1: Reactions 1–24 in the Miller–Melius mechanism.

No.	Reaction	A	n	E_a
25.	$CH_4 + H \rightleftharpoons CH_3 + H_2$	0.220E+05	3.000	8750.000
26.	$CH_4 + OH \rightleftharpoons CH_3 + H_2O$	0.160E+07	2.100	2460.000
27.	$CH_4 + O \rightleftharpoons CH_3 + OH$	1.020E+09	1.500	8604.000
28.	$CH_4 + HO_2 \rightleftharpoons CH_3 + H_2O_2$	0.180E+12	0.000	18700.000
29.	$CH_3 + HO_2 \rightleftharpoons CH_3O + OH$	0.200E+14	0.000	0.000
30.	$CH_3 + O \rightleftharpoons CH_2O + H$	8.000E+13	0.000	0.000
31.	$CH_3 + O_2 \rightleftharpoons CH_3O + O$	0.205E+19	-1.570	29229.000
32.	$CH_2OH + H \rightleftharpoons CH_3 + OH$	0.100E+15	0.000	0.000
33.	$CH_3O + H \rightleftharpoons CH_3 + OH$	0.100E+15	0.000	0.000
34.	$CH_3 + OH \rightleftharpoons CH_2 + H_2O$	0.750E+07	2.000	5000.000
35.	$CH_3 + H \rightleftharpoons CH_2 + H_2$	0.900E+14	0.000	15100.000
36.	$CH_3O + M \rightleftharpoons CH_2O + H + M$	0.100E+15	0.000	25000.000
37.	$CH_2OH + M \rightleftharpoons CH_2O + H + M$	0.100E+15	0.000	25000.000
38.	$CH_3O + H \rightleftharpoons CH_2O + H_2$	0.200E+14	0.000	0.000
39.	$CH_2OH + H \rightleftharpoons CH_2O + H_2$	0.200E+14	0.000	0.000
40.	$CH_3O + OH \rightleftharpoons CH_2O + H_2O$	0.100E+14	0.000	0.000
41.	$CH_2OH + OH \rightleftharpoons CH_2O + H_2O$	0.100E+14	0.000	0.000
42.	$CH_3O + O \rightleftharpoons CH_2O + OH$	0.100E+14	0.000	0.000
43.	$CH_2OH + O \rightleftharpoons CH_2O + OH$	0.100E+14	0.000	0.000
44.	$CH_3O + O_2 \rightleftharpoons CH_2O + HO_2$	0.630E+11	0.000	2600.000
45.	$CH_2OH + O_2 \rightleftharpoons CH_2O + HO_2$	0.148E+14	0.000	1500.000
46.	$CH_2 + H \rightleftharpoons CH + H_2$	0.100E+19	-1.560	0.000
47.	$CH_2 + OH \rightleftharpoons CH + H_2O$	0.113E+08	2.000	3000.000
48.	$CH_2 + OH \rightleftharpoons CH_2O + H$	0.250E+14	0.000	0.000
49.	$CH + O_2 \rightleftharpoons HCO + O$	0.330E+14	0.000	0.000
50.	$CH + O \rightleftharpoons CO + H$	0.570E+14	0.000	0.000
51.	$CH + OH \rightleftharpoons HCO + H$	0.300E+14	0.000	0.000
52.	$CH + OH \rightleftharpoons C + H_2O$	4.000E+07	2.000	3000.000
53.	$CH + CO_2 \rightleftharpoons HCO + CO$	0.340E+13	0.000	690.000
54.	$CH + H \rightleftharpoons C + H_2$	0.150E+15	0.000	0.000
55.	$CH + H_2O \rightleftharpoons CH_2O + H$	1.170E+15	-0.750	0.000
56.	$CH + CH_2O \rightleftharpoons CH_2CO + H$	0.946E+14	0.000	-515.000
57.	$CH + C_2H_2 \rightleftharpoons C_3H_2 + H$	0.100E+15	0.000	0.000
58.	$CH + CH_2 \rightleftharpoons C_2H_2 + H$	0.400E+14	0.000	0.000
59.	$CH + CH_3 \rightleftharpoons C_2H_3 + H$	0.300E+14	0.000	0.000

Table A.2: Reactions 25–59 in the Miller–Melius mechanism.

No.	Reaction	A	n	E_a
60.	$CH + CH_4 \rightleftharpoons C_2H_4 + H$	0.600E+14	0.000	0.000
61.	$C + O_2 \rightleftharpoons CO + O$	0.200E+14	0.000	0.000
62.	$C + OH \rightleftharpoons CO + H$	0.500E+14	0.000	0.000
63.	$C + CH_3 \rightleftharpoons C_2H_2 + H$	0.500E+14	0.000	0.000
64.	$C + CH_2 \rightleftharpoons C_2H + H$	0.500E+14	0.000	0.000
65.	$CH_2 + CO_2 \rightleftharpoons CH_2O + CO$	0.110E+12	0.000	1000.000
66.	$CH_2 + O \rightleftharpoons CO + H + H$	0.500E+14	0.000	0.000
67.	$CH_2 + O \rightleftharpoons CO + H_2$	0.300E+14	0.000	0.000
68.	$CH_2 + O_2 \rightleftharpoons CO_2 + H + H$	0.160E+13	0.000	1000.000
69.	$CH_2 + O_2 \rightleftharpoons CH_2O + O$	0.500E+14	0.000	9000.000
70.	$CH_2 + O_2 \rightleftharpoons CO_2 + H_2$	0.690E+12	0.000	500.000
71.	$CH_2 + O_2 \rightleftharpoons CO + H_2O$	0.190E+11	0.000	-1000.000
72.	$CH_2 + O_2 \rightleftharpoons CO + OH + H$	0.860E+11	0.000	-500.000
73.	$CH_2 + O_2 \rightleftharpoons HCO + OH$	0.430E+11	0.000	-500.000
74.	$CH_2O + OH \rightleftharpoons HCO + H_2O$	0.343E+10	1.180	-447.000
75.	$CH_2O + H \rightleftharpoons HCO + H_2$	0.219E+09	1.770	3000.000
76.	$CH_2O + M \rightleftharpoons HCO + H + M$	0.331E+17	0.000	81000.000
77.	$CH_2O + O \rightleftharpoons HCO + OH$	0.180E+14	0.000	3080.000
78.	$HCO + OH \rightleftharpoons H_2O + CO$	0.100E+15	0.000	0.000
79.	$HCO + M \rightleftharpoons H + CO + M$	0.250E+15	0.000	16802.000
	3rd body efficiencies: CO: 1.87, H_2: 1.87, CH_4: 2.81, CO_2: 3., H_2O: 5.			
80.	$HCO + H \rightleftharpoons CO + H_2$	0.119E+14	0.250	0.000
81.	$HCO + O \rightleftharpoons CO + OH$	0.300E+14	0.000	0.000
82.	$HCO + O \rightleftharpoons CO_2 + H$	0.300E+14	0.000	0.000
83.	$HCO + O_2 \rightleftharpoons HO_2 + CO$	0.330E+14	-0.400	0.000
84.	$CO + O + M \rightleftharpoons CO_2 + M$	0.617E+15	0.000	3000.000
85.	$CO + OH \rightleftharpoons CO_2 + H$	0.151E+08	1.300	-758.000
86.	$CO + O_2 \rightleftharpoons CO_2 + O$	2.53E+12	0.000	47688.000
87.	$HO_2 + CO \rightleftharpoons CO_2 + OH$	0.580E+14	0.000	22934.000
88.	$C_2H_6 + CH_3 \rightleftharpoons C_2H_5 + CH_4$	0.550E+00	4.000	8300.000
89.	$C_2H_6 + H \rightleftharpoons C_2H_5 + H_2$	0.540E+03	3.500	5210.000
90.	$C_2H_6 + O \rightleftharpoons C_2H_5 + OH$	0.300E+08	2.000	5115.000
91.	$C_2H_6 + OH \rightleftharpoons C_2H_5 + H_2O$	0.870E+10	1.050	1810.000
92.	$C_2H_4 + H \rightleftharpoons C_2H_3 + H_2$	0.110E+15	0.000	8500.000
93.	$C_2H_4 + O \rightleftharpoons CH_3 + HCO$	0.160E+10	1.200	746.000
94.	$C_2H_4 + OH \rightleftharpoons C_2H_3 + H_2O$	0.202E+14	0.000	5955.000

Table A.3: Reactions 60–94 in the Miller–Melius mechanism.

No.	Reaction	A	n	E_a
95.	$CH_2 + CH_3 \rightleftharpoons C_2H_4 + H$	0.400E+14	0.000	0.000
96.	$H + C_2H_4(+M) \rightleftharpoons C_2H_5(+M)$	0.221E+14	0.000	2066.000
	Low Pressure limit: 6.369E27 -2.76 -54.0			
	3rd body efficiencies: H_2: 2, CO: 2, CO_2: 3, H_2O: 5			
97.	$C_2H_5 + H \rightleftharpoons CH_3 + CH_3$	1.000E+14	0.000	0.000
98.	$C_2H_5 + O_2 \rightleftharpoons C_2H_4 + HO_2$	0.843E+12	0.000	3875.000
99.	$C_2H_2 + O \rightleftharpoons CH_2 + CO$	0.102E+08	2.000	1900.000
100.	$C_2H_2 + O \rightleftharpoons HCCO + H$	0.102E+08	2.000	1900.000
101.	$H_2 + C_2H \rightleftharpoons C_2H_2 + H$	0.409E+06	2.390	864.300
102.	$H + C_2H_2(+M) \rightleftharpoons C_2H_3(+M)$	0.554E+13	0.000	2410.000
	Low Pressure limit: 2.67E27 -3.5 2410.			
	3rd body efficiencies: H_2: 2, CO: 2, CO_2: 3, H_2O: 5			
103.	$C_2H_3 + H \rightleftharpoons C_2H_2 + H_2$	0.400E+14	0.000	0.000
104.	$C_2H_3 + O \rightleftharpoons CH_2CO + H$	0.300E+14	0.000	0.000
105.	$C_2H_3 + O_2 \rightleftharpoons CH_2O + HCO$	0.400E+13	0.000	-250.000
106.	$C_2H_3 + OH \rightleftharpoons C_2H_2 + H_2O$	2.000E+13	0.000	0.000
107.	$C_2H_3 + CH_2 \rightleftharpoons C_3H_4 + H$	3.000E+13	0.000	0.000
108.	$C_2H_3 + C_2H \rightleftharpoons C_2H_2 + C_2H_2$	0.300E+14	0.000	0.000
109.	$C_2H_3 + C_2H_3 \rightleftharpoons CH_2CHCCH_2 + H$	4.000E+13	0.000	0.000
110.	$C_2H_3 + CH \rightleftharpoons CH_2 + C_2H_2$	0.500E+14	0.000	0.000
111.	$OH + C_2H_2 \rightleftharpoons C_2H + H_2O$	3.370E+07	2.000	14000.000
112.	$OH + C_2H_2 \rightleftharpoons HCCOH + H$	5.040E+05	2.300	13500.000
113.	$OH + C_2H_2 \rightleftharpoons CH_2CO + H$	2.180E-04	4.500	-1000.000
114.	$OH + C_2H_2 \rightleftharpoons CH_3 + CO$	4.830E-04	4.000	-2000.000
115.	$HCCOH + H \rightleftharpoons CH_2CO + H$	0.100E+14	0.000	0.000
116.	$C_2H_2 + O \rightleftharpoons C_2H + OH$	0.316E+16	-0.600	15000.000
117.	$CH_2CO + O \rightleftharpoons CO_2 + CH_2$	0.175E+13	0.000	1350.000
118.	$CH_2CO + H \rightleftharpoons CH_3 + CO$	0.113E+14	0.000	3428.000
119.	$CH_2CO + H \rightleftharpoons HCCO + H_2$	0.500E+14	0.000	8000.000
120.	$CH_2CO + O \rightleftharpoons HCCO + OH$	0.100E+14	0.000	8000.000
121.	$CH_2CO + OH \rightleftharpoons HCCO + H_2O$	0.750E+13	0.000	2000.000
122.	$CH_2CO(+M) \rightleftharpoons CH_2 + CO(+M)$	0.300E+15	0.000	70980.000
	Low Pressure limit: 3.6E15 0.0 59270.			
123.	$C_2H + O_2 \rightleftharpoons CO + CO + H$	3.520E+13	0.000	0.000
124.	$C_2H + C_2H_2 \rightleftharpoons C_4H_2 + H$	0.300E+14	0.000	0.000
125.	$HCCO + C_2H_2 \rightleftharpoons H_2CCCH + CO$	1.000E+11	0.000	3000.000
126.	$H + HCCO \rightleftharpoons CH_2^1 + CO$	0.100E+15	0.000	0.000

Table A.4: Reactions 95–126 in the Miller–Melius mechanism.

No.	Reaction	A	n	E_a
127.	$O + HCCO \rightleftharpoons H + CO + CO$	0.100E+15	0.000	0.000
128.	$HCCO + O_2 \rightleftharpoons CO_2 + CO + H$	1.400E+09	1.000	0.000
129.	$CH + HCCO \rightleftharpoons C_2H_2 + CO$	0.500E+14	0.000	0.000
130.	$HCCO + HCCO \rightleftharpoons C_2H_2 + CO + CO$	0.100E+14	0.000	0.000
131.	$HCCO + OH \rightleftharpoons C_2O + H_2O$	3.000E+13	0.000	0.000
132.	$C_2O + H \rightleftharpoons CH + CO$	5.000E+13	0.000	0.000
133.	$C_2O + O \rightleftharpoons CO + CO$	5.000E+13	0.000	0.000
134.	$C_2O + OH \rightleftharpoons CO + CO + H$	2.000E+13	0.000	0.000
135.	$C_2O + O_2 \rightleftharpoons CO + CO + O$	2.000E+13	0.000	0.000
136.	$CH_2^1 + M \rightleftharpoons CH_2 + M$	0.100E+14	0.000	0.000
	3rd body efficiencies: H: 0.0, H_2O: 0.0, C_2H_2: 0.0			
137.	$CH_2^1 + CH_4 \rightleftharpoons CH_3 + CH_3$	0.400E+14	0.000	0.000
138.	$CH_2^1 + C_2H_6 \rightleftharpoons CH_3 + C_2H_5$	0.120E+15	0.000	0.000
139.	$CH_2^1 + O_2 \rightleftharpoons CO + OH + H$	7.000E+13	0.000	0.000
140.	$CH_2^1 + H_2 \rightleftharpoons CH_3 + H$	0.700E+14	0.000	0.000
141.	$CH_2^1 + H_2O \rightleftharpoons CH_3 + OH$	1.000E+14	0.000	0.000
142.	$CH_2^1 + H_2O \rightleftharpoons CH_2 + H_2O$	3.000E+13	0.000	0.000
143.	$CH_2^1 + C_2H_2 \rightleftharpoons H_2CCCH + H$	1.800E+14	0.000	0.000
144.	$CH_2^1 + C_2H_2 \rightleftharpoons CH_2 + C_2H_2$	4.000E+13	0.000	0.000
145.	$CH_2^1 + H \rightleftharpoons CH_2 + H$	0.200E+15	0.000	0.000
146.	$CH_2^1 + O \rightleftharpoons CO + H + H$	3.000E+13	0.000	0.000
147.	$CH_2^1 + OH \rightleftharpoons CH_2O + H$	3.000E+13	0.000	0.000
148.	$CH_2^1 + H \rightleftharpoons CH + H_2$	3.000E+13	0.000	0.000
149.	$CH_2^1 + CO_2 \rightleftharpoons CH_2O + CO$	3.000E+12	0.000	0.000
150.	$CH_2^1 + CH_3 \rightleftharpoons C_2H_4 + H$	2.000E+13	0.000	0.000
151.	$CH_2^1 + CH_2CO \rightleftharpoons C_2H_4 + CO$	1.600E+14	0.000	0.000
152.	$C_2H + O \rightleftharpoons CH + CO$	0.500E+14	0.000	0.000
153.	$C_2H + OH \rightleftharpoons HCCO + H$	0.200E+14	0.000	0.000
154.	$C_2H + OH \rightleftharpoons C_2 + H_2O$	4.000E+07	2.000	8000.000
155.	$C_2 + H_2 \rightleftharpoons C_2H + H$	4.000E+05	2.400	1000.000
156.	$C_2 + O_2 \rightleftharpoons CO + CO$	5.000E+13	0.000	0.000
157.	$C_2 + OH \rightleftharpoons C_2O + H$	5.000E+13	0.000	0.000
158.	$CH_2 + CH_2 \rightleftharpoons C_2H_2 + H + H$	0.400E+14	0.000	0.000
159.	$CH_2 + HCCO \rightleftharpoons C_2H_3 + CO$	0.300E+14	0.000	0.000
160.	$CH_2 + C_2H_2 \rightleftharpoons H_2CCCH + H$	0.120E+14	0.000	6600.000
161.	$C_4H_2 + OH \rightleftharpoons H_2C_4O + H$	0.666E+13	0.000	-410.000
162.	$C_3H_2 + O_2 \rightleftharpoons HCCO + CO + H$	5.000E+13	0.000	0.000

Table A.5: Reactions 127–162 in the Miller–Melius mechanism.

No.	Reaction	A	n	E_a
163.	$C_3H_2 + OH \rightleftharpoons C_2H_2 + HCO$	5.000E+13	0.000	0.000
164.	$C_3H_2 + CH_2 \rightleftharpoons H_2CCCCH + H$	3.000E+13	0.000	0.000
165.	$H_2C_4O + H \rightleftharpoons C_2H_2 + HCCO$	5.000E+13	0.000	3000.000
166.	$H_2C_4O + OH \rightleftharpoons CH_2CO + HCCO$	1.000E+07	2.000	2000.000
167.	$H_2CCCH + O_2 \rightleftharpoons CH_2CO + HCO$	0.300E+11	0.000	2868.000
168.	$H_2CCCH + O \rightleftharpoons CH_2O + C_2H$	0.200E+14	0.000	0.000
169.	$H_2CCCH + H \rightleftharpoons C_3H_2 + H_2$	5.000E+13	0.000	3000.000
170.	$H_2CCCH + OH \rightleftharpoons C_3H_2 + H_2O$	0.200E+14	0.000	0.000
171.	$H_2CCCH + CH_2 \rightleftharpoons CH_2CHCCH + H$	4.000E+13	0.000	0.000
172.	$H_2CCCH + CH \rightleftharpoons HCCHCCH + H$	7.000E+13	0.000	0.000
173.	$H_2CCCH + CH \rightleftharpoons H_2CCCCH + H$	7.000E+13	0.000	0.000
174.	$CH_2CHCCH + OH \rightleftharpoons HCCHCCH + H_2O$	7.500E+06	2.000	5000.000
175.	$CH_2CHCCH + H \rightleftharpoons HCCHCCH + H_2$	2.000E+07	2.000	15000.000
176.	$CH_2CHCCH + OH \rightleftharpoons H_2CCCCH + H_2O$	1.000E+07	2.000	2000.000
177.	$H + HCCHCCH \rightleftharpoons H_2CCCCH + H$	1.000E+14	0.000	0.000
178.	$H_2CCCCH + O_2 \rightleftharpoons CH_2CO + HCCO$	1.000E+12	0.000	0.000
179.	$H_2CCCCH + OH \rightleftharpoons C_4H_2 + H_2O$	3.000E+13	0.000	0.000
180.	$H_2CCCCH + O \rightleftharpoons CH_2CO + C_2H$	2.000E+13	0.000	0.000
181.	$H_2CCCCH + O \rightleftharpoons H_2C_4O + H$	2.000E+13	0.000	0.000
182.	$H_2CCCCH + H \rightleftharpoons C_4H_2 + H_2$	5.000E+13	0.000	0.000
183.	$H_2CCCCH + CH_2 \rightleftharpoons C_3H_4 + C_2H$	2.000E+13	0.000	0.000
184.	$CH_2CHCCH + H \rightleftharpoons H_2CCCCH + H_2$	3.000E+07	2.000	5000.000
185.	$CH_2CHCHCH + OH \rightleftharpoons CH_2CHCCH + H_2O$	2.000E+07	2.000	1000.000
186.	$CH_2CHCHCH + H \rightleftharpoons CH_2CHCCH + H_2$	3.000E+07	2.000	1000.000
187.	$C_6H_6 + H \rightleftharpoons C_6H_5 + H_2$	3.000E+07	2.000	5000.000
188.	$C_6H_6 + OH \rightleftharpoons C_6H_5 + H_2O$	7.500E+06	2.000	5000.000
189.	$C_2H_3 + C_2H_2 \rightleftharpoons CH_2CHCCH + H$	2.000E+12	0.000	5000.000
190.	$C_2H_2 + CH_2CHCHCH \rightleftharpoons C_6H_6 + H$	2.800E+03	2.900	1400.000
191.	$HCCHCCH + C_2H_2 \rightleftharpoons C_6H_5$	2.800E+03	2.900	1400.000
192.	$C_3H_4 + H \rightleftharpoons H_2CCCH + H_2$	5.000E+07	2.000	5000.000
193.	$C_3H_4 + OH \rightleftharpoons H_2CCCH + H_2O$	2.000E+07	2.000	1000.000
194.	$C_3H_4P + H \rightleftharpoons H_2CCCH + H_2$	5.000E+07	2.000	5000.000
195.	$C_3H_4P + H \rightleftharpoons CH_3 + C_2H_2$	1.000E+14	0.000	4000.000
196.	$C_3H_4P + OH \rightleftharpoons H_2CCCH + H_2O$	2.000E+07	2.000	1000.000
197.	$C_6H_5 + OH \rightleftharpoons C_6H_5O + H$	5.000E+13	0.000	0.000
198.	$C_6H_5 + O_2 \rightleftharpoons C_6H_5O + O$	1.000E+13	0.000	0.000
199.	$CH_2 + C_4H_2 \rightleftharpoons C_5H_3 + H$	0.130E+14	0.000	4326.000

Table A.6: Reactions 163–199 in the Miller–Melius mechanism.

No.	Reaction	A	n	E_a
200.	$CH + C_4H_2 \rightleftharpoons C_5H_2 + H$	0.100E+15	0.0	0.0
201.	$CH_2^1 + C_4H_2 \rightleftharpoons C_5H_3 + H$	0.300E+14	0.0	0.0
202.	$C_4H_2 + O \rightleftharpoons C_3H_2 + CO$	0.120E+13	0.0	0.0
203.	$C_4H_2 + C_2H \rightleftharpoons C_6H_2 + H$	0.400E+14	0.0	0.0
204.	$C_2H_2 + O_2 \rightleftharpoons HCCO + OH$	0.200E+09	1.5	30100.0
205.	$C_2H_2 + M \rightleftharpoons C_2H + H + M$	0.420E+17	0.0	107000.0
206.	$C_2H_4 + M \rightleftharpoons C_2H_2 + H_2 + M$	0.150E+16	0.0	55800.0
207.	$C_2H_4 + M \rightleftharpoons C_2H_3 + H + M$	0.140E+17	0.0	82360.0
208.	$C_2H_3 + C_2H_4 \rightleftharpoons CH_2CHCHCH_2 + H$	3.000E+12	0.0	1000.0
209.	$CH_2CHCHCH_2 + H \rightleftharpoons CH_2CHCHCH + H_2$	3.000E+07	2.0	13000.0
210.	$CH_2CHCHCH_2 + H \rightleftharpoons CH_2CHCCH_2 + H_2$	3.000E+07	2.0	6000.0
211.	$CH_2CHCHCH_2 + OH \rightleftharpoons CH_2CHCHCH + H_2O$	2.000E+07	2.0	5000.0
212.	$CH_2CHCHCH_2 + OH \rightleftharpoons CH_2CHCCH_2 + H_2O$	2.000E+07	2.0	2000.0
213.	$CH_2CHCHCH + H \rightleftharpoons CH_2CHCCH_2 + H$	1.000E+14	0.0	0.0
214.	$H_2CCCCH(+M) \rightleftharpoons C_4H_2 + H(+M)$	1.000E+14	0.0	55000.0
	Low Pressure limit: 2.0E15 0.0 48000.			
215.	$HCCHCCH(+M) \rightleftharpoons C_4H_2 + H(+M)$	1.000E+14	0.0	36000.0
	Low Pressure limit: 1.0E14 0.0 30000.			
216.	$CH_2CHCCH_2(+M) \rightleftharpoons CH_2CHCCH + H(+M)$	1.000E+14	0.0	50000.0
	Low Pressure limit: 2.0E15 0.0 42000.			
217.	$CH_2CHCHCH(+M) \rightleftharpoons CH_2CHCCH + H(+M)$	1.000E+14	0.0	37000.0
	Low Pressure limit: 1.0E14 0.0 30000.			
218.	$H + C_6H_5 \rightleftharpoons C_6H_6$	5.000E+13	0.0	0.0

Table A.7: Reactions 200–218 in the Miller–Melius mechanism.

A.2 Dagaut–Cathonnet–Boettner Mechanism

The gas phase chemistry mechanism for MAPP, propylene, ethylene, and propane flames is that of Dagaut, Cathonnet, and Boettner [66, 67]. It consists of 391 reactions among 57 species. The reaction rates are given in the form:

$$k = A\,T^n\,exp(-E_a/RT) \tag{A.2}$$

The unit for A is $cm^3/mol/sec$, and E_a is given in cal/mol. The following 57 species are considered in the model:

Monatomic species: H, O

Homonuclear diatomics: H_2, O_2

H-O compounds: OH, HO_2, H_2O, H_2O_2

C-O compounds: CO, CO_2, C_2O

C_1 hydrocarbons: CH, CH_2, CH_3, CH_4

C_2 hydrocarbons: C_2H, C_2H_2, C_2H_3, C_2H_4, C_2H_5, C_2H_6

C_3 hydrocarbons: C_3H_2, C_3H_3, AC_3H_4, PC_3H_4, C_3H_4C, AC_3H_5, SC_3H_5, TC_3H_5, C_3H_6, IC_3H_7, NC_3H_7, C_3H_8

C_4 hydrocarbons: C_4H, C_4H_2, C_4H_3, C_4H_5, C_4H_6, C_4H_7, IC_4H_8, $T2C_4H_8$, $C2C_4H_8$

C_6 hydrocarbons: C_6H_6, C_6H_9, C_6H_{10}

H-C-O compounds: HCO, HCCO, HCCOH, CH_2O, CH_2OH, CH_2CO, CH_3O, CH_3OH, CH_3CO, CH_3HCO, C_2H_4O, C_3H_6O

No.	Reaction	A	n	E_a
1.	$H + H + M \rightleftharpoons H_2 + M$	7.31E+17	-1.0	.0
2.	$O + O + M \rightleftharpoons O_2 + M$	1.14E+17	-1.0	.0
3.	$O + H + M \rightleftharpoons OH + M$	6.20E+16	-.6	.0
4.	$H_2 + O_2 \rightleftharpoons OH + OH$	1.70E+13	.0	47780.0
5.	$O + H_2 \rightleftharpoons OH + H$	3.87E+04	2.7	6260.0
6.	$H + O_2 \rightleftharpoons OH + O$	1.90E+14	.0	16812.0
7.	$H + O_2 + M \rightleftharpoons HO_2 + M$	8.00E+17	-.8	.0
8.	$H + OH + M \rightleftharpoons H_2O + M$	8.62E+21	-2.0	.0
9.	$H_2 + OH \rightleftharpoons H_2O + H$	2.16E+08	1.5	3430.0
10.	$H_2O + O \rightleftharpoons OH + OH$	1.50E+10	1.1	17260.0
11.	$HO_2 + OH \rightleftharpoons H_2O + O_2$	2.89E+13	.0	-497.0
12.	$HO_2 + O \rightleftharpoons OH + O_2$	1.81E+13	.0	-400.0
13.	$H + HO_2 \rightleftharpoons H_2 + O_2$	4.22E+13	.0	1411.0
14.	$H + HO_2 \rightleftharpoons OH + OH$	4.95E+13	.0	143.0
15.	$H + HO_2 \rightleftharpoons H_2O + O$	1.18E+14	.0	2730.0
16.	$HO_2 + HO_2 \rightleftharpoons H_2O_2 + O_2$	1.46E+13	.0	5088.0
17.	$OH + OH \rightleftharpoons H_2O_2$	1.56E+16	-1.5	149.0
18.	$H_2O_2 + OH \rightleftharpoons HO_2 + H_2O$	1.78E+12	.0	326.0
19.	$H_2O_2 + H \rightleftharpoons HO_2 + H_2$	1.70E+12	.0	3750.0
20.	$H_2O_2 + H \rightleftharpoons H_2O + OH$	1.00E+13	.0	3590.0
21.	$H_2O_2 + O \rightleftharpoons HO_2 + OH$	2.80E+13	.0	6400.0
22.	$CO + HO_2 \rightleftharpoons CO_2 + OH$	1.50E+14	.0	23650.0
23.	$CO + OH \rightleftharpoons CO_2 + H$	4.40E+06	1.5	-740.0
24.	$CO + O + M \rightleftharpoons CO_2 + M$	2.83E+13	.0	-4540.0
25.	$CO + O_2 \rightleftharpoons CO_2 + O$	2.53E+12	.0	47700.0
26.	$HCO + M \rightleftharpoons H + CO + M$	1.85E+17	-1.0	17000.0
27.	$HCO + OH \rightleftharpoons CO + H_2O$	1.00E+14	.0	.0
28.	$HCO + O \rightleftharpoons CO + OH$	3.00E+13	.0	.0
29.	$HCO + O \rightleftharpoons CO_2 + H$	3.00E+13	.0	.0
30.	$HCO + H \rightleftharpoons CO + H_2$	7.22E+13	.0	.0
31.	$HCO + O_2 \rightleftharpoons CO + HO_2$	4.22E+12	.0	.0
32.	$HCO + CH_3 \rightleftharpoons CO + CH_4$	1.20E+14	.0	.0
33.	$HCO + HO_2 \rightleftharpoons CO_2 + OH + H$	3.00E+13	.0	.0
34.	$HCO + C_2H_6 \rightleftharpoons CH_2O + C_2H_5$	4.70E+04	2.7	18235.0
35.	$HCO + HCO \rightleftharpoons CH_2O + CO$	1.80E+13	.0	.0
36.	$HCO + HCO \rightleftharpoons H_2 + CO + CO$	3.00E+12	.0	.0

Table A.8: Reactions 1–36 in the Dagaut–Cathonnet–Boettner mechanism.

No.	Reaction	A	n	E_a
37.	$CH_4 \rightleftharpoons CH_3 + H$	5.99E+30	-4.9	108553.0
38.	$CH_4 + HO_2 \rightleftharpoons CH_3 + H_2O_2$	1.12E+13	.0	24641.0
39.	$CH_4 + OH \rightleftharpoons CH_3 + H_2O$	1.55E+07	1.8	2774.0
40.	$CH_4 + O \rightleftharpoons CH_3 + OH$	6.92E+08	1.6	8486.0
41.	$CH_4 + H \rightleftharpoons CH_3 + H_2$	8.58E+03	3.1	7941.0
42.	$CH_4 + CH_2 \rightleftharpoons CH_3 + CH_3$	4.30E+12	.0	10038.0
43.	$CH_3 + M \rightleftharpoons CH_2 + H + M$	1.90E+16	.0	91600.0
44.	$CH_3 + HO_2 \rightleftharpoons CH_3O + OH$	4.00E+13	.0	5000.0
45.	$CH_4 + O_2 \rightleftharpoons CH_3 + HO_2$	7.63E+13	.0	58590.0
46.	$CH_3 + OH \rightleftharpoons CH_2OH + H$	2.64E+19	-1.8	8068.0
47.	$CH_3 + OH \rightleftharpoons CH_3O + H$	5.74E+12	-.2	13931.0
48.	$CH_3 + OH \rightleftharpoons CH_2 + H_2O$	8.90E+18	-1.8	8067.0
49.	$CH_3 + OH \rightleftharpoons CH_2O + H_2$	3.19E+12	-.5	10810.0
50.	$CH_3 + O \rightleftharpoons CH_2O + H$	8.43E+13	.0	.0
51.	$CH_3 + H \rightleftharpoons CH_2 + H_2$	7.00E+13	.0	15100.0
52.	$CH_3 + O_2 \rightleftharpoons CH_3O + O$	6.00E+12	.0	33700.0
53.	$CH_3 + O_2 \rightleftharpoons CH_2O + OH$	3.05E+30	-4.7	36571.0
54.	$CH_3 + CH_3 \rightleftharpoons C_2H_5 + H$	3.01E+13	.0	13513.0
55.	$CH_3 + CH_3 \rightleftharpoons C_2H_6$	2.39E+38	-7.6	11359.0
56.	$CH_3 + CH_3O \rightleftharpoons CH_4 + CH_2O$	2.41E+13	.0	.0
57.	$CH_3 + CH_2OH \rightleftharpoons CH_4 + CH_2O$	2.41E+12	.0	.0
58.	$CH_2 + OH \rightleftharpoons CH + H_2O$	1.13E+07	2.0	3000.0
59.	$CH_2 + OH \rightleftharpoons CH_2O + H$	2.50E+13	.0	.0
60.	$CH_2 + O \rightleftharpoons CO + H + H$	9.08E+13	.0	656.0
61.	$CH_2 + O \rightleftharpoons CO + H_2$	3.89E+13	.0	-149.0
62.	$CH_2 + H \rightleftharpoons CH + H_2$	5.52E+12	.0	-2026.0
63.	$CH_2 + O_2 \rightleftharpoons HCO + OH$	4.30E+10	.0	-500.0
64.	$CH_2 + O_2 \rightleftharpoons CO_2 + H_2$	6.90E+11	.0	500.0
65.	$CH_2 + O_2 \rightleftharpoons CO_2 + H + H$	1.60E+12	.0	1000.0
66.	$CH_2 + O_2 \rightleftharpoons CO + H_2O$	1.87E+10	.0	-1000.0
67.	$CH_2 + O_2 \rightleftharpoons CO + OH + H$	8.64E+10	.0	-500.0
68.	$CH_2 + O_2 \rightleftharpoons CH_2O + O$	1.00E+14	.0	4500.0
69.	$CH_2 + CO_2 \rightleftharpoons CH_2O + CO$	1.10E+11	.0	1000.0
70.	$CH_2 + CH_2 \rightleftharpoons C_2H_2 + H_2$	3.20E+13	.0	.0
71.	$CH_2 + CH_3 \rightleftharpoons C_2H_4 + H$	4.00E+13	.0	.0
72.	$CH_2 + CH \rightleftharpoons C_2H_2 + H$	4.00E+13	.0	.0

Table A.9: Reactions 37–72 in the Dagaut–Cathonnet–Boettner mechanism.

No.	Reaction	A	n	E_a
73.	$CH_2 + C_2H_2 \rightleftharpoons H + C_3H_3$	1.20E+13	.0	6620.0
74.	$CH_2 + C_2H_4 \rightleftharpoons C_3H_6$	4.30E+12	.0	10038.0
75.	$CH_2 + C_2H_6 \rightleftharpoons CH_3 + C_2H_5$	6.50E+12	.0	7911.0
76.	$CH_2 + C_3H_8 \rightleftharpoons CH_3 + IC_3H_7$	2.19E+12	.0	6405.0
77.	$CH_2 + C_3H_8 \rightleftharpoons CH_3 + NC_3H_7$	1.79E+12	.0	6405.0
78.	$C\dot{H} + OH \rightleftharpoons HCO + H$	3.00E+13	.0	.0
79.	$CH + O \rightleftharpoons CO + H$	1.00E+14	.0	.0
80.	$CH + O_2 \rightleftharpoons HCO + O$	3.30E+13	.0	.0
81.	$CH + O_2 \rightleftharpoons CO + OH$	2.00E+13	.0	.0
82.	$CH + CO_2 \rightleftharpoons HCO + CO$	3.40E+12	.0	690.0
83.	$CH + CH_4 \rightleftharpoons C_2H_4 + H$	6.00E+13	.0	.0
84.	$CH + CH_3 \rightleftharpoons C_2H_3 + H$	3.00E+13	.0	.0
85.	$CH_3O + M \rightleftharpoons CH_2O + H + M$	4.88E+15	.0	22773.0
86.	$CH_3O + HO_2 \rightleftharpoons CH_2O + H_2O_2$	3.00E+11	.0	.0
87.	$CH_3O + OH \rightleftharpoons CH_2O + H_2O$	1.00E+13	.0	.0
88.	$CH_3O + O \rightleftharpoons CH_2O + OH$	1.30E+13	.0	.0
89.	$CH_3O + H \rightleftharpoons CH_2O + H_2$	2.00E+13	.0	.0
90.	$CH_3O + O_2 \rightleftharpoons CH_2O + HO_2$	2.35E+10	.0	1788.0
91.	$CH_3O + CH_2O \rightleftharpoons CH_3OH + HCO$	1.15E+11	.0	1280.0
92.	$CH_3O + CO \rightleftharpoons CH_3 + CO_2$	1.57E+13	.0	2981.0
93.	$CH_3O + HCO \rightleftharpoons CH_3OH + CO$	9.00E+13	.0	.0
94.	$CH_3O + C_2H_5 \rightleftharpoons CH_2O + C_2H_6$	2.41E+13	.0	.0
95.	$CH_3O + C_2H_3 \rightleftharpoons CH_2O + C_2H_4$	2.41E+13	.0	.0
96.	$CH_3O + C_2H_4 \rightleftharpoons CH_2O + C_2H_5$	1.20E+11	.0	7000.0
97.	$CH_2O + M \rightleftharpoons HCO + H + M$	5.72E+16	.0	76480.0
98.	$CH_2O + HO_2 \rightleftharpoons HCO + H_2O_2$	4.00E+12	.0	11665.0
99.	$CH_2O + OH \rightleftharpoons HCO + H_2O$	3.43E+09	1.2	-447.0
100.	$CH_2O + O \rightleftharpoons HCO + OH$	1.81E+13	.0	3088.0
101.	$CH_2O + H \rightleftharpoons HCO + H_2$	1.12E+08	1.7	2127.0
102.	$CH_2O + O_2 \rightleftharpoons HCO + HO_2$	2.04E+13	.0	39000.0
103.	$CH_2O + CH_3 \rightleftharpoons HCO + CH_4$	8.91E-13	7.4	-960.0
104.	$C_2H_6 \rightleftharpoons C_2H_5 + H$	2.08E+38	-7.1	106507.0
105.	$C_2H_6 + HO_2 \rightleftharpoons C_2H_5 + H_2O_2$	1.21E+12	.0	17600.0
106.	$C_2H_6 + OH \rightleftharpoons C_2H_5 + H_2O$	5.13E+06	2.1	860.0
107.	$C_2H_6 + O \rightleftharpoons C_2H_5 + OH$	1.14E-07	6.5	274.0
108.	$C_2H_6 + H \rightleftharpoons C_2H_5 + H_2$	5.00E+02	3.5	5210.0

Table A.10: Reactions 73–108 in the Dagaut–Cathonnet–Boettner mechanism.

No.	Reaction	A	n	E_a
109.	$C_2H_6 + O_2 \rightleftharpoons C_2H_5 + HO_2$	1.00E+13	.0	51000.0
110.	$C_2H_6 + CH_3O \rightleftharpoons C_2H_5 + CH_3OH$	3.02E+11	.0	7000.0
111.	$C_2H_6 + CH_3 \rightleftharpoons C_2H_5 + CH_4$	3.97E+05	2.5	17684.0
112.	$C_2H_5 + HO_2 \rightleftharpoons C_2H_4 + H_2O_2$	3.00E+11	.0	.0
113.	$C_2H_5 + HO_2 \rightarrow CH_3 + CH_2O + OH$	2.50E+13	.0	.0
114.	$C_2H_5 + OH \rightleftharpoons C_2H_4 + H_2O$	2.41E+13	.0	.0
115.	$C_2H_5 + OH \rightarrow CH_3 + CH_2O + H$	2.41E+13	.0	.0
116.	$C_2H_5 + O \rightleftharpoons CH_2O + CH_3$	4.24E+13	.0	.0
117.	$C_2H_5 + O \rightleftharpoons CH_3HCO + H$	5.30E+13	.0	.0
118.	$C_2H_5 + O \rightleftharpoons C_2H_4 + OH$	3.05E+13	.0	.0
119.	$C_2H_5 + H \rightleftharpoons C_2H_4 + H_2$	1.25E+14	.0	8000.0
120.	$C_2H_5 + O_2 \rightleftharpoons C_2H_4 + HO_2$	1.70E+10	.0	-670.0
121.	$C_2H_5 + CH_3 \rightleftharpoons C_2H_4 + CH_4$	4.37E-04	5.0	8300.0
122.	$C_2H_5 + C_2H_5 \rightleftharpoons C_2H_4 + C_2H_6$	1.40E+12	.0	.0
123.	$C_2H_4 + M \rightleftharpoons C_2H_2 + H_2 + M$	3.00E+17	.0	79350.0
124.	$C_2H_4 + M \rightleftharpoons C_2H_3 + H + M$	2.97E+17	.0	96560.0
125.	$C_2H_4 + HO_2 \rightarrow C_2H_4O + OH$	6.22E+12	.0	18962.0
126.	$C_2H_4 + OH \rightleftharpoons C_2H_3 + H_2O$	2.02E+13	.0	5960.0
127.	$C_2H_4 + O \rightleftharpoons CH_3 + HCO$	1.08E+14	.0	7432.0
128.	$C_2H_4 + O \rightarrow CH_2 + HCO + H$	5.66E+12	.0	1488.0
129.	$C_2H_4 + H \rightleftharpoons C_2H_3 + H_2$	3.36E-07	6.0	1692.0
130.	$C_2H_4 + H \rightleftharpoons C_2H_5$	1.05E+14	-.5	655.0
131.	$C_2H_4 + O_2 \rightleftharpoons C_2H_3 + HO_2$	4.00E+13	.0	61500.0
132.	$C_2H_4 + C_2H_4 \rightleftharpoons C_2H_5 + C_2H_3$	5.00E+14	.0	64700.0
133.	$C_2H_4 + CH_3 \rightleftharpoons C_2H_3 + CH_4$	3.97E+05	2.5	20000.0
134.	$C_2H_4O \rightleftharpoons CH_4 + CO$	3.16E+14	.0	57000.0
135.	$C_2H_3 \rightleftharpoons C_2H_2 + H$	2.10E+44	-8.4	51106.0
136.	$C_2H_3 + HO_2 \rightarrow CH_3 + CO + OH$	3.00E+13	.0	.0
137.	$C_2H_3 + OH \rightleftharpoons C_2H_2 + H_2O$	3.00E+13	.0	.0
138.	$C_2H_3 + OH \rightleftharpoons CH_3HCO$	3.00E+13	.0	.0
139.	$C_2H_3 + O \rightleftharpoons CH_3 + CO$	3.00E+13	.0	.0
140.	$C_2H_3 + H \rightleftharpoons C_2H_2 + H_2$	3.00E+13	.0	.0
141.	$C_2H_3 + O_2 \rightleftharpoons CH_2O + HCO$	3.00E+12	.0	-250.0
142.	$C_2H_3 + CH_3 \rightleftharpoons C_2H_2 + CH_4$	4.37E-04	5.0	8300.0
143.	$C_2H_3 + C_2H_6 \rightleftharpoons C_2H_4 + C_2H_5$	1.50E+13	.0	10000.0
144.	$C_2H_3 + HCO \rightleftharpoons C_2H_4 + CO$	9.03E+13	.0	.0

Table A.11: Reactions 109–144 in the Dagaut–Cathonnet–Boettner mechanism.

No.	Reaction	A	n	E_a
145.	$C_2H_3 + CH_2O \rightleftharpoons C_2H_4 + HCO$	5.42E+03	2.8	5862.0
146.	$C_2H_3 + C_2H_3 \rightleftharpoons C_2H_2 + C_2H_4$	1.08E+13	.0	.0
147.	$C_2H_3 + C_2H_3 \rightleftharpoons C_4H_6$	4.94E+13	.0	.0
148.	$C_2H_2 \rightleftharpoons C_2H + H$	2.37E+32	-5.3	130688.0
149.	$C_2H_2 + HO_2 \rightleftharpoons CH_2CO + OH$	1.00E+13	.0	18280.0
150.	$C_2H_2 + OH \rightleftharpoons C_2H + H_2O$	3.39E+07	2.0	14000.0
151.	$C_2H_2 + OH \rightleftharpoons HCCOH + H$	5.06E+05	2.3	13500.0
152.	$C_2H_2 + OH \rightleftharpoons CH_2CO + H$	2.19E-04	4.5	-1000.0
153.	$C_2H_2 + OH \rightleftharpoons CH_3 + CO$	4.85E-04	4.0	-2000.0
154.	$C_2H_2 + H \rightleftharpoons C_2H + H_2$	6.02E+13	.0	22257.0
155.	$C_2H_2 + O \rightleftharpoons CH_2 + CO$	1.52E+04	2.8	497.0
156.	$C_2H_2 + O \rightleftharpoons HCCO + H$	6.50E+03	2.8	497.0
157.	$C_2H_2 + O_2 \rightleftharpoons HCCO + OH$	2.00E+08	1.5	30100.0
158.	$C_2H_2 + O_2 \rightleftharpoons C_2H + HO_2$	1.20E+13	.0	74520.0
159.	$C_2H_2 + CH_3 \rightleftharpoons SC_3H_5$	1.61E+40	-8.6	20331.0
160.	$C_2H_2 + CH_3 \rightleftharpoons PC_3H_4 + H$	2.73E+17	-2.0	20592.0
161.	$C_2H_2 + CH_3 \rightleftharpoons AC_3H_5$	2.61E+46	-9.8	36951.0
162.	$C_2H_2 + CH_3 \rightleftharpoons AC_3H_4 + H$	6.74E+19	-2.1	31591.0
163.	$HCCOH + H \rightleftharpoons CH_2CO + H$	1.00E+13	.0	.0
164.	$C_2H + OH \rightleftharpoons HCCO + H$	2.00E+13	.0	.0
165.	$C_2H + O \rightleftharpoons CO + CH$	1.00E+13	.0	.0
166.	$C_2H + O_2 \rightleftharpoons CO + CO + H$	5.00E+13	.0	1510.0
167.	$CH_2CO + M \rightleftharpoons CH_2 + CO + M$	4.11E+15	.0	59270.0
168.	$CH_2CO + O_2 \rightleftharpoons CH_2O + CO_2$	2.00E+13	.0	61500.0
169.	$CH_2CO + HO_2 \rightarrow CH_2O + CO + OH$	6.00E+11	.0	12738.0
170.	$CH_2CO + OH \rightleftharpoons HCCO + H_2O$	7.50E+12	.0	2000.0
171.	$CH_2CO + O \rightleftharpoons CH_2 + CO_2$	1.76E+12	.0	1349.0
172.	$CH_2CO + O \rightleftharpoons HCCO + OH$	1.00E+13	.0	8000.0
173.	$CH_2CO + H \rightleftharpoons CH_3 + CO$	1.50E+04	2.8	673.0
174.	$CH_2CO + H \rightleftharpoons HCCO + H_2$	5.00E+13	.0	8000.0
175.	$HCCO + M \rightleftharpoons CH + CO + M$	6.00E+15	.0	58821.0
176.	$HCCO + OH \rightleftharpoons HCO + CO + H$	1.00E+13	.0	.0
177.	$HCCO + O \rightleftharpoons CO + CO + H$	1.93E+14	.0	590.0
178.	$HCCO + H \rightleftharpoons CH_2 + CO$	1.50E+14	.0	.0
179.	$HCCO + O_2 \rightleftharpoons CO + CO + OH$	1.46E+12	.0	2500.0
180.	$HCCO + CH_2 \rightleftharpoons C_2H + CH_2O$	1.00E+13	.0	2000.0

Table A.12: Reactions 145–180 in the Dagaut–Cathonnet–Boettner mechanism.

No.	Reaction	A	n	E_a
181.	$HCCO + CH_2 \rightleftharpoons C_2H_3 + CO$	3.00E+13	.0	.0
182.	$CH_3OH \rightleftharpoons CH_3 + OH$	1.57E+46	-9.3	103522.0
183.	$CH_3OH + HO_2 \rightleftharpoons CH_2OH + H_2O_2$	6.30E+12	.0	19360.0
184.	$CH_3OH + OH \rightleftharpoons CH_2OH + H_2O$	4.53E+11	.3	1160.0
185.	$CH_3OH + OH \rightleftharpoons CH_3O + H_2O$	3.63E+11	.7	5868.0
186.	$CH_3OH + O \rightleftharpoons CH_2OH + OH$	1.00E+13	.0	4690.0
187.	$CH_3OH + H \rightleftharpoons CH_2OH + H_2$	4.00E+13	.0	6100.0
188.	$CH_3OH + CH_2O \rightleftharpoons CH_3O + CH_3O$	1.55E+12	.0	79570.0
189.	$CH_3OH + CH_3 \rightleftharpoons CH_2OH + CH_4$	3.57E+11	.0	8663.0
190.	$CH_3OH + CH_3 \rightleftharpoons CH_3O + CH_4$	4.68E+05	2.3	12764.0
191.	$CH_2OH + M \rightleftharpoons CH_2O + H + M$	1.00E+14	.0	25100.0
192.	$CH_2OH + H \rightleftharpoons CH_2O + H_2$	3.00E+13	.0	.0
193.	$CH_2OH + O_2 \rightleftharpoons CH_2O + HO_2$	2.17E+14	.0	4690.0
194.	$CH_3HCO \rightleftharpoons CH_3 + HCO$	2.45E+16	.0	84128.0
195.	$CH_3HCO + HO_2 \rightleftharpoons CH_3CO + H_2O_2$	1.70E+12	.0	10700.0
196.	$CH_3HCO + OH \rightleftharpoons CH_3CO + H_2O$	1.00E+13	.0	.0
197.	$CH_3HCO + O \rightleftharpoons CH_3CO + OH$	5.00E+12	.0	1790.0
198.	$CH_3HCO + H \rightleftharpoons CH_3CO + H_2$	4.00E+13	.0	4210.0
199.	$CH_3HCO + O_2 \rightleftharpoons CH_3CO + HO_2$	2.00E+13	.5	42200.0
200.	$CH_3HCO + CH_3 \rightleftharpoons CH_3CO + CH_4$	2.00E-06	5.6	2464.0
201.	$CH_3CO + M \rightleftharpoons CH_3 + CO + M$	8.64E+15	.0	14400.0
202.	$C_3H_8 \rightleftharpoons C_2H_5 + CH_3$	6.03E+94	-22.7	130427.0
203.	$C_3H_8 + O_2 \rightleftharpoons NC_3H_7 + HO_2$	4.00E+13	.0	47500.0
204.	$C_3H_8 + O_2 \rightleftharpoons IC_3H_7 + HO_2$	4.00E+13	.0	47500.0
205.	$C_3H_8 + HO_2 \rightleftharpoons NC_3H_7 + H_2O_2$	4.76E+04	2.5	16494.0
206.	$C_3H_8 + HO_2 \rightleftharpoons IC_3H_7 + H_2O_2$	9.64E+03	2.6	13910.0
207.	$C_3H_8 + OH \rightleftharpoons NC_3H_7 + H_2O$	4.16E+07	1.7	540.0
208.	$C_3H_8 + OH \rightleftharpoons IC_3H_7 + H_2O$	1.84E+05	2.4	-573.0
209.	$C_3H_8 + O \rightleftharpoons NC_3H_7 + OH$	3.72E+06	2.4	5505.0
210.	$C_3H_8 + O \rightleftharpoons IC_3H_7 + OH$	5.50E+05	2.5	3140.0
211.	$C_3H_8 + H \rightleftharpoons NC_3H_7 + H_2$	2.00E+14	.0	9959.0
212.	$C_3H_8 + H \rightleftharpoons IC_3H_7 + H_2$	1.30E+13	.0	5638.0
213.	$C_3H_8 + CH_3 \rightleftharpoons NC_3H_7 + CH_4$	3.00E+12	.0	11710.0
214.	$C_3H_8 + CH_3 \rightleftharpoons IC_3H_7 + CH_4$	8.07E+11	.0	10110.0
215.	$C_3H_8 + C_2H_5 \rightleftharpoons NC_3H_7 + C_2H_6$	3.16E+11	.0	12300.0

Table A.13: Reactions 181–215 in the Dagaut–Cathonnet–Boettner mechanism.

No.	Reaction	A	n	E_a
216.	$C_3H_8 + C_2H_5 \rightleftharpoons IC_3H_7 + C_2H_6$	5.01E+10	.0	10400.0
217.	$C_3H_8 + C_2H_3 \rightleftharpoons NC_3H_7 + C_2H_4$	6.00E+02	3.3	10502.0
218.	$C_3H_8 + C_2H_3 \rightleftharpoons IC_3H_7 + C_2H_4$	1.00E+03	3.1	8829.0
219.	$C_3H_8 + IC_3H_7 \rightleftharpoons NC_3H_7 + C_3H_8$	1.00E+11	.0	12900.0
220.	$C_3H_8 + AC_3H_5 \rightleftharpoons NC_3H_7 + C_3H_6$	7.94E+11	.0	20500.0
221.	$C_3H_8 + AC_3H_5 \rightleftharpoons IC_3H_7 + C_3H_6$	7.94E+11	.0	16200.0
222.	$C_3H_8 + CH_3O \rightleftharpoons NC_3H_7 + CH_3OH$	3.18E+11	.0	7050.0
223.	$C_3H_8 + CH_3O \rightleftharpoons IC_3H_7 + CH_3OH$	7.20E+10	.0	4470.0
224.	$NC_3H_7 \rightleftharpoons C_2H_4 + CH_3$	4.07E+12	.0	29580.0
225.	$NC_3H_7 + O_2 \rightleftharpoons C_3H_6 + HO_2$	3.58E+09	.0	-3532.0
226.	$IC_3H_7 \rightleftharpoons C_2H_4 + CH_3$	1.00E+14	.0	45000.0
227.	$IC_3H_7 + O_2 \rightleftharpoons C_3H_6 + HO_2$	1.84E+10	.0	-2151.0
228.	$C_3H_6 \rightleftharpoons AC_3H_5 + H$	4.57E+14	.0	88900.0
229.	$C_3H_6 \rightleftharpoons SC_3H_5 + H$	7.59E+14	.0	101300.0
230.	$C_3H_6 \rightleftharpoons TC_3H_5 + H$	1.45E+15	.0	98060.0
231.	$C_3H_6 \rightleftharpoons C_2H_3 + CH_3$	7.10E+15	.0	87240.0
232.	$C_3H_6 + HO_2 \rightleftharpoons C_3H_6O + OH$	1.02E+12	.0	14964.0
233.	$C_3H_6 + HO_2 \rightleftharpoons AC_3H_5 + H_2O_2$	1.50E+11	.0	14190.0
234.	$C_3H_6 + HO_2 \rightleftharpoons SC_3H_5 + H_2O_2$	7.50E+09	.0	12570.0
235.	$C_3H_6 + HO_2 \rightleftharpoons TC_3H_5 + H_2O_2$	3.00E+09	.0	9930.0
236.	$C_3H_6 + OH \rightleftharpoons AC_3H_5 + H_2O$	7.70E+05	2.2	622.0
237.	$C_3H_6 + OH \rightleftharpoons SC_3H_5 + H_2O$	1.01E+13	.0	5960.0
238.	$C_3H_6 + OH \rightleftharpoons TC_3H_5 + H_2O$	1.17E+09	1.0	-424.0
239.	$C_3H_6 + OH \rightleftharpoons C_2H_5 + CH_2O$	3.91 + 145	-40.0	65733.0
240.	$C_3H_6 + OH + O_2 \rightarrow CH_3HCO + CH_2O + OH$	3.00E+10	.0	-8280.0
241.	$C_3H_6 + O \rightleftharpoons C_2H_5 + HCO$	5.22E+07	1.6	-628.0
242.	$C_3H_6 + O \rightleftharpoons CH_3 + CH_3CO$	6.96E+07	1.6	-628.0
243.	$C_3H_6 + O \rightleftharpoons C_2H_4 + CH_2O$	3.48E+07	1.6	-628.0
244.	$NC_3H_7 \rightleftharpoons C_3H_6 + H$	6.30E+13	.0	36807.0
245.	$C_3H_6 + H \rightleftharpoons IC_3H_7$	3.00E+12	.0	960.0
246.	$C_3H_6 + H \rightleftharpoons AC_3H_5 + H_2$	6.46E+12	.0	4445.0
247.	$C_3H_6 + H \rightleftharpoons SC_3H_5 + H_2$	3.25E+11	.0	4445.0
248.	$C_3H_6 + O_2 \rightleftharpoons SC_3H_5 + HO_2$	2.00E+13	.0	47600.0
249.	$C_3H_6 + O_2 \rightleftharpoons TC_3H_5 + HO_2$	2.00E+13	.0	44000.0
250.	$C_3H_6 + O_2 \rightleftharpoons AC_3H_5 + HO_2$	1.95E+12	.0	39000.0

Table A.14: Reactions 216–250 in the Dagaut–Cathonnet–Boettner mechanism.

No.	Reaction	A	n	E_a
251.	$C_3H_6 + CH_3 \rightleftharpoons AC_3H_5 + CH_4$	1.60E+11	.0	8800.0
252.	$C_3H_6 + CH_3 \rightleftharpoons SC_3H_5 + CH_4$	3.30E+11	.0	10110.0
253.	$C_3H_6 + CH_3 \rightleftharpoons TC_3H_5 + CH_4$	5.00E+10	.0	8030.0
254.	$C_3H_6 + C_2H_5 \rightleftharpoons AC_3H_5 + C_2H_6$	1.00E+11	.0	9800.0
255.	$C_3H_6O \rightarrow C_2H_5 + HCO$	1.26E+14	.0	58000.0
256.	$AC_3H_5 + O_2 \rightarrow CH_2O + CH_2O + CH$	6.31E+11	.0	17210.0
257.	$AC_3H_5 + HO_2 \rightarrow C_2H_3 + CH_2O + OH$	4.50E+12	.0	.0
258.	$AC_3H_5 + H \rightleftharpoons AC_3H_4 + H_2$	3.33E+12	.0	.0
259.	$AC_3H_5 + O \rightarrow C_2H_4 + CO + H$	1.81E+14	.0	.0
260.	$AC_3H_5 + CH_3 \rightleftharpoons AC_3H_4 + CH_4$	1.00E+11	.0	.0
261.	$AC_3H_5 + C_2H_5 \rightleftharpoons AC_3H_4 + C_2H_6$	4.00E+11	.0	.0
262.	$AC_3H_5 + C_2H_3 \rightleftharpoons AC_3H_4 + C_2H_4$	1.00E+12	.0	.0
263.	$SC_3H_5 + O_2 \rightleftharpoons CH_3HCO + HCO$	4.34E+12	.0	.0
264.	$SC_3H_5 + HO_2 \rightarrow CH_2CO + CH_3 + OH$	4.50E+12	.0	.0
265.	$SC_3H_5 + H \rightleftharpoons AC_3H_4 + H_2$	3.33E+12	.0	.0
266.	$SC_3H_5 + O \rightarrow CH_2CO + CH_3$	1.81E+14	.0	.0
267.	$SC_3H_5 + CH_3 \rightleftharpoons AC_3H_4 + CH_4$	1.00E+11	.0	.0
268.	$SC_3H_5 + C_2H_5 \rightleftharpoons AC_3H_4 + C_2H_6$	1.00E+11	.0	.0
269.	$SC_3H_5 + C_2H_3 \rightleftharpoons AC_3H_4 + C_2H_4$	1.00E+11	.0	.0
270.	$TC_3H_5 + O_2 \rightleftharpoons CH_3CO + CH_2O$	4.34E+11	.0	.0
271.	$TC_3H_5 + HO_2 \rightarrow CH_2CO + CH_3 + OH$	4.50E+12	.0	.0
272.	$TC_3H_5 + H \rightleftharpoons AC_3H_4 + H_2$	3.33E+12	.0	.0
273.	$TC_3H_5 + O \rightarrow HCCO + CH_3 + H$	1.81E+14	.0	.0
274.	$TC_3H_5 + CH_3 \rightleftharpoons AC_3H_4 + CH_4$	1.00E+11	.0	.0
275.	$TC_3H_5 + C_2H_5 \rightleftharpoons AC_3H_4 + C_2H_6$	1.00E+11	.0	.0
276.	$TC_3H_5 + C_2H_3 \rightleftharpoons AC_3H_4 + C_2H_4$	1.00E+11	.0	.0
277.	$AC_3H_4 + M \rightleftharpoons C_3H_3 + H + M$	2.00E+18	.0	80000.0
278.	$AC_3H_4 + AC_3H_4 \rightleftharpoons AC_3H_5 + C_3H_3$	5.00E+14	.0	64700.0
279.	$AC_3H_4 \rightleftharpoons PC_3H_4$	1.20E+15	.0	92400.0
280.	$AC_3H_4 + O_2 \rightleftharpoons C_3H_3 + HO_2$	4.00E+13	.0	61500.0
281.	$AC_3H_4 + HO_2 \rightarrow CH_2CO + CH_2 + OH$	8.00E+12	.0	19000.0
282.	$AC_3H_4 + OH \rightleftharpoons CH_2CO + CH_3$	3.12E+12	.0	-397.0
283.	$AC_3H_4 + OH \rightleftharpoons C_3H_3 + H_2O$	1.45E+13	.0	4173.0
284.	$AC_3H_4 + O \rightleftharpoons C_2H_3 + HCO$	1.10E-02	4.6	-4243.0
285.	$AC_3H_4 + H \rightleftharpoons AC_3H_5$	2.00E+12	.0	2700.0

Table A.15: Reactions 250–285 in the Dagaut–Cathonnet–Boettner mechanism.

No.	Reaction	A	n	E_a
286.	$AC_3H_4 + H \rightleftharpoons TC_3H_5$	6.50E+12	.0	2000.0
287.	$AC_3H_4 + H \rightleftharpoons C_3H_3 + H_2$	1.00E+12	.0	1500.0
288.	$AC_3H_4 + CH_3 \rightleftharpoons C_3H_3 + CH_4$	2.00E+12	.0	7700.0
289.	$AC_3H_4 + AC_3H_5 \rightleftharpoons C_3H_3 + C_3H_6$	2.00E+12	.0	7700.0
290.	$AC_3H_4 + C_2H \rightleftharpoons C_3H_3 + C_2H_2$	1.00E+13	.0	.0
291.	$PC_3H_4 + M \rightleftharpoons C_3H_3 + H + M$	4.70E+18	.0	80000.0
292.	$PC_3H_4 \rightleftharpoons C_2H + CH_3$	4.20E+16	.0	100000.0
293.	$C_3H_4C \rightleftharpoons AC_3H_4$	1.51E+14	.0	50400.0
294.	$C_3H_4C \rightleftharpoons PC_3H_4$	7.08E+13	.0	43700.0
295.	$PC_3H_4 + O_2 \rightarrow HCCO + OH + CH_2$	2.00E+08	1.5	30100.0
296.	$PC_3H_4 + O_2 \rightleftharpoons C_3H_3 + HO_2$	5.00E+12	.0	51000.0
297.	$PC_3H_4 + HO_2 \rightarrow C_2H_4 + CO + OH$	3.00E+12	.0	19000.0
298.	$PC_3H_4 + OH \rightleftharpoons C_3H_3 + H_2O$	3.00E+03	3.0	200.0
299.	$PC_3H_4 + OH \rightleftharpoons CH_2CO + CH_3$	5.00E-04	4.5	-1000.0
300.	$PC_3H_4 + O \rightleftharpoons CH_2CO + CH_2$	6.40E+12	.0	2010.0
301.	$PC_3H_4 + O \rightleftharpoons C_2H_3 + HCO$	3.20E+12	.0	2010.0
302.	$PC_3H_4 + O \rightleftharpoons HCCO + CH_3$	6.30E+12	.0	2010.0
303.	$PC_3H_4 + O \rightarrow HCCO + CH_2 + H$	3.20E+11	.0	2010.0
304.	$PC_3H_4 + H \rightleftharpoons TC_3H_5$	6.50E+12	.0	2000.0
305.	$PC_3H_4 + H \rightleftharpoons C_3H_3 + H_2$	1.00E+12	.0	1500.0
306.	$PC_3H_4 + CH_3 \rightleftharpoons C_3H_3 + CH_4$	2.00E+12	.0	7700.0
307.	$PC_3H_4 + C_2H \rightleftharpoons C_3H_3 + C_2H_2$	1.00E+12	.0	.0
308.	$PC_3H_4 + C_2H_3 \rightleftharpoons C_3H_3 + C_2H_4$	1.00E+12	.0	7700.0
309.	$PC_3H_4 + AC_3H_5 \rightleftharpoons C_3H_3 + C_3H_6$	2.00E+12	.0	7700.0
310.	$C_3H_3 + H \rightleftharpoons C_3H_2 + H_2$	1.60E+14	.0	.0
311.	$C_3H_3 + O \rightarrow C_2H + HCO + H$	1.39E+14	.0	.0
312.	$C_3H_3 + O \rightarrow C_2H_2 + CO + H$	1.40E+14	.0	.0
313.	$C_3H_3 + OH \rightleftharpoons C_3H_2 + H_2O$	1.00E+13	.0	.0
314.	$C_3H_3 + O_2 \rightleftharpoons CH_2CO + HCO$	3.01E+10	.0	2870.0
315.	$C_3H_3 + CH_3 \rightleftharpoons C_2H_5 + C_2H$	1.00E+13	.0	37500.0
316.	$C_3H_3 + CH_3 \rightleftharpoons C_4H_6$	1.00E+12	.0	.0
317.	$CH + C_2H_2 \rightleftharpoons C_3H_2 + H$	1.00E+14	.0	.0
318.	$C_3H_2 + O_2 \rightleftharpoons HCO + HCCO$	1.00E+13	.0	.0
319.	$C_2H_3 + C_2H_4 \rightleftharpoons C_4H_6 + H$	1.00E+12	.0	7300.0
320.	$C_2H_2 + C_2H_2 \rightleftharpoons C_4H_3 + H$	2.00E+12	.0	45900.0

Table A.16: Reactions 286–320 in the Dagaut–Cathonnet–Boettner mechanism.

No.	Reaction	A	n	E_a
321.	$C_2H_2 + C_2H \rightleftharpoons C_4H_2 + H$	3.50E+13	.0	.0
322.	$C_4H_3 + M \rightleftharpoons C_4H_2 + H + M$	1.00E+16	.0	59700.0
323.	$C_4H_2 + OH \rightleftharpoons C_3H_2 + HCO$	6.66E+12	.0	-410.0
324.	$C_4H_2 + O \rightleftharpoons C_3H_2 + CO$	1.20E+12	.0	.0
325.	$C_4H_7 \rightleftharpoons C_4H_6 + H$	1.20E+14	.0	49300.0
326.	$C_4H_7 \rightleftharpoons C_2H_4 + C_2H_3$	1.00E+11	.0	37000.0
327.	$C_4H_7 + H \rightleftharpoons C_4H_6 + H_2$	3.16E+12	.0	.0
328.	$C_4H_7 + O_2 \rightleftharpoons C_4H_6 + HO_2$	1.00E+11	.0	.0
329.	$C_4H_7 + CH_3 \rightleftharpoons C_4H_6 + CH_4$	1.00E+13	.0	.0
330.	$C_4H_7 + C_2H_3 \rightleftharpoons C_4H_6 + C_2H_4$	4.00E+12	.0	.0
331.	$C_4H_7 + C_2H_5 \rightleftharpoons C_4H_6 + C_2H_6$	4.00E+12	.0	.0
332.	$C_4H_7 + C_2H_5 \rightleftharpoons IC_4H_8 + C_2H_4$	5.00E+11	.0	.0
333.	$C_4H_7 + C_2H_5 \rightleftharpoons T2C_4H_8 + C_2H_4$	5.00E+11	.0	.0
334.	$C_4H_7 + C_2H_5 \rightleftharpoons C2C_4H_8 + C_2H_4$	5.00E+11	.0	.0
335.	$C_4H_7 + AC_3H_5 \rightleftharpoons C_4H_6 + C_3H_6$	4.00E+13	.0	.0
336.	$C_4H_7 + C_4H_7 \rightleftharpoons C_4H_6 + IC_4H_8$	3.16E+12	.0	.0
337.	$C_4H_6 + OH \rightleftharpoons AC_3H_5 + CH_2O$	7.23E+12	.0	-994.0
338.	$C_4H_6 + OH \rightleftharpoons C_4H_5 + H_2O$	2.17E+13	.0	4173.0
339.	$C_4H_6 + O \rightleftharpoons C_2H_4 + CH_2CO$	1.00E+12	.0	.0
340.	$C_4H_6 + O \rightleftharpoons PC_3H_4 + CH_2O$	1.00E+12	.0	.0
341.	$IC_4H_8 \rightleftharpoons C_4H_7 + H$	4.08E+18	-1.0	97350.0
342.	$IC_4H_8 \rightleftharpoons C2C_4H_8$	4.00E+11	.0	60000.0
343.	$IC_4H_8 \rightleftharpoons T2C_4H_8$	4.00E+11	.0	60000.0
344.	$IC_4H_8 \rightleftharpoons AC_3H_5 + CH_3$	8.00E+16	.0	74000.0
345.	$IC_4H_8 \rightleftharpoons C_2H_3 + C_2H_5$	2.00E+18	-1.0	96770.0
346.	$IC_4H_8 + O_2 \rightleftharpoons C_4H_7 + HO_2$	4.00E+12	.0	40000.0
347.	$IC_4H_8 + HO_2 \rightleftharpoons C_4H_7 + H_2O_2$	1.00E+11	.0	17060.0
348.	$IC_4H_8 + OH \rightleftharpoons NC_3H_7 + CH_2O$	6.50E+12	.0	.0
349.	$IC_4H_8 + OH \rightleftharpoons CH_3HCO + C_2H_5$	1.00E+11	.0	.0
350.	$IC_4H_8 + OH \rightleftharpoons C_2H_6 + CH_3CO$	1.00E+10	.0	.0
351.	$IC_4H_8 + OH \rightleftharpoons C_4H_7 + H_2O$	1.75E+13	.0	3060.0
352.	$IC_4H_8 + O \rightleftharpoons C_3H_6 + CH_2O$	2.51E+12	.0	.0
353.	$IC_4H_8 + O \rightleftharpoons CH_3HCO + C_2H_4$	1.25E+12	.0	850.0
354.	$IC_4H_8 + O \rightleftharpoons C_2H_5 + CH_3CO$	1.63E+13	.0	850.0
355.	$IC_4H_8 + O \rightleftharpoons C_4H_7 + OH$	1.30E+13	.0	4500.0

Table A.17: Reactions 321–355 in the Dagaut–Cathonnet–Boettner mechanism.

No.	Reaction	A	n	E_a
356.	$IC_4H_8 + H \rightleftharpoons C_4H_7 + H_2$	5.00E+13	.0	3900.0
357.	$IC_4H_8 + CH_3 \rightleftharpoons C_4H_7 + CH_4$	1.00E+11	.0	7300.0
358.	$IC_4H_8 + C_2H_5 \rightleftharpoons C_4H_7 + C_2H_6$	1.00E+11	.0	8000.0
359.	$IC_4H_8 + AC_3H_5 \rightleftharpoons C_4H_7 + C_3H_6$	8.00E+10	.0	12400.0
360.	$IC_4H_8 + SC_3H_5 \rightleftharpoons C_4H_7 + C_3H_6$	8.00E+10	.0	12400.0
361.	$IC_4H_8 + TC_3H_5 \rightleftharpoons C_4H_7 + C_3H_6$	8.00E+10	.0	12400.0
362.	$IC_4H_8 + C_4H_7 \rightleftharpoons C_4H_7 + C2C_4H_8$	3.98E+10	.0	12400.0
363.	$IC_4H_8 + C_4H_7 \rightleftharpoons C_4H_7 + T2C_4H_8$	3.98E+10	.0	12400.0
364.	$C2C_4H_8 \rightleftharpoons T2C_4H_8$	1.72E+14	.0	64280.0
365.	$C2C_4H_8 \rightleftharpoons C_4H_6 + H_2$	1.00E+13	.0	65500.0
366.	$C2C_4H_8 \rightleftharpoons C_4H_7 + H$	4.07E+18	-1.0	97350.0
367.	$C2C_4H_8 \rightleftharpoons SC_3H_5 + CH_3$	2.00E+16	.0	71300.0
368.	$C2C_4H_8 + OH \rightleftharpoons C_4H_7 + H_2O$	1.25E+14	.0	3060.0
369.	$C2C_4H_8 + OH \rightleftharpoons CH_3HCO + C_2H_5$	1.40E+13	.0	.0
370.	$C2C_4H_8 + O \rightleftharpoons IC_3H_7 + HCO$	6.03E+12	.0	.0
371.	$C2C_4H_8 + O \rightleftharpoons CH_3HCO + C_2H_4$	1.00E+12	.0	.0
372.	$C2C_4H_8 + H \rightleftharpoons C_4H_7 + H_2$	1.00E+13	.0	3500.0
373.	$C2C_4H_8 + CH_3 \rightleftharpoons C_4H_7 + CH_4$	1.00E+11	.0	8200.0
374.	$T2C_4H_8 \rightleftharpoons C_4H_7 + H$	4.07E+18	-1.0	97350.0
375.	$T2C_4H_8 \rightleftharpoons SC_3H_5 + CH_3$	2.00E+16	.0	71300.0
376.	$T2C_4H_8 + OH \rightleftharpoons C_4H_7 + H_2O$	1.00E+14	.0	3060.0
377.	$T2C_4H_8 + OH \rightleftharpoons CH_3HCO + C_2H_5$	1.50E+13	.0	.0
378.	$T2C_4H_8 + O \rightleftharpoons IC_3H_7 + HCO$	6.03E+12	.0	.0
379.	$T2C_4H_8 + O \rightleftharpoons CH_3HCO + C_2H_4$	1.00E+12	.0	.0
380.	$T2C_4H_8 + H \rightleftharpoons C_4H_7 + H_2$	5.00E+12	.0	3500.0
381.	$T2C_4H_8 + CH_3 \rightleftharpoons C_4H_7 + CH_4$	1.00E+11	.0	8200.0
382.	$C_4H_2 + M \rightleftharpoons C_4H + H + M$	3.50E+17	.0	80000.0
383.	$C_3H_3 + C_3H_3 \rightleftharpoons C_6H_6$	3.00E+11	.0	.0
384.	$C_3H_3 + AC_3H_4 \rightarrow C_6H_6 + H$	1.40E+12	.0	10000.0
385.	$AC_3H_5 + AC_3H_5 \rightleftharpoons C_6H_{10}$	1.02E+13	.0	-263.0
386.	$C_6H_{10} \rightarrow C_6H_9 + H$	1.00E+16	.0	85000.0
387.	$C_6H_{10} + OH \rightarrow C_6H_9 + H_2O$	3.70E+13	.0	.0
388.	$C_6H_9 \rightleftharpoons C_2H_3 + C_4H_6$	5.00E+13	.0	38000.0
389.	$CH_2CO + CH_3 \rightleftharpoons C_2H_5 + CO$	1.00E+12	.0	3000.0
390.	$CH_2CO + C_2H_3 \rightleftharpoons AC_3H_5 + CO$	1.00E+12	.0	3000.0
391.	$CH_2CO + CH_2 \rightleftharpoons C_2H_4 + CO$	2.00E+12	.0	3000.0

Table A.18: Reactions 356–391 in the Dagaut–Cathonnet–Boettner mechanism.

Appendix B

Surface Mechanism

The surface chemistry mechanism used in the flame model is listed in Table B.1. To describe the growth of diamond at the substrate surface, 21 surface reactions are considered [38]. This mechanism includes deposition and etching of diamond and recombination of some radical species at the substrate surface.

The model assumes a surface site density of 3×10^{-9} moles/cm^2, which is the surface carbon density on the (111) surface of diamond. The unit of A is cm^3/mol/sec and E_a is given in kcal/mol. Rates are given in terms of the sticking probability for reactions with "Stick" in the "Comments" column. "Fast" denotes that the reaction rate is set high enough such that the reaction is not the rate limiting step in the mechanism.

Eight different surface site types are assumed to be present at the surface. C_dH represents a hydrogen terminated site, C_d* an active site, and C_dM an adsorbed

methyl radical. C_dM^* represents a C_dM site after abstraction of an H atom. Four others are SA, SB, SD, and SE, which represent intermediate sites at the surface.

Reactions 1–6 implement a reduced form [14] of the methyl growth mechanism for diamond proposed by Harris [36].

Reactions 7 and 8 account for recombination of O and OH radicals at the surface by abstraction of an H atom.

Reactions 9 and 10 account for diamond etching by O_2 with an empirical fit to the experimental data of Sun and Alam [61].

Etching of diamond by OH and O is estimated in the upper limit by reactions 11 and 12. A single carbon atom is assumed to be etched into the gas phase each time an OH or O radical strikes an active site.

Reactions 13 and 14 allow recombination of CH at the surface through the intermediate site SD. The overall reaction is:

$$2CH + C_dH \rightarrow C_2H_2 + C_dH \tag{B.1}$$

Reactions 15–16 account for recombination of CH_2 at the surface in the same manner through the intermediate site SE. The overall reaction is:

$$2CH_2 + C_dH \rightarrow C_2H_4 + C_dH \tag{B.2}$$

Reactions 17–18 account for recombination of $CH_2(S)$ at the surface in the same

manner through the intermediate site SE. The overall reaction is:

$$2CH_2(S) + C_dH \rightarrow C_2H_4 + C_dH \tag{B.3}$$

Reactions 19-21 similarly account for recombination of C at the surface through the intermediate sites SA and SB. The overall reaction is:

$$2C + H_2 + C_dH \rightarrow C_2H_2 + C_dH \tag{B.4}$$

No.	Reaction	A	n	E_a	Comments
1.	$C_dH + H \rightleftharpoons C_d^* + H_2$	5.06E13	0	6.84	ΔG:-16.0
2.	$C_d^* + H \rightarrow C_dH$	0.43	0	0.0	Stick
3.	$C_d^* + CH_3 \rightarrow C_dM$	3.3E12	0	0.0	
4.	$C_dM \rightarrow C_d^* + CH_3$	1.E4	0	0.0	
5.	$C_dM + H \rightarrow C_dM^* + H_2$	2.E12	0	0.0	
6.	$C_dM^* + H \rightarrow C_dH + H_2$	1.E16	0	0.0	
7.	$C_dH + OH \rightleftharpoons C_d^* + H_2O$	2.47E6	2.152	0.3217	ΔG:-31.14
8.	$C_dH + O \rightleftharpoons C_d^* + OH$	2.14E5	2.5	0.924	ΔG:-19.74
9.	$C_dH + O_2 \rightarrow CO_2 + C_dH$	2.1E16	0	54.7	Order in O_2: 0.6
10.	$C_d^* + O_2 \rightarrow CO_2 + C_d^*$	2.1E16	0	54.7	Order in O_2: 0.6
11.	$C_d^* + OH \rightarrow CO + C_dH$	1.0	0	0.0	Stick
12.	$C_d^* + O \rightarrow C_d^* + CO$	1.0	0	0.0	Stick
13.	$CH + C_dH \rightarrow SD$	1.0	0	0.0	Stick
14.	$CH + SD \rightarrow C_dH + C_2H_2$	1.0E17	0	0.0	Fast
15.	$CH_2 + C_dH \rightarrow SE$	1.0	0	0.0	Stick
16.	$CH_2 + SE \rightarrow C_2H_4 + C_dH$	1.0E17	0	0.0	Fast
17.	$CH_2(S) + C_dH \rightarrow SE$	1.0	0	0.0	Stick
18.	$CH_2(S) + SE \rightarrow C_2H_4 + C_dH$	1.0E17	0	0.0	Fast
19.	$C + C_dH \rightarrow SA$	1.0	0	0.0	Stick
20.	$C + SA \rightarrow SB$	1.0E17	0	0.0	Fast
21.	$H_2 + SB \rightarrow C_dH + C_2H_2$	1.0E17	0	0.0	Fast

Table B.1: 21 Reactions in the surface chemistry mechanism.

References

[1] F. P. Bundy, H. T. Hall, H. M. Strong, and R. J. Wentorf, Nature **176**, 51 (1955).

[2] P. W. Bridgman, Sci. Am. **193**, 42 (1955).

[3] J. E. Field, *The Properties of Diamond* (Academic Press, London, 1979).

[4] W. Eversole, Synthesis of Diamond; U.S. Patents 3,030,187 and 3,030,188, (1962).

[5] J. C. Angus, H. A. Will, and W. S. Stanko, J. Appl. Phys. **39**, 2915 (1968).

[6] B. V. Spitsyn, L. L. Bouilov, and B. V. Derjaguin, J. Cryst. Growth **52**, 219 (1981).

[7] S. Matsumoto, Y. Sato, M. Kamo, and N. Setaka, Jpn. J. Appl. Phys. **21**, L183 (1982).

[8] P. K. Bachmann and W. V. Enckevort, Diamond and Related Materials **1**, 1021 (1992).

[9] G. Lu *et al.*, in *Proc. 3rd European Conf. on Diamond, Diamond-like and Related Coatings*, edited by P. K. Bachmann, A. T. Collins, and M. Seal (Elsevler, Heidelberg, Germany, 1992), pp. 1064–1068.

[10] N. Ohtake *et al.*, in *Proc. 1st Intl. Symp. Diamond and Diamond-like Films* (The Electrochemical Society, Pennington, NJ, 1989), p. 93.

[11] A. R. Badzian and R. C. DeVries, Mat. Res. Bull. **23**, 385 (1988).

[12] J. E. Butler and R. L. Woodin, Philos. Trans. R. Soc. London **342**, 209 (1993).

[13] J. C. Angus, Y. Wang, and M. Sunkara, Ann. Rev. Mater. Sci. **21**, 221 (1991).

[14] D. G. Goodwin, J. Appl. Phys. **74**, 6888 (1993).

[15] S. J. Harris, A. M. Weiner, and T. A. Perry, Appl. Phys. Lett. **53**, 1605 (1988).

[16] L. R. Martin and M. W. Hill, J. Mater. Sci. Lett. **9**, 621 (1990).

[17] S. J. Harris and L. R. Martin, J. Mater. Res. **5**, 2313 (1990).

[18] C. J. Chu, M. P. D'Evelyn, R. H. Hauge, and J. L. Margrave, J. Appl. Phys. **70**, 1695 (1991).

[19] C. J. Chu, M. P. D'Evelyn, R. H. Hauge, and J. L. Margrave, J. Mater. Res. **5**, 2405 (1990).

[20] S. J. Harris and A. M. Weiner, Thin Solid Films **212**, 201 (1992).

[21] S. J. Harris and A. M. Weiner, J. Appl. Phys. **70**, 1385 (1991).

[22] M. H. Loh and M. A. Cappelli, Diamond and Related Materials **2**, 454 (1993).

[23] Y. Hirose and M. Mitsuizumi, New Diamond **4**, 34 (1988).

[24] M. Murayama, S. Kojima, and K. Uchida, J. Appl. Phys. **69**, 7924 (1991).

[25] M. Murayama and K. Uchida, Combustion and Flame **91**, 239 (1992).

[26] K. V. Ravi, C. A. Koch, and D. Olson, in *Proc. 2nd Intl. Conf. Applications of Diamond Films and Related Materials*, edited by M. Yoshikawa, M. Murakawa, Y. Tzeng, and W. A. Yarbrough (MYU, Tokyo, 1993), pp. 491–496.

[27] K. F. McCarty, E. Meeks, R. J. Kee, and A. E. Lutz, Appl. Phys. Lett. **63**, 1498 (1993).

[28] J. A. Cooper, Jr. and W. A. Yarbrough, in *Diamond Optics III (SPIE Proceedings Vol. 1325)*, edited by A. Feldman and S. Holly (SPIE, Bellingham, Washington, 1990), pp. 41–54.

[29] N. G. Glumac and D. G. Goodwin, Thin Solid Films **212**, 122 (1992).

[30] N. G. Glumac and D. G. Goodwin, Materials Letters **18**, 119 (1993).

[31] J. S. Kim and M. A. Cappelli, J. Mater. Res. **10**, 149 (1995).

[32] D. G. Goodwin, Appl. Phys. Lett. **59**, 277 (1991).

[33] J. S. Kim and M. A. Cappelli, J. Appl. Phys. **72**, 5461 (1992).

[34] J. A. Miller and C. T. Bowman, Prog. Energy Combust. Sci. **15**, 287 (1989).

[35] J. A. Miller and C. F. Melius, Comb. Flame **91**, 21 (1992).

[36] S. J. Harris, Appl. Phys. Lett. **56**, 2298 (1990).

[37] E. Meeks, R. J. Kee, D. S. Dandy, and M. E. Coltrin, Combustion and Flame **92**, 144 (1993).

[38] N. G. Glumac, Ph.D. thesis, California Institute of Technology, Pasadena, CA, 1994.

[39] K. E. Bertagnolli and R. P. Lucht, Temperature measurements in a stagnation-flow, diamond-forming flame using CARS spectroscopy of hydrogen, 1995, spring meeting, The Combustion Institute.

[40] W. Carrington *et al.*, Metallurgical Transactions **20A**, 1282 (1989).

[41] K. A. Snail *et al.*, Carbon **28**, 794 (1990).

[42] J. S. Kim and M. A. Cappelli, Appl. Phys. Lett. **65**, 2786 (1994).

[43] S. S. Zabrodsky, *Hydrodynamics and Heat Transfer in Fluidized Beds* (The M.I.T. Press, Cambridge, 1966).

[44] S. Morooka, T. Okubo, and K. Kusakabe, Powder Technology **63**, 105 (1990).

[45] D. G. Goodwin, J. Appl. Phys. **74**, 6895 (1993).

[46] T. Okubo, H. Kawamura, K. Kusakabe, and S. Morooka, J. Am. Ceram. Soc. **73**, 1150 (1990).

[47] H. Kawamura, T. Okubo, K. Kusakabe, and S. Morooka, J. Mater. Sci. Lett. **9**, 1033 (1990).

[48] Jpn. Kokai Tokkyo Koho, Jpn Pat. unexamined application, S59-137311 (1984).

[49] Jpn. Kokai Tokkyo Koho, Jpn Pat. unexamined application, H1-157497 (1989).

[50] T. Takarada *et al.*, J. Mater. Sci. **28**, 1545 (1993).

[51] E. Kondoh, T. Ohta, T. Mitomo, and K. Ohtsuka, Appl. Phys. Lett. **59**, 488 (1991).

[52] W. L. Hsu, in *Proc. 2nd Intl. Symp. Diamond and Related Materials*, edited by A. J. Purdes *et al.* (The Electrochemical Society, Pennington, NJ, 1991), pp. 217–223.

[53] D. G. Goodwin and G. G. Gavillet, J. Appl. Phys. **68**, 6393 (1990).

[54] D. G. Goodwin, *Program STBL Documentation*, California Institute of Technology, 1994.

[55] R. J. Kee, F. M. Rupley, and J. A. Miller, Technical Report No. SAND89-8009, Sandia National Laboratories (unpublished).

[56] R. J. Kee *et al.*, Technical Report No. SAND86-8246, Sandia National Laboratories (unpublished).

[57] J. S. Kim and M. A. Cappelli, J. Appl. Phys. **72**, 5461 (1992).

[58] R. J. Kee, J. A. Miller, G. H. Evans, and G. Dixon-Lewis, in *Twenty-second Symposium (International) on Combustion* (The Combustion Institute, Pittsburgh, Pa., 1988), pp. 1479–1494.

[59] R. J. Kee, F. M. Rupley, and J. A. Miller, Technical Report No. SAND87-8215, Sandia National Laboratories (unpublished).

[60] S. J. Harris and D. G. Goodwin, J. Phys. Chem. **97**, 23 (1993).

[61] Q. Sun and M. Alam, J. Electrochem. Soc. **139**, 933 (1992).

[62] S. J. Harris, A. M. Weiner, R. J. Blint, and J. E. M. Goldsmith, in *Twenty-first Symposium (International) on Combustion* (The Combustion Institute, Pittsburgh, PA, 1986), p. 1033.

[63] W. L. Hsu, Appl. Phys. Lett. **59**, 1427 (1991).

[64] Welding, Cutting and Heating Guide, Victor Equipment Company, 1988.

[65] D. Smock, Plastics World **52**, 67 (1994).

[66] P. Dagaut, M. Cathonnet, and J. C. Boettner, International Journal of Chemical Kinetics **24**, 813 (1992).

[67] P. Dagaut, M. Cathonnet, and J. C. Boettner, Combustion Science and Technology **83**, 167 (1992).

[68] A. Sepehrad, R. M. Marshall, and H. Purnell, International Journal of Chemical Kinetics **11**, 411 (1979).

[69] M. Yoder, in *Proc. 2nd Intl. Symp. Diamond Materials*, edited by A. J. Purdes *et al.* (The Electrochemical Society, Pennington, NJ, 1991), pp. 513–522.

[70] Y. Liou *et al.*, J. Mater. Res. **5**, 2305 (1990).

[71] K. V. Ravi, in *Proc. 2nd Intl. Symp. Diamond Materials*, edited by A. J. Purdes *et al.* (The Electrochemical Society, Pennington, NJ, 1991), pp. 31–38.

[72] W. A. Weimer and C. E. Johnson, in *Diamond Optics III*, edited by A. Feldman and S. Holly (SPIE-The International Society for Optical Engineering, Bellingham, WA, 1990), pp. 56–62.